UNCLASSIFIED

DTIC FILE COPY

AD-A229 493

DTIC ELECTE NOV 30 1990 S B D

DOCUMENTATION PAGE

Form Approved
OMB No 0704 0188

| | |
|---|---|
| 1b RESTRICTIVE MARKINGS | |
| 2b DECLASSIFICATION / DOWNGRADING SCHEDULE | 3 DISTRIBUTION/AVAILABILITY OF REPORT<br>Approved for public release; distribution unlimited |
| 4 PERFORMING ORGANIZATION REPORT NUMBER(S)<br>VPI-AOE-174 | 5 MONITORING ORGANIZATION REPORT NUMBER(S) |

| 6a NAME OF PERFORMING ORGANIZATION<br>Aerospace and Ocean Engineering Department | 6b OFFICE SYMBOL<br>(If applicable) | 7a NAME OF MONITORING ORGANIZATION<br>Office of Naval Research<br>Applied Hydrodynamics Research Program |
|---|---|---|
| 6c ADDRESS (City, State, and ZIP Code)<br>Virginia Polytechnic Institute and State University<br>Blacksburg, VA 24061 | | 7b ADDRESS (City, State, and ZIP Code)<br>800 N. Quincy St.<br>Arlington, VA 22217 |
| 8a NAME OF FUNDING/SPONSORING ORGANIZATION Office of Naval Research, Applied Hydrodynamics Research Program | 8b OFFICE SYMBOL<br>(If applicable) | 9 PROCUREMENT INSTRUMENT IDENTIFICATION NUMBER<br>N00014-87-K-0816 |
| 8c ADDRESS (City, State, and ZIP Code)<br>800 N. Quincy St.<br>Arlington, VA 22217 | | 10 SOURCE OF FUNDING NUMBERS |

| PROGRAM ELEMENT NO | PROJECT NO | TASK NO | WORK UNIT ACCESSION NO |
|---|---|---|---|
| | | | |

11 TITLE (Include Security Classification)

Mean Velocity and Turbulence Measurements of Flow Around a 6:1 Prolate Spheroid

12 PERSONAL AUTHOR(S)
K. M. Barber and R. L. Simpson

| 13a TYPE OF REPORT<br>Technical | 13b TIME COVERED<br>FROM 10/1/88 TO 5/31/90 | 14 DATE OF REPORT (Year, Month, Day)<br>1990 July 10 | 15 PAGE COUNT<br>255 |
|---|---|---|---|

16 SUPPLEMENTARY NOTATION

| 17 | COSATI CODES | | 18 SUBJECT TERMS (Continue on reverse if necessary and identify by block number) |
|---|---|---|---|
| FIELD | GROUP | SUB-GROUP | Three-dimensional separated turbulent flow |
| 13 | 10 | 01 | |
| 20 | 04 | | |

19. ABSTRACT (Continue on reverse if necessary and identify by block number)

Investigations of three-dimensional flow around a 6:1 prolate spheroid model were conducted in the separation and near wake regions along the leeward side. Mean velocity flow field measurements, at $\alpha = 10°$ and $15°$, and at Re $= 4.3 \times 10^6$, were obtained at four axial locations along the afterbody. Boundary layer profiles and Reynolds shear stress measurements were obtained at two axial locations, with $\alpha = 10°$ and Re $= 4.0 \times 10^6$.

Results of the flow field measurements indicate vortical flow along the surface of the body, growing in strength with increasing Reynolds number and increasing angle of attack. Skewing of the three-dimensional boundary layer is seen in the boundary layer profiles, with the surface shear stress direction lagging the local free-stream velocity direction. Growth of the boundary layer is evident circumferentially and axially along the body. Results of the turbulence measurements show that the distribution of Reynolds stress quantities is different from that of a two-dimensional flow over a flat plate, due to the three-dimensional flow and separation that is present. Estimates of x and z eddy viscosities show that the eddy viscosity is not isotropic. Estimates of the mixing length compared to values for a two-dimensional flow model indicate that the model predicts high values for the mixing length. Comparisons made with results obtained at DFVLR in West Germany show good agreement for the mean velocity and Reynolds normal stress values; however, the agreement of the Reynolds shear stresses is not as good. Keywords: Aerodynamics; Turbulent flow; Boundary layer transition; Turbulent boundary layer; Flow separation; Wind tunnel models;

| 20 DISTRIBUTION/AVAILABILITY OF ABSTRACT<br>[X] UNCLASSIFIED/UNLIMITED ☐ SAME AS RPT ☐ DTIC USERS | 21 ABSTRACT SECURITY CLASSIFICATION<br>None |
|---|---|
| 22a NAME OF RESPONSIBLE INDIVIDUAL | 22b TELEPHONE (Include Area Code) | 22c OFFICE SYMBOL |

DD Form 1473, JUN 86     Previous editions are obsolete     SECURITY CLASSIFICATION OF THIS PAGE

UNCLASSIFIED

iii

# Table of Contents

# List of Illustrations

# List of Tables

# List of Symbols

Al . . . . . Townsend's structural parameter

H . . . . . . shape factor, $H = \delta^*/\theta$

$I_1, I_2, I_3$ . . . Reynolds stress tensor invariants

k . . . . . . turbulent kinetic energy, $k = \dfrac{\overline{u^2} + \overline{v^2} + \overline{w^2}}{2}$

L . . . . . . length of 6:1 prolate spheroid model

$L_m$ . . . . . mixing length

$L_{m2D}$ . . . . mixing length from model for two-dimensional zero pressure gradient boundary layer

N . . . . . . eddy viscosity anisotropic constant, $N = v_z/v_x$

$P_t$ . . . . . . stagnation pressure

q . . . . . . dynamic pressure, $q = \rho U^2/2$

Re . . . . . Reynolds number based on length of model

U . . . . . . local mean velocity in X-direction of respective coordinate system

$U_c$ . . . . . component of $U_{rc}$ in X-direction

$U_r$ . . . . . . resultant local mean velocity

$U_{rc}$ . . . . . local free-stream velocity

$U_\infty$ . . . . . tunnel free stream velocity

$\overline{u^2}$ . . . . . mean square of velocity fluctuation in X-direction

$-\overline{uv}$ . . . . . kinematic Reynolds shear stress, $\tau_{xy}/\rho$

$-\overline{uw}$ . . . . kinematic Reynolds shear stress, $\tau_{xz}/\rho$

$V$ . . . . . . local mean velocity in Y-direction of respective coordinate system

$V_c$ . . . . . . component of $U_{rc}$ in Y-direction

$\overline{v^2}$ . . . . . mean square of velocity fluctuation in Y-direction

$-\overline{vw}$ . . . . . kinematic Reynolds shear stress, $\tau_{yz}/\rho$

$W$ . . . . . . local mean velocity in Z-direction of respective coordinate system

$W_c$ . . . . . component of $U_{rc}$ in Z-direction

$\overline{w^2}$ . . . . . mean square of velocity fluctuation in Z-direction

$X$ . . . . . . distance measured from nose of model along model centerline

$X_B$ . . . . . body-fixed coordinate axis

$X_b$ . . . . . local body coordinate axis

$X_{fs}$ . . . . . local free stream coordinate axis

$X_H$ . . . . . x-wire probe coordinate axis

$X_T$ . . . . . tunnel coordinate axis

$Y_B$ . . . . . body-fixed coordinate axis

$Y_b$ . . . . . local body coordinate axis

$Y_{fs}$ . . . . . local free stream coordinate axis

$Y_H$ . . . . . x-wire probe coordinate axis

$Y_T$ . . . . . tunnel coordinate axis

$Z_B$ . . . . . body-fixed coordinate axis

$Z_b$ . . . . . . local body coordinate axis

$Z_{fs}$ . . . . . local free stream coordinate axis

$Z_H$ . . . . . x-wire probe coordinate axis

$Z_T$ . . . . . tunnel coordinate axis


Greek Symbols


$\alpha$ . . . . . . angle of attack of model. pitch angle

$\alpha_{fs}$ . . . . . angle for turbulence data tensor transformation

$\alpha_g$ . . . . . . flow gradient angle

$\alpha_m$ . . . . . yawhead probe pitch misalignment angle

$\alpha_s$ . . . . . . shear stress angle

$\beta$ . . . . . . flow angle

$\beta_{fs}$ . . . . . local free stream velocity flow angle

$\beta_m$ . . . . . yawhead probe yaw misalignment angle

$\beta_{surf}$ . . . . . flow angle of velocity at surface of body

$\delta_{99}$ . . . . . boundary layer thickness, where $U_r/U_{rc}=0.99$

$\delta^*$ . . . . . . displacement thickness

$\theta$ . . . . . . momentum thickness

$\theta_1,\theta_2$ . . . . effective angles of x-wire sensors

$\nu_x,\nu_z$ . . . . . kinematic eddy viscosities in X and Z directions

$\rho$ . . . . . . density of the flow

$\tau$ . . . . . . total turbulent shear stress, $\tau = \sqrt{\overline{(uv)}^2 + \overline{(vw)}^2}$

$\varphi$ . . . . . . circumferential angle, measured with respect to $-Z_T$ axis

$\varphi_m$ . . . . . yawhead probe roll misalignment angle

$\psi$ . . . . . . x-wire probe roll angle

$\Omega_X$ . . . . . vorticity in $X_T$-direction

# 1.0 Introduction

The physical processes that occur in the boundary layer along a streamlined body at incidence are very complex and far from being completely understood. These include such phenomena as transition from laminar to turbulent flow, the presence of a three-dimensional laminar or turbulent boundary layer with strong crossflow, three-dimensional laminar or turbulent boundary layer separation, and the formation of longitudinal vortices extending into the wake.

The successful understanding and modeling of these physical processes can prove fruitful in many applications. The ability to control transition and separation can aid in decreasing the aerodynamic drag on a body. Improvements in the maneuverability of aircraft, missiles, and submarines can result from the understanding of the processes involved in three-dimensional turbulent boundary layers and the formation of longitudinal vortices.

Solutions of the Navier-Stokes equations can yield accurate predictions for complex flows, including separation; however, such solutions would require tremendous

computer resources and their accuracy is dependent upon results from turbulence models. In the past, attempts to develop three dimensional boundary layer models including separation and transition have not met with great success and the extension of two-dimensional models to three-dimensional situations has not provided consistently useful results. For the time being, experimental data must be used as a basis for understanding these complex flows.

The great interest in transition and separation phenomena, and in flow characteristics in the presence of vortical flow, is shown by the amount of experimental research that has been dedicated to investigating the processes that occur in these flows. A number of experimentalists have investigated flow around generic axisymmetric bodies, such as a 6:1 prolate spheroid, because the flow field around such a body is made up of the same features that are of interest when considering the flow field around an aircraft fuselage, a missile, or a submarine.

Research conducted at DFVLR in West Germany on a 2.4 meter long 6:1 prolate spheroid has obtained a great amount of experimental data. Wall shear stress measurements, surface oil flow visualization, surface pressure measurements, and mean velocity field measurements have yielded information about boundary layer transition and separation (Kreplin, *et al.*, 1980, 1982; Meier and Kreplin, 1980; Meier, *et al.*, 1981a, 1981b, 1982, 1983a, 1983b). Mean boundary layer profile measurements are presented in Meier, *et al.*(1984), and outer mean velocity field measurements are given in Vollmers, *et al.*(1985). Results of some preliminary turbulence measurements obtained at DFVLR are presented in Kreplin and Vollmers (1981). Table 1 shows the flow

conditions for the various measurements conducted at DFVLR. The results of all these experiments are used as a test case by other researchers.

Cooperative research conducted between DFVLR and ONERA has resulted in detailed investigations of turbulent separation on an oblate spheroid, including surface flow visualization, surface pressure measurements and velocity field measurements (Chanetz, 1986; Barberis and Chanetz, 1986; Chanetz and Delery, 1988).

A Sino-Italian research program investigating the three-dimensional flow around a 6:1 prolate spheroid has yielded results for flow visualization, pressure and force measurements, boundary layer measurements, and velocity field measurements (Iuso, *et al.*, 1988).

Besides investigating transition and separation phenomena around an axisymmetric body, a number of researchers have studied the interactions of a vortex and a turbulent boundary layer. Westphal, *et al.* (1985) investigated such interactions in the presence of a streamwise pressure gradient. Pauley and Eaton (1988, 1989) studied the effects of vortex pairs embedded in a turbulent boundary layer. Other work has been don  by Bradshaw and his co-workers (Cutler and Bradshaw, 1986; Shabaka, Mehta and Bradshaw, 1985; Mehta and Bradshaw, 1988). All of these investigations include mean velocity and Reynolds shear stress measurements to study the behavior of the flows.

This research is part of an overall investigation of the flow field around a 6:1 prolate spheroid, in both steady and unsteady flows. The present study involves the investigation of the region of separation on the leeward surface of the 6:1 prolate spheroid at moderate angles of attack in a steady flow. Mean velocity field measurements

in the near wake region with the model at angles of attack $\alpha = 10°$ and $15°$ and $Re = 1.3 \times 10^6$ and $4.0 \times 10^6$ allow the analysis and description of the structure of the vortical flow field. Mean velocity and turbulence measurements in the boundary layer at $\alpha = 10°$ and $Re = 4.0 \times 10^6$ allow the analysis and description of the three-dimensional turbulent boundary layer. including the growth of the boundary layer along the surface of the model. and any crossflow and separation phenomena that are evident. The turbulence measurements are used to attempt to appraise the extension of two-dimensional turbulence models to three-dimensional flows. The choices of angle of attack $\alpha$ and $Re$ are based upon the results of the mean flow field measurements and the surface oil flow measurements which indicate that at these conditions. flow phenomena leading to separation occur over an extended region along the surface of the model.

The results of this study can possibly be used as a basis for testing the validity of three-dimensional turbulence models by providing experimental data for comparison. More importantly. the results can be useful for comparison when future measurements are made for unsteady flow around the same 6:1 prolate spheroid model. as part of a continuing investigation of transition and separation processes.

# 2.0 Experimental Apparatus and Instrumentation

## 2.1 Wind Tunnel

All the measurements were conducted in the Virginia Polytechnic Institute and State University Stability Wind Tunnel. This wind tunnel is a continuous, closed test section subsonic wind tunnel with interchangeable round and square cross-section test sections. Originally constructed in 1940 at NASA Langley in Hampton, Virginia, the tunnel was moved to Virginia Tech in 1958.

As shown in Figure 1, this wind tunnel is a closed-loop tunnel powered by a 600 HP D.C. motor driving a propeller 4.27 meters in diameter. This provides a maximum speed of 67 mps in a normal six feet by six feet test section configuration. An air-exchange tower located downstream of the fan and motor assembly provides temperature stabilization. Each corner of the wind tunnel circuit has streamlined turning vanes spaced along the diagonal of the corner to provide uniform flow. Upstream of the test section, in the settling chamber, are seven turbulence screens. Between the test section and the

settling chamber is a nozzle with a 9:1 contraction ratio. Downstream of the test section is a diffuser with an angle of 3°. Vortex generators located at the beginning of the diffuser aid in efficient diffuser operation.

The test section used in these measurements is 23 feet long, with a six feet by six feet square cross section. An air-tight test and control room encloses the test section to minimize air leakage into the test section. The 6:1 prolate spheroid model was mounted on a dummy balance and sting and supported in the test section by a six-feet tall strut. The strut and sting allowed the model to be set at angles of attack between approximately -15° and +22°.

## 2.2 6:1 Prolate Spheroid Model

The 6:1 prolate spheroid model used in these experiments is 1.37 meters (54 inches) in length and has a maximum diameter of 0.23 meters (9 inches). The model, shown in Figure 2 and 3, consists of a forward and aft section of identical design, with an aluminum internal framework of four bulkheads and eight longerons surrounded by a fiberglass skin. The two sections are joined together by a center section, an aluminum cylinder covered by fiberglass skin, that can accommodate a balance and sting. Interchangeable aluminum nose and tail pieces are mounted at the respective ends of the forward and aft sections. The tail piece allows the sting and balance to pass through the hollow interior of the model for mating with the center section.

## 2.3 Tunnel Traverse and Coordinate System

The probes used in all the measurements were mounted on a traverse unit that allowed movement in both horizontal and vertical directions. These directions correspond to $Z_T$ and $Y_T$, respectively, as defined by the right-hand orthogonal tunnel coordinate system, shown in Figure 4, used throughout the experiments. The circumferential angle $\varphi$ is measured with respect to the $-Z_T$ axis and is positive in the direction of the $Y_T$ axis. The traverse mechanism, controlled by two separate manually-operated control units, allowed a minimum movement of 0.254 mm (0.01 inches) in the horizontal ($Z_T$) direction and 0.1 mm (0.0039 inches) in the vertical ($Y_T$) direction. Before each run, the probes were placed at the desired location in the $X_T$ direction by changing the position of adjustable brackets used to mount the probes on the traverse.

## 2.4 Three-Dimensional Yawhead Probe Instrumentation

A United Sensor DC125 three-dimensional yawhead probe (United Sensor Catalog) was used to obtain mean velocity field measurements in the near wake region. This probe has a blunt conical head with five pressure ports, one port in the center surrounded by four ports spaced 90° apart. The magnitude of the velocity and its pitch

and yaw angles are found by measuring the pressure at all five ports. The probe calibration used (Sung, 1985) allowed the determination of velocity vectors within a $60°$ cone from the axis of the probe.

The probe was mounted on the $Y_T$-$Z_T$ traverse described in Section 3.3.1, and oriented parallel to the $X_T$ direction. Any probe misalignment with the $X_T$ axis was measured using a cathetometer and a digital protractor, and corrections were made during the data reduction. The position of the probe with respect to the body was measured using a cathetometer.

The five pressure ports on the probe were connected to a Scanivalve Model D pressure scanner capable of scanning 48 pressure ports. A Hewlett Packard 59306A Relay Actuator and a pressure scanner controller actuated the pressure scanner. The pressure from each port of the pressure scanner was read by a Druck Type PDCR22 differential pressure transducer with an input range of $\pm 1$ psid.

A Pitot-static tube with a Datametric Model 1173 manometer measured the free-stream dynamic pressure. A Valdyne Model DB99 digital barometer measured the test section static pressure. An Instrulab Model 1563 digital thermometer measured the free-stream temperature. The signals from these and from the pressure transducer were scanned by a Hewlett Packard 3495A scanner and measured by a Hewlett Packard 3455A digital voltmeter. A Hewlett Packard 9836 computer controlled the data acquisition system. A schematic diagram of the data acquisition and control system is shown in Figure 5.

## 2.5 Hot-Wire Anemometry Instrumentation

Velocity profiles and Reynolds stress components in the boundary layer of the inclined prolate spheroid were measured using a DANTEC 55P61 x-wire probe in conjunction with two Miller-type (Miller, 1976) integrated circuit constant temperature hot wire anemometers and linearizers, as modified by Simpson, et al. (1979) The x-wire probe consists of two platinum-plated tungsten wire sensors 1.25 mm in length and 5 $\mu$m in diameter, with a spacing of 1 mm between the sensor wires. The geometry of the probe is shown in Figure 6. An overheat ratio of 1.7 was used, and the linearized calibrations had low dispersion from a straight line, with a correlation coefficient greater than 0.999.

To obtain all six Reynolds stress values at a data point, an x-wire probe must be rotated around its axis. In addition, the probe should be aligned within 10° of the mean flow direction for accuracy. As shown in Figure 7, a probe support with rolling and pitching capabilities was designed and built to accommodate these requirements. This support was manufactured by the Virginia Tech Aerospace and Ocean Engineering Shop. When mounted on the $Y_T$-$Z_T$ traverse described previously in Section 2.3, this support allowed the x-wire probe to be pitched from 0° to 15°, enabling alignment of the probe as closely as possible with the mean velocity for a given profile. A Compumotor CXT32-39 stepper motor and indexer (Compumotor Catalog, 1987) controlled by an IBM PS/2 Model 30 computer through an RS-232 interface was utilized to roll the probe along its axis. This stepper motor allowed highly accurate angular displacement of the probe,

with 25,000 microsteps per revolution and an absolute accuracy of 0.0835°. As shown in Figure 7, a guide tube with two struts mounted on the face of the probe support insured that the probe was aligned along its axis. A dial indicator and a cathetometer were used to measure the probe tip displacement from centerline to adjust the alignment.

As shown in the schematic diagram of Figure 8, the voltage signals for the two wire sensors were sampled using an R.C. Electronics ISC-16 A/D board mounted in an IBM PS/2 Model 30 computer. This A/D board has sixteen channels with an aggregate sampling rate of up to 1 Mhz and 12-bit accuracy over an input range of -10 to +10 volts. A Hewlett Packard 3478A multimeter and a Tektronix oscilloscope were used to monitor the hot wire signals. The PS/2 Model 30 also controlled the indexer for the stepper motor as mentioned previously. The Stability Tunnel Hewlett Packard computer system, described in Section 2.4, was used to monitor the tunnel status and obtain the free-stream conditions.

# 3.0 Experimental Techniques and Data Reduction

## 3.1 Test Conditions and Measurement Locations

The investigations were performed at different axial locations along the afterbody of the model. These locations are designated by X/L, where X is the distance measured from the nose of the model along its axis of symmetry, and L is the length of the model, 1.37 meters (54 inches). Figure 9 shows the planes where the measurements were made. These are X/L=0.6, 0.7, 0.8, and 0.9. At each axial location, data were obtained in a plane parallel to the $Y_T$-$Z_T$ plane.

For the outer velocity field measurements, the model was inclined at angles of attack $\alpha = 10°$ and 15°. Measurements were made at X/L=0.6, 0.7, 0.8, and 0.9. For all the locations, free-stream velocities of approximately 15.2 mps (50 fps) and 45.7 mps (150 fps) were used, giving Reynolds numbers based on the length of the model of $1.3 \times 10^6$ and $4.0 \times 10^6$, respectively, at a temperature of 25°C.

Boundary layer mean velocity and turbulence measurements were obtained for a Reynolds number of $4.0 \times 10^6$ at $\alpha = 10°$ and X/L=0.7 and 0.8.

## 3.2 Mean Velocity Field Measurements

Outer mean velocity field measurements in the $Y_T$-$Z_T$ plane at each axial location of the inclined prolate spheroid were made using the yawhead probe described in Section 2.4. At each data point, the five ports were scanned and the pressure from each port was averaged over 25 samples. A computer program used by Choi and Simpson (1987) controlled the scanning operation. This program also performed online data reduction using the yawhead probe calibration and data reduction method of Sung (1985). This method is explained in Appendix A. The free-stream temperature, dynamic pressure, and barometric pressure were recorded for each data point. The velocity components were first found in probe coordinates and then transformed into tunnel coordinates, taking into account probe misalignment with the $X_T$-axis. Probe misalignment angles are shown in Figure 10 along with their relation to tunnel coordinates.

The sensitivity of the differential pressure transducer was found using a three point calibration. An AMTEK Model MK 100 pneumatic pressure tester was used to apply pressures of 0 psid and $\pm 1$ psid to the transducer, and the transducer voltage output was assumed linear in this range. During the data acquisition, a sixth port on the Scanivalve pressure scanner was fed 1 psi of pressure to monitor the calibration of the transducer.

## 3.3 Velocity Profiles and Turbulence Measurements

Velocity profiles and Reynolds stress quantities near the surface of the inclined prolate spheroid were obtained in the $Y_T$-$Z_T$ plane at two axial locations using the x-wire probe supported by the rolling and pitching mount described in Section 2.5. Figure 6 shows the probe coordinate system and the definitions of roll angle $\psi$ and wire angles $\theta_1$ and $\theta_2$. To obtain all six Reynolds stress quantities and all three mean velocity components. the probe was rolled to the following positions:

(a) U-V plane      ($\psi = 0°$)

(b) +45° plane      ($\psi = 45°$)

(c) U-W plane      ($\psi = 90°$)

(d) +135° plane      ($\psi = 135°$)

(e) U-V plane      ($\psi = 180°$)

A description of the data reduction method. equations used. and derivations is given in Appendix B.

Initial calibrations of the x-wire probe were made using a TSI Model 1125 calibrator at various probe orientations with respect to the flow to obtain tangential and normal cooling factors. A description of the choice for these factors is given in Appendix B. Before and after each run. the probe was placed in the tunnel free stream and aligned in the $X_T$ direction. and in-tunnel calibrations were made at various flow speeds. As

mentioned previously, each linearized calibration had a correlation coefficient greater than 0.999.

Before acquiring data, the probe was pitched to the desired angle, based on the previous mean flow measurements, to align the probe as closely as possible to the mean velocity for a given profile. The probe was adjusted to the proper axial ($X_T$) location along the model. Setting the pitch angle of the probe and positioning the probe at the proper $X_T$ location were accomplished using the probe support with adjustable pitch angle capabilities described in Section 2.5 and shown in Figure 7. A cathetometer was used to measure the pitch angle of the probe with respect to the $X_T$ axis. The $Y_T$-$Z_T$ traverse was used to place the probe in the correct position for a given profile. During the measurements, the probe was moved to each data point in the profile using the $Y_T$-$Z_T$ traverse. A cathetometer was used to measure the location of the probe relative to the model. At each data point, the probe was rolled about its axis to the angles described above. For each angle, the voltage pairs were sampled at 820 Hz to obtain 16384 samples over a twenty second period. Mean and RMS quantities of the voltages were stored on disk. In addition, the tunnel free-stream dynamic pressure, temperature, and barometric pressure were recorded for each data point.

The data were reduced using the method outlined in Appendix B to obtain mean velocity components and Reynolds stresses at each point in probe coordinates, and a tensor transformation was used to find these values in tunnel coordinates. The method of Larsen and Busch (1974), described in Appendix B, was used to correct for

temperature differences between the calibrations and the acquired data. The computer program listed in Appendix B was used to perform the data reduction.

## 3.4 Uncertainty Analysis

Uncertainties in the yawhead probe measurements include uncertainties in measuring the probe misalignment with respect to the $X_T$-axis. Other uncertainties include those in velocity vector field measurements made using the yawhead probe. The following RMS errors are given by Sung (1985) for this probe:

| | |
|---|---|
| Pitch angle $\alpha$ | $\pm 3.93°$ |
| Yaw angle $\beta$ | $\pm 2.36°$ |
| Stagnation pressure $P_t$ | $\pm 4.82\%$ |
| Dynamic pressure q | $\pm 5.33\%$ |
| Total Velocity $U_{tot}$ | $\pm 2.73\%$ |

The effects of these uncertainties on the measured mean velocities in tunnel coordinates were estimated. and the following values were found:

| | |
|---|---|
| Mean Velocity U | $\pm 0.035U$ |
| Mean Velocity V | $\pm 0.045U$ |
| Mean Velocity W | $\pm 0.050U$ |

Appendix B briefly details the agreement among the estimates for each of the quantities obtained using the x-wire probe. In addition, various sources of uncertainty exist that must be considered, including the following:

1. Probe position

2. Probe pitch angle misalignment

3. Angle of attack of model

4. Hot-wire instrumentation and calibration

5. Resolution of voltage signals

6. Probe geometry

7. Tunnel free-stream temperature

8. Tunnel free-stream dynamic pressure

9. Tunnel static pressure

An attempt was made to determine the magnitude of the uncertainty associated with each source of error. An additional source of error exists due to the 1 mm spacing between the two sensors on the x-wire probe. Because the probe is rolled about its longitudinal axis to obtain all six Reynolds stress components, the data are acquired for a measurement volume, instead of a measurement point. Therefore, some uncertainties in the measured quantities exist due to this uncertainty in the actual measurement location.

The overall effects of the uncertainties listed above on the mean velocities and the turbulence quantities were investigated using a perturbation computer program incorporating the methods of Kline and McClintock (1953) and Moffat (1982). The following estimates for the uncertainties in the measured quantities were found:

| | |
|---|---|
| Mean Velocity U | $\pm 0.033U$ |
| Mean Velocity V | $\pm 0.035U$ |
| Mean Velocity W | $\pm 0.040U$ |
| Reynolds Stress $\overline{u^2}$ | $\pm 0.090\overline{u^2}_{max}$ |
| Reynolds Stress $\overline{v^2}$ | $\pm 0.090\overline{u^2}_{max}$ |
| Reynolds Stress $\overline{w^2}$ | $\pm 0.12\overline{u^2}_{max}$ |
| Reynolds Stress $\overline{uv}$ | $\pm 0.16\overline{uv}_{max}$ |
| Reynolds Stress $\overline{uw}$ | $\pm 0.17\overline{uv}_{max}$ |
| Reynolds Stress $\overline{vw}$ | $\pm 0.27\overline{uv}_{max}$ |

For the uncertainties in the Reynolds stress values. $\overline{u^2}_{max}$ and $\overline{uv}_{max}$ refer to the maximum values in each measurement profile.

# 4.0 Experimental Results and Discussion

## 4.1 Mean Velocity Field Measurements

Mean velocity field measurements were made in vertical planes along the leeward side of the body at $X/L = 0.6$, 0.7, 0.8, and 0.9, measured along the centerline axis of the model. The model was placed at angles of attack $\alpha$ of $10°$ and $15°$ with respect to the wind tunnel free stream, and data were obtained for Reynolds numbers of $1.3 \times 10^6$ and $4.0 \times 10^6$. The measurements were made with a grid spacing of 1.27 cm (0.5 inches) in the $Y_T$ and $Z_T$ directions in each plane, from $Y_T = -2.54$ cm to 21.57 cm and from $Z_T = -15.23$ cm to 2.54 cm. Components U, V, and W of the velocity vector at each data point were found in tunnel coordinates.

Before discussing these results, it is worthwhile to consider the surface oil-flow visualization experiments conducted by Ahn (1990) on the same 6:1 prolate spheroid model at various conditions. The results of these oil-flow experiments reveal skin friction

lines and regions of converging streamlines on the surface, and these converging streamlines can indicate the locations of surface flow separation.

These surface oil-flow experiments cannot conclusively show whether the flow over the 6:1 prolate spheroid at Re$=1.3\times10^6$ and $\alpha=10°$ and $15°$ is laminar or turbulent. However, the results of surface skin friction measurements on a 6:1 prolate spheroid performed by Kreplin, et al. (1980) indicate that at Re$=1.6\times10^6$ and $\alpha=10°$ the flow is laminar up to separation. Thus, in the present study at Re$=1.3\times10^6$ and $\alpha=10°$ and $15°$, the flow over the body is possibly laminar up to separation.

Results of surface oil-flow visualizations for Re$=4.0\times10^6$ and $\alpha=10°$ are shown in Figures 11 and 12. For these conditions, transition occurs along the forebody and the flow becomes turbulent. Surface skin friction lines extending from the windward side of the forebody converge towards skin friction lines from the leeward side. At X/L$=0.6$, this convergence occurs between $\varphi=35°$ and $40°$; at X/L$=0.7$, it occurs between $\varphi=25°$ and $30°$; at X/L$=0.8$, it occurs between $\varphi=15°$ and $20°$; and at X/L$=0.9$, the convergence occurs below $\varphi=10°$. Between X/L$=0.8$ and $0.9$, primary separation begins along the line of converging skin friction lines. Aft of X/L$=0.9$, secondary separation is evident.

For $\alpha=15°$ and Re$=4.0\times10^6$, oil-flow results are shown in Figures 13 and 14. For these conditions, transition occurs around X/L$=0.3$ and the flow becomes turbulent. Regions of converging skin friction lines are evident at X/L$=0.6$ between $\varphi=40°$ and $45°$, at X/L$=0.7$ between $\varphi=30°$ and $35°$, at X/L$=0.8$ between $\varphi=20°$ and $25°$, and

at $X/L=0.9$ around $\varphi=0°$. Primary separation occurs farther forward along the body than for $\alpha=10°$, starting at $X/L=0.5$.

Based upon discussions of the topology of separated flow, such as those by Lighthill (1963) and Peake and Tobak (1982), the separating flow along this body can be considered as a sheet of fluid that comes out from the surface in the regions of converging skin friction lines indicated by the oil-flow experiments. Along the surface of the body, this sheet rolls up by turning in toward the leeward side of the body, down toward the surface, then away from the leeward side, as indicated in Figure 15. In the context of this discussion, the phrase "vortical" refers to this roll-up of the separating sheet of fluid.

When viewed along the longitudinal axis of the body, vector plots of the secondary velocity components can reveal the nature of the flow field as the separating fluid turns and rolls over in the manner previously described. Therefore, the data were transformed by a rotation about the $Z_T$ axis of $-\alpha$ to a body-fixed coordinate system to obtain, in effect, a view along the longitudinal body axis. This body-fixed system is denoted by the axes $X_B$, $Y_B$, and $Z_B$; with $X_B$ corresponding to the longitudinal axis of the body. The rollover of the flow becomes more apparent in the resulting secondary velocity vector plots, as can be seen by comparing Figure 16 to Figure 32. For $Re=1.3\times10^6$, Figures 17 to 20 show the results for $\alpha=10°$ and Figures 21 to 24 show the results for $\alpha=15°$. For $Re=4.0\times10^6$, Figures 25 to 28 show the results for $\alpha=10°$ and Figures 29 to 32 show the results for $\alpha=15°$.

For $\alpha = 10°$ and $Re = 1.3 \times 10^6$, the secondary velocity vectors show some turning of the flow, as indicated by the change in the direction of the V component of velocity. The magnitude of turning increases and spreads further from the surface as the flow progresses toward the tail of the body.

For $\alpha = 10°$ and $Re = 4.0 \times 10^6$, the turning of the flow is again shown as described above. However, the magnitude of the turning increases in such a manner that, starting at X/L=0.8 and continuing at X/L =0.9, a region of definite vortical flow appears, although the location of its center is difficult to ascertain.

For $Re = 1.3 \times 10^6$, the turning of the flow at each axial location occurs further from the surface at $\alpha = 15°$ than at $\alpha = 10°$. Vortical flow encompassing a large region appears starting at X/L=0.8. The small magnitudes of the V and W components indicate the weak nature of this flow.

For $\alpha = 15°$ and $Re = 4.0 \times 10^6$, a distinct vortical pattern appears close to the surface at X/L=0.6, and the magnitudes of the secondary velocities increase and the region of vortical flow grows as the flow progresses aft along the body to X/L=0.9. This vortical flow appears to be strong, considering the magnitude of the secondary velocities. Again, the location of the center of the region is difficult to judge, although the center appears to be moving away from the surface at X/L=0.9.

More detailed information about the development of the vortical flow on the leeward side of the body for each test condition can be seen by examining contours of streamwise vorticity at each axial location. In the presence of a vortex, the location and size of the vortex can be found by studying any concentric contours that might appear,

and the core of the vortex can be located by finding the position of the maximum vorticity within such concentric contours (Pauley and Eaton, 1988). In addition, a region or layer of strong streamwise vorticity growth can be seen in closely spaced contour lines across which occurs a large increase in vorticity. Such a growth layer coincides with a line of separation in the flow field, as described by Barberis and Chanetz (1986). These curves of constant vorticity can give a good image of a sheet of fluid that separates from the body and winds up to form vortical flow. By studying vorticity contours for the present conditions, some conclusions can be made concerning the size, location, and strength of any vortical flow regions.

Measurements of the secondary velocity components V and W in tunnel coordinates allow, at each data point, the determination of the vorticity in the $X_T$ direction, given by:

$$\Omega_X = \left( \frac{\partial W}{\partial Y} - \frac{\partial V}{\partial Z} \right)$$

The local gradients in the $Y_T$ and $Z_T$ directions were found by fitting a parabola through five consecutive data points and calculating the derivative at the central point. A possible source of error in the values calculated for the gradients exists due to the spacing of the data points. The 1.27 cm spacing may be too large to accurately capture the gradients in each direction. No attempt was made to estimate the possible error. The resulting contours of $\Omega_X/U_\infty$ are shown in Figures 33 to 48.

The results for $\alpha = 10°$ and $Re = 1.3 \times 10^6$ are shown in Figures 33 to 36. At $X/L = 0.6$, the only noticeable feature is a region between $\varphi = 35°$ to $\varphi = 50°$ close to the

surface in which the vorticity $\Omega_x/U_\infty$ increases from 0.0/cm to 0.10/cm. Note that $\varphi$ is the angle measured from the $-Z_T$ axis as shown in Figure 4. At X/L=0.7, this same type of region is seen. In addition, between $\varphi=45°$ and $\varphi=75°$, the contours spread out from the surface, indicating diffusion of vorticity into the flow field surrounding the body. This spreading is even more evident at X/L=0.8 between $\varphi=40°$ and $\varphi=80°$. The vorticity $\Omega_x/U_\infty$ increases from 0.0/cm to a maximum of 0.10/cm between $\varphi=45°$ and $\varphi=65°$. At X/L=0.9, contours are almost concentric at higher $\varphi$'s, increasing from 0.0/cm at the edges to 0.08/cm towards the center. However, the maximum value occurs at approximately $\varphi=35°$, in a region of vorticity growth from 0.0/cm to 0.14/cm close to the surface.

These vorticity contours for $\alpha=10°$ and Re=$1.3\times10^6$ show the diffusion of vorticity out into the flow field as indicated by regions of vorticity that originate close to the body and spread out away from the surface as the flow progresses aft along the body. The maximum vorticity $\Omega_x/U_\infty$ is fairly constant at 0.10/cm until X/L=0.9, when it reaches 0.14/cm, indicating a slight increase due to the early stages of the rollup of separating fluid at the tail of the body.

Figures 37 to 40 show the $\Omega_x/U_\infty$ vorticity contours for $\alpha=10°$ and Re=$4.0\times10^6$. At X/L=0.6, the vorticity $\Omega_x/U_\infty$ goes from 0.0/cm to 0.06/cm at $\varphi=70°$ to 75°. This is at a higher $\varphi$ than the lower Re case at the same axial location and angle of attack. At X/L=0.7, the vorticity increases from 0.0/cm to 0.14/cm in a region between $\varphi=40°$ and $\varphi=50°$. The contours are spreading out away from the surface between $\varphi=60°$ and $\varphi=85°$. At X/L=0.8, the vorticity $\Omega_x/U_\infty$ increases from 0.0/cm to a maximum of

0.16/cm across a layer in the same $\varphi$ locations as at X/L=0.7. Again, the contours are spreading out away from the body between $\varphi=60°$ and $\varphi=85°$. Contours that are almost concentric are evident at X/L=0.9, indicating vortical flow centered between $\varphi=55°$ and $\varphi=60°$ and approximately 2 cm out from the surface. The maximum vorticity $\Omega_x/U_\infty$ is greater than 0.16/cm at the center of this region.

These contours show that the separation results in vortical flow centered close to the body at X/L=0.9. The contours appear to take on an elliptical shape. The maximum vorticity $\Omega_x/U_\infty$ at each axial location increases from 0.06/cm at X/L=0.6 to greater than 0.16/cm at X/L=0.9.

For $\alpha=15°$ and Re=1.3×10⁶, the constant vorticity contours are shown in Figures 41 to 44. At X/L=0.6, the values increase from 0.0/cm to 0.16/cm between $\varphi=35°$ and $\varphi=50°$. At higher $\varphi$'s, the contour lines spread out from the body. The vorticity $\Omega_x/U_\infty$ increases from 0.0/cm to 0.20/cm between $\varphi=5°$ and 45° at X/L=0.7. Again, spreading of the contours is seen at higher $\varphi$'s. At X/L=0.8 the vorticity $\Omega_x/U_\infty$ increases from 0.0/cm to 0.20/cm in a region centered at $\varphi=40°$. At X/L=0.9, the values increase from 0.0/cm to 0.32/cm between $\varphi$'s of 0° and 35°. An interesting feature to note is that contour lines of 0.04/cm and 0.08/cm have wrapped around and moved close to the surface between $\varphi=45°$ and $\varphi=90°$. This was not seen in the case with $\alpha=10°$ and Re=1.3×10⁶. These wrapped contours indicate that the separation fluid sheet has started to roll up, resulting in vortical flow centered between $\varphi=60°$ and 75°, with a maximum vorticity in the center of approximately 0.10/cm. The spread of the contour lines indicate diffusion of vorticity over a large area away from the body.

As these results for the case of $\alpha=15°$ and $Re=1.3\times10^6$ show, the maximum vorticity $\Omega_x/U_\infty$ increases from 0.16/cm to 0.32/cm between X/L=0.6 and X/L=0.9, and in all four axial locations this maximum vorticity occurs close to the surface at $\varphi$'s less than 45°. Contour lines indicate diffusion of streamwise vorticity over a large region away from the body at $\varphi$'s greater than 45°. Weak, rapidly diffusing vortical flow due to the rollup of the separating fluid appears to have formed by X/L=0.9.

The results for the case of $\alpha=15°$ and $Re=4.0\times10^6$ are shown in Figures 45 to 48. At X/L=0.6, a maximum vorticity $\Omega_x/U_\infty$ of 0.16/cm is seen at approximately $\varphi=55°$. Between $\varphi=60°$ and $\varphi=85°$, contour lines spread out away from the surface. At X/L=0.7, a maximum vorticity of 0.25/cm occurs in a contour that is almost closed, indicating early stages of the formation of vortical flow centered at approximately $\varphi=55°$. In the region above $\varphi=60°$, the contours are spread out slightly compared to those at X/L=0.6. Definite concentric contours are seen at X/L=0.8, indicating vortical flow centered 2 cm from the surface at $\varphi=55°$ to 65°. The maximum vorticity $\Omega_x/U_\infty$ at the center of these contours is 0.30/cm. Note that the vorticity contours have not spread out away from the body any more than at X/L=0.7, indicating that the vortical flow contains the vorticity and slows its diffusion. At X/L=0.9, the center has moved away from the body, as was also shown previously by the secondary velocity vectors. The vortical flow is centered 3 cm from the surface at $\varphi=60°$ and the contours have a definite elliptical shape. The strength of the vortical flow is indicated by the maximum vorticity $\Omega_x/U_\infty$ of 0.36/cm at its center. Again, diffusion of vorticity appears to be

prevented in the presence of this flow, as seen by the fact that contour lines are contained without spreading.

As these results show for $\alpha = 15°$ and $Re = 4.0 \times 10^6$, strong vortical flow has formed, originating between $X/L = 0.6$ and $X/L = 0.7$ and gaining in strength to $X/L = 0.9$ as indicated by the increase in maximum vorticity $\Omega_X/U_\infty$ from 0.16/cm to 0.30/cm.

Overall, the results from the secondary velocity vectors and the contours of vorticity in the $X_T$ direction indicate that for $Re = 1.3 \times 10^6$ at both angles of attack, any vortical formation is very weak and rapidly diffusing. In contrast, both cases at $Re = 4.0 \times 10^6$ show the formation of vortical flow of increasing strength.

## 4.2 Mean Velocity Profiles and Turbulence Measurements

Mean velocity profiles and turbulence measurements were made at $X/L = 0.7$ and $X/L = 0.8$ at $\alpha = 10°$ and $Re = 4.0 \times 10^6$. Data were obtained in vertical and horizontal traverses in the $Y_T$ and $Z_T$ directions in each plane as shown in Figures 49 and 50.

In Figures 51 to 57, mean velocity components obtained using the x-wire probe are compared to mean velocity components obtained using the five-hole yawhead probe in vertical profiles at the same $Z_T$ locations. As these comparisons show, the values of $U/U_{re}$ agree to within approximately 4%. In most cases, the values of $V/U_{re}$ and $W/U_{re}$ agree to within 10%. Consideration of these comparisons appears to show that the

uncertainties in the mean velocities discussed in Section 3.4 are reasonable, and any disagreements may possibly be attributed to interference from the probes and supports.

To discuss the results and compare with work performed by other researchers, the data were linearly interpolated to obtain profiles extending radially outward from the surface of the body. As shown in Figures 49 and 50, these profiles are located from $\varphi = 20°$ to $\varphi = 90°$ at each axial location.

## 4.2.1 Velocity Profile Measurements

Mean velocity profile measurements are presented in a local body coordinate system shown in Figure 58. The origin of this system is on the surface of the model, with the $X_b$ axis aligned with the axis of the model, the $Y_b$ axis extending radially outward from the surface, and the $Z_b$ axis tangential to the surface. The data were transformed by rotating around the $Z_T$ axis by $-\alpha$ and then rotating around the X axis by $-(90° - \varphi)$ to the $X_b$-$Y_b$-$Z_b$ coordinate system for each profile. In this coordinate system, for each data point, $Y_b$ is the distance from the model surface and $Z_b = 0.0$. This coordinate system was chosen to make comparisons with the data of Meier, et al. (1984a), because in this system W is the spanwise (circumferential) velocity component and a change in the sign of W corresponds to a spanwise flow reversal. The velocities were nondimensionalized by the local free stream velocity, $U_{re}$. This local free stream velocity

for each radial profile was determined by plotting the resultant velocity $U_r = (U^2 + V^2 + W^2)^{1/2}$ versus $Y_b$ and determining $U_r$ at the edge of the boundary layer. This was considered to be $U_{re}$ for that profile.

The resulting velocity profiles are shown in Figures 59 to 74. Due to the size of the x-wire probe used to obtain the data, measurements could not be made closer than approximately 0.25 cm from the surface. Therefore, almost all of the data are in the outer region of the boundary layer and no measurements were made in the inner region or laminar sublayer. This is reflected in the velocity profiles.

The boundary layer thickness at each radial location was estimated by calculating $\delta_{99}$, given by $Y_b$ where $U_r = 0.99 U_{re}$. The displacement thickness $\delta^*$ and the momentum thickness $\theta$, defined by:

$$\delta^* = \int_0^{\delta_{99}} \left(1 - \frac{u}{U_{re}}\right) dy$$

$$\theta = \int_0^{\delta_{99}} \left(1 - \frac{u}{U_{re}}\right) \frac{u}{U_{re}} \, dy$$

can give an indication of the growth of the boundary layer over the leeward side of the body. To estimate these values, the velocity profiles were extended to the surface of the body using the following log law for a turbulent flat-plate boundary layer taken from Schetz (1984):

$$\frac{U}{u_.} = A \, \log \left( \frac{Yu_.}{v} \right) + C$$

The three data points closest to the surface in each profile were used to determine the values of A, C, and u. for that profile. The displacement thickness and momentum thickness were then calculated using the trapezoidal rule to evaluate the integrals. The shape factor for each profile, $H = \delta^*/\theta$, was also calculated. Results are given in Table 2 and Table 3. Although this log law is not exactly valid for the present flow, the method of extending the profiles to the surface provides better estimates of the displacement thickness and momentum thickness than those obtained when neglecting such extensions.

Figure 75 shows the circumferential development of the boundary layer given by displacement thickness $\delta^*$ versus $\varphi$ for X/L=0.7 and X/L=0.8. This figure also shows the results from Meier. et al. (1984a) for Re=$7.2 \times 10^6$ at X/L=0.73 and X/L=0.64. The effects of Reynolds number on the growth of the boundary layer are clearly evident. At the higher Reynolds number, the displacement thickness is greater and the location of the maximum displacement thickness is shifted towards the leeward side of the body. A possible explanation for the larger displacement thickness at the higher Reynolds number is given by considering the locations of transition in each case. At Re=$7.2 \times 10^6$, boundary layer transition begins to occur in an axial location closer to the nose of the body than at Re=$4.0 \times 10^6$. For the higher Reynolds number, this earlier transition allows the turbulent boundary layer to grow more before reaching the locations of separation.

The profiles of circumferential crossflow $W/U_{re}$, in Figures 59 to 74, indicate a change of sign of the crossflow close to the surface of the body at $\varphi = 50°$ for $X/L = 0.7$ and at slightly over $\varphi = 40°$ for $X/L = 0.8$, taking into account that the measurements were not made closer than 0.25 cm from the surface. Data from Meier, et al. (1984a) show that, at the higher Reynolds number, this negative crossflow occurs at $\varphi = 35°$ for $X/L = 0.73$ and at $\varphi = 50°$ for $X/L = 0.64$. Thus, the higher Reynolds number causes negative crossflow to occur further away from the leeward side at a given axial location. This negative crossflow coincides roughly with a substantial increase in the displacement thickness at the locations that it occurs, as shown in Figure 75. Meier, et al. (1984a) report that the movement of the location of negative crossflow away from the leeward side is accompanied by a shift in the location of the maximum displacement thickness. The present data appear to support this. The change in sign of the crossflow $W/U_{re}$ near the surface does not indicate the location of separation, because the location of negative crossflow depends upon the choice of coordinate system (Meier, et al., 1983b).

Although at $\varphi = 90°$ the crossflow velocity $W/U_{re}$ should be approximately zero, the data at $X/L = 0.7$ in Figure 66 give non-zero values. However, most of these values are within the uncertainty range for W given in Section 3.4.

In addition to showing the velocity profiles, Figures 59 to 74 present hodograph plots that show the variation of the direction of U-W crossflow velocity vectors between the edge of the boundary layer and the surface, in the $Z_b$ direction. This variation, or skewing, has significance because in a three-dimensional boundary layer, fluid can move laterally, as opposed to a two-dimensional layer in which the fluid is constrained on time

average to a plane. Investigating such skewing is difficult in the presence of large rotation of the flow because the distinction between the outer inviscid fluid and the boundary layer is blurred (Barberis and Chanetz, 1986). However, the present data were obtained in a region without large fluid rotation, and studying this variation in the direction of U-W crossflow vectors can be meaningful. The velocity vector at the surface is in a direction parallel to the surface stress, and the variations show how the direction of the surface stress vectors lag when compared with the direction of the local free-stream velocity (Townsend, 1976).

Figure 76 and 77 show profiles of the flow angle, $\beta = \arctan(W/U)$, in local body coordinates, for all radial profiles at $X/L = 0.7$ and $0.8$. These give an indication of the variation of the direction, or skewing, of the flow through the layer. The amount of skewing in each radial profile can be determined by finding the difference between the flow angle of the local free stream, $\beta_{fs}$, and the flow angle of the velocity at the surface, $\beta_{surf}$. This difference is given by $\Delta\beta = \beta_{fs}-\beta_{surf}$. However, because measurements were not obtained close to the surface in the laminar sublayer, the present data can give only an estimate of $\Delta\beta$. The results are shown in Figure 78, along with data from Meier, *et al.*(1984a) taken at $Re = 7.2 \times 10^6$. A higher Reynolds number appears to cause greater skewing through the boundary layer, in effect causing greater lag in the surface stress. The maximum skewing for all the axial locations occurs at $\varphi = 60°$; thus, this appears to be independent of the location of negative crossflow $W/U_{re}$ and maximum displacement thickness. A comparison between the location of maximum skewing and the location of

maximum $\delta^*$ for a given axial location shows that the maximum skewing occurs closer to the leeward side.

## 4.2.2 Turbulence Measurements

Turbulence measurements are presented in a local free-stream velocity coordinate system shown in Figure 79. The origin of this system is on the surface of the model, with the $X_{fs}$ axis aligned with the local free-stream velocity $U_{re}$ at the edge of the boundary layer, the $Y_{fs}$ axis extending radially outward from the surface, and the $Z_{fs}$ axis completing the right-hand rule. With the components of $U_{re}$ denoted as $U_e$, $V_e$, and $W_e$, the data were transformed from tunnel coordinates by rotating around the $Z_T$ axis by $\alpha_{fs} = \tan^{-1}(V_e/U_e)$, rotating around the Y axis by $\beta_{fs} = \tan^{-1}(W_e/U_e)$, and then rotating around the X axis by $-(90° - \varphi)$ to the $X_{fs}$-$Y_{fs}$-$Z_{fs}$ coordinate system for each radial profile. In this coordinate system, for each data point, $Y_{fs}$ is the distance from the model surface and $Z_{fs} = 0.0$. At the location in each profile where the resultant velocity $U_r = U_{re}$, V and W are zero and $U = U_r = U_{re}$. This coordinate axis system was chosen as the proper local free-stream coordinate system to use to present the turbulence measurements and derived quantities so that they have meaning. However, because the measurements were made in the vertical $Y_T$-$Z_T$ plane, any distortions in the locations of the points in the X-directions were ignored after the data were transformed to the local free stream coordinate system. Also, when finding the mean velocity gradients in the $Y_{fs}$-direction for the

derived quantities discussed in Section 4.3, any gradients in the $X_T$-direction were ignored.

As a basis to consider the validity of the turbulent measurement results, the realizability conditions outlined in Schumann (1977) were utilized. Basically, the Reynolds stress tensor for each data point must satisfy the following:

$$
\begin{aligned}
I_1 &= \overline{u^2} + \overline{v^2} + \overline{w^2} \geq 0 \\
I_2 &\equiv \overline{u^2 v^2} - (\overline{uv})^2 + \overline{u^2 w^2} - (\overline{uw})^2 \\
&\quad - \overline{v^2 w^2} - (\overline{vw})^2 \geq 0 \\
I_3 &= \overline{u^2}(\overline{v^2 w^2} - \overline{vw^2}) \\
&\quad - \overline{uv}(\overline{uv w^2} - \overline{vw}\,\overline{uw}) \\
&\quad + \overline{uw}(\overline{uv\,vw} - \overline{v^2}\overline{uw}) \geq 0
\end{aligned}
$$

If any of the above conditions are not satisfied for a given Reynolds stress tensor, then the validity of the data at that point must be questioned. The present measurements were tested using the above conditions, and for all the data at all the points, the conditions were satisfied. Hence, from the point of view of the realizability of the Reynolds stress tensor, the data are valid.

Figures 80 to 85 show the normal stresses nondimensionalized by $U_{re}$ for all the radial profiles at $X/L=0.7$ and $X/L=0.8$. At each axial location, an increase in these quantities occurs at a further distance from the surface, given by $Y_{fs}$, as $\varphi$ increases from $20°$ to $70°$. At $\varphi=80°$ and $90°$, this distance decreases. This corresponds to the growth of the boundary layer circumferentially towards the leeward side, as seen in the velocity profiles, because the sudden increase in each quantity occurs at the edge of the boundary layer. The turbulent kinetic energy, given by:

$$k = \frac{\overline{u^2} + \overline{v^2} + \overline{w^2}}{2}$$

is shown in Figures 86 and 87 for both axial locations. In general, the turbulent kinetic energy increases in the proximity of the surface in the same manner as a two-dimensional boundary layer, and there appears to be little evidence of turbulent energy being convected away from the surface by the vortical flow.

Figures 88 to 95 show the normal stress quantities for each profile for X/L=0.7 and Figures 96 to 103 show these quantities for X/L=0.8. For both axial locations, at $\varphi = 20°$, $\overline{w^2}$ is greater than $\overline{v^2}$. At $\varphi = 30°$, these quantities are approximately equal at X/L=0.7, and at X/L=0.8, $\overline{v^2}$ is greater than $\overline{w^2}$ closer to the surface. At $\varphi = 40°$ and 50° for both axial locations, $\overline{v^2}$ is greater than $\overline{w^2}$. At $\varphi = 60°$, $\overline{v^2}$ is greater than $\overline{w^2}$ until close to the surface, where these quantities are equal. At $\varphi = 70°$, these quantities are approximately equal throughout the boundary layer, and at $\varphi = 80°$ and 90°, $\overline{w^2}$ is again greater than $\overline{v^2}$.

The locations just described where $\overline{v^2}$ is greater than $\overline{w^2}$ occur in regions in which the processes of separation are beginning to occur along the surface of the body and vortical flow becomes evident. Although Klebanoff (1954) showed that $\overline{w^2}$ is greater than $\overline{v^2}$ throughout the boundary layer for turbulent flow over a flat plate, the present

data show distortion from this due to the separation phenomena and the presence of three-dimensional vortical flow, and these distortions are consistent when comparing data at both axial locations. The variations of the relative magnitudes of $\overline{v^2}$ and $\overline{w^2}$ can possibly be attributed to the folding over of the separating flow. Overall, $\overline{u^2}$ is greater than either $\overline{v^2}$ or $\overline{w^2}$ in all the profiles, and this quantity makes up most of the turbulent kinetic energy through the boundary layer.

Shear stress quantities $-\overline{uv}$, $-\overline{uw}$, and $-\overline{vw}$ are shown in Figures 104 to 109 for all the profiles at X/L=0.7 and X/L=0.8. As with the normal stresses, the shear stress magnitudes begin to increase at the edge of the boundary layer.

The shear stress quantities for each profile are shown in Figures 110 to 117 for X/L=0.7 and in Figures 118 to 125 for X/L=0.8. In all cases except X/L=0.8 and $\varphi=90°$, $\overline{uv}$ has the largest magnitude, but the behavior of $\overline{uw}$ and $\overline{vw}$ are still significant. As was previously described concerning the relative magnitude of $\overline{w^2}$ and $\overline{v^2}$ at the same $\varphi$ for both axial locations, the behavior of $\overline{uw}$ and $\overline{vw}$ is consistent when comparing values at the same $\varphi$ at both axial locations. At $\varphi=20°$, $\overline{vw}$ is negative at the edge of the boundary layer and becomes positive at approximately $Y_{fs}/\delta_{99}=0.5$, and $\overline{uw}$ is initially negative and starts to become positive. At $\varphi=30°$, $\overline{vw}$ is positive and $\overline{uw}$ has a smaller magnitude than $\overline{vw}$. At $\varphi=40°$, both values are positive. However, at

$\varphi = 50°$, $\overline{vw}$ is negative, and $\overline{uw}$ and $\overline{vw}$ have approximately the same magnitude. At $\varphi = 60°$ and $\varphi = 70°$, $\overline{uw}$ becomes negative below $Y_{fs}/\delta_{\varphi\varphi} = 0.4$. At $\varphi = 80°$, both quantities are negative except below $Y_{fs}/\delta_{\varphi\varphi} = 0.2$, where $\overline{vw}$ becomes positive.

Kreplin and Vollmers (1981) obtained Reynolds stress components on a 6:1 prolate spheroid at $X/L = 0.64$ and $\alpha = 10°$. These measurements were taken in regions of converging wall streamlines for $Re = 7.2 \times 10^6$, at $\varphi = 60°$ and $\varphi = 45°$. Although these data were obtained at a higher Reynolds number, comparisons can still be made with the present data for regions of converging wall streamlines. Based on the discussion in Section 4.1 concerning results of oil flows done by Ahn (1990), these regions occur at approximately $\varphi = 30°$ for $X/L = 0.7$ and $\varphi = 20°$ for $X/L = 0.8$.

Figure 126 shows the comparison of the $\overline{u^2}$ Reynolds stresses. The data at $\varphi = 20°$ and $X/L = 0.8$ show good agreement with the data from Kreplin and Vollmers. However, the data at $\varphi = 30°$ and $X/L = 0.7$ give lower values. As seen in Figure 127, the present data generally give higher values of $\overline{v^2}$ than the data from Kreplin and Vollmers. The comparison of $\overline{w^2}$ in Figure 128 shows that the present data at $X/L = 0.7$ and $\varphi = 30°$ agree well with the values from Kreplin and Vollmers, but the data at $X/L = 0.8$ and $\varphi = 20°$ show higher values.

The comparison of $\overline{uv}$ in Figure 129 shows that the present data exhibit the same trends as the data from Kreplin and Vollmers; however, the magnitudes of the present data are generally higher. The comparison of $\overline{uw}$ in Figure 130 does not show good

correlation between the data. The present data are generally positive, whereas the data from Kreplin and Vollmers are negative. The comparison of $\overline{vw}$ in Figure 131 shows somewhat better agreement, although the values from Kreplin and Vollmers have a larger magnitude overall.

Some of the differences in the previously described comparisons can be attributed to both the different Reynolds numbers and the different locations. Also, the x-wire data reduction method used by Kreplin and Vollmers (1981) neglected tangential cooling and assumed a cosine cooling law for the wires.

## 4.3 Derived Quantities

The Reynolds stress quantities obtained in the measurements were used to estimate various derived quantities, defined in the following discussion, in local free stream coordinates. These quantities are listed below, along with the estimated uncertainties of each quantity:

| | |
|---|---|
| Turbulent shear stress $\tau$ | $\pm 0.17 \tau_{max}$ |
| Townsend's structural parameter A1 | $\pm 0.18 A1_{max}$ |
| Kinematic eddy viscosity $v_x$ | $\pm 0.16 v_{x\text{-}max}$ |
| Kinematic eddy viscosity $v_z$ | $\pm 0.37 v_{z\text{-}max}$ |
| Anisotropic constant N | $\pm 0.40 N_{max}$ |
| Mixing length $L_m$ | $\pm 0.13 L_{m\text{-}max}$ |

Flow gradient angle $\alpha_g$ $\pm 0.095 \alpha_{g\text{-max}}$

Shear stress angle $\alpha_s$ $\pm 0.35 \alpha_{s\text{-max}}$

The given estimated uncertainties are valid for data within the inner two-thirds of the boundary layer. At the edge of the layer and outside the layer, the results have increasing uncertainties due to the small magnitudes of the velocity gradients and Reynolds stress quantities involved in the calculations. Therefore, values of the derived quantities at $Y_{fs}/\delta_{99}$ greater than approximately 0.9 are not presented.

The total turbulent shear stress $\tau$ in planes parallel to the $X_{fs}$-$Z_{fs}$ plane of the local free stream coordinate system can be obtained from $\overline{uv}$ and $\overline{vw}$ by:

$$\tau = \sqrt{(\overline{uv})^2 + (\overline{vw})^2}$$

The results for $X/L = 0.7$ and $X/L = 0.8$, nondimensionalized by $U_{re}^2$, are shown in Figure 132 and 133. The magnitude of $\tau$ increases through the boundary layer and is highest near the wall.

Townsend's structural parameter $A1$ relates the turbulent kinetic energy $k$ to the Reynolds shear stresses, and is given by the ratio of $\tau$ to $k$ as follows:

$$A1 = \frac{\sqrt{(\overline{uv})^2 + (\overline{vw})^2}}{(\overline{u^2} + \overline{v^2} + \overline{w^2})}$$

This parameter has been found to be nearly constant at a value of 0.15 in two-dimensional boundary layers.

The results for this three-dimensional boundary layer at X/L=0.7 and X/L=0.8 are shown in Figures 134 and 135. At the edges of the layer, A1 tends to vary from approximately 0.05 to 0.17. However, as $Y_{fs}/\delta_{99}$ decreases, the values for A1 remain within a band from 0.13 to 0.17. Thus, although the parameter is distorted somewhat from the value of 0.15 for two-dimensional layers, the ability of turbulence to generate transport of momentum in this three-dimensional layer appears to be similar to that of a two-dimensional layer, and assuming a value of 0.15 for Townsend's structural parameter A1 is not wholly inaccurate.

The kinematic eddy viscosities in the x direction and in the z direction for the local free stream coordinate system are given by:

$$v_x = \frac{-\overline{uv}}{\left(\frac{\partial U}{\partial y}\right)}$$

$$v_z = \frac{-\overline{vw}}{\left(\frac{\partial W}{\partial y}\right)}$$

The gradients in the $Y_{fs}$ direction were estimated by fitting a parabola through five consecutive points and finding the derivative at the third (middle) point.

The results for $v_x$, shown in Figure 136 and 137, are everywhere positive in the boundary layer. Above about $Y_{fs}/\delta_{99}=0.3$, the x-eddy viscosity appears to be varying non-linearly with respect to $\log(Y_{fs}/\delta_{99})$. Below this, the variation is more linear. The results for $v_z$, shown in Figures 138 and 139, are more difficult to interpret. In some

cases a linear variation with respect to $\log(Y_{fs}/\delta_{yy})$ is evident; however, there is no overall consistency in the behavior. Most of the values are in a band within $\pm 0.004$ m$^2$/s.

To determine whether a correlation exists between the eddy viscosity and the displacement thickness, the x eddy viscosity was normalized as $v_x/(U_{re}\delta^*)$. According to the Clauser eddy viscosity model for a flat-plate zero pressure gradient flow, as taken from Schetz (1984), this normalization leads to a value of 0.018. However, for the present flow, this normalization does not appear to provide any collapse of the curves, as shown in Figures 140 to 141. Within the boundary layer, the values for $X/L=0.7$ are generally between 0.010 and 0.020, and the values for $X/L=0.8$ are between 0.005 and 0.010. Generally, as $\varphi$ increases from 20° to 50°, the values decrease. As $\varphi$ increases further to 90°, the values increase.

Isotropic eddy viscosity models have been used by researchers to relate the transfer of momentum by velocity fluctuations to local mean flow gradients. Such models utilize an eddy viscosity in a formulation analogous to the kinematic viscosity in laminar flow. However, the eddy viscosity is not a thermophysical property of the fluid, but is a property of the flow. In order to test the validity of the isotropic assumption as applied to the present three-dimensional turbulent flow, the anisotropic constant $N=v_z/v_x$ can be examined. If the isotropic assumption is valid, then $N=1$. However, as shown in Figures 142 and 143, the anisotropic constant varies through the boundary layer in a band within $\pm 2$. Thus, the eddy viscosity appears not to be isotropic in this turbulent three-dimensional boundary layer.

In addition to eddy viscosity methods, the mixing length $L_m$ is used to relate turbulent shear to mean velocity gradients. The mixing length is defined by some interaction distance between eddies analogous to a molecular mean free path, and for a three-dimensional boundary layer $L_m$ is given by:

$$L_m = \frac{\left[(\overline{uv})^2 + (\overline{vw})^2\right]^{\frac{1}{4}}}{\left[\left(\frac{\partial U}{\partial y}\right)^2 + \left(\frac{\partial W}{\partial y}\right)^2\right]^{\frac{1}{2}}}$$

For the outer region of the boundary layer, where most of the present data were obtained, a generally-accepted expression for the mixing length for two-dimensional zero pressure gradient boundary layers is given by $L_{m2D} = 0.09\delta$ (Schetz, 1984), resulting in a constant mixing length for such a boundary layer. To determine the applicability of this expression to the present data, the ratio of the mixing length $L_m$ to the two-dimensional mixing length $L_{m2D}$ was found and the results are shown in Figure 144 and 145. In general, the expression for two-dimensional boundary layers overestimates the value of the mixing length, and the ratio ranges from 0.5 to 1.0. However, the assumption of a constant mixing length for the outer region of the layer appears to be valid.

The flow gradient angle $\alpha_g$ and the shear stress angle $\alpha_s$, given by:

$$\alpha_g = \arctan\frac{\left(\frac{\partial W}{\partial y}\right)}{\left(\frac{\partial U}{\partial y}\right)}$$

$$\alpha_s = \arctan\frac{(\overline{vw})}{(\overline{uv})}$$

were calculated in an attempt to determine if the mean velocity gradients align in the same directions as the shear stresses. The results for $\alpha_g$ and $\alpha_s$ are given in Figures 146 to 149 for X/L=0.7 and X/L=0.8. The flow gradient angle tends to increase through the layer, except at $\varphi=60°$, 70°, and 80°, whereas the shear angle tends to decrease. Between $\varphi=50°$ and $\varphi=80°$, the trends in both $\alpha_g$ and $\alpha_s$ appear consistent for a given profile; however, the actual magnitudes differ greatly. Overall, a comparison between the flow gradient angle and the shear stress angle does not yield consistent results, except that the directions of the mean velocity gradients and the corresponding shear stresses do not appear aligned.

In an effort to examine the lag or lead of the shear stress angle with respect to the mean velocity flow gradient angle, the values of the difference $\alpha_g$-$\alpha_s$ were found and are shown in Figures 150 and 151. Overall, the values generally vary from negative at the edge of the boundary layer to positive at the surface, indicating that at the edge of the layer the shear stress angle leads with respect to the flow gradient angle while at the surface the shear stress angle lags when compared to the flow gradient angle. A notable exception appears at $\varphi=80°$ for both axial locations, in which cases the values tend to decrease through the layer and then increase close to the surface. At each axial location, the curves for $\varphi=50°$ and $\varphi=60°$ have the least variation through the boundary layer. As shown in Figure 75, these are regions where the displacement thickness is largest.

# 5.0 Conclusions and Recommendations

The mean velocity field and turbulence measurements were made along the leeward side of a 6:1 prolate spheroid, in regions leading to and including separation.

For the cases of $Re = 1.3 \times 10^6$ at $\alpha = 10°$ and $15°$, separation results in weak vortical flow, as shown by the magnitudes of the secondary velocities and by the maximum vorticity $\Omega_x/U_\infty$ of 0.10/cm in the center of the region of vortical flow at $X/L = 0.9$. Based upon results of surface skin friction measurements from Kreplin, *et al.* (1980), the flow in each case may possibly be laminar up to separation.

For $Re = 4.0 \times 10^6$, transition occurs along the forebody, and the flow is turbulent in the locations of the measurements. At $\alpha = 10°$, separation begins to occur between $X/L = 0.8$ and $X/L = 0.9$ and the resulting vortical flow is stronger than in the lower Reynolds number case, with larger secondary velocities and a maximum vorticity $\Omega_x/U_\infty$ greater than 0.16/cm at $X/L = 0.9$. At $\alpha = 15°$, separation occurs further forward and the resultant vortical flow is the strongest of any of the cases, with a maximum vorticity $\Omega_x/U_\infty$ at $X/L = 0.9$ of 0.30/cm. At both angles of attack, the diffusion of vorticity away

from the body is contained by the presence of the vortical flow. The centers of the regions of strong vortical flow appear to move away from the surface slightly by $X/L = 0.9$.

Estimates of the boundary layer thickness $\delta_{yy}$ and the displacement thickness $\delta^*$ indicate the growth of the boundary layer circumferentially and axially along the body for $\alpha = 10°$ and $Re = 4.0 \times 10^6$. Comparisons with data from Meier, *et al.* (1984a) show that at a higher Reynolds number, the displacement thickness increases and the location of maximum displacement thickness shifts toward the leeward side. The locations of negative crossflow $W/U_{re}$ (in the local body coordinate system) indicated by a change in the sign of $W/U_{re}$ occur further away from the leeward side at a higher Reynolds number. This flow reversal is coincident with a large increase in the displacement thickness.

Skewing of the boundary layer is indicated by the variation of the direction of the velocity vectors through the layer. Maximum skewing occurs at $\varphi = 60°$, independent of axial location and Reynolds number, and this location is closer to the leeward side than the location of maximum displacement thickness. Again, comparison with Meier, *et al.* (1984a) shows good agreement, considering Reynolds number effects.

Turbulence measurements in the regions leading up to separation show that the distribution of Reynolds stresses is distorted compared to the distribution of a two-dimensional boundary layer. This distortion can be attributed to the separation phenomena and the presence of three-dimensional vortical flow. Comparing the distributions at $X/L = 0.7$ with those at $X/L = 0.8$ indicates that they are consistent axially along the body. Comparison of Reynolds stresses in regions of converging streamlines

with those from Kreplin and Vollmers (1981) show good agreement in most cases for the Reynolds normal stresses; however, the correlation is not as good for the Reynolds shear stresses.

Estimates of Townsend's structural parameter A1 relating turbulent kinetic energy to the Reynolds shear stresses indicates that the distribution is similar to that of a two-dimensional layer with $A1 = 0.15$. However, estimates of eddy viscosity in the x and z directions and the resulting anisotropy constant N indicate that eddy viscosity is not isotropic through the boundary layer. Hence, isotropic models for eddy viscosity will not give accurate results. Estimates of the mixing length compared to a generally-accepted theoretical two-dimensional model show that the model overestimates the mixing length for the outer region. A comparison of the flow gradient angles and the shear stress angles shows that the mean velocity gradients and the shear stresses are not aligned in this three-dimensional boundary layer. Overall, the shear stress angle leads the mean velocity flow gradient angle at the edge of the boundary layer, while at the surface the shear stress angle lags compared to the flow gradient angle.

For this study, turbulence measurements were obtained in the outer region of the boundary layer only, using an x-wire mounted on a traverse external to the model. Future work could include measurements closer to the surface, using hot-wire anemometry and laser doppler velocimetry with probes mounted and traversed inside the model. The present data could be used for comparison purposes. Since this is part of an overall study of transition and separation, future measurements should be obtained in both steady and unsteady flow.

In addition to turbulence measurements, skin friction measurements are important in the study of transition and separation. Such data would confirm results from surface oil flow measurements and would aid in the analysis of turbulence data for the inner region and lamina · sublayer of the boundary layer in both steady and unsteady cases.

# References

Acrivlellis. M.. "An Improved Method for Determining the Flow Field of Multidimensional Flows of Any Turbulence Intensity", *DISA Information*, No. 23, September, 1978.

Ahn. S., "Aerodynamic Characteristics of a 6 to 1 Prolate Spheroid Undergoing Unsteady Transient Motions", Ph.D. Dissertation in Preparation, Virginia Polytechnic Institute and State University, Blacksburg, VA, 1990.

Barberis. D. and Chanetz, B., "Decollement en ecoulement incompressible tridimensionnel. Experiences de validation et modelisation", *23rd Colloque d'Aerodynamique Appliquee*, Aussoic, France, November 1986.

Browne, L. W. B., Antonia, R. A. and Chua, L. P., "Calibration of X-Probes For Turbulent Flow Measurements", *Experiments in Fluids*, Vol. 7, pp. 201-208, 1989.

Chanetz. B., "Contribution a l'etude du decollement tridimensionnel en ecoulement turbulent incompressible", Doctoral Thesis, Universite Lyon-I, Claude-Bernard, 1986.

Chanetz, B. and Delery, J., "Experimental Analysis of Turbulent Separation on an Oblate Ellipsoid-Cylinder", *La Recherche Aerospatiale*, No. 3, pp. 59-77, 1988.

Chew, Y. T. and Ha, S. M., "The Directional Sensitivities of Crossed and Triple Hot-Wire Probes", *J. of Physics E.: Sci. Instrum.* 21, pp. 613-620, 1988.

Chew, Y. T. and Simpson, R. L., "An Explicit Non-Real Time Data Reduction Method of Triple Sensors Hot-Wire Anemometer in Three-Dimensional Flow", *Journal of Fluids Engineering*, Vol. 110, pp. 110-119, June 1988.

Chew, Y. T. and Simpson, R. L., "The Non-Real Time Explicit Data Analysis Method of Crossed Hot-Wire Anemometer Measurements Including Tangential Cooling Velocity Correction", *J. of Physics E.: Sci. Instrum.* 21, pp. 310-316, 1988.

Choi, K. and Simpson, R. L., *Some Mean Velocity, Turbulence, and Unsteadiness Characteristics of the VPI&SU Stability Wind Tunnel*, Report, AOE Dept., VPI&SU, 1987.

*Compumotor Programmable Motion Control*, Parker-Hannifin Corporation Catalog, 1987.

Cutler, A. D. and Bradshaw, P., *The Interaction Between a Strong Longitudinal Vortex and a Turbulent Boundary Layer*, AIAA Paper No. 86-1071, 1986.

Ha, S. M., "The Effect of Turbulence Length Scales on Turbulence Intensity Measurements", Master's Thesis, National University of Singapore, 1989.

Iuso, G., Onorato, M., Oggiano, M. S., De Ponte, S., Yuzhong, B. and Xiaodi, Z., *Experimental Investigation of the Complex 3-D Flow Around a Body of Revolution at Incidence / A Sino-Italian Cooperative Research Program*, ICAS-88-4.9.1, 1988.

Jorgensen, F. E., "Directional Sensitivity of Wire and Fiber Film Probes", *DISA Information*, No. 11, May 1971.

Klebanoff, P. S., "Characteristics of Turbulence in a Boundary Layer with Zero Pressure Gradient", *NACA TN-3178*, 1954.

Kline, S. J. and McClintock, F. A., "Describing Uncertainties in Single-Sample Experiments", *Mechanical Engineering*, January 1953.

Kreplin, H. P. and Vollmers, H., "Preliminary Turbulence Measurements in Three-Dimensional Boundary Layers on a Prolate Spheroid", *Viscous and Interacting Flow Field Effects; 6th US/FRG/DEA Meeting*, IB 222-81/CP1, pp. 218-229, 1981.

Kreplin, H.-P., Vollmers, H. and Meier, H. U., "Experimental Determination of Wall Shear Stress Vectors on an Inclined Prolate Spheroid", *Viscous and Interacting Flow Field Effects; Proceedings of the 5th U.S. Air Force and the Federal Republic of Germany Data Exchange Agreement Meeting*, AFFDL-TR-80-3088, pp. 315-332, June 1980.

Kreplin, H.-P., Vollmers, H. and Meier, H. U., "Measurements of the Wall Shear Stress on an Inclined Prolate Spheroid", *Zeitschrift fur Flugwissneschaften und Weltraumforschung*, Vol. 6, No. 4, pp. 248-252, 1982.

Larsen, S. E. and Busch, N. E., "Hot-wire Measurements in the Atmosphere. Part I: Calibration and Response Characteristics", *DISA Information* No. 16, pp. 15-34, July 1974.

Lighthill, J., "Attachment and Separation in Three Dimensional Flow", *Laminar Boundary Layer Theory*, Oxford University Press, 1963.

Lofdahl, L., "Hot-Wire Techniques for the Determination of the Reynolds Stress Tensor in Three-Dimensional Flows", *DANTEC Information*, No. 3, pp. 2-8, September 1986.

Mehta, R. D. and Bradshaw, P., "Longitudinal Vortices Imbedded in Turbulent Boundary Layers: Part 2. Vortex Pair with 'Common Flow' Upwards", *Journal of Fluid Mechanics*, Vol. 188, pp 529-546, 1988.

Meier, H. U. and Kreplin, H.-P., "Experimental Investigation of the Boundary Layer Transition and Separation on a Body of Revolution", *Zeitschrift fur Flugwissneschaften und Weltraumforschung*, Vol. 4, No. 2, pp. 65-71, 1980.

Meier, H. U., Kreplin, H.-P. and Fang, L. W., "Experimental Study of Two- and Three-Dimensional Boundary Layer Separation", *Unsteady Turbulent Shear Flows*, IUTAM Symposium, Toulouse, France 1981a.

Meier, H. U., Kreplin, H.-P., Landhauber, A. and Baumgarten, D., *Mean Velocity Distributions in Three-Dimensional Boundary Layers, Developing on a 1:6 Prolate Spheroid with Natural Transition*, Data Report, IB 222-4/A 10 1984a.

Meier, H. U., Kreplin, H.-P., Landhauber, A. and Baumgarten, D., *Mean Velocity Distributions in Three-Dimensional Boundary Layers, Developing on a 1:6 Prolate Spheroid with Artificial Transition*, Data Report, IB 222-4/A 11 1984b.

Meier, H. U., Kreplin, H.-P. and Ming, X., *Problems Associated with Artificial Boundary Layer Transition*, AIAA Paper No. 83-1673, July 1983a.

Meier, H. U., Kreplin, H.-P. and Vollmers, H., "Development of Boundary Layers and Separation Pattern on a Body of Revolution at Incidence", *2nd Symposium on Numerical and Physical Aspects of Aerodynamic Flows*, State University, Long Beach, CA, January 1983b.

Meier, H. U., Kreplin, H.-P. and Vollmers, H., *The Effect of Artificial Transition on the Boundary Layer Development on an Inclined Body of Revolution*, DFVLR-AVA IB 222-82 A 18, April 1982.

Meier, H. U., Kreplin, H.-P. and Vollmers, H., "Velocity Distributions in 3-D Boundary Layers and Vortex Flows Developing on an Inclined Prolate Spheroid", *Viscous and Interacting Flow Field Effects; 6th US/FRG/DEA Meeting*, IB 222-81/CP1, pp. 202-217, 1981b.

Meier, H. U., Kreplin, H.-P. and Vollmers, H., *Wall Shear Stress Measurements on a Prolate Spheroid at Zero Incidence in the ONERA F1 Wind Tunnel*, Data Report, IB 222-84/A 35 1984c.

Meier, H. U., Kreplin, H.-P. and Vollmers, H., *Wall Shear Stress Measurements on an Inclined Prolate Spheroid in the ONERA F1 Wind Tunnel*, Data Report, IB 222-84/A 34 1984d.

Merati, P. and Adrian, R. J., "Directional Sensitivity of Single and Multiple Sensor Probes", *TSI Quarterly*, Vol. 10, Issue 2, pp. 3-12, April-June 1984.

Miller, J. A., "Simple Linearized Hot-Wire Anemometer", *Journal of Fluids Engineering*, Vol. 98, pp. 550-557, 1976.

Moffat, R. J., "Contributions to the Theory of Single-Sample Uncertainty Analysis", *Journal of Fluids Engineering*, Vol. 104, pp. 250-260, June 1982.

Muller, U. R., "On the Accuracy of Turbulence Measurements with Inclined Hot Wires", *Journal of Fluid Mechanics*, Vol. 119, pp. 155-172, 1982.

Pauley, W. R. and Eaton, J. K., "Boundary Layer Turbulence Structure in the Presence of Embedded Streamwise Vortex Pairs", *Seventh Symposium on Turbulent Shear Flows*, Stanford University, pp. 5.2.1-5.2.6, August 1989.

Pauley, W. R. and Eaton, J. K., "The Fluid Dynamics and Heat Transfer Effects of Streamwise Vortices Embedded in a Turbulent Boundary Layer", Stanford University Thermosciences Division Report MD-51, 1988.

Peake, M. and Tobak, D. J., "Topology of Three Dimensional Separated Flow", *Annual Review of Fluid Mechanics*, Vol. 14, pp. 61-85, 1982.

Phillips, W. R. C. and Graham, J. A. H., "Reynolds-Stress Measurements in a Turbulent Trailing Vortex", *Journal of Fluid Mechanics*, Vol. 147, pp 353-371, 1984.

Rodi, W., "A New Method of Analysing Hot-Wire Signals in Highly Turbulent Flow, and Its Evaluation in a Round Jet", *DISA Information* No. 17, 1975.

Schetz, J. A., *Foundations of Boundary Layer Theory for Momentum, Heat, and Mass Transfer*, Prentice-Hall, 1984.

Schumann, U., "Realizability of Reynolds Stress Turbulence Models", *The Physics of Fluids*, Vol. 20, No. 5, pp. 721-725, May 1977.

Shabaka, I. M. M. A., Mehta, R. D., and Bradshaw, P., "Longitudinal Vortices Imbedded in Turbulent Boundary Layers: Part 1. Single Vortex", *Journal of Fluid Mechanics*, Vol. 155, pp. 37-57, 1985.

Simpson, R. L., Heizer, K. W., and Nasburg, R. E., "Performance Characteristics of a Simple Linearized Hot-Wire Anemometer", *Journal of Fluids Engineering*, Vol. 101, pp. 381-382, September 1979.

Sung, B., "Analysis of the Vortical Flows Around a 60 Degree Delta Wing with Vortex Flaps", Ph.D. Dissertation, Virginia Polytechnic Institute and State University, Blacksburg, VA, 1985.

Townsend, A. A., *The Structure of Turbulent Shear Flows*, Cambridge University Press, 1976.

"United Sensor Probes Catalog", S-7 Rev-B.

Vollmers, H., Kreplin, H.-P., Meier, H.U. and Kuhn, A., *Measured Mean Velocity Field Around a 1:6 Prolate Spheroid at Various Cross Sections*, Data Report, IB221-85/A 08 1985.

Vollmers, H., Kreplin, H.-P. and Meier, H. U., "Separation and Vortical-Type Flow Around a Prolate Spheroid - Evaluation of Relevant Parameters", AGARD-CP-342.

Westphal, R. V., Eaton, J. K. and Pauley, W. R., "Interaction Between a Vortex and a Turbulent Boundary Layer in a Streamwise Pressure Gradient", *Turbulent Shear Flows 5*, Springer Verlag, pp. 266-277, 1985.

References

# Illustrations
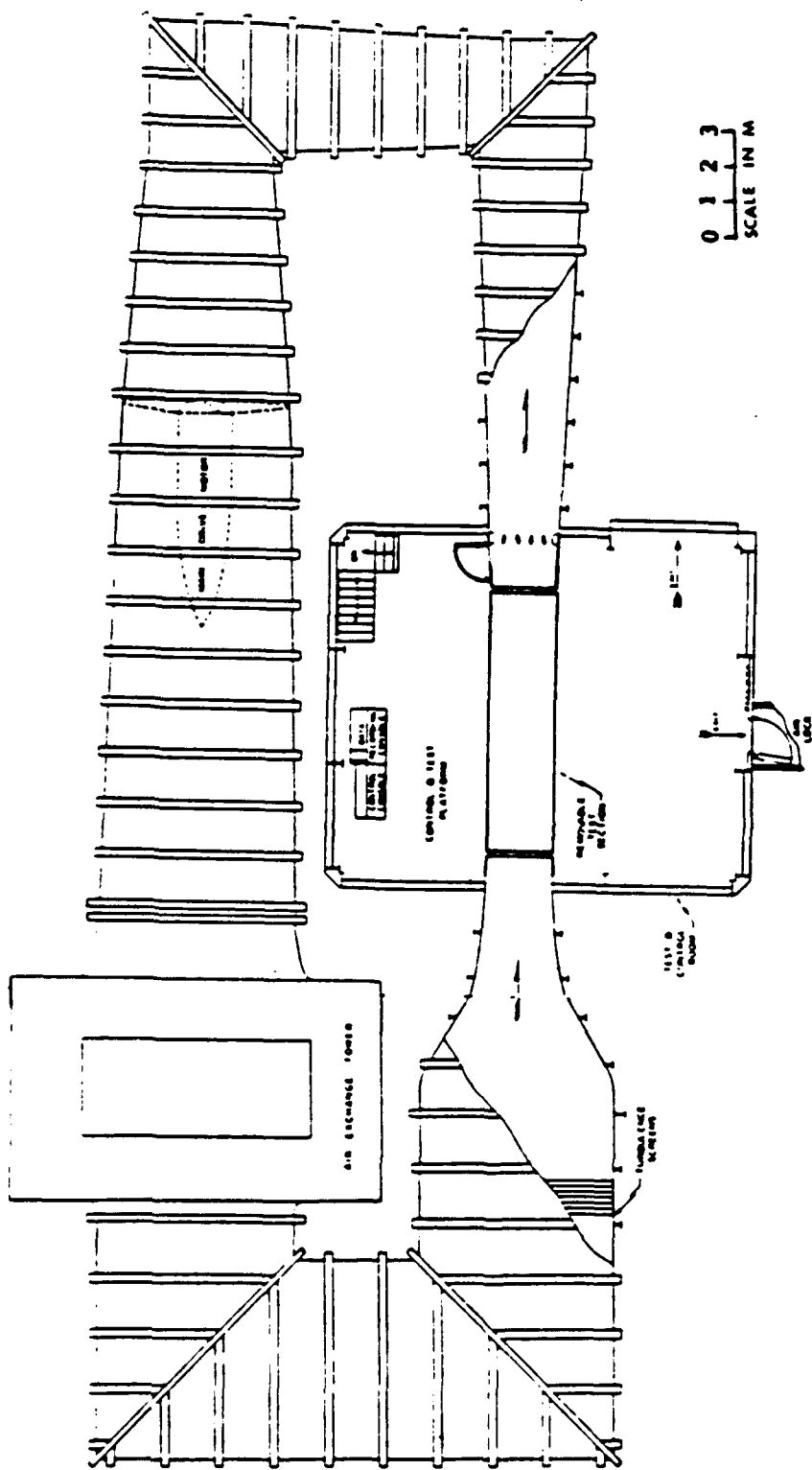
Figure 1. Diagram of VPI & SU Stability Wind Tunnel.
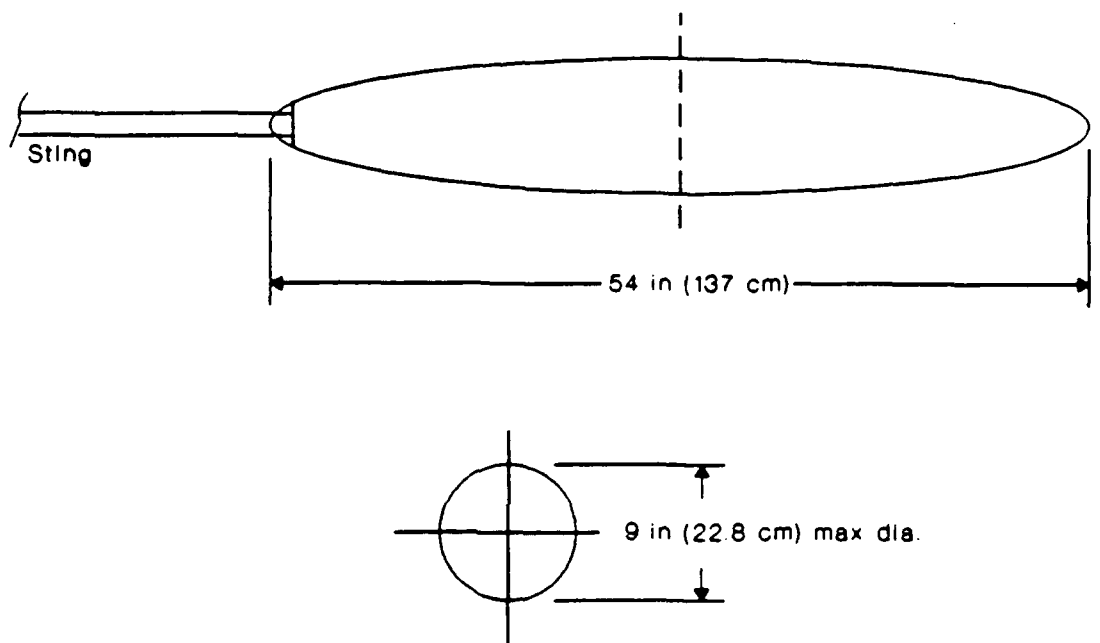
Figure 2.    6:1 Prolate Spheroid Model.
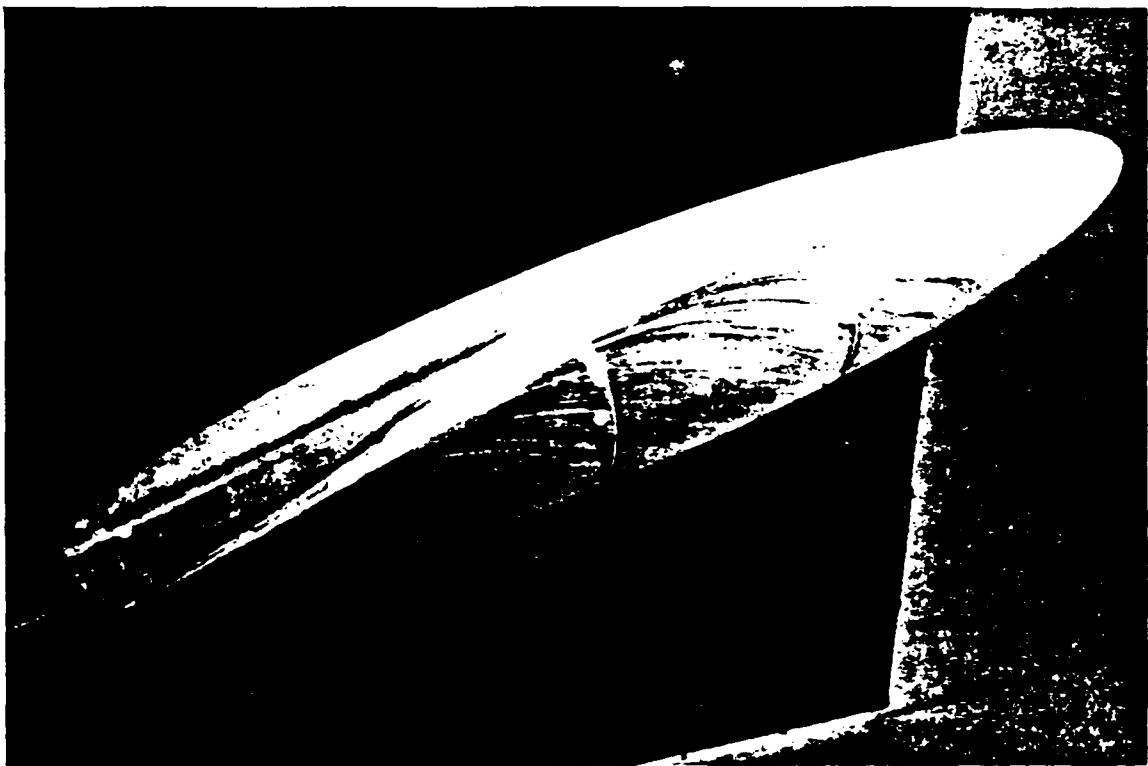
Figure 3.    6:1 Prolate Spheroid Model Mounted in Wind Tunnel.
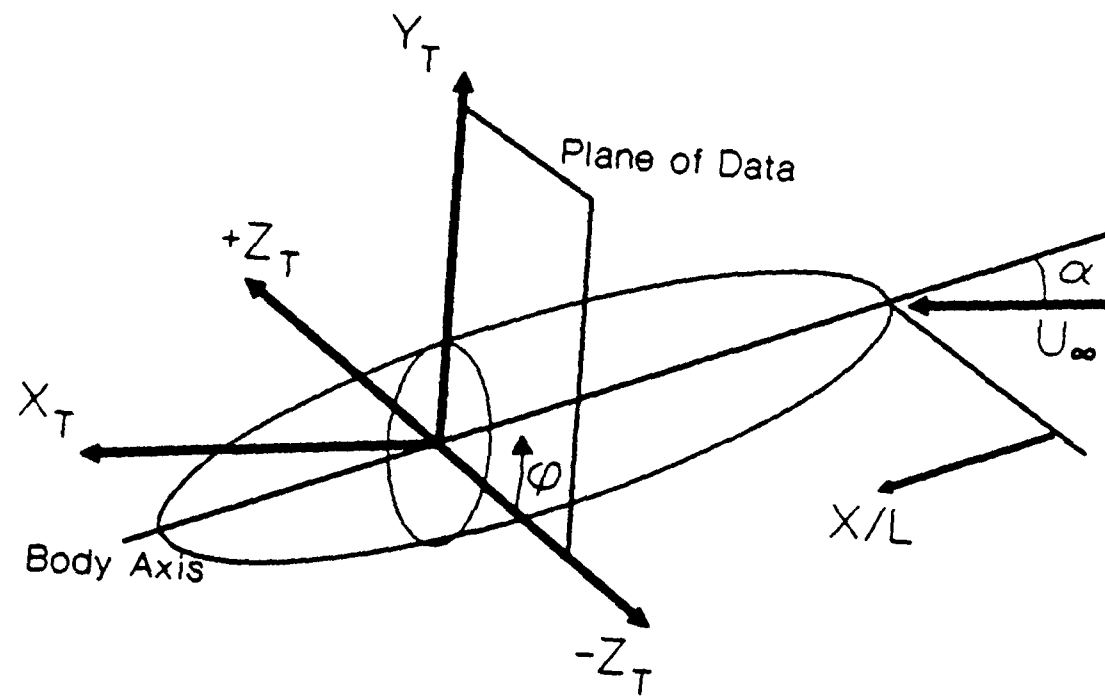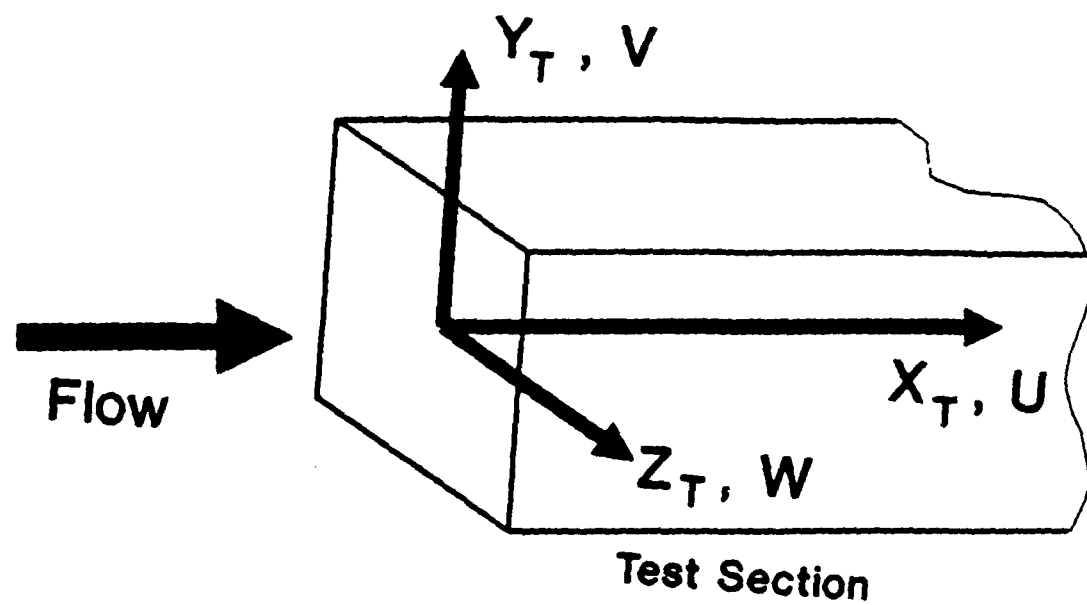
Figure 4.    Tunnel ($X_T$-$Y_T$-$Z_T$) Coordinate System.

Illustrations
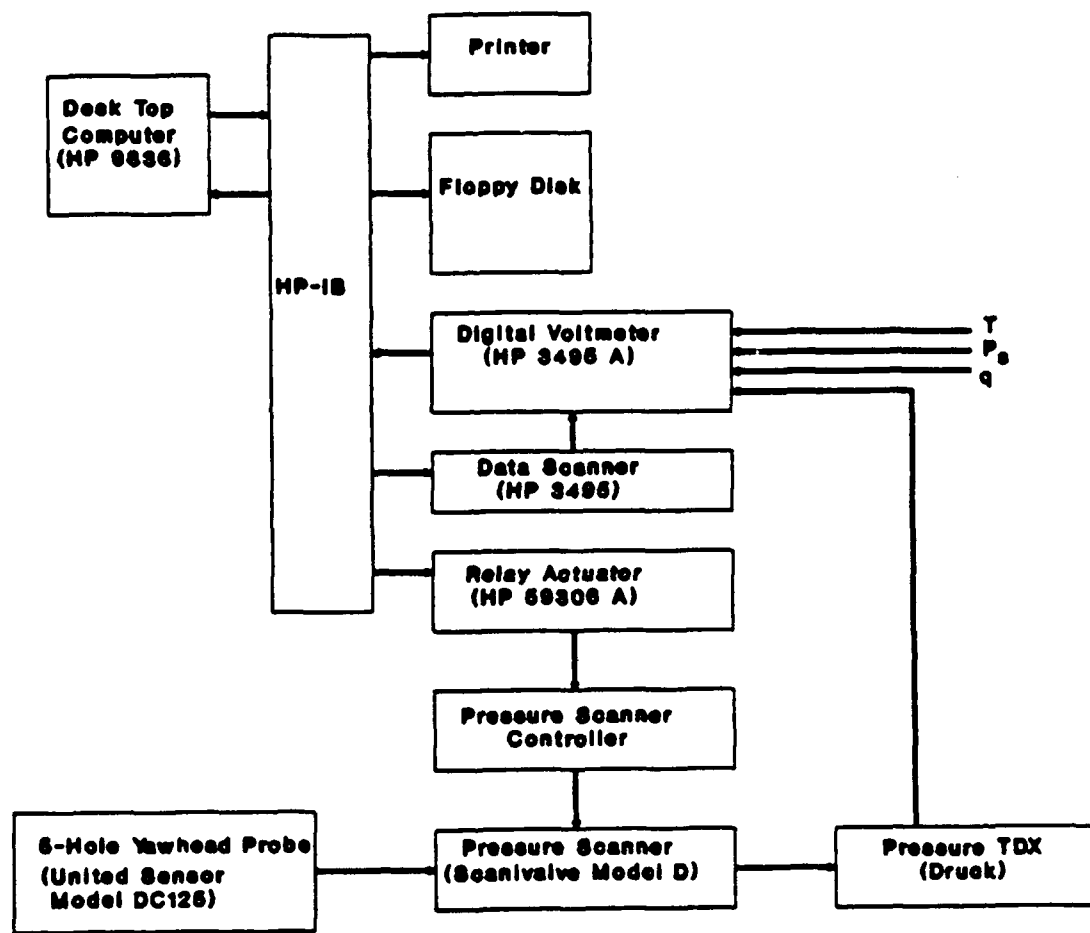
Figure 5.     Diagram of Instrumentation for 5-Hole Yawhead Probe.
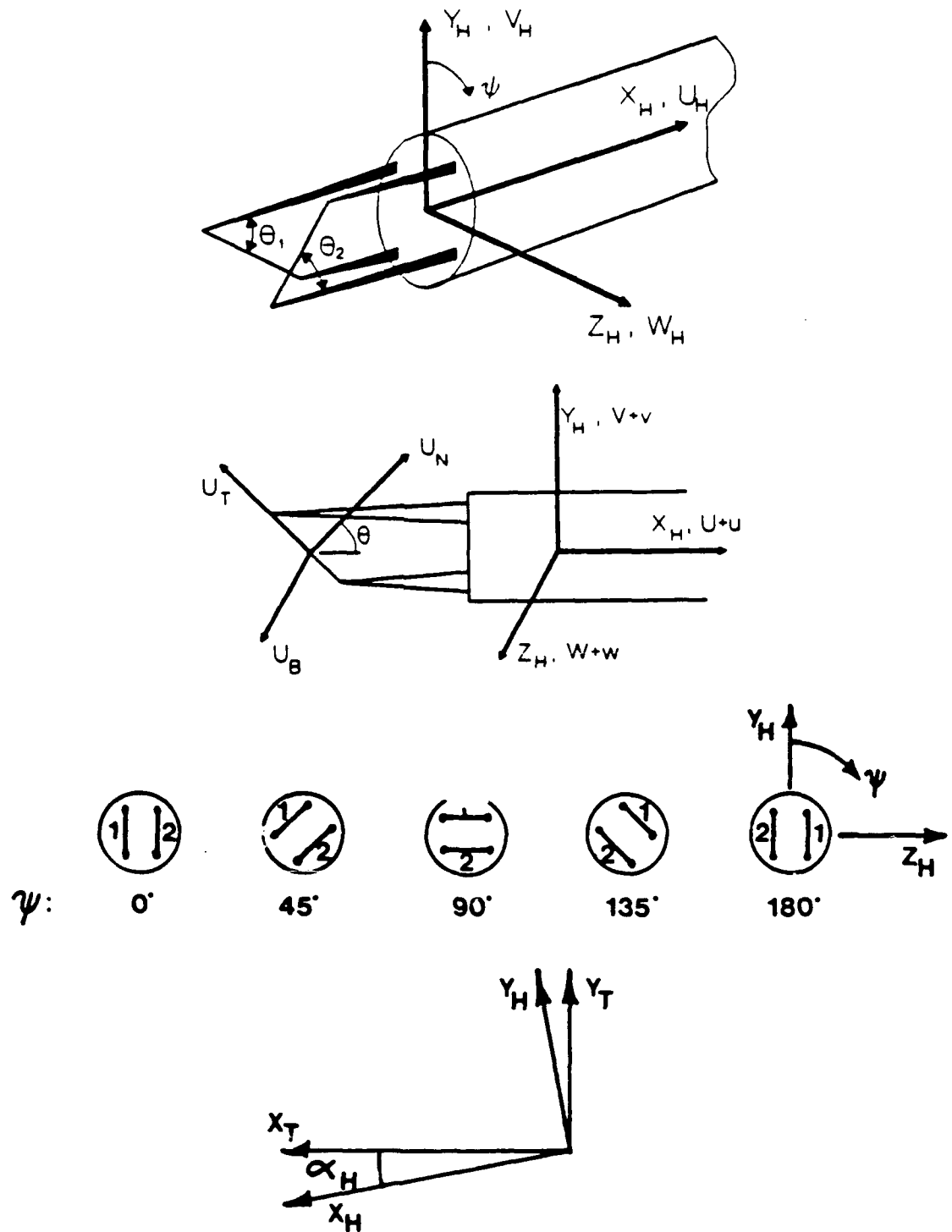
Figure 6. Geometry of X-Wire Probe, with Hot-Wire ($X_H$-$Y_H$-$Z_H$) Coordinate System; and Definitions of Roll Angle $\psi$, Pitch Angle $\alpha_H$, and Wire Angles $\theta_1$ and $\theta_2$.
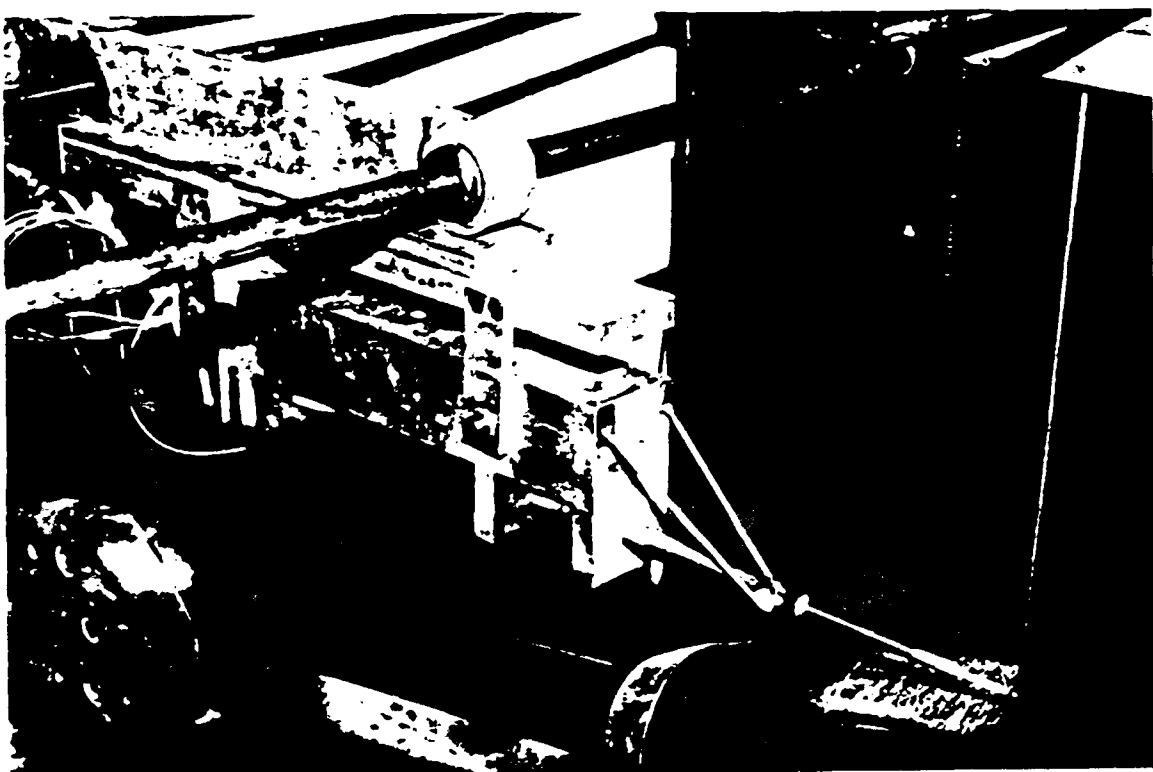
Figure 7.    X-Wire Probe Support with Pitch and Roll Capabilities.
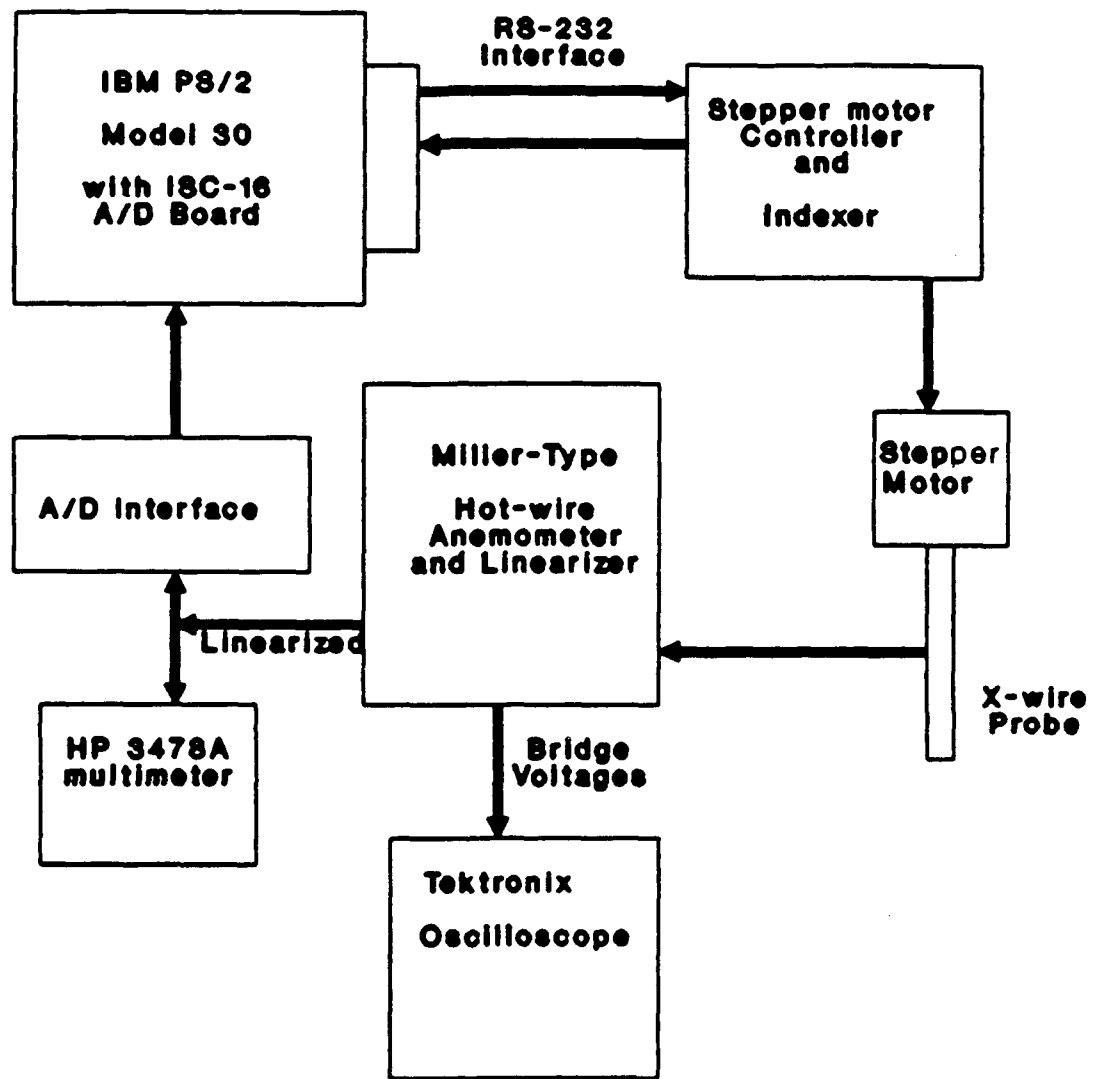
Figure 8.    Diagram of Instrumentation for X-Wire Probe.

Figure 12.  Results of Surface Oil-Flow Visualization Experiments. $\alpha = 10°$, $Re = 4.0 \times 10^6$. (Ahn, 1990).
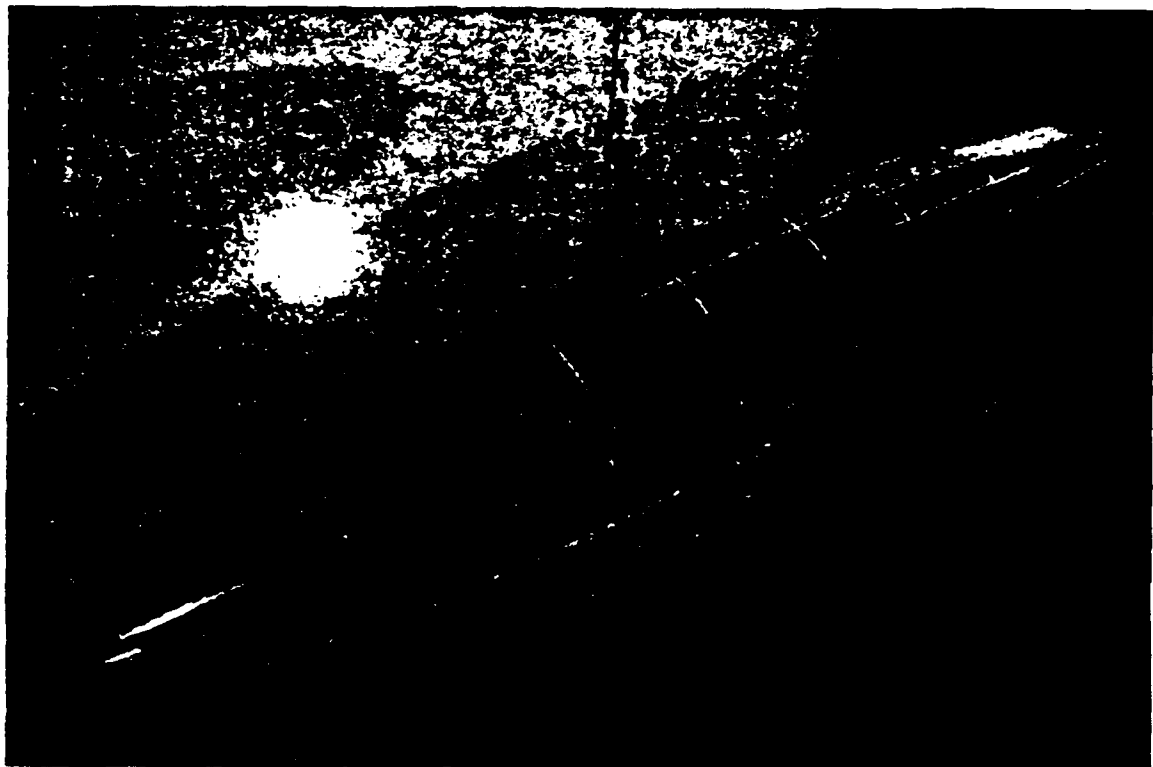
Figure 13.    Results of Surface Oil-Flow Visualization Experiments. $\alpha = 15°$, $Re = 4.0 \times 10^6$. (Ahn, 1990).

Figure 14.    Results of Surface Oil-Flow Visualization Experiments. $\alpha = 15°$. $Re = 4.0 \times 10^6$. (Ahn, 1990).
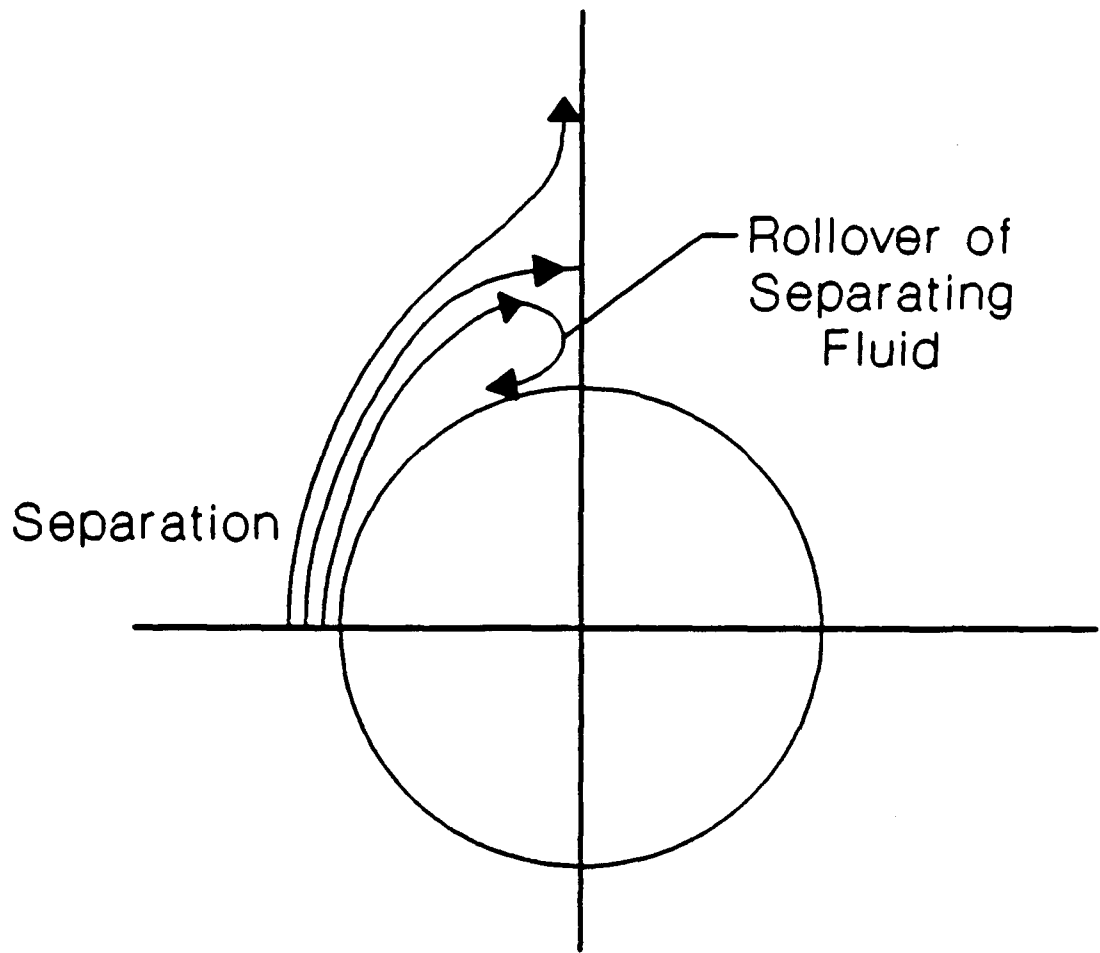
Figure 15.    Diagram of Cross-Section of Separation Sheet of Fluid.
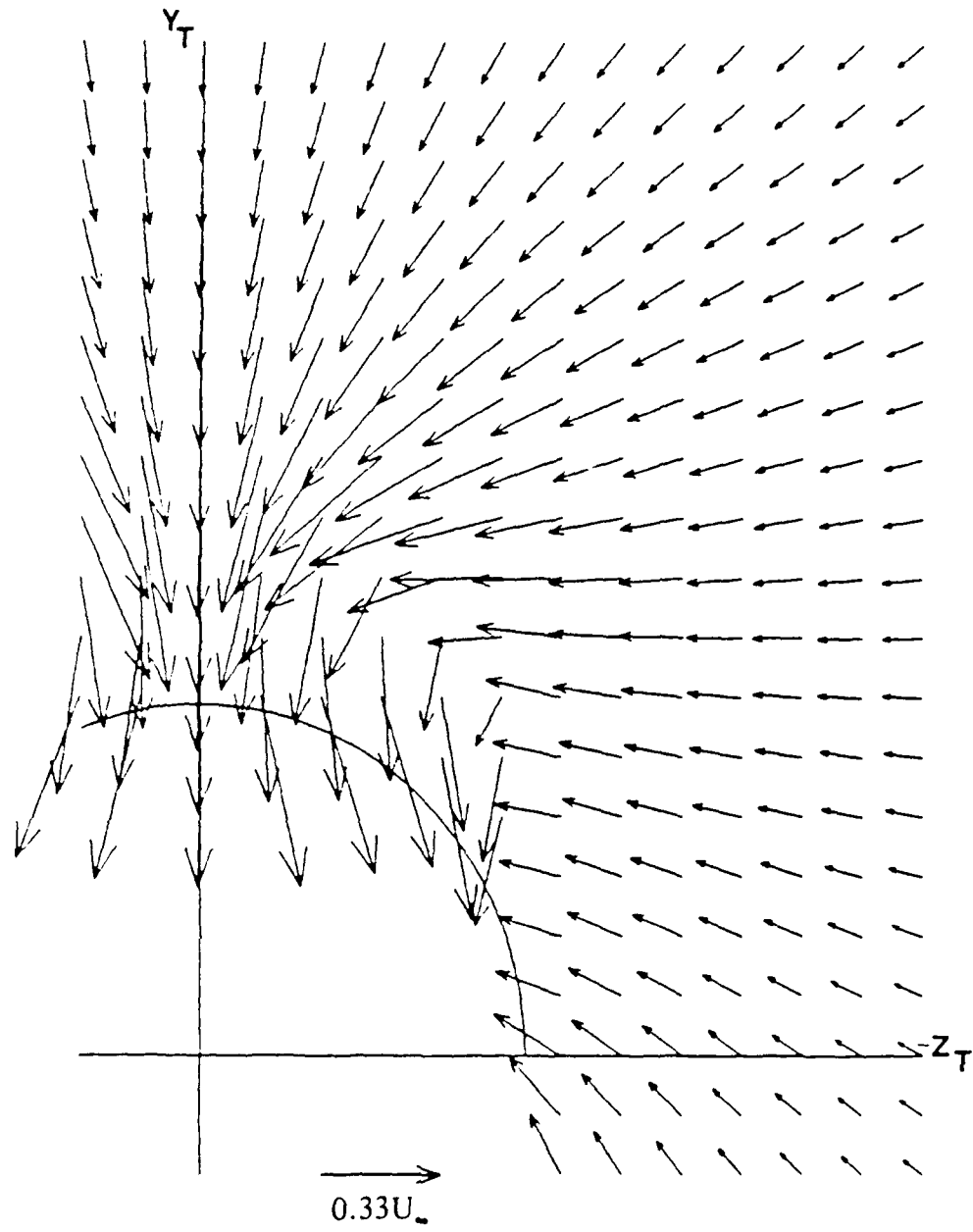
Figure 16.    Secondary Velocity Vectors from Yawhead Probe Measurements, in Tunnel
Coordinates, X/L=0.9, α=15°, Re=4.0×10⁶, Grid Spacing=1.27cm
(0.5in). Compare with Figure 32 to see Results of Rotation.

Illustrations
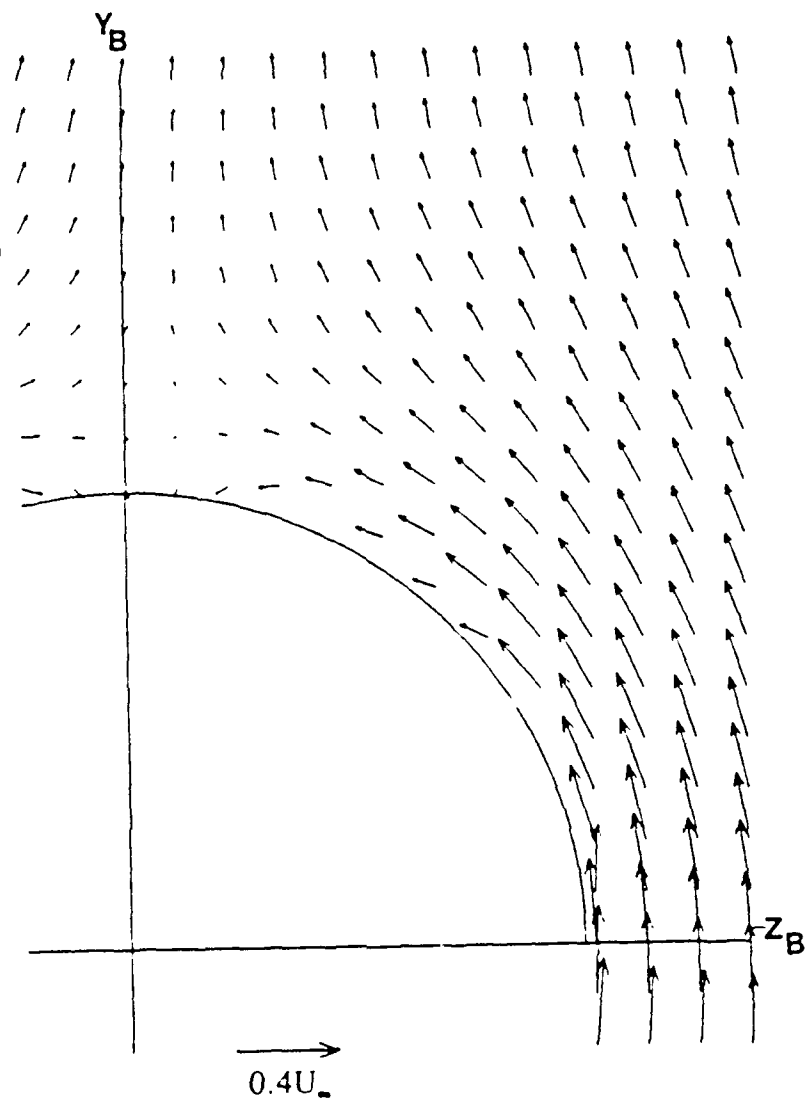
Figure 17. Secondary Velocity Vectors from Yawhead Probe Measurements, X/L=0.6, $\alpha$ = 10°, Re = 1.3 × 10⁶, Grid Spacing of 1.27cm (0.5in).
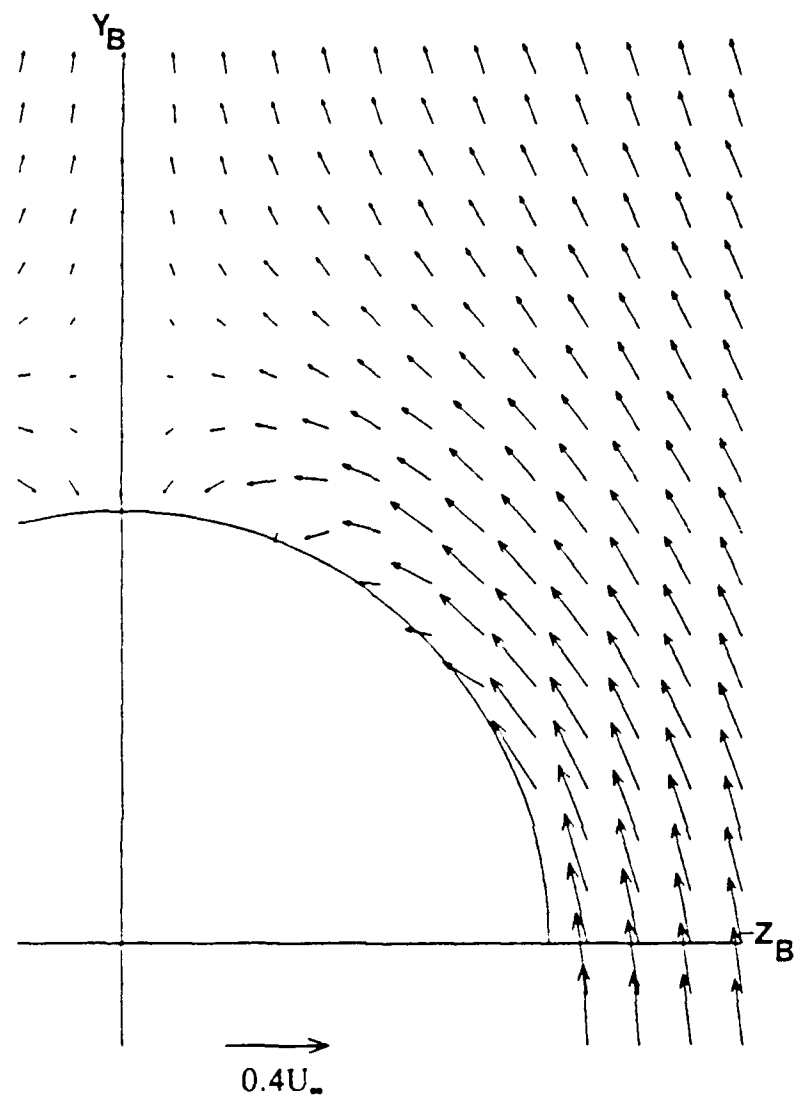
Figure 18.    Secondary Velocity Vectors from Yawhead Probe Measurements.
X/L=0.7, $\alpha = 10°$, Re = $1.3 \times 10^6$, Grid Spacing of 1.27cm (0.5in).
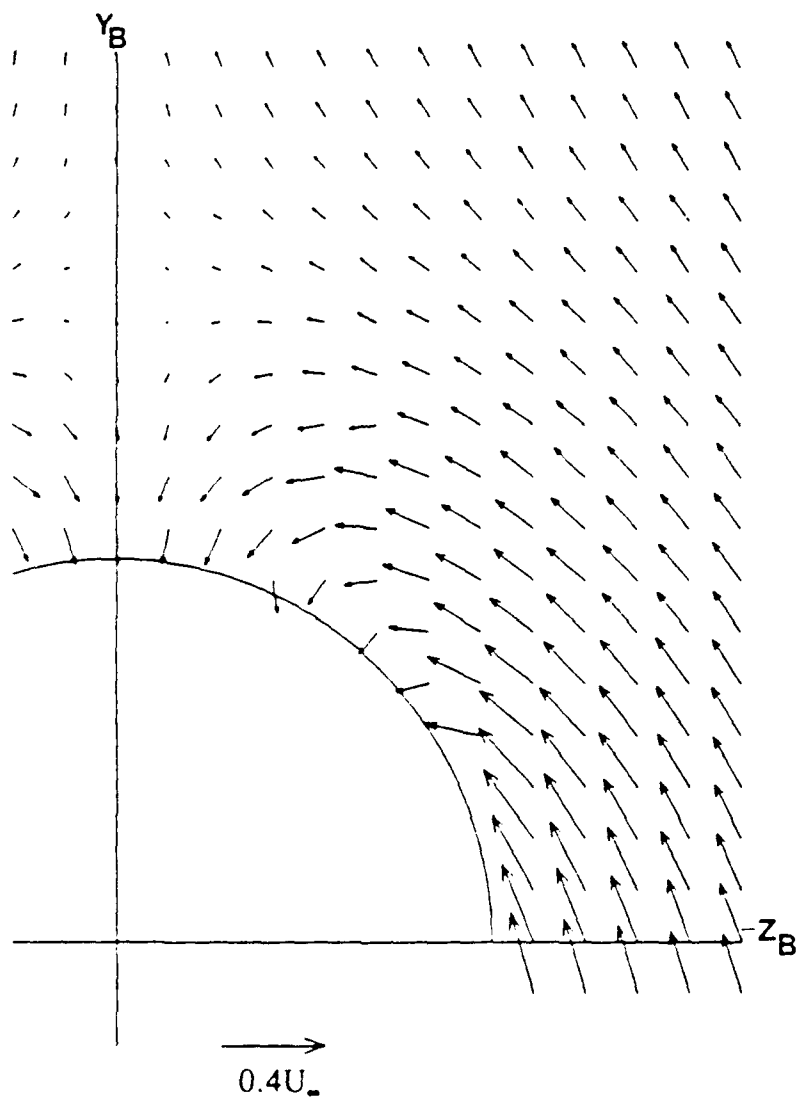
Figure 19. Secondary Velocity Vectors from Yawhead Probe Measurements. X/L = 0.8, $\alpha$ = 10°, Re = 1.3 × 10⁶, Grid Spacing of 1.27cm (0.5in).
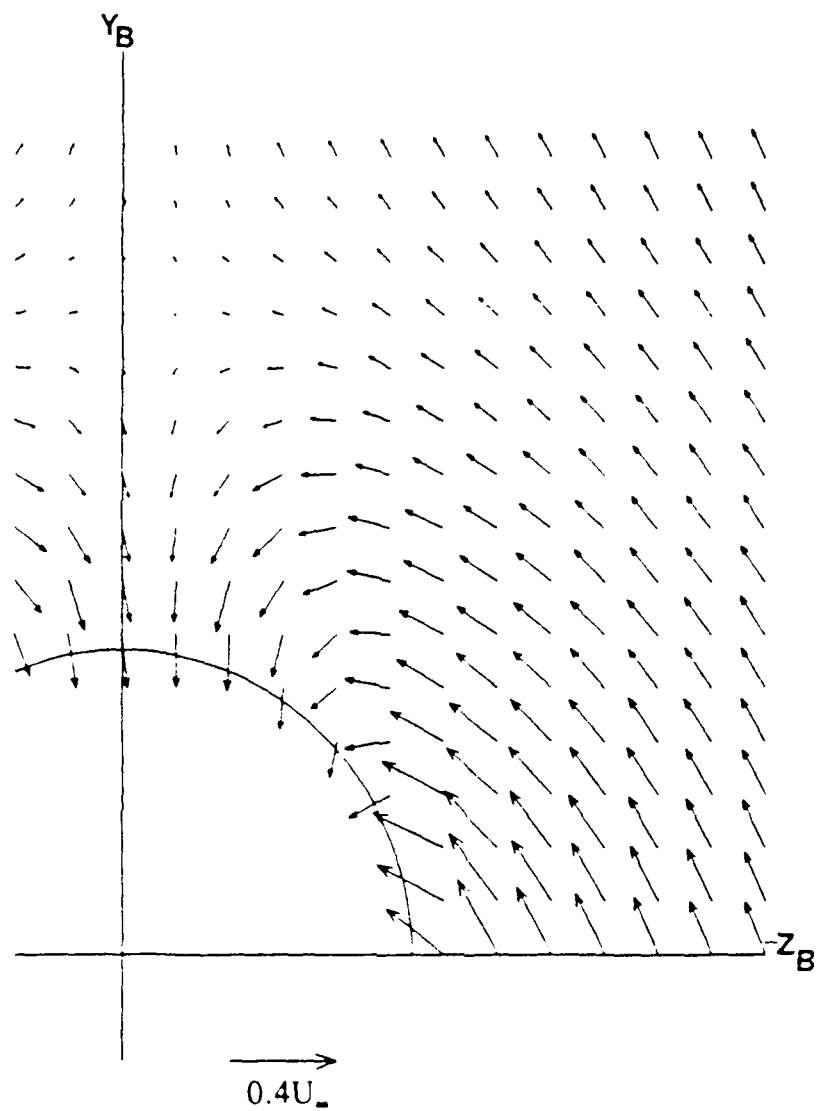
Figure 20.    Secondary Velocity Vectors from Yawhead Probe Measurements.
X/L=0.9, $\alpha=10°$, Re=$1.3\times10^6$, Grid Spacing of 1.27cm (0.5in).
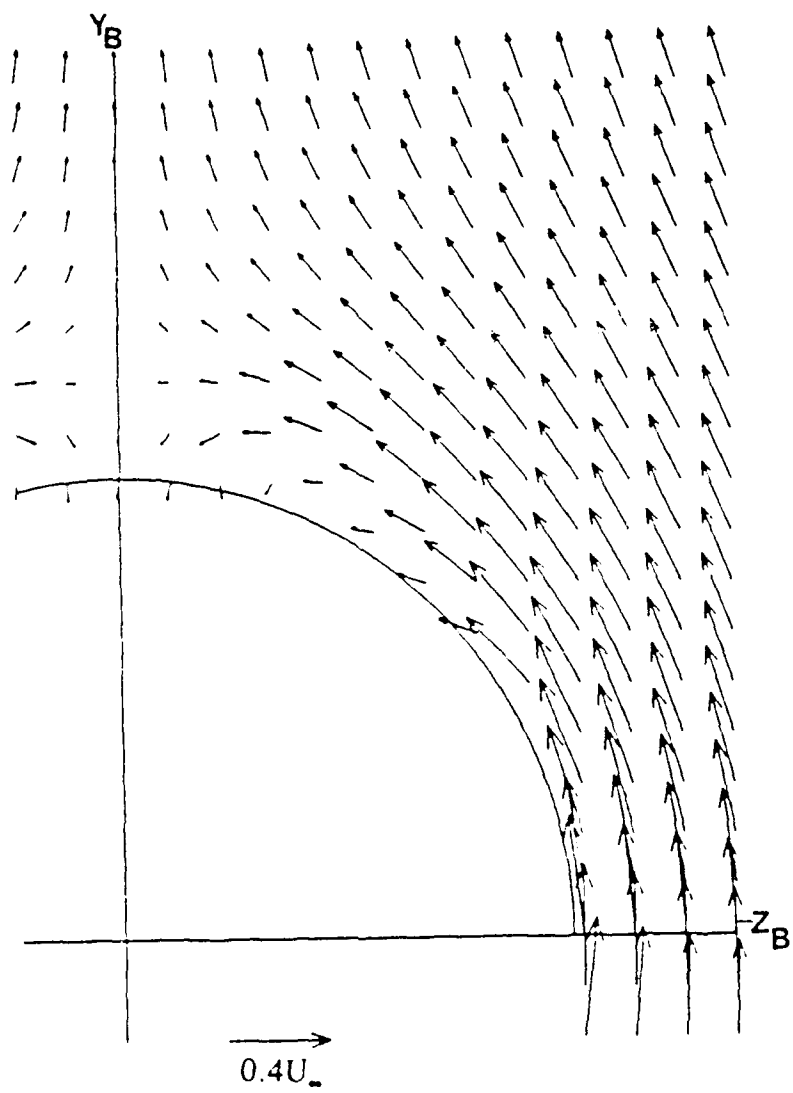
Figure 21.   Secondary Velocity Vectors from Yawhead Probe Measurements.
X/L=0.6, $\alpha=15°$, Re=$1.3\times10^6$, Grid Spacing of 1.27cm (0.5in).
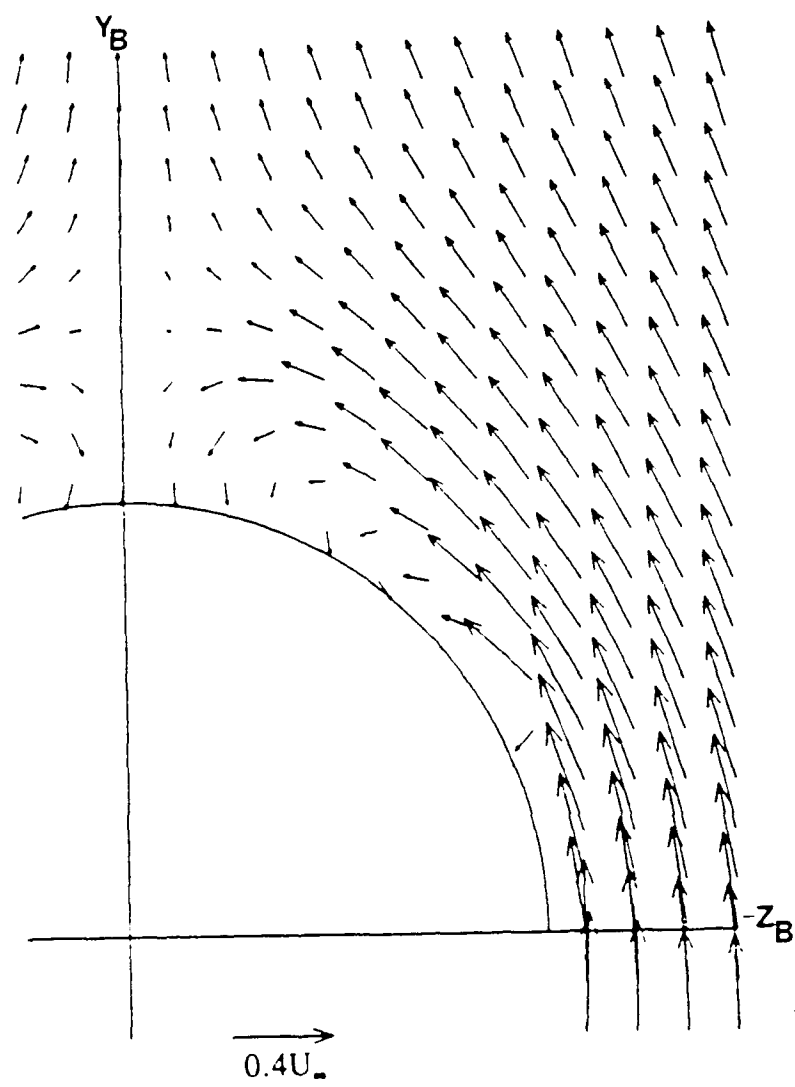
Figure 22.    Secondary Velocity Vectors from Yawhead Probe Measurements.
X/L=0.7, $\alpha$=15°, Re=1.3×10$^6$. Grid Spacing of 1.27cm (0.5in).
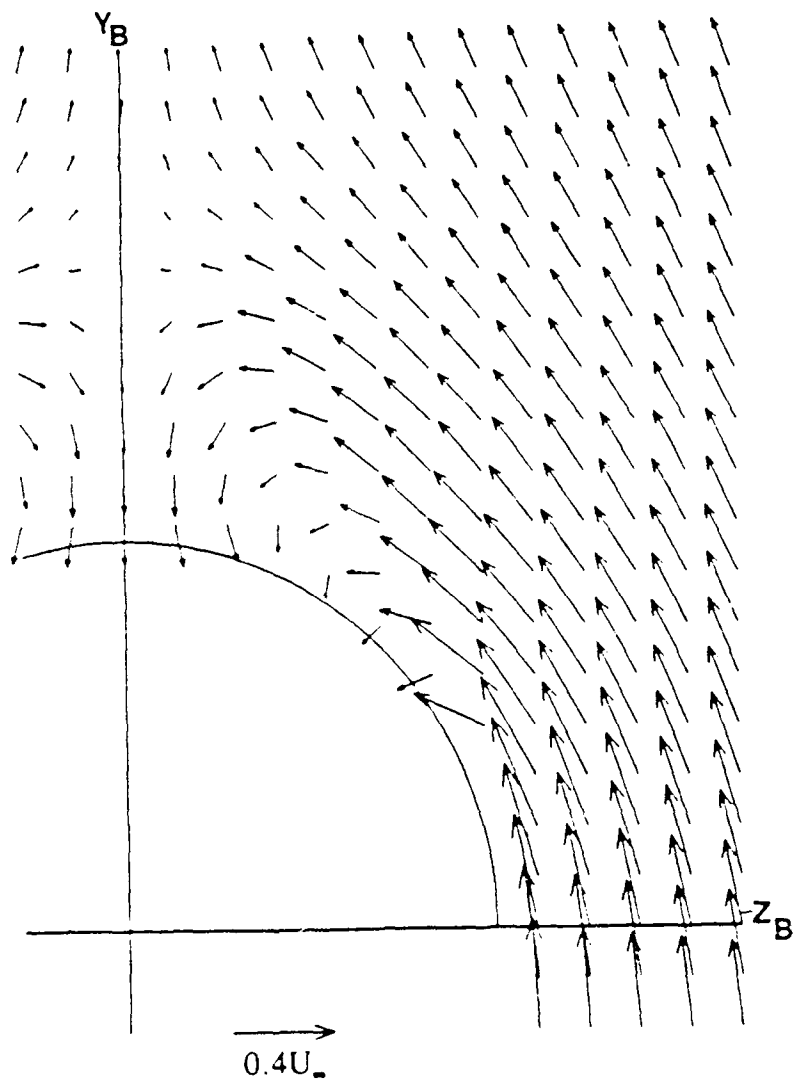
Figure 23. Secondary Velocity Vectors from Yawhead Probe Measurements, X/L=0.8, $\alpha=15°$, Re=$1.3\times10^{6}$, Grid Spacing of 1.27cm (0.5in).
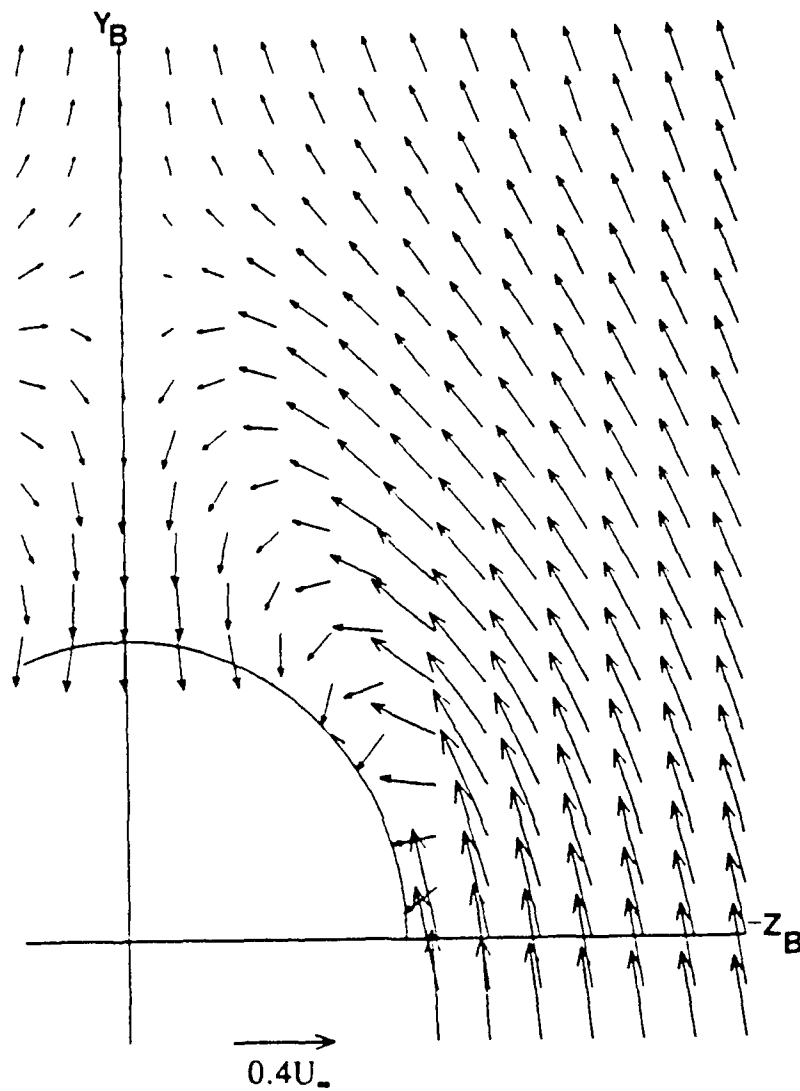
Figure 24.    Secondary Velocity Vectors from Yawhead Probe Measurements %w
          X/L=0.9, α=15°, Re=1.3×10⁶. Grid Spacing of 1.27cm (0.5in).
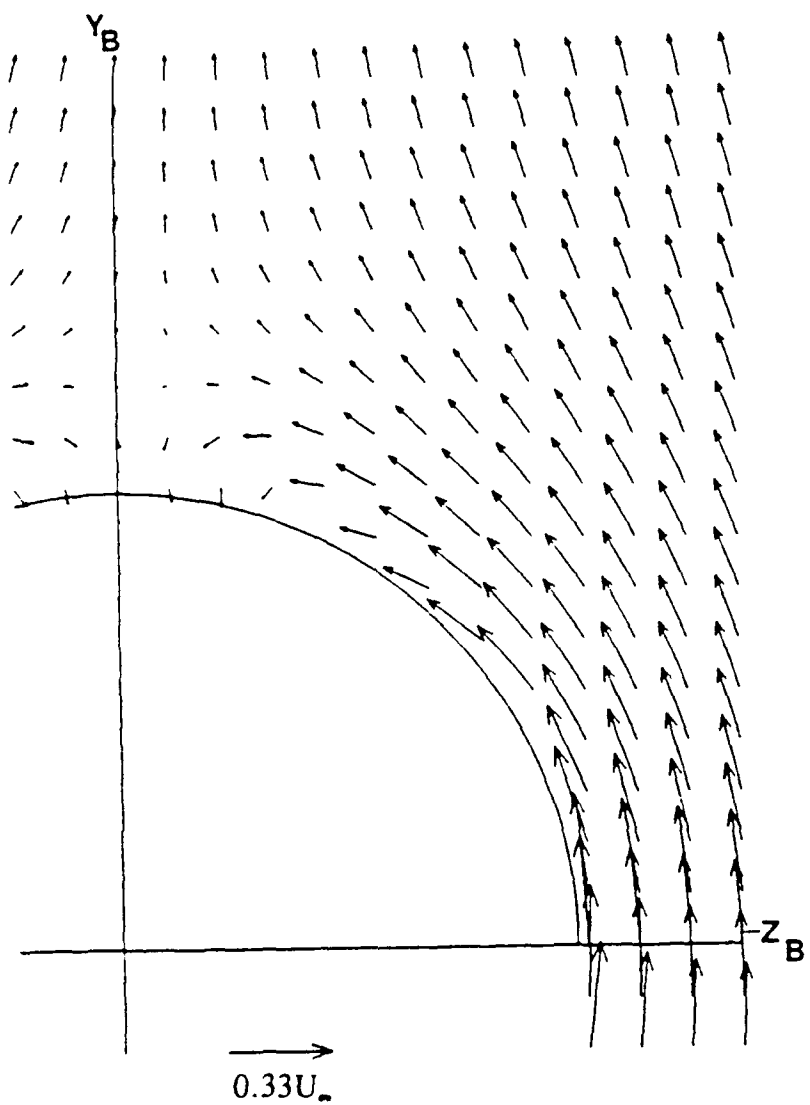
Figure 25.    Secondary Velocity Vectors from Yawhead Probe Measurements,
X/L=0.6, $\alpha = 10°$, Re=$4.0 \times 10^6$, Grid Spacing of 1.27cm (0.5in).
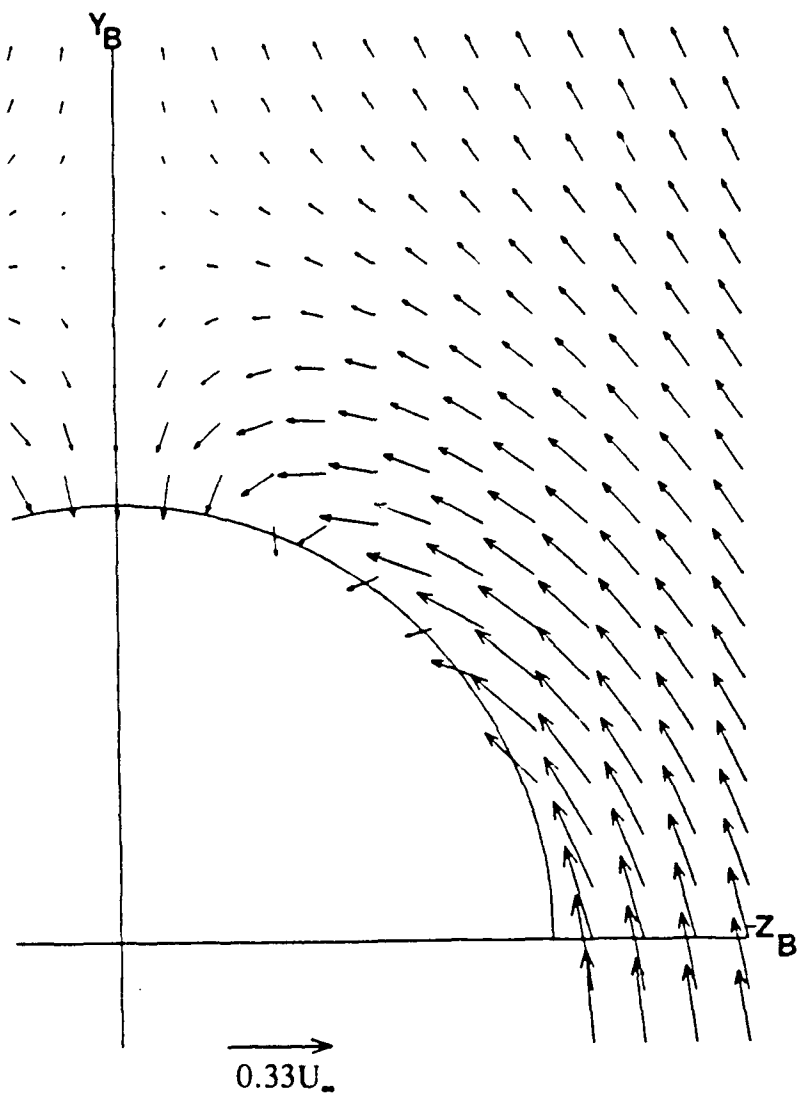
Figure 26.    Secondary Velocity Vectors from Yawhead Probe Measurements,
X/L=0.7, $\alpha$=10°, Re=4.0×10⁶, Grid Spacing of 1.27cm (0.5in).
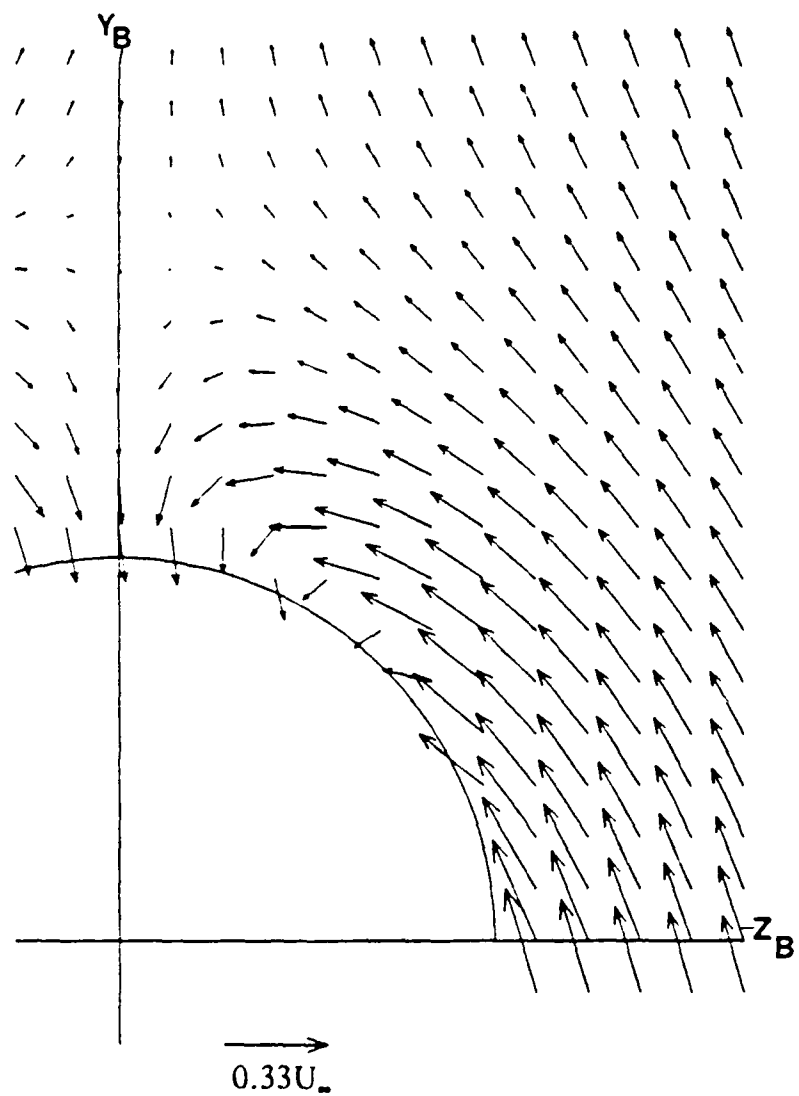
Figure 27.    Secondary Velocity Vectors from Yawhead Probe Measurements,
X/L=0.8. $\alpha$=10°, Re=4.0×10$^6$. Grid Spacing of 1.27cm (0.5in).

Illustrations
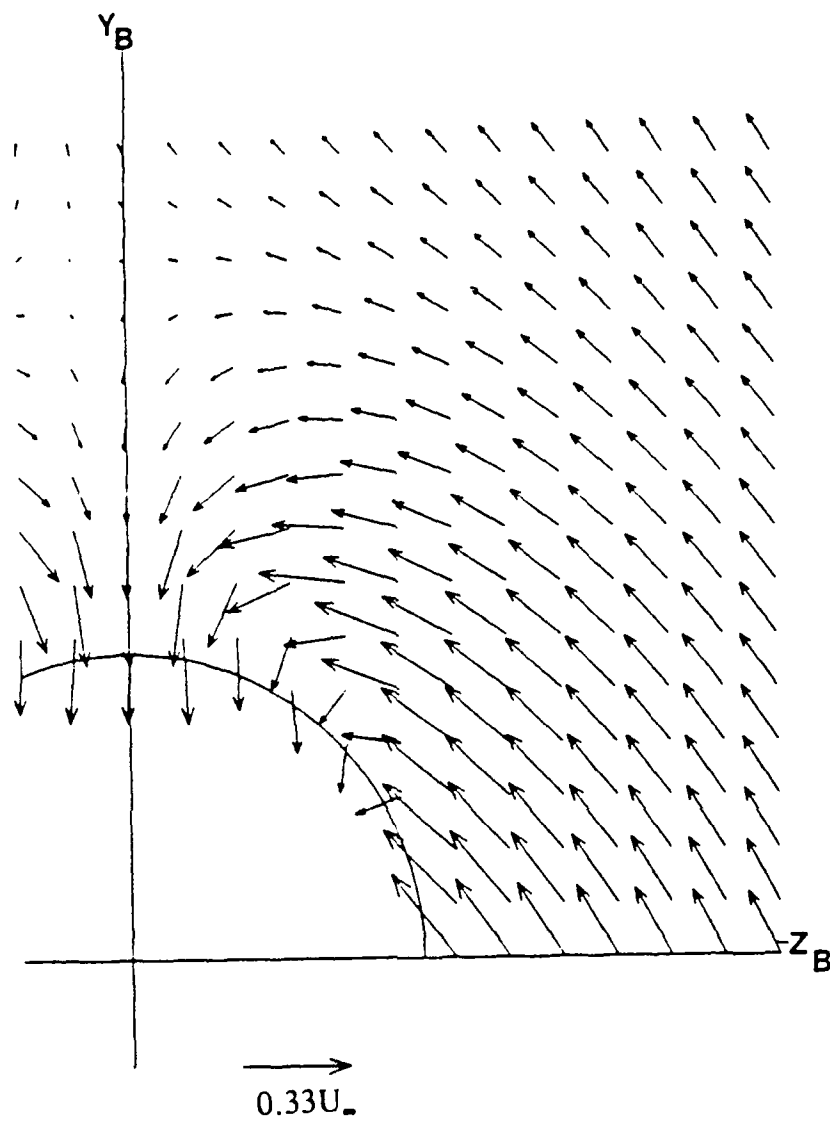
Figure 28.    Secondary  Velocity  Vectors  from  Yawhead  Probe  Measurements.
X/L=0.9,  $\alpha$=10°,  Re=4.0×10$^6$,  Grid Spacing of 1.27cm (0.5in).
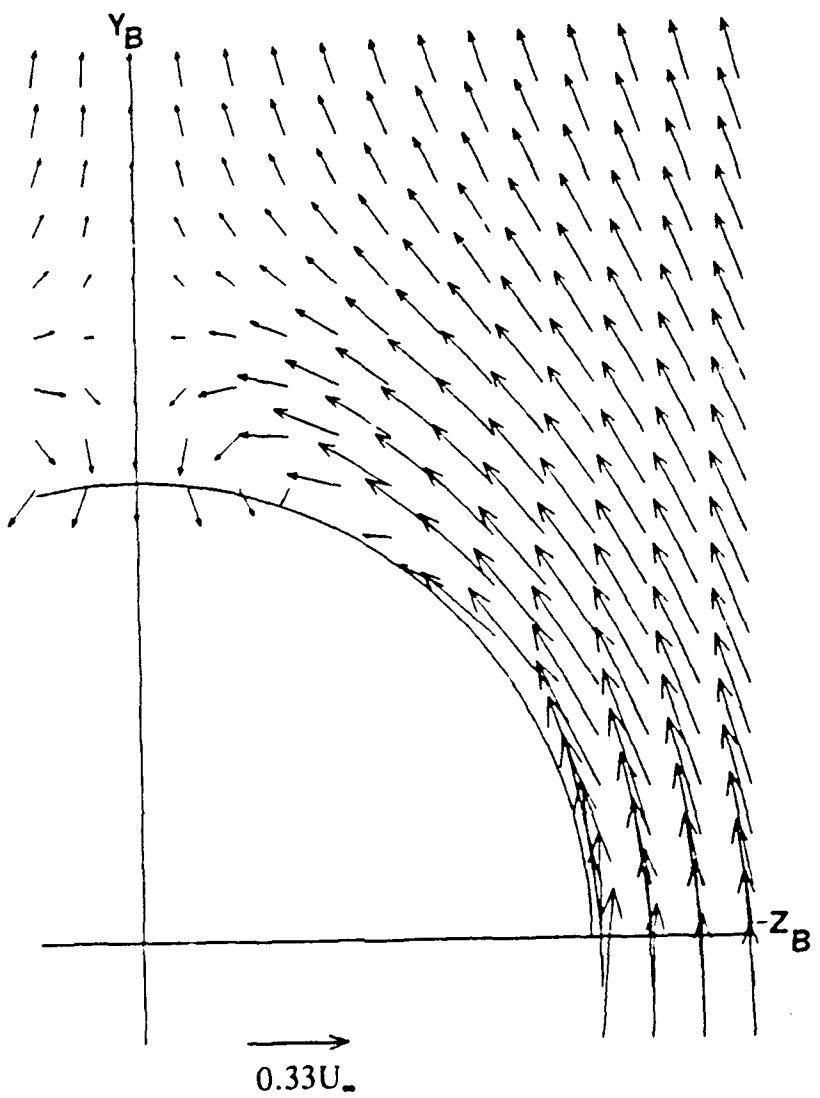
Figure 29.    Secondary Velocity Vectors from Yawhead Probe Measurements,
X/L=0.6, $\alpha$=15°, Re=4.0×10$^6$, Grid Spacing of 1.27cm (0.5in).
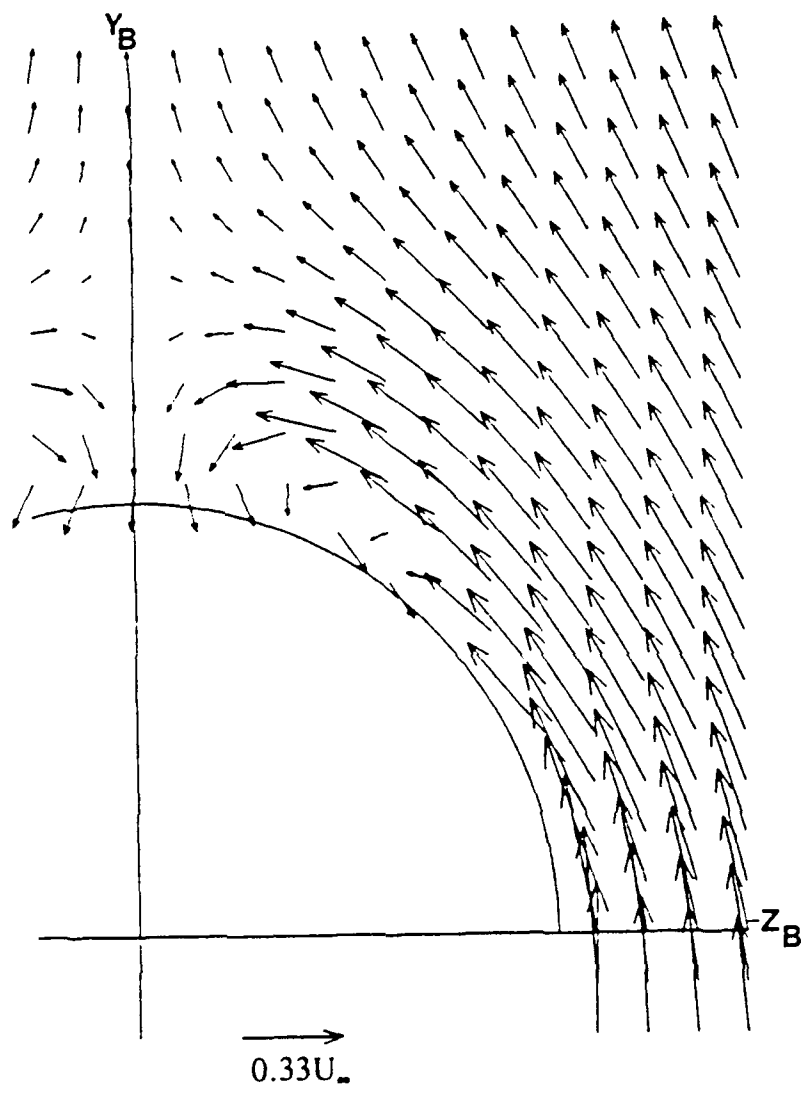
Figure 30.   Secondary Velocity Vectors from Yawhead Probe Measurements,
$X/L=0.7$, $\alpha=15°$, $Re=4.0\times10^6$, Grid Spacing of 1.27cm (0.5in).
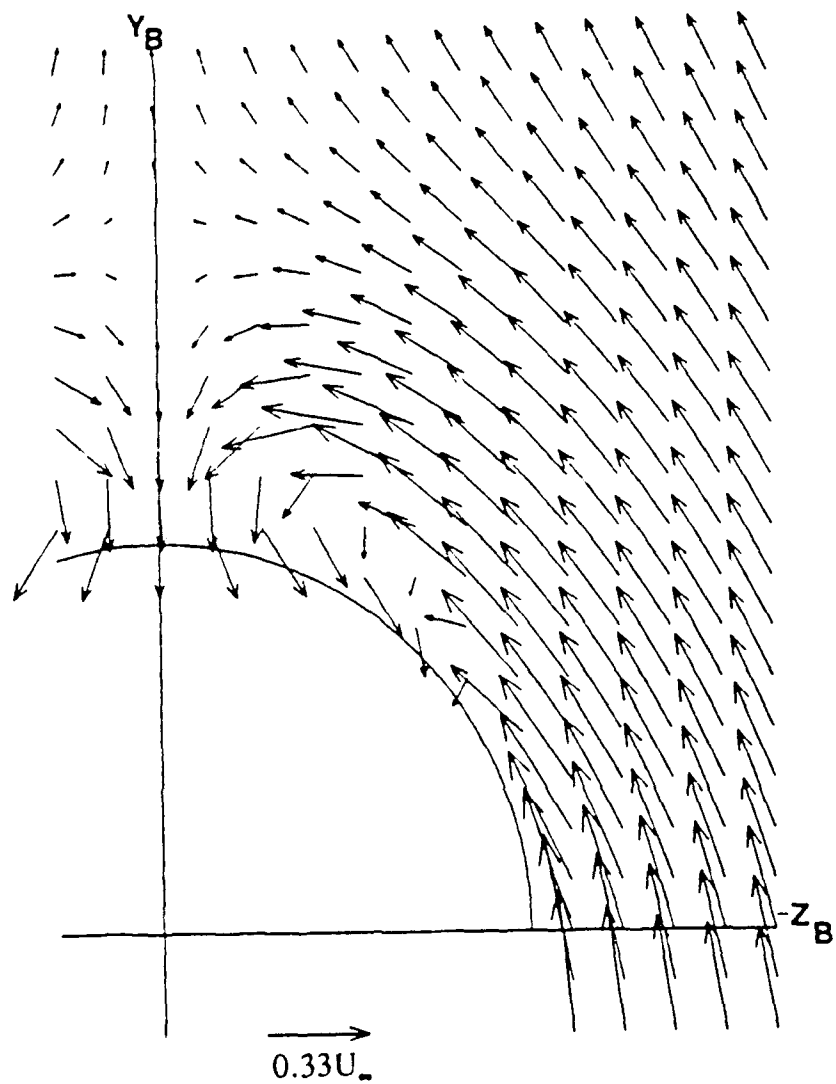
Figure 31.    Secondary Velocity Vectors from Yawhead Probe Measurements.
X/L=0.8, $\alpha = 15°$, Re=4.0×10$^6$, Grid Spacing of 1.27cm (0.5in).
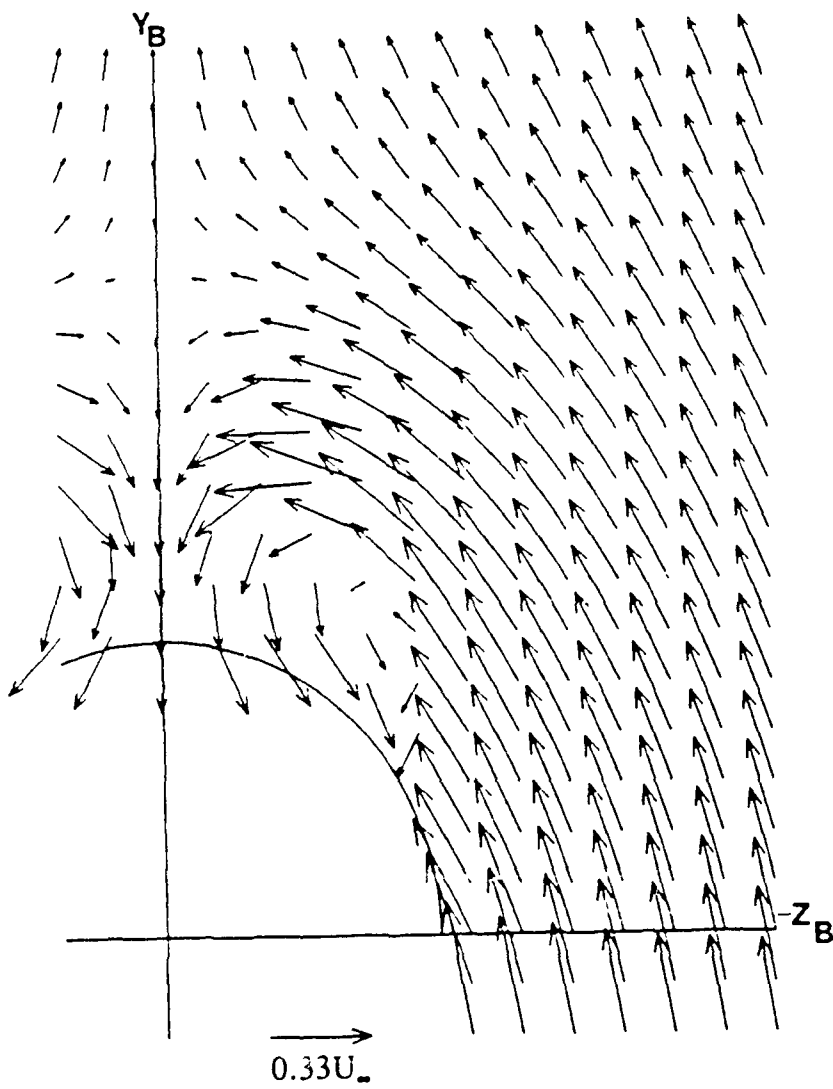
Figure 32.    Secondary Velocity Vectors from Yawhead Probe Measurements.
X/L=0.9, $\alpha$ = 15°, Re=4.0×10⁶, Grid Spacing of 1.27cm (0.5in).
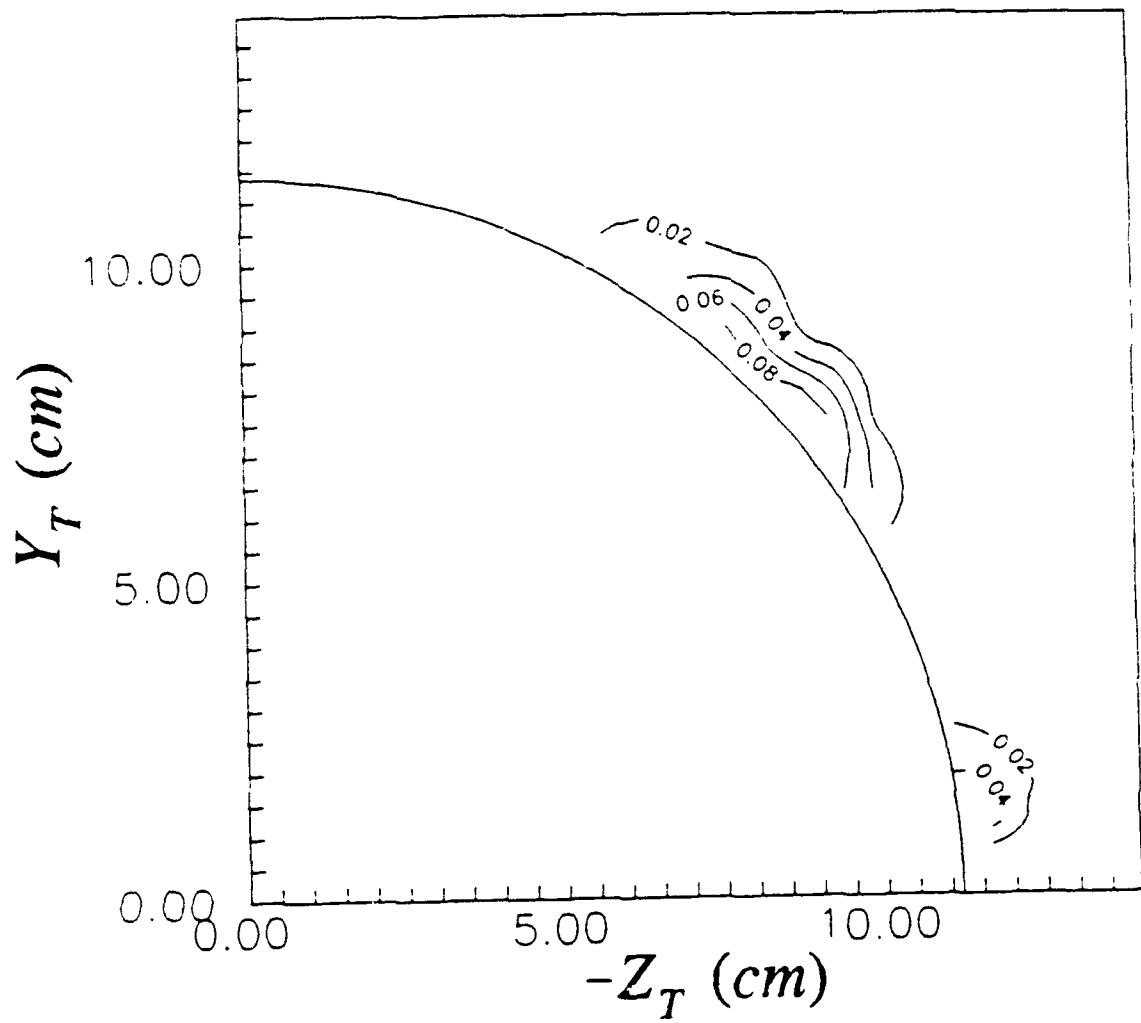
Figure 33.    Contours of $\Omega_X/U_\infty$ (1/cm). $X/L=0.6$, $\alpha=10°$, $Re=1.3\times10^6$.
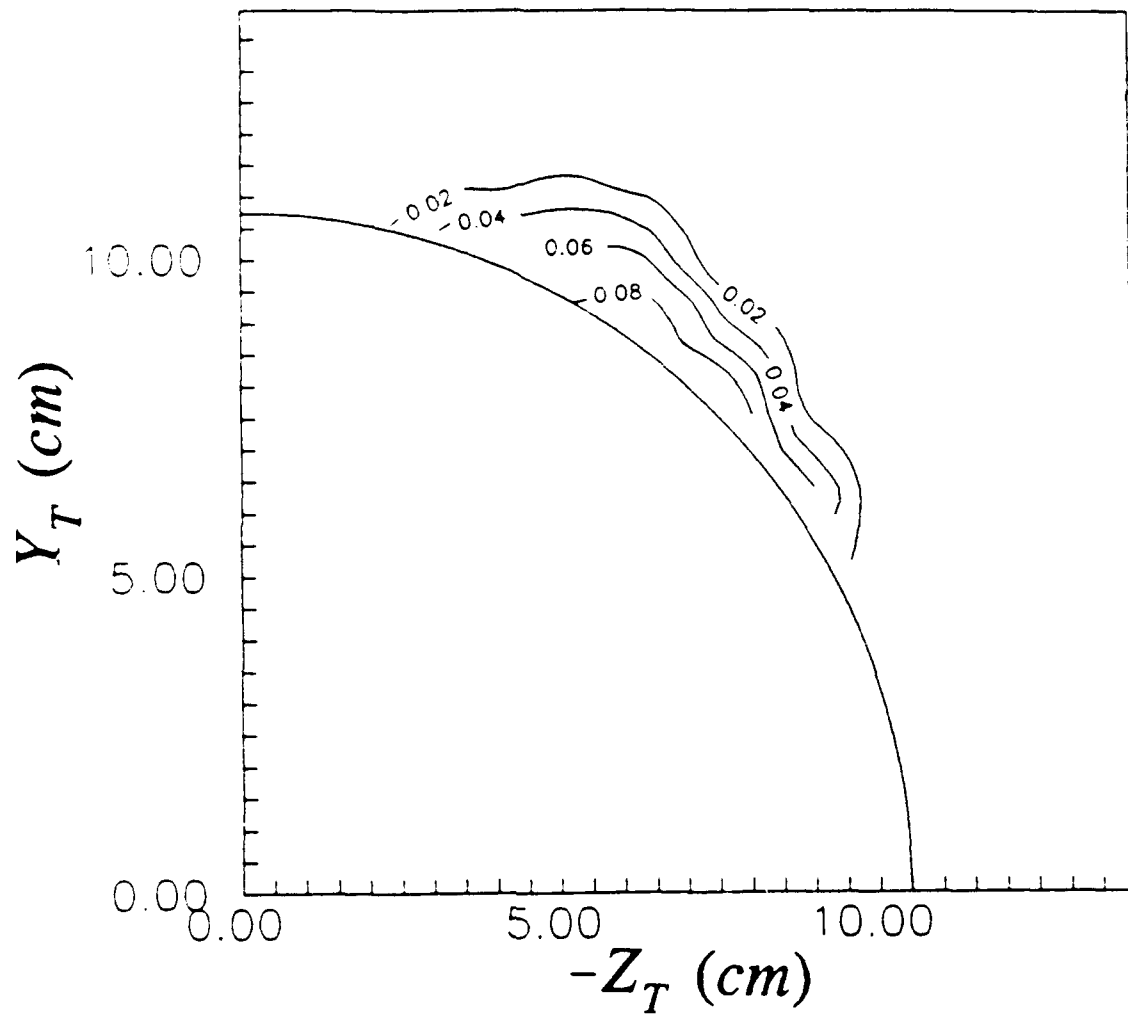
Figure 34    Contours of $\Omega_x/U_\infty$ (1/cm), X/L=0.7, $\alpha=10°$, Re=$1.3\times10^6$.
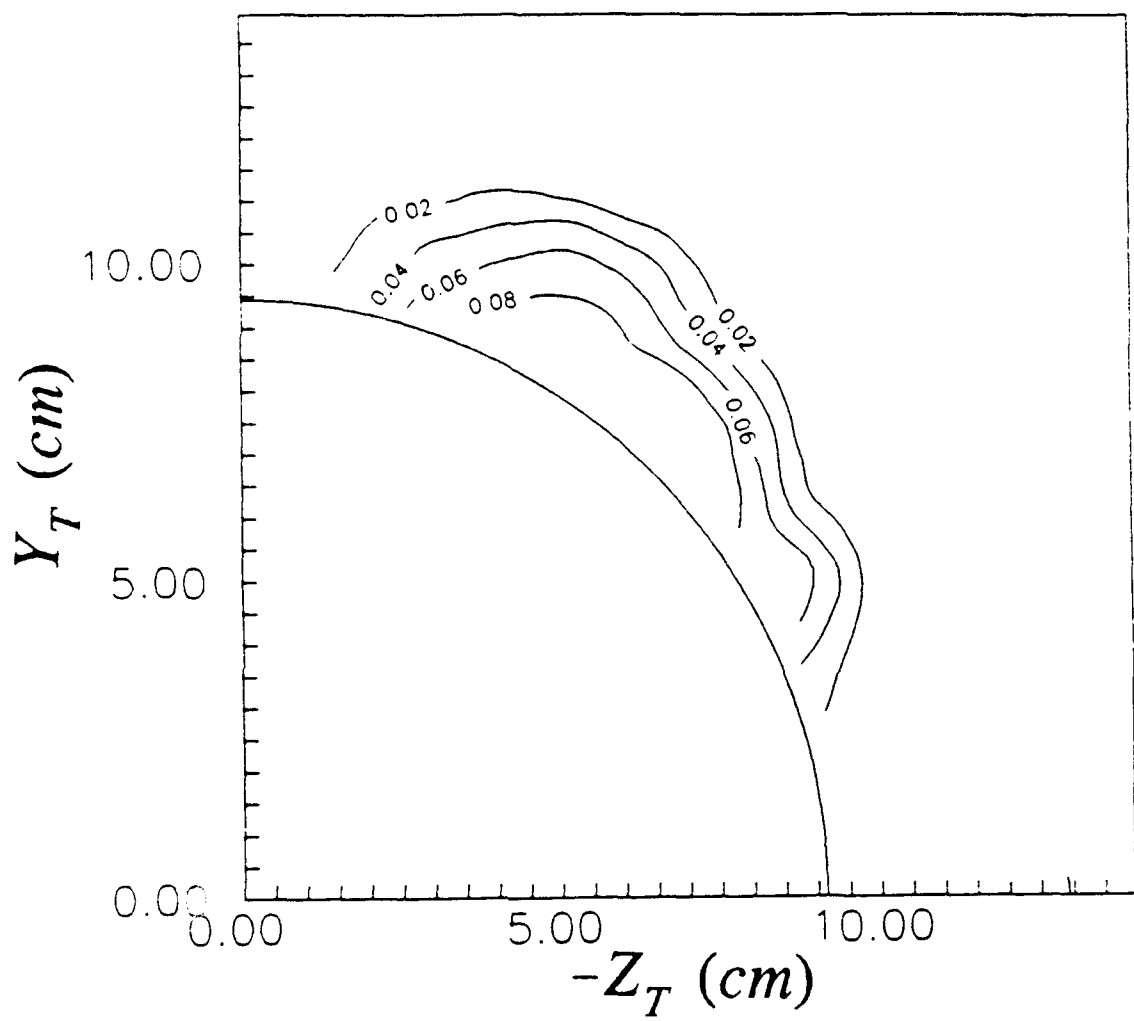
Figure 35.    Contours of $\Omega_X/U_\infty$ (1/cm), X/L=0.8, $\alpha$=10°, Re=1.3×10⁶.
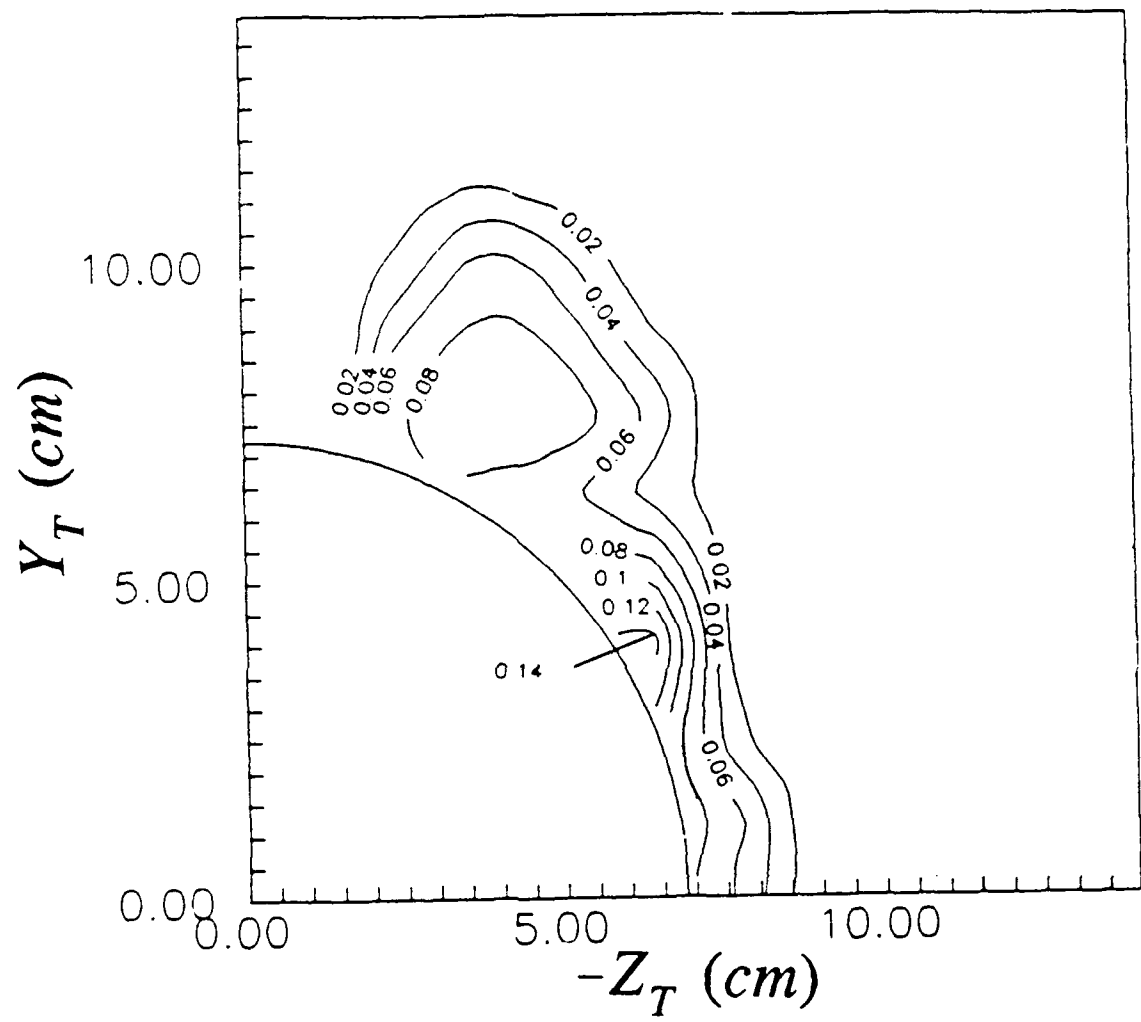
Figure 36.    Contours of $\Omega_X/U_\infty$ (1/cm), X/L=0.9, $\alpha=10°$, Re=$1.3\times10^6$.
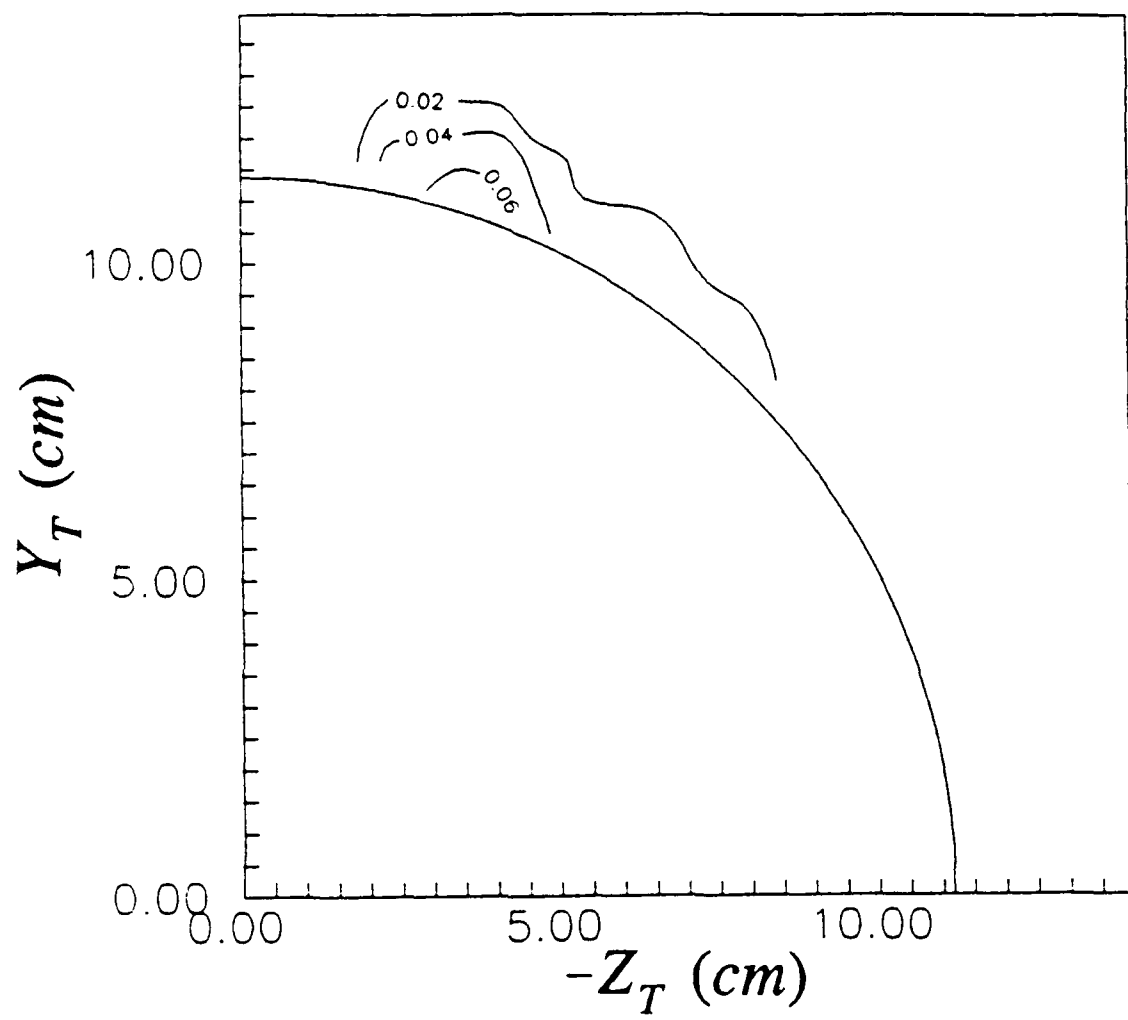
Figure 37.    Contours of $\Omega_X/U_\infty$ (1/cm), X/L=0.6, $\alpha=10°$, Re=$4.0\times10^6$.
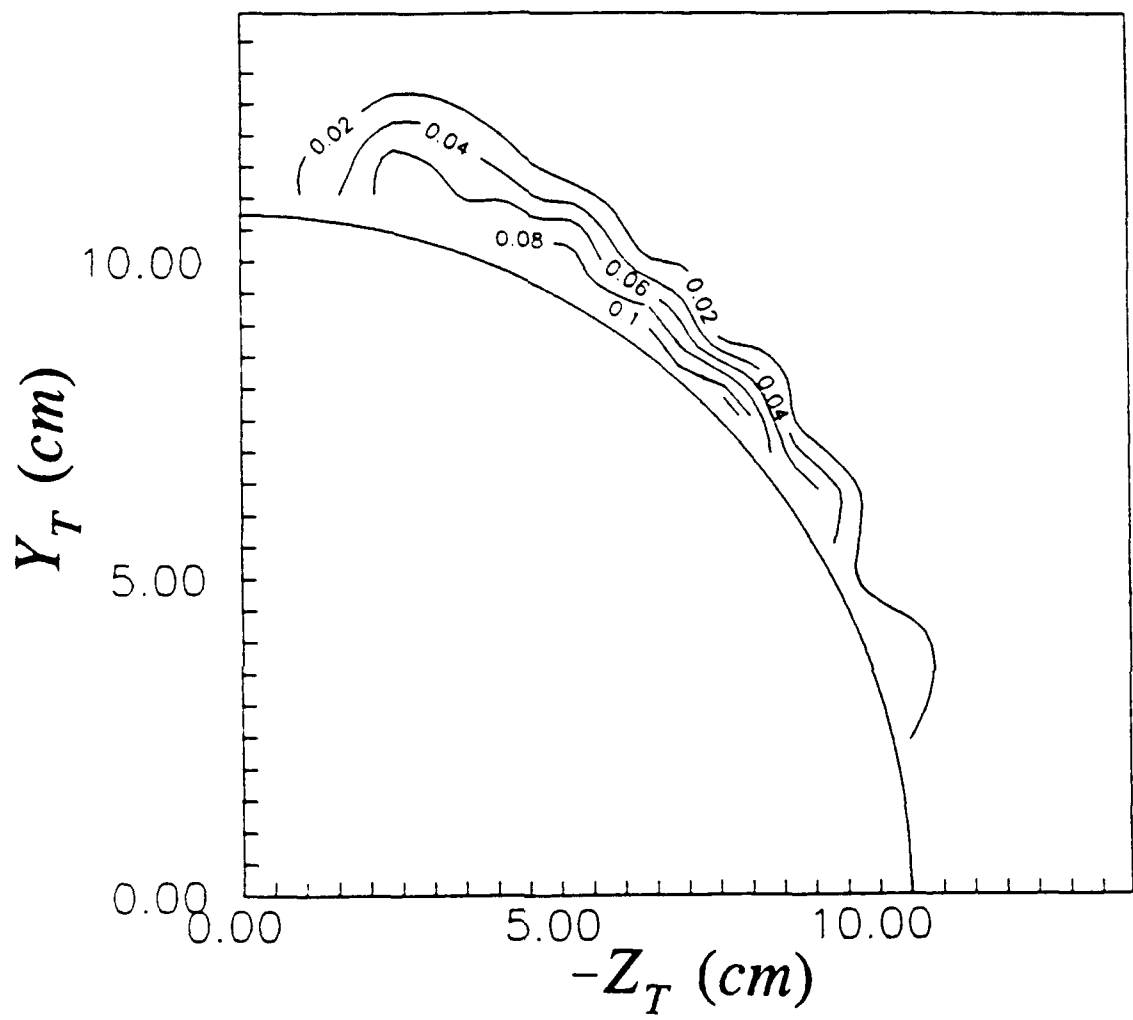
Figure 38.    Contours of $\Omega_X/U_\infty$ (1/cm), X/L=0.7, $\alpha$=10°, Re=4.0×10⁶.
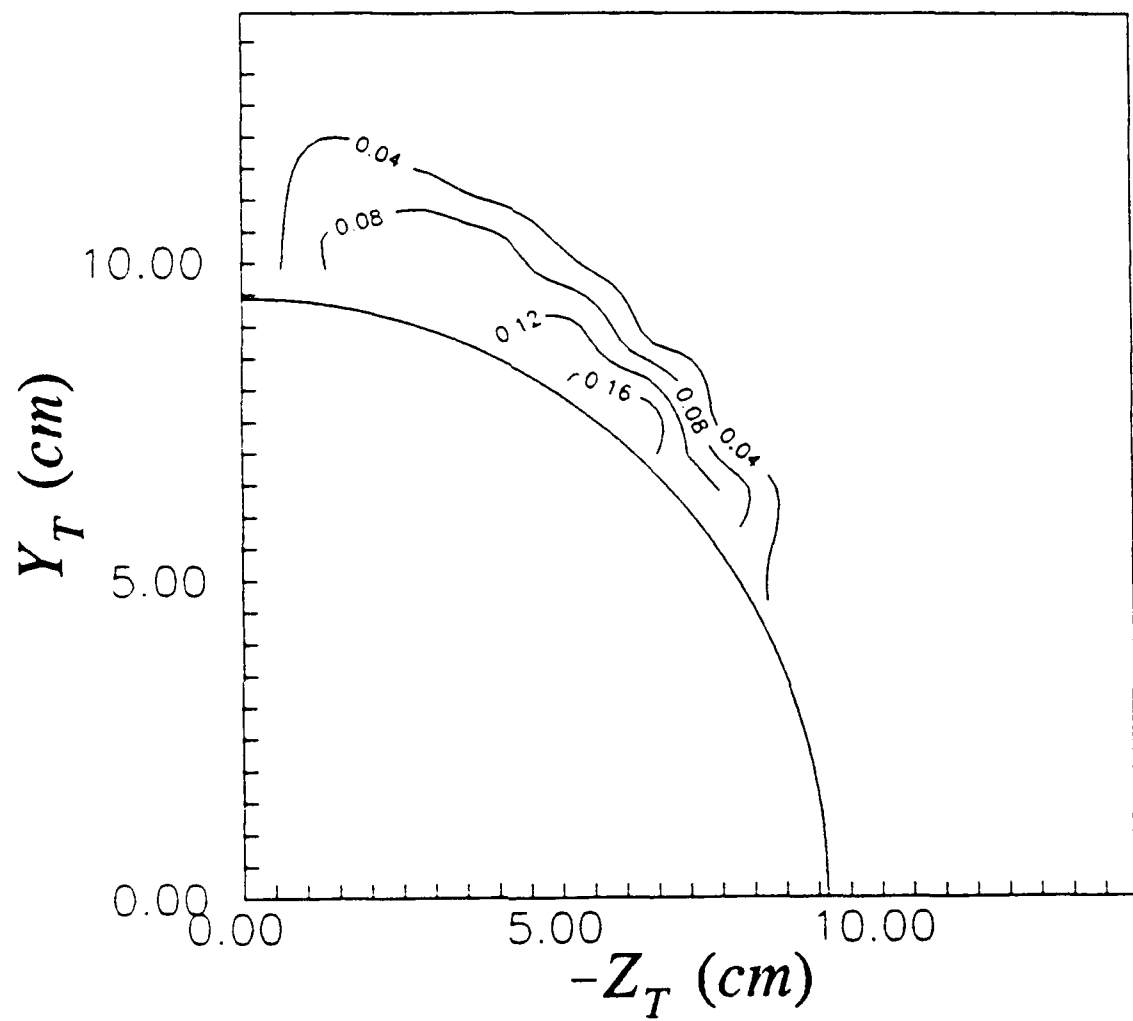
Figure 39.   Contours of $\Omega_X/U_\infty$ (1/cm), X/L=0.8, $\alpha=10°$, Re=$4.0\times10^6$.
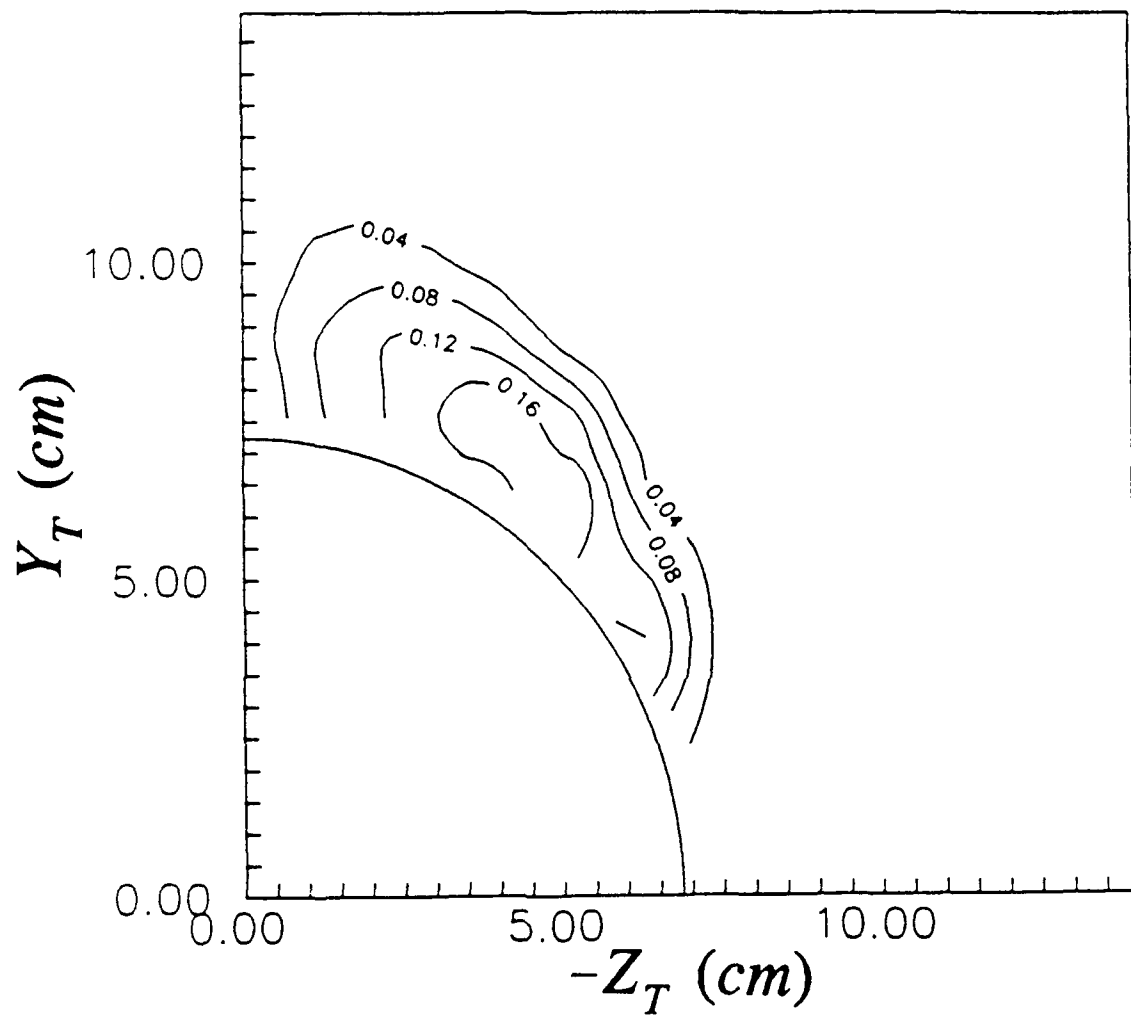
Figure 40.    Contours of $\Omega_X/U_\infty$ (1/cm), X/L=0.9, $\alpha=10°$, Re=$4.0\times10^6$.
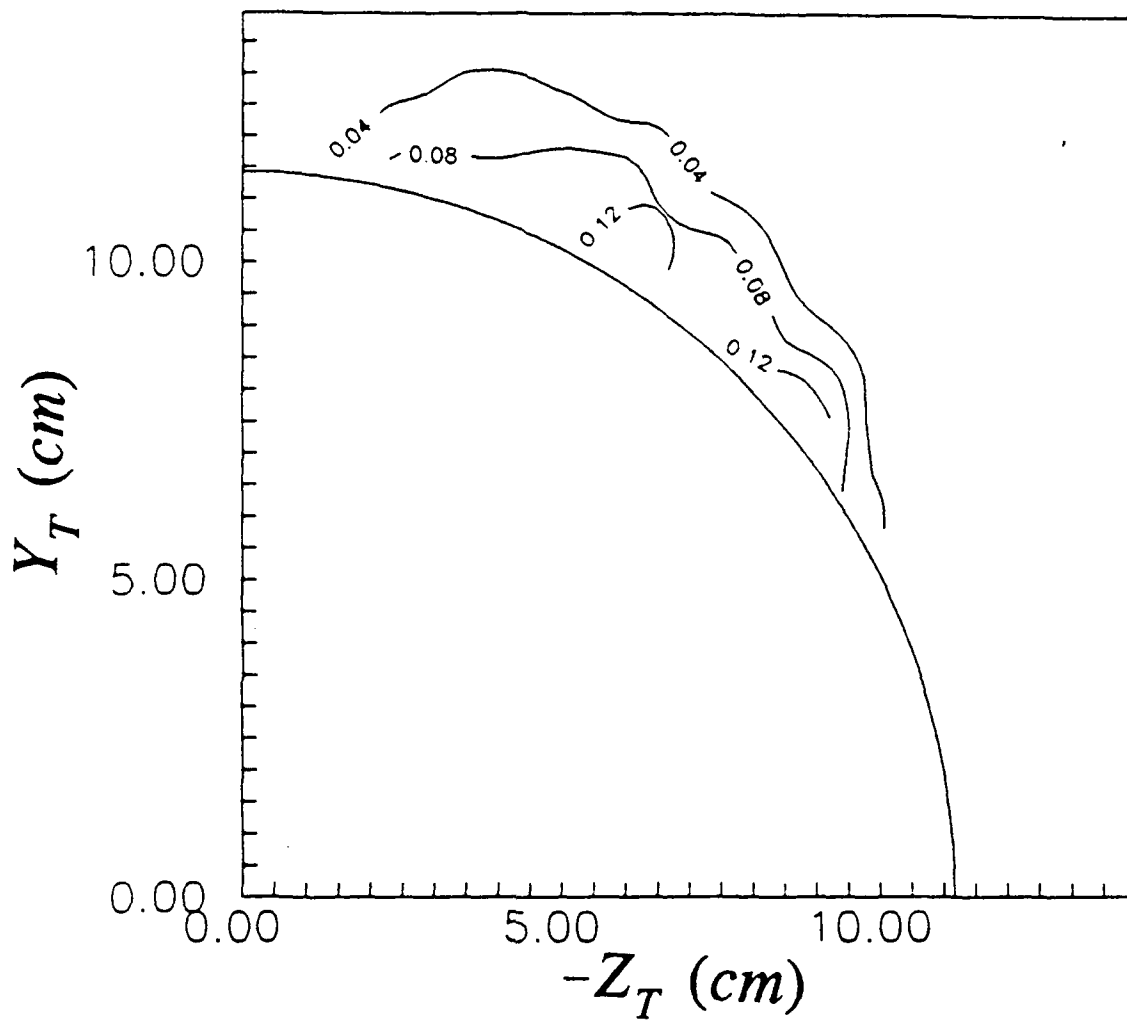
Figure 41.    Contours of $\Omega_X/U_\infty$ (1/cm), X/L=0.6, $\alpha = 15°$, Re=1.3×10^6.
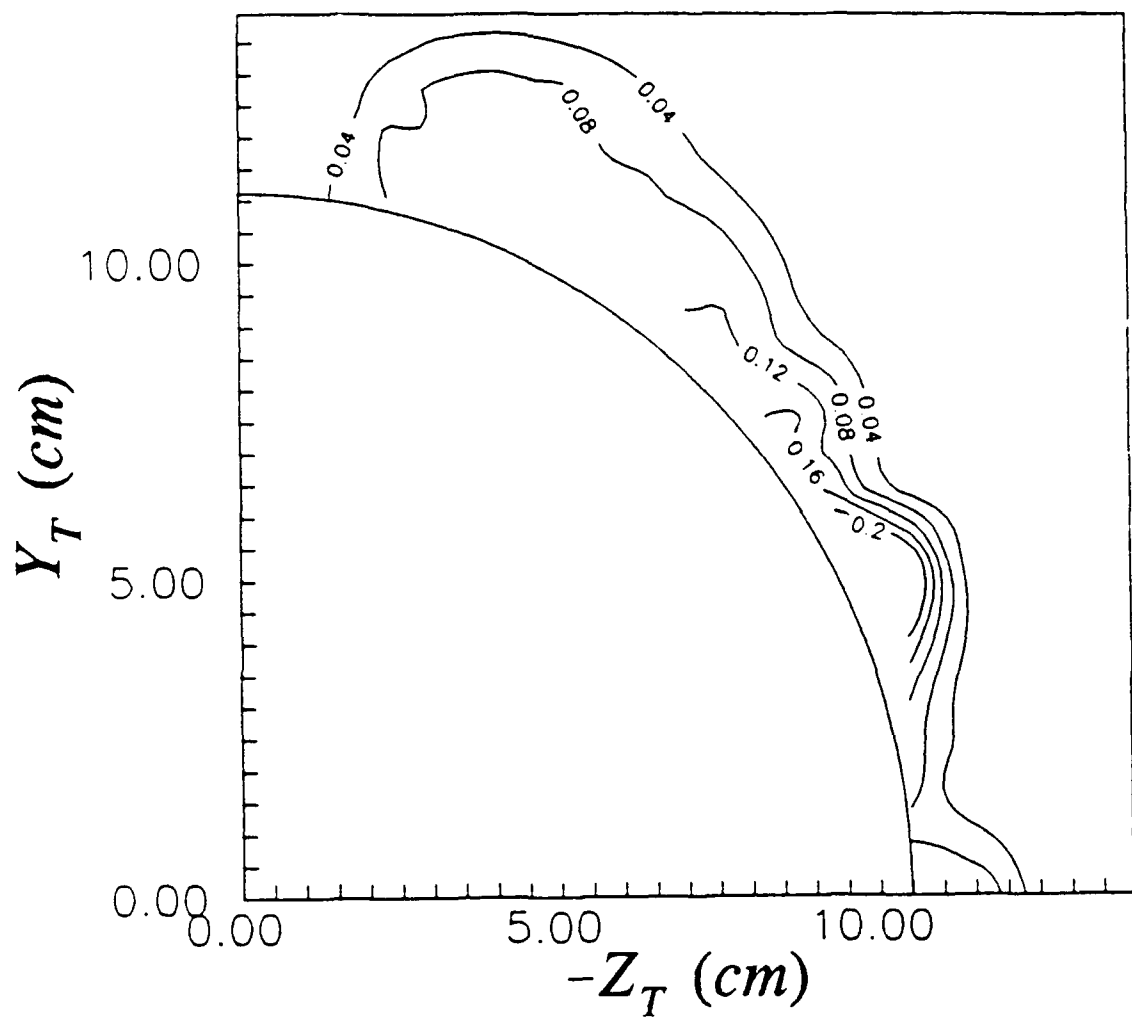
Figure 42.    Contours of $\Omega_X/U_\infty$ (1/cm), X/L=0.7, $\alpha = 15°$, Re=$1.3 \times 10^6$.
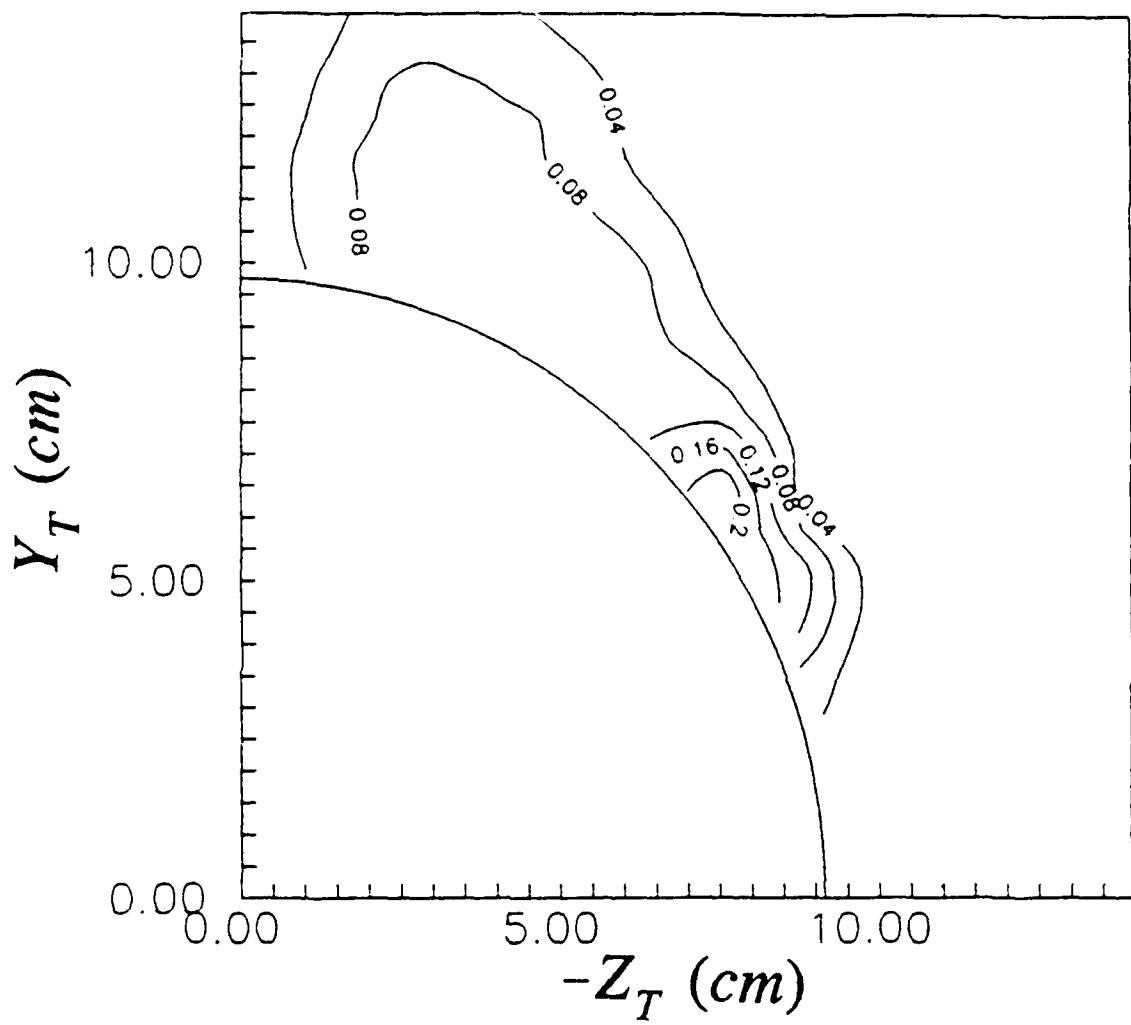
Figure 43. Contours of $\Omega_X/U_\infty$ (1/cm), X/L=0.8, $\alpha$=15°, $R_L$ = 1.3×10⁶.
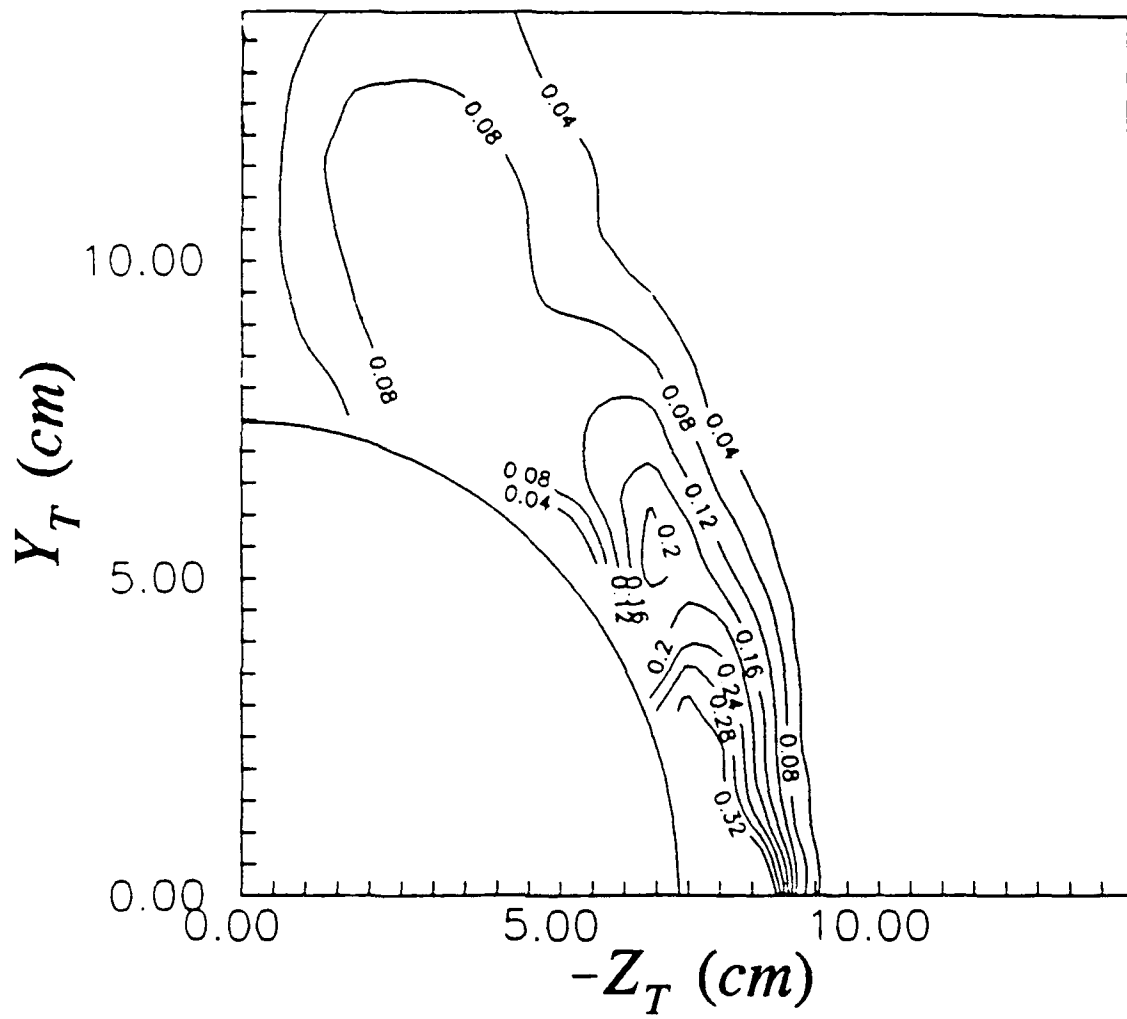
Figure 44.    Contours of $\Omega_X/U_\infty$ (1/cm), X/L=0.9, $\alpha=15°$, Re=$1.3\times10^6$.
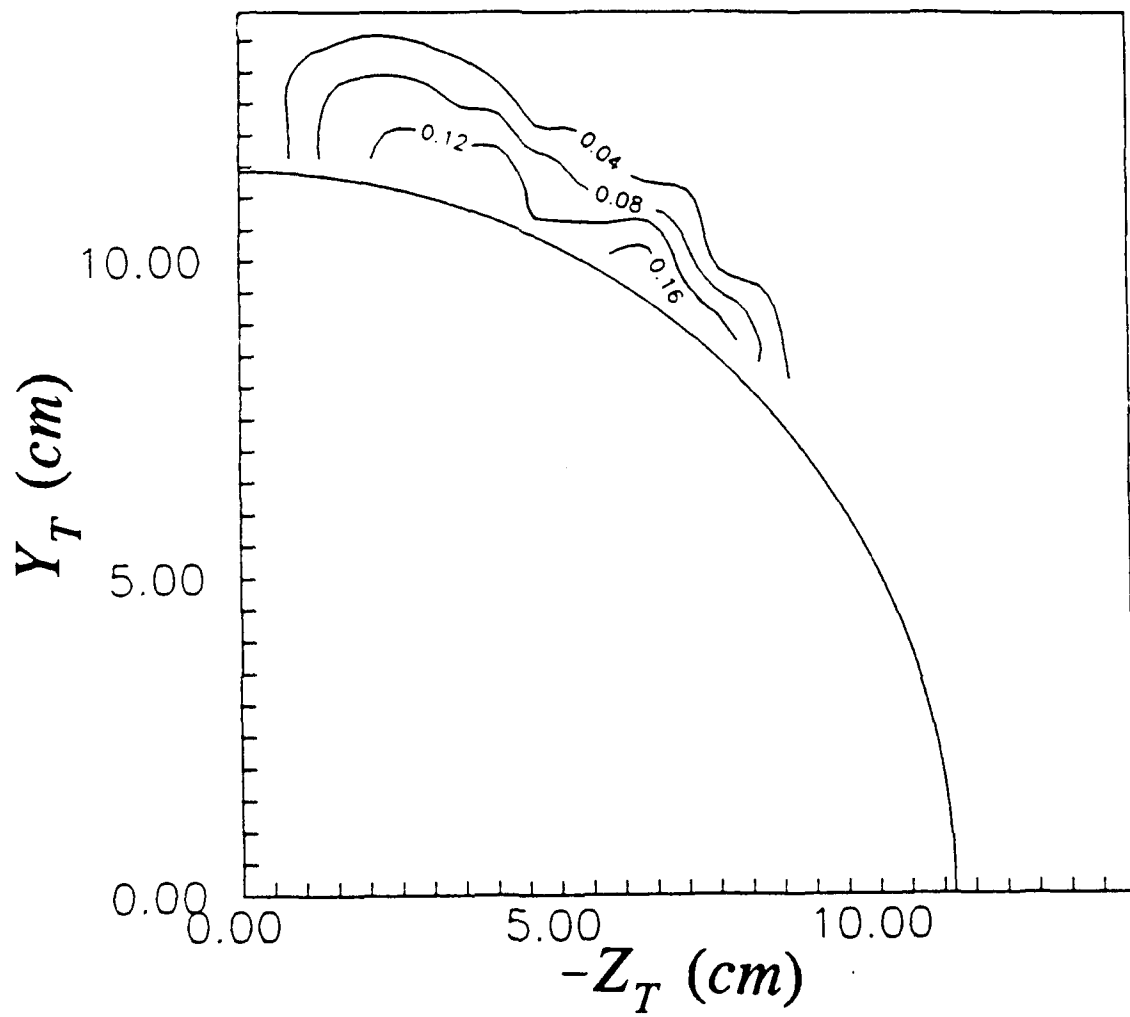
Figure 45.    Contours of $\Omega_X/U_\infty$ (1/cm), X/L=0.6, $\alpha$=15°, Re=4.0×10⁶.
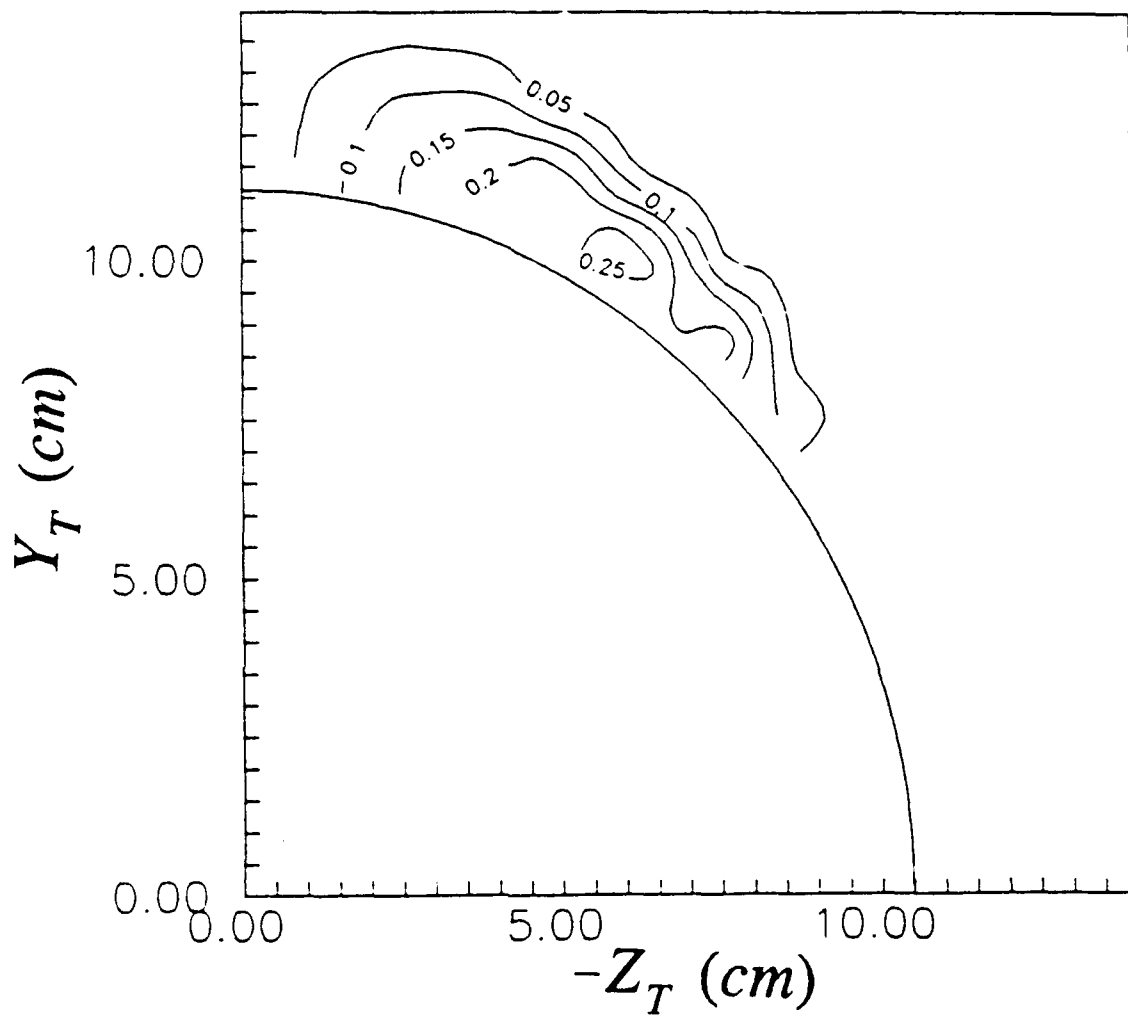
Figure 46. Contours of $\Omega_X/U_\infty$ (1/cm), X/L=0.7, $\alpha$=15°, Re=4.0×10⁶.
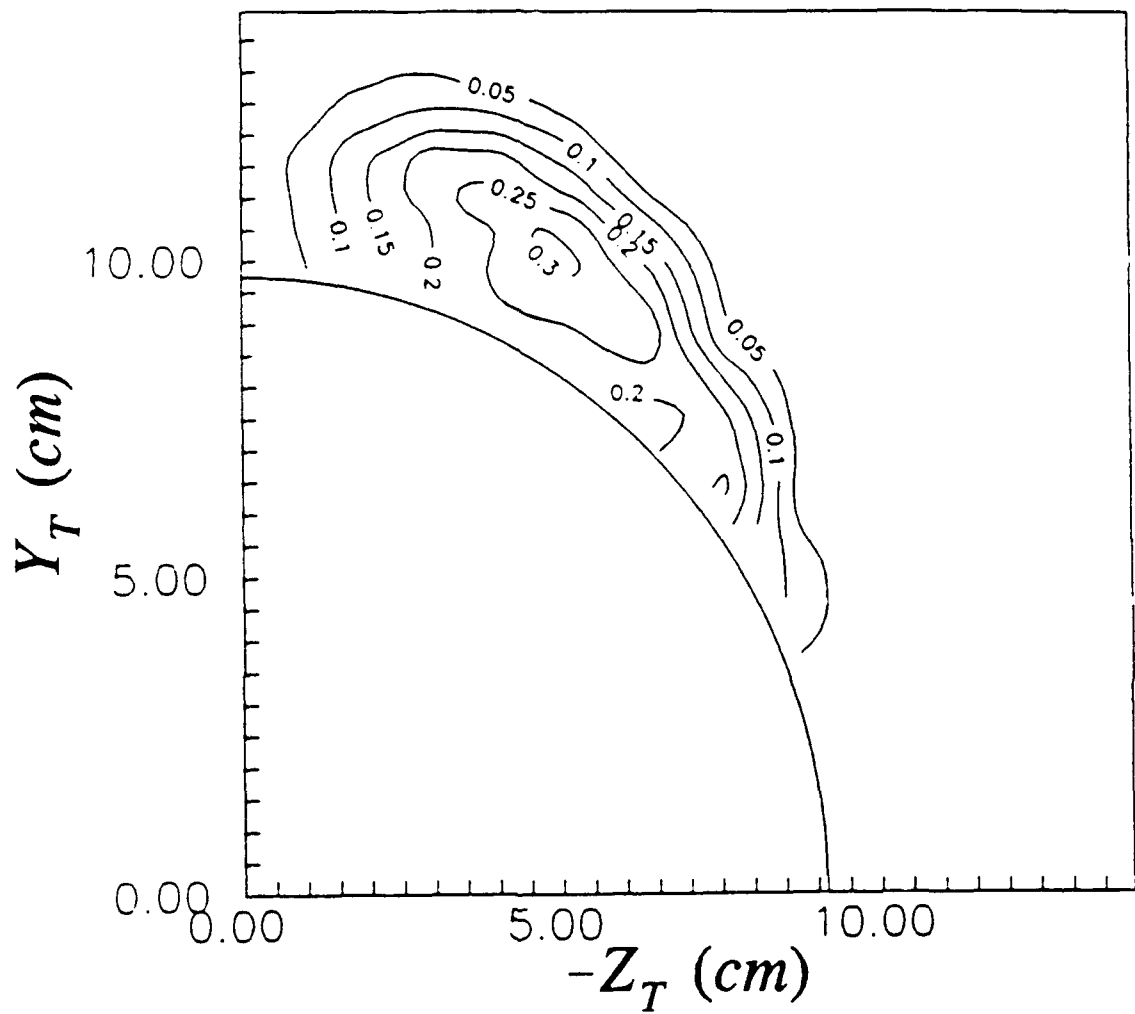
Figure 47.　　Contours of $\Omega_X/U_\infty$ (1/cm), X/L=0.8, $\alpha=15°$, Re=4.0×10$^6$.
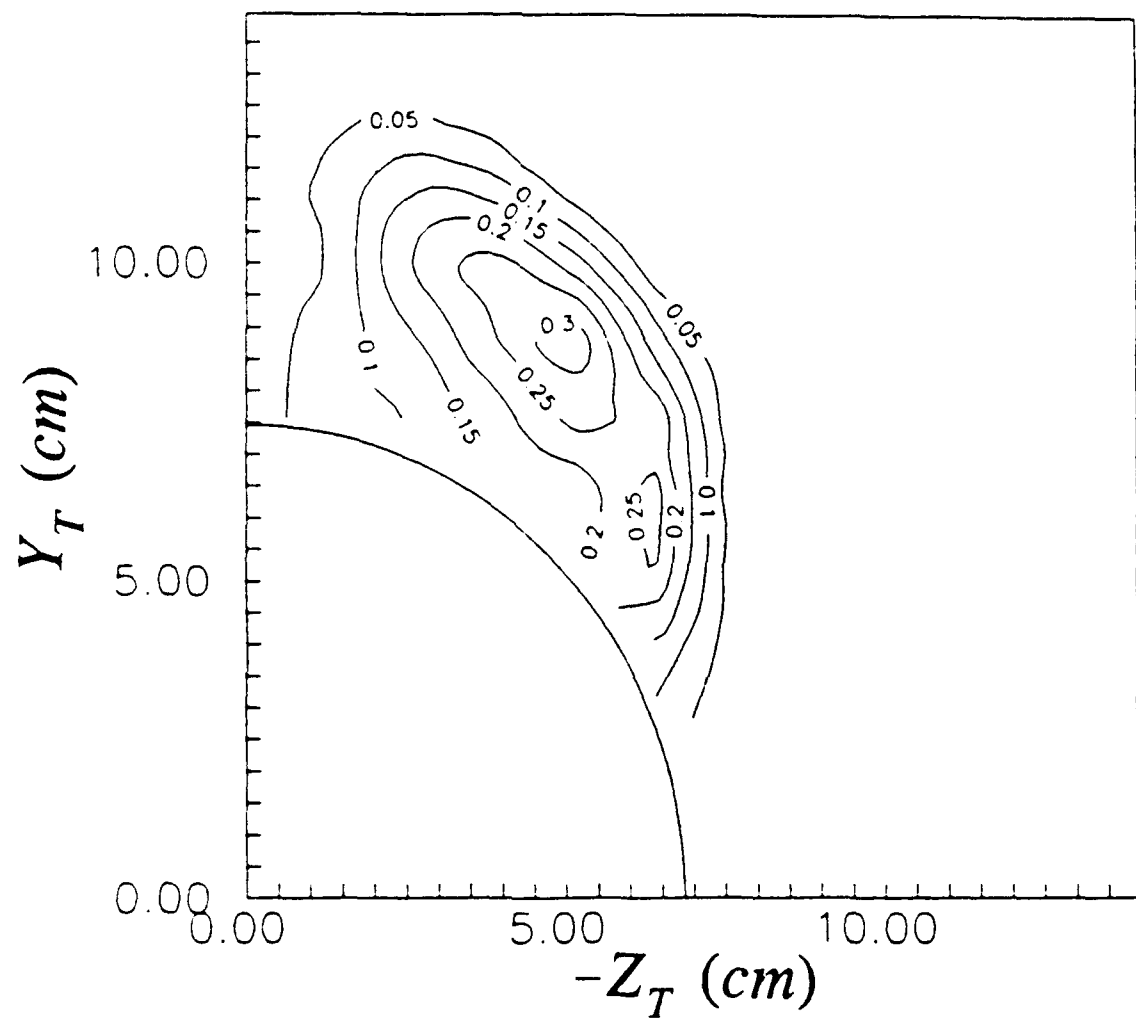
Figure 48.    Contours of $\Omega_X/U_\infty$ (1/cm), X/L=0.9, $\alpha$=15°, Re=4.0×10⁶.
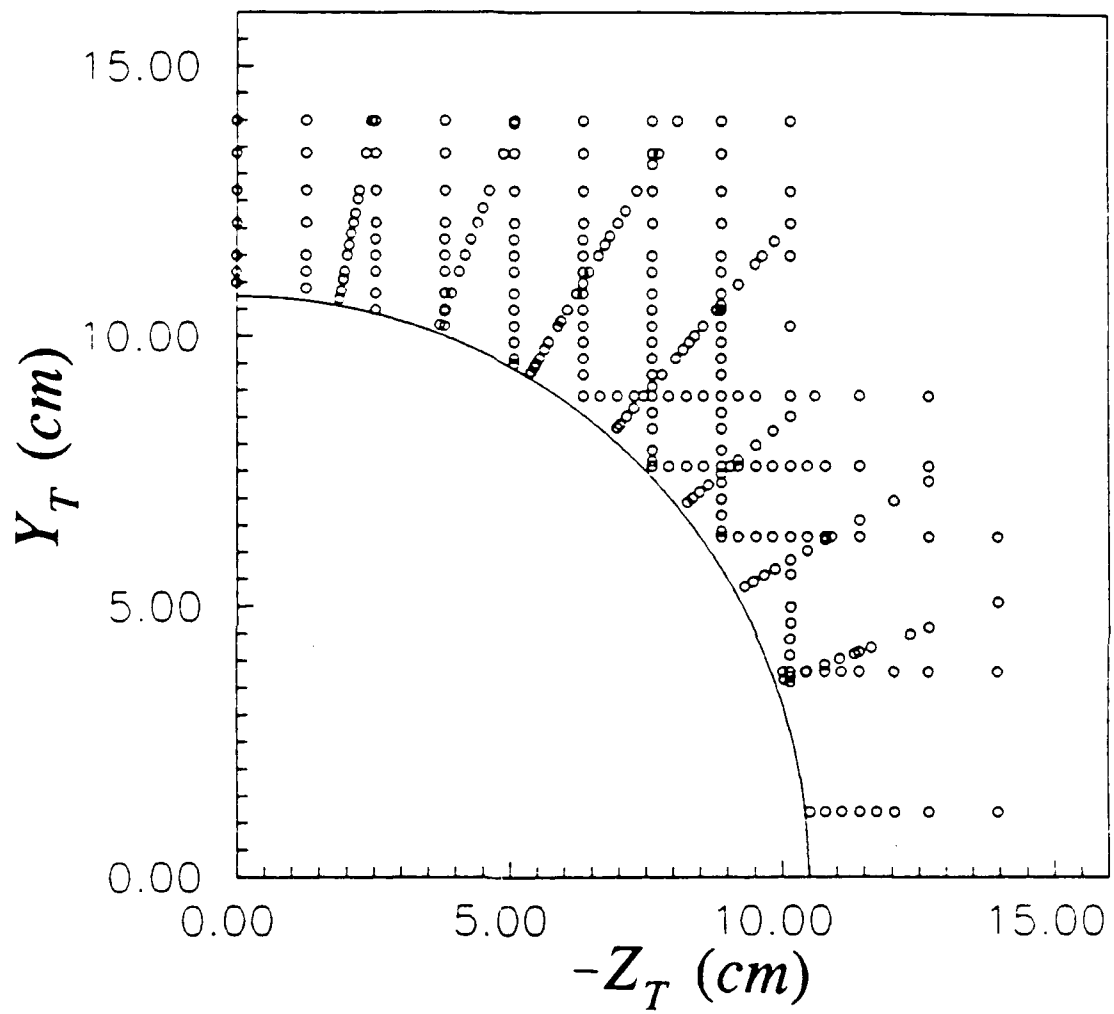
Figure 49. Locations of X-Wire Measurement Points in Horizontal and Vertical Profiles and Locations of Interpolated Points in Radial Profiles. X/L=0.7.
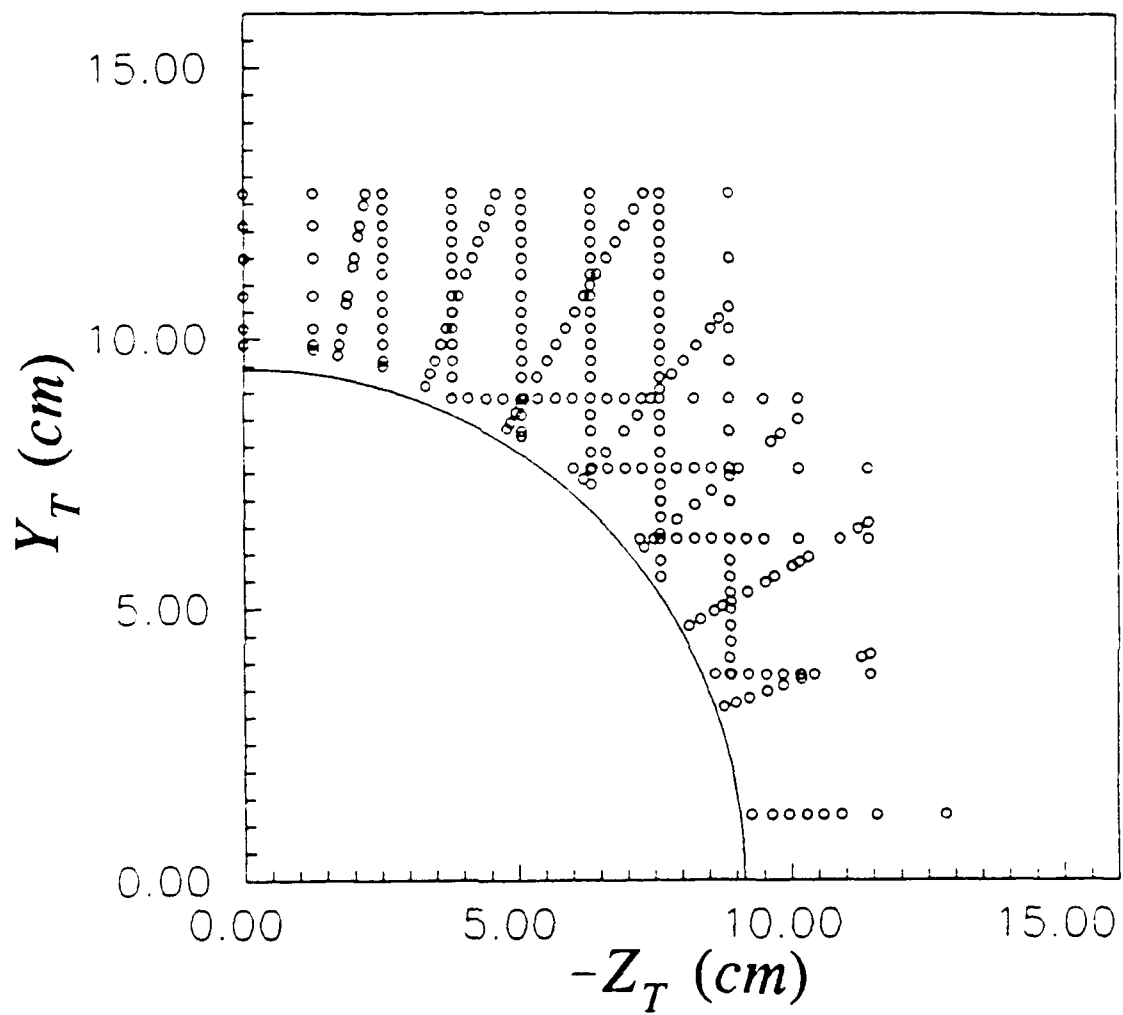
Figure 50.    Locations of X-Wire Measurement Points in Horizontal and Vertical
Profiles and Locations of Interpolated Points in Radial Profiles.
X/L=0.8.
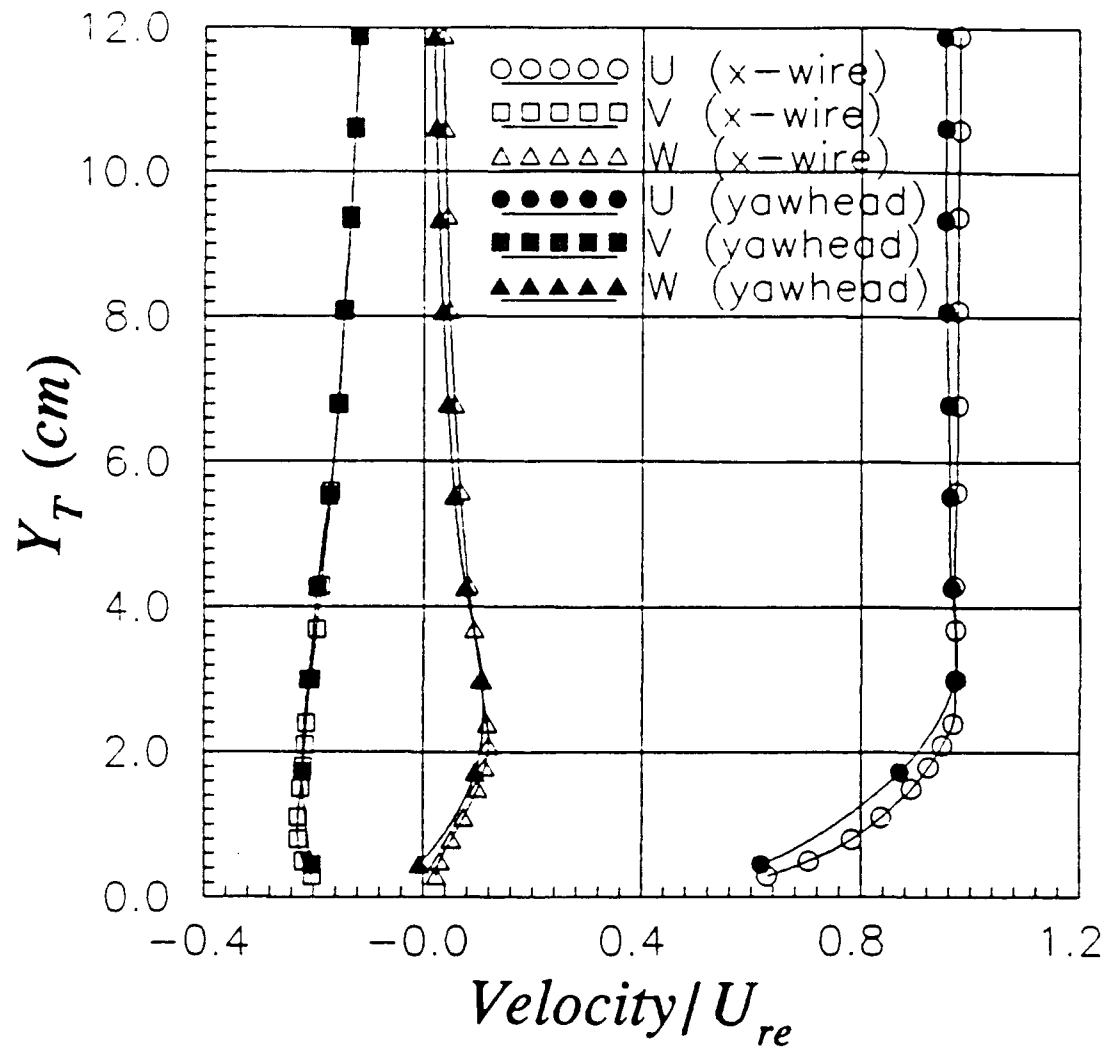
Figure 51. Comparison of Mean Velocity Components in Tunnel Coordinates from X-Wire Measurements and Yawhead Probe Measurements, $Z_T = -3.81$cm. $X/L = 0.7$, $Re = 4.0 \times 10^6$, $\alpha = 10°$.
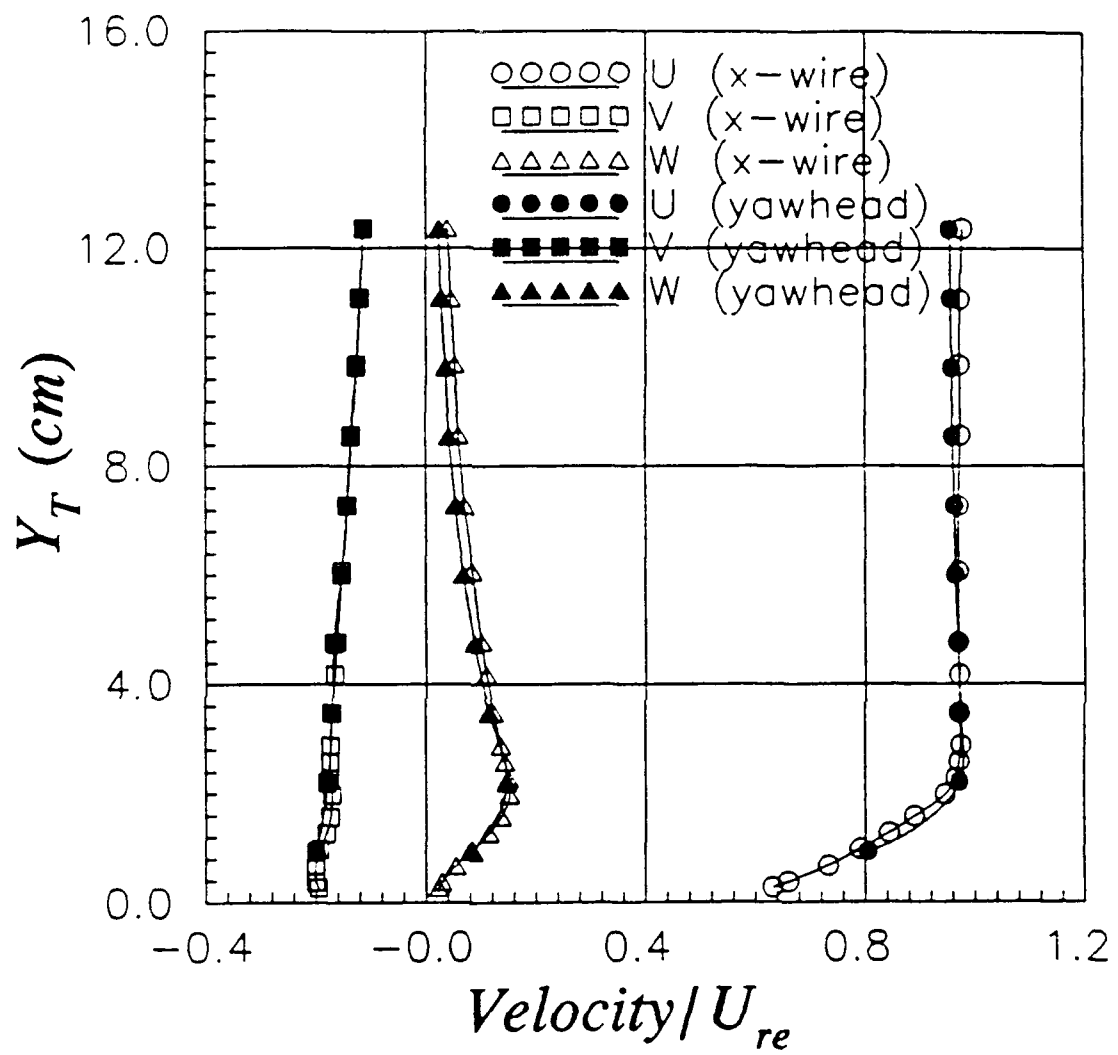
Figure 52.  Comparison of Mean Velocity Components in Tunnel Coordinates from X-Wire Measurements and Yawhead Probe Measurements, $Z_T$=-5.08cm, X/L=0.7, Re=4.0×10⁶, α=10°.
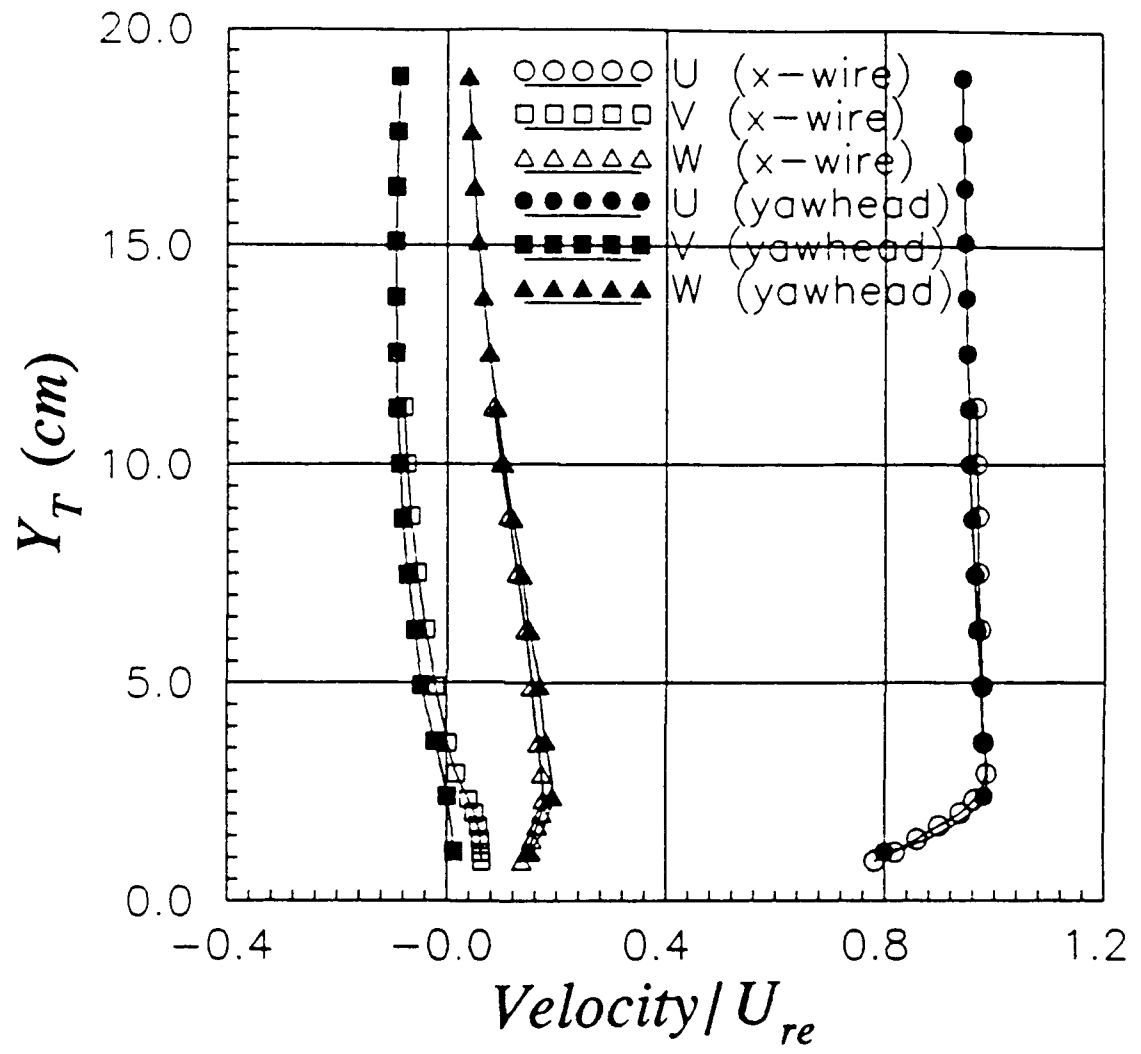
Figure 53. Comparison of Mean Velocity Components in Tunnel Coordinates from X-Wire Measurements and Yawhead Probe Measurements. $Z_T = -10.15$cm, X/L=0.7, Re=$4.0 \times 10^6$, $\alpha = 10°$.
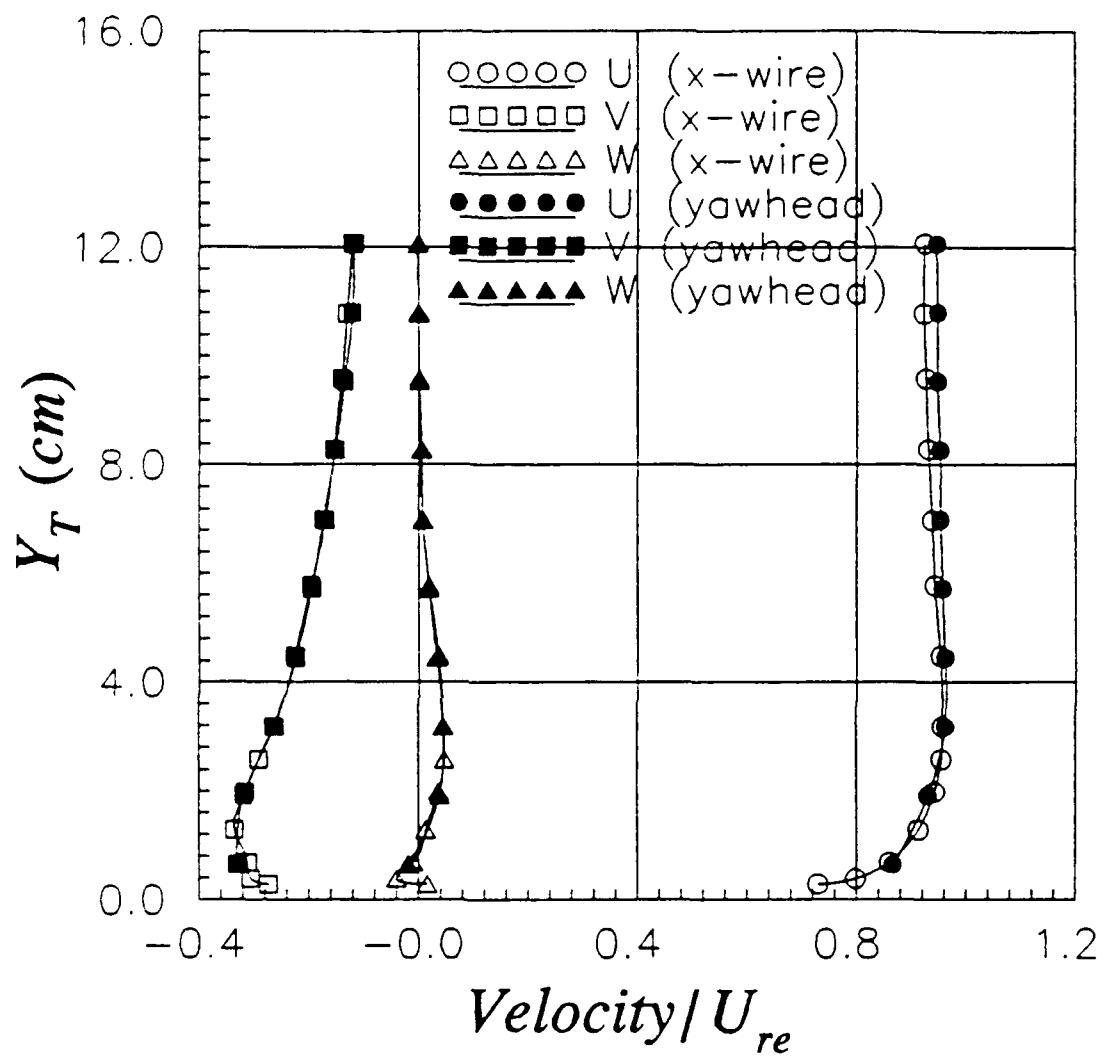
Figure 54.    Comparison of Mean Velocity Components in Tunnel Coordinates from
X-Wire Measurements and Yawhead Probe Measurements, $Z_T = -1.27$cm,
X/L=0.8, Re=4.0×10⁶, α=10°.
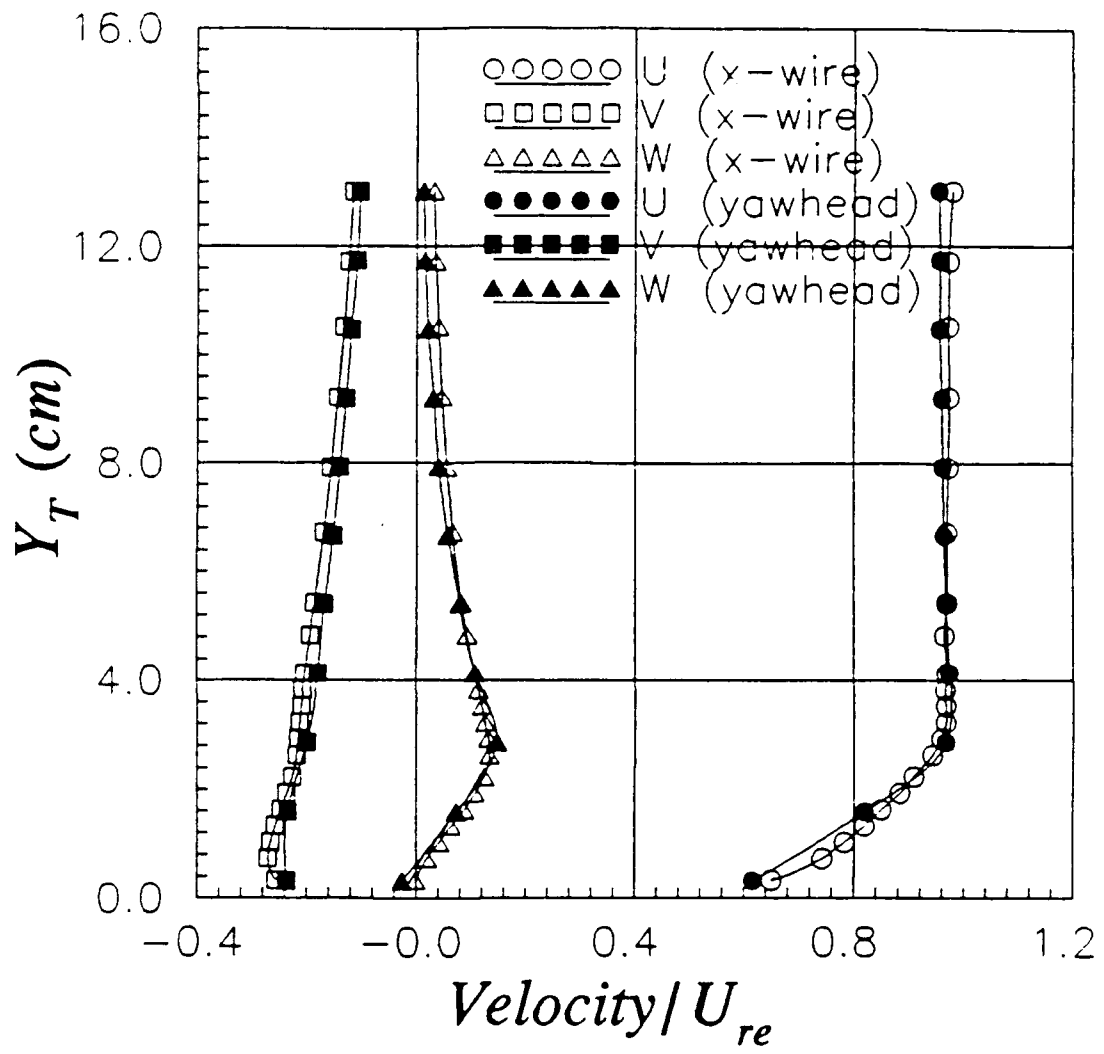
Figure 55. Comparison of Mean Velocity Components in Tunnel Coordinates from X-Wire Measurements and Yawhead Probe Measurements, $Z_T = -3.81$cm. $X/L = 0.8$, $Re = 4.0 \times 10^6$, $\alpha = 10°$.
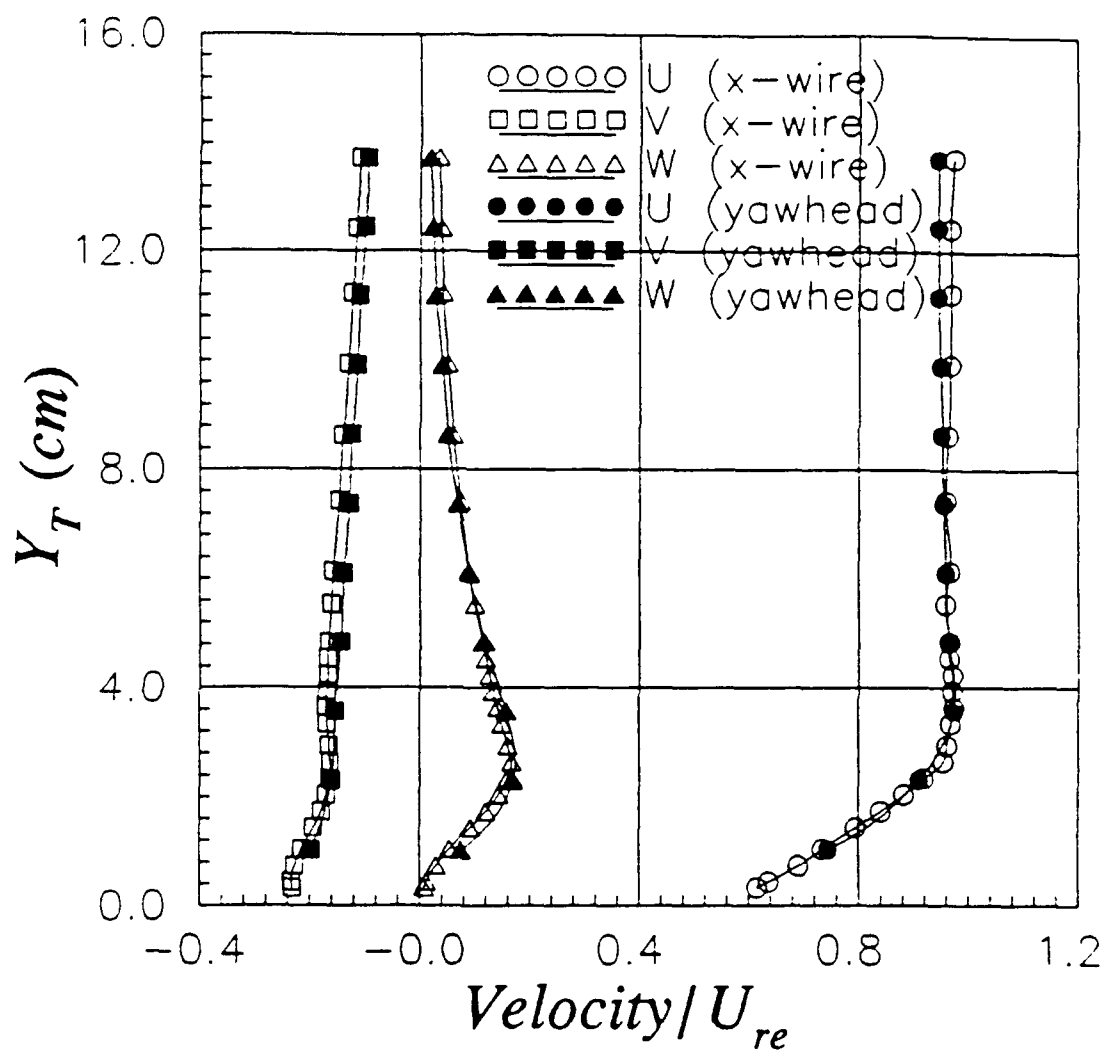
Figure 56.    Comparison of Mean Velocity Components in Tunnel Coordinates from
             X-Wire Measurements and Yawhead Probe Measurements. $Z_T = -5.08$cm,
             $X/L=0.8$, $Re=4.0 \times 10^6$, $\alpha=10°$.
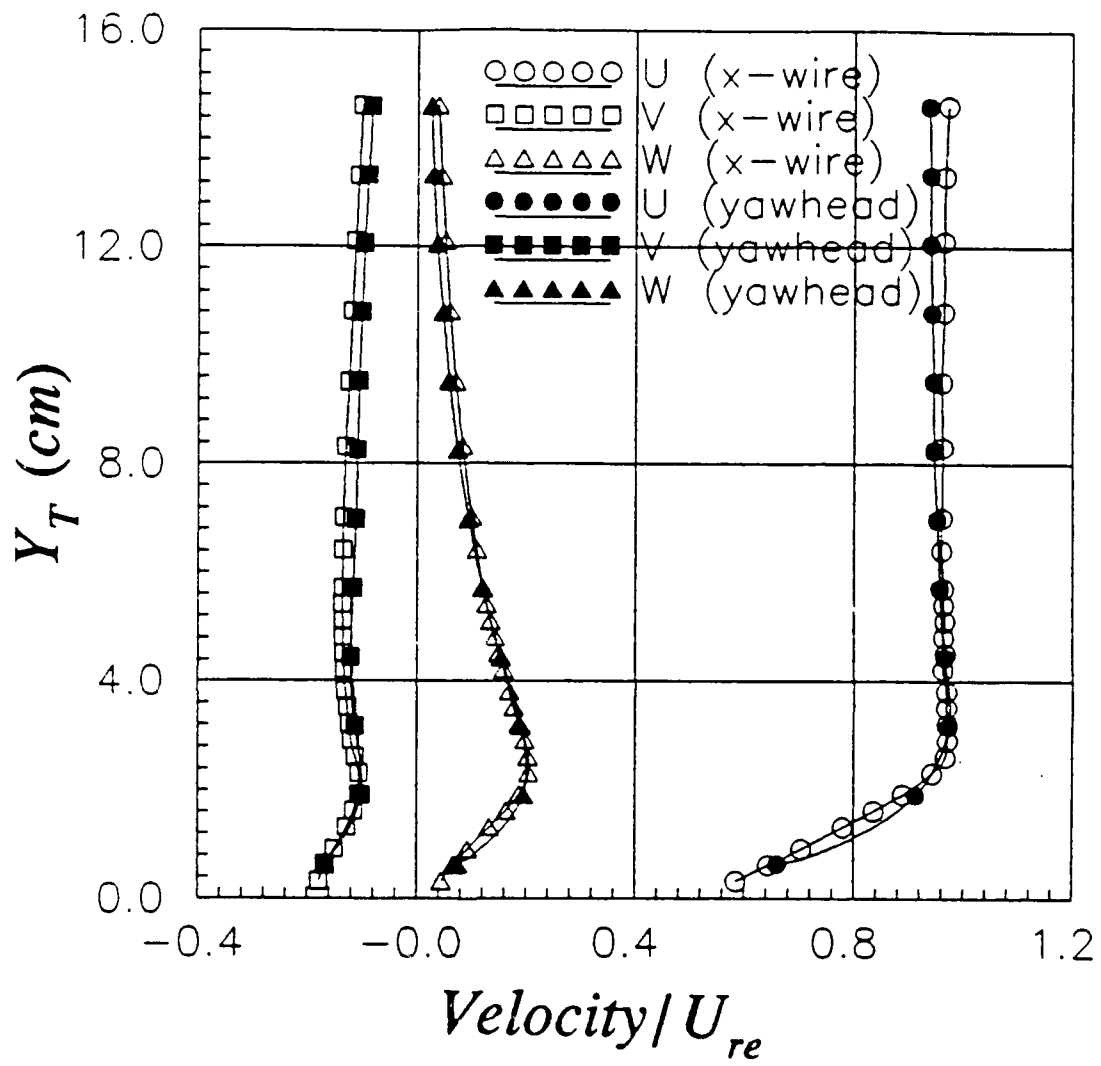
Figure 57.   Comparison of Mean Velocity Components in Tunnel Coordinates from X-Wire Measurements and Yawhead Probe Measurements, $Z_T = -6.35$cm, X/L=0.8, Re=4.0×10⁶, $\alpha = 10°$.
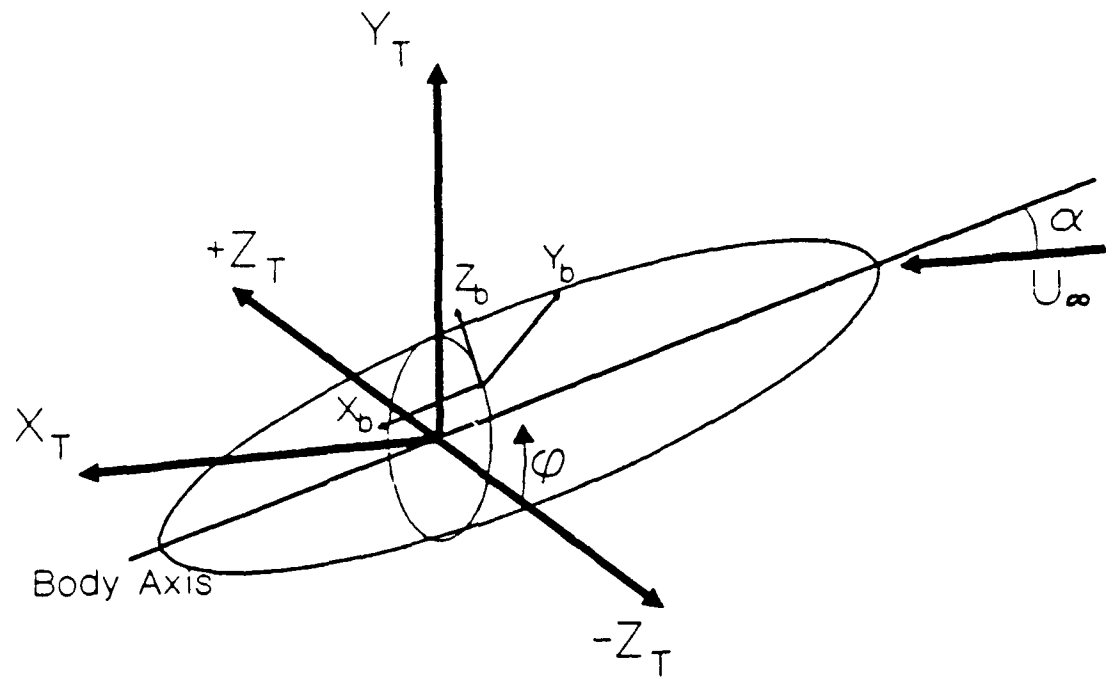
Figure 58. Local Body ($X_b$-$Y_b$-$Z_b$) Coordinate System, with $X_b$ Parallel to Longitudinal Axis of Model and $Y_b$ out from Surface.
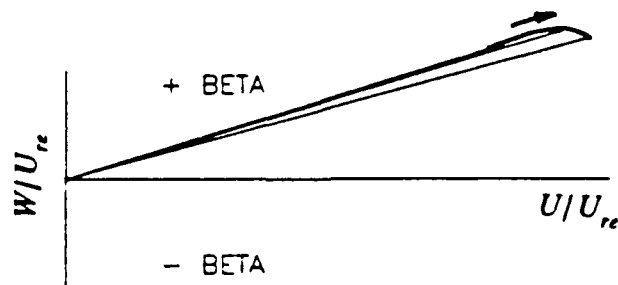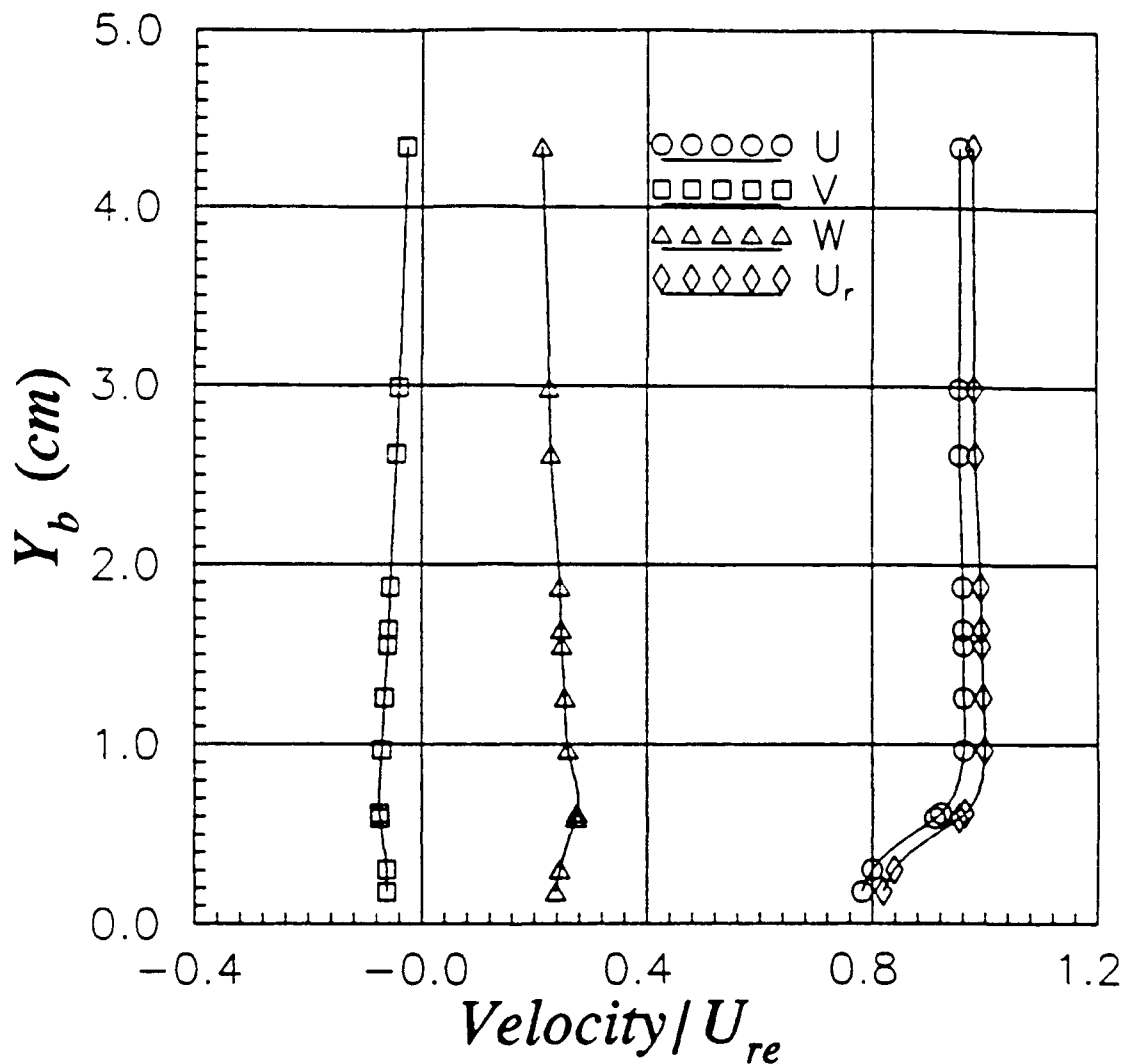
Figure 59.  X-Wire Velocity Profiles and U-W Crossflow Vectors, $\varphi=20°$, X/L=0.7, Re=$4.0\times10^6$, $\alpha=10°$, Local Body Coordinates, Direction of Arrow on Hodograph Plot Indicates Variation from Wall to Free Stream.
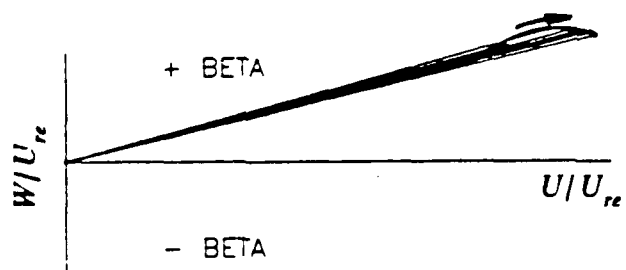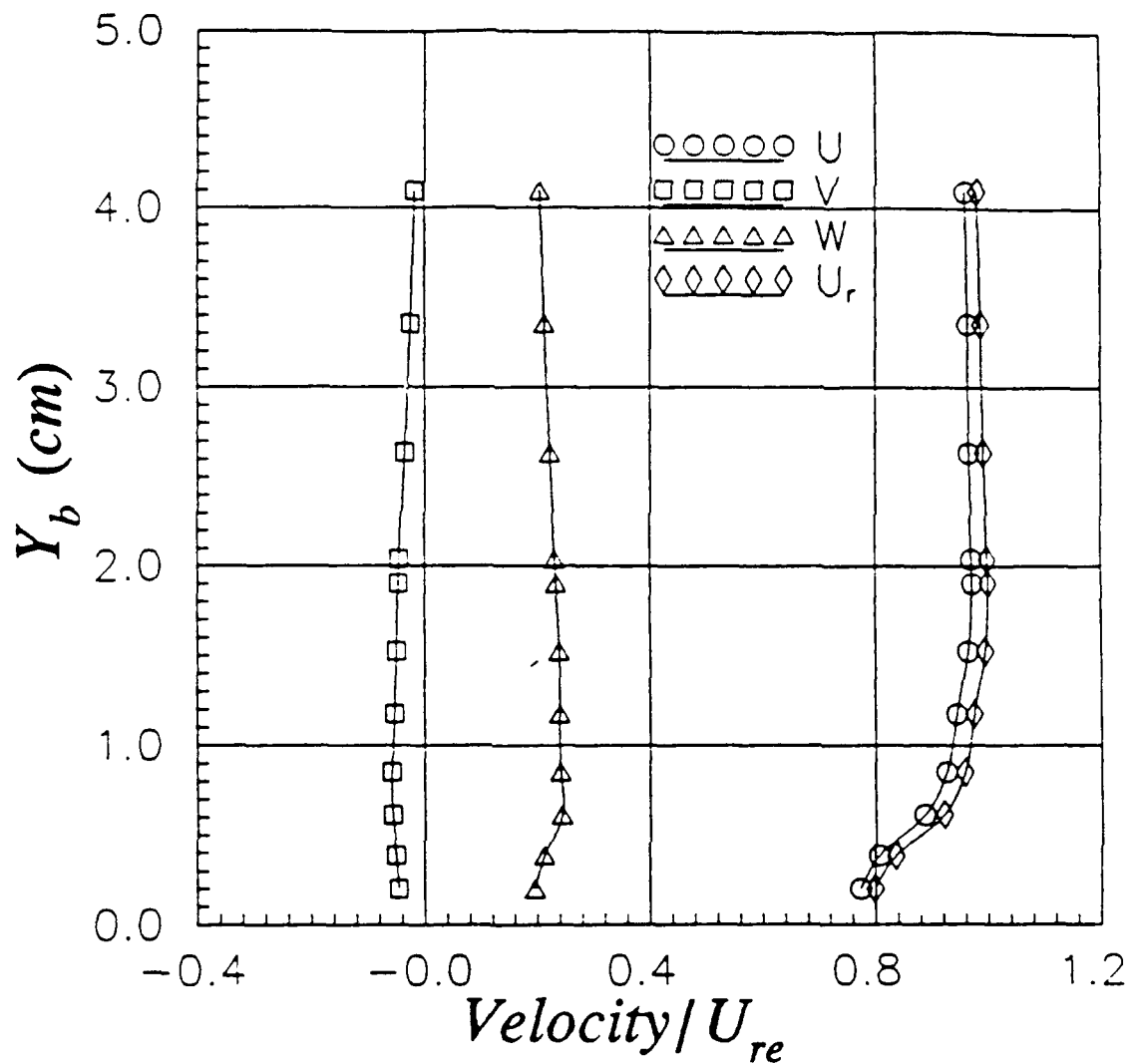
Figure 60.    X-Wire Velocity Profiles and U-W Crossflow Vectors, $\varphi=30°$, X/L=0.7, Re=$4.0\times10^6$, $\alpha=10°$, Local Body Coordinates, Direction of Arrow on Hodograph Plot Indicates Variation from Wall to Free Stream.
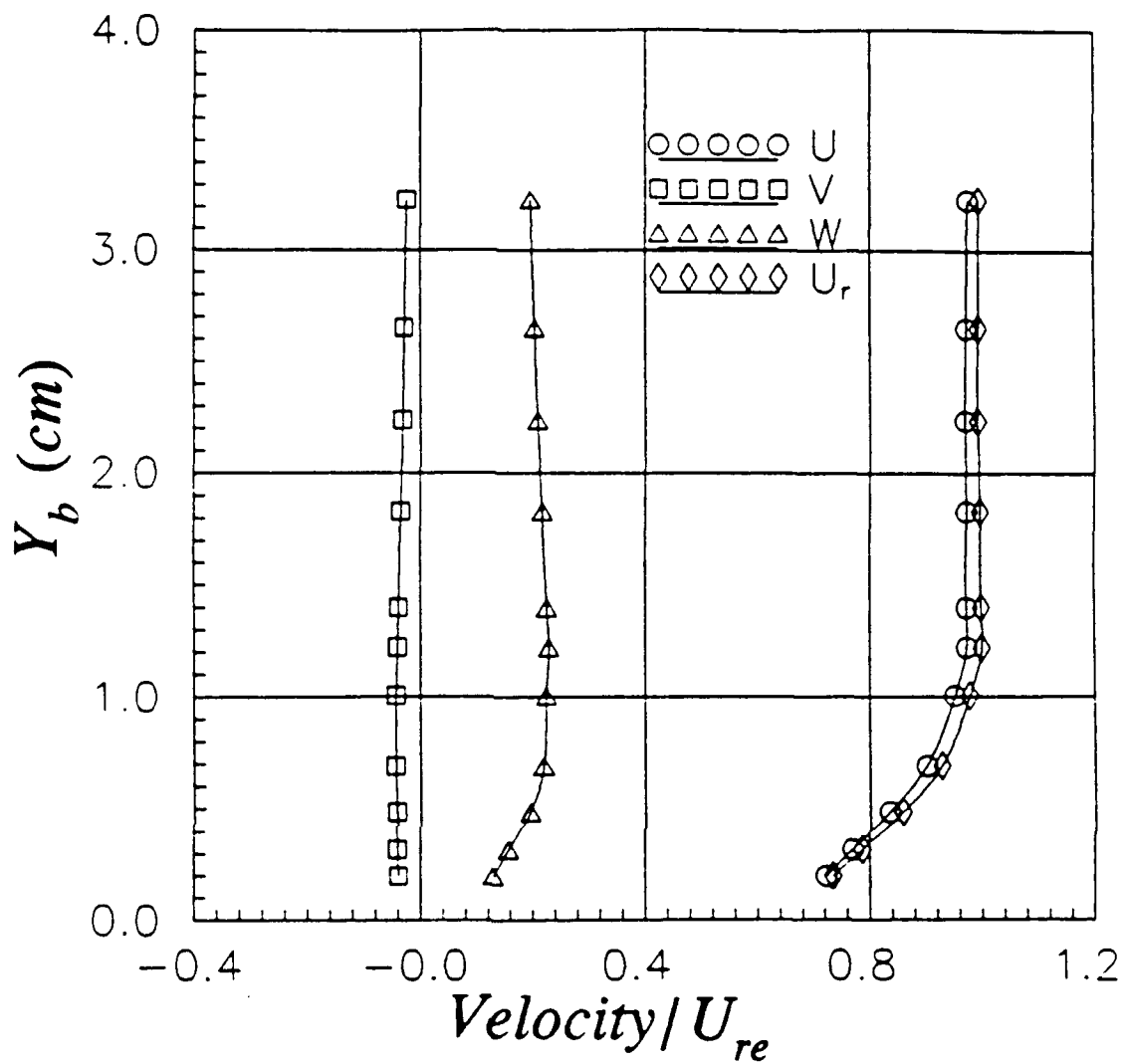
Figure 61.   X-Wire Velocity Profiles and U-W Crossflow Vectors, $\varphi=40°$, X/L=0.7, Re=$4.0\times10^6$, $\alpha=10°$, Local Body Coordinates, Direction of Arrow on Hodograph Plot Indicates Variation from Wall to Free Stream.
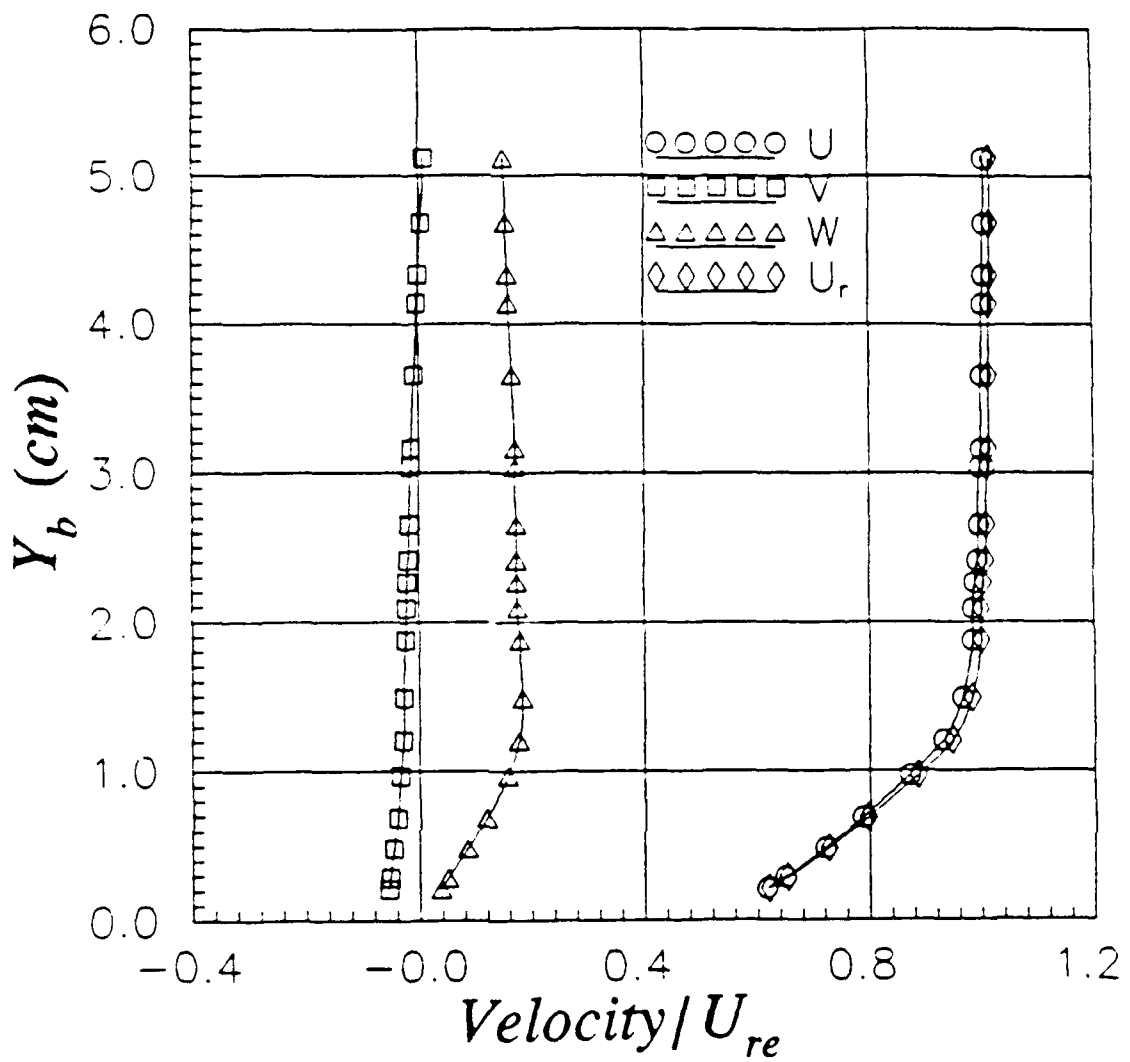
Figure 62.    X-Wire Velocity Profiles and U-W Crossflow Vectors, $\varphi = 50°$, X/L=0.7, Re=$4.0 \times 10^6$, $\alpha = 10°$, Local Body Coordinates, Direction of Arrow on Hodograph Plot Indicates Variation from Wall to Free Stream.
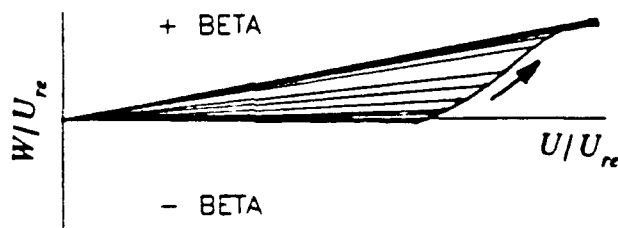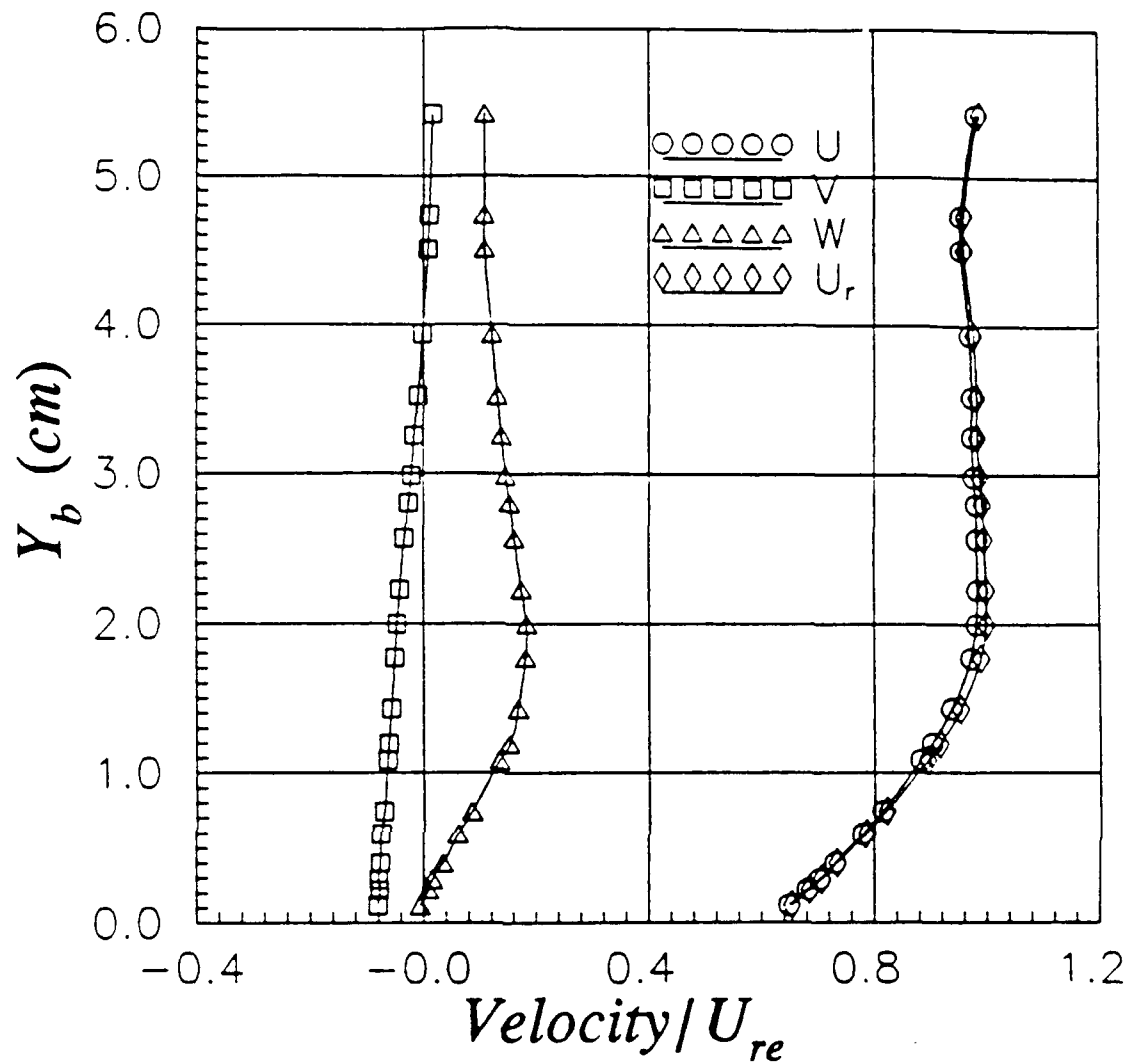
Figure 63. X-Wire Velocity Profiles and U-W Crossflow Vectors, $\varphi = 6$ ?, X/L=0.7, Re=4.0×10$^6$, $\alpha$=10°, Local Body Coordinates, Direction of Arrow on Hodograph Plot Indicates Variation from Wall to Free Su.:.m.
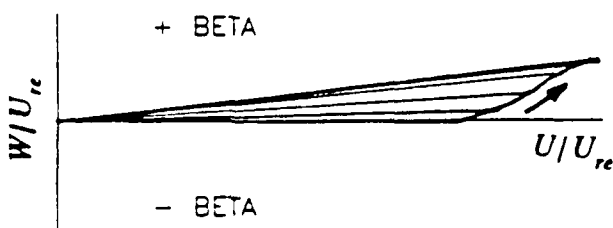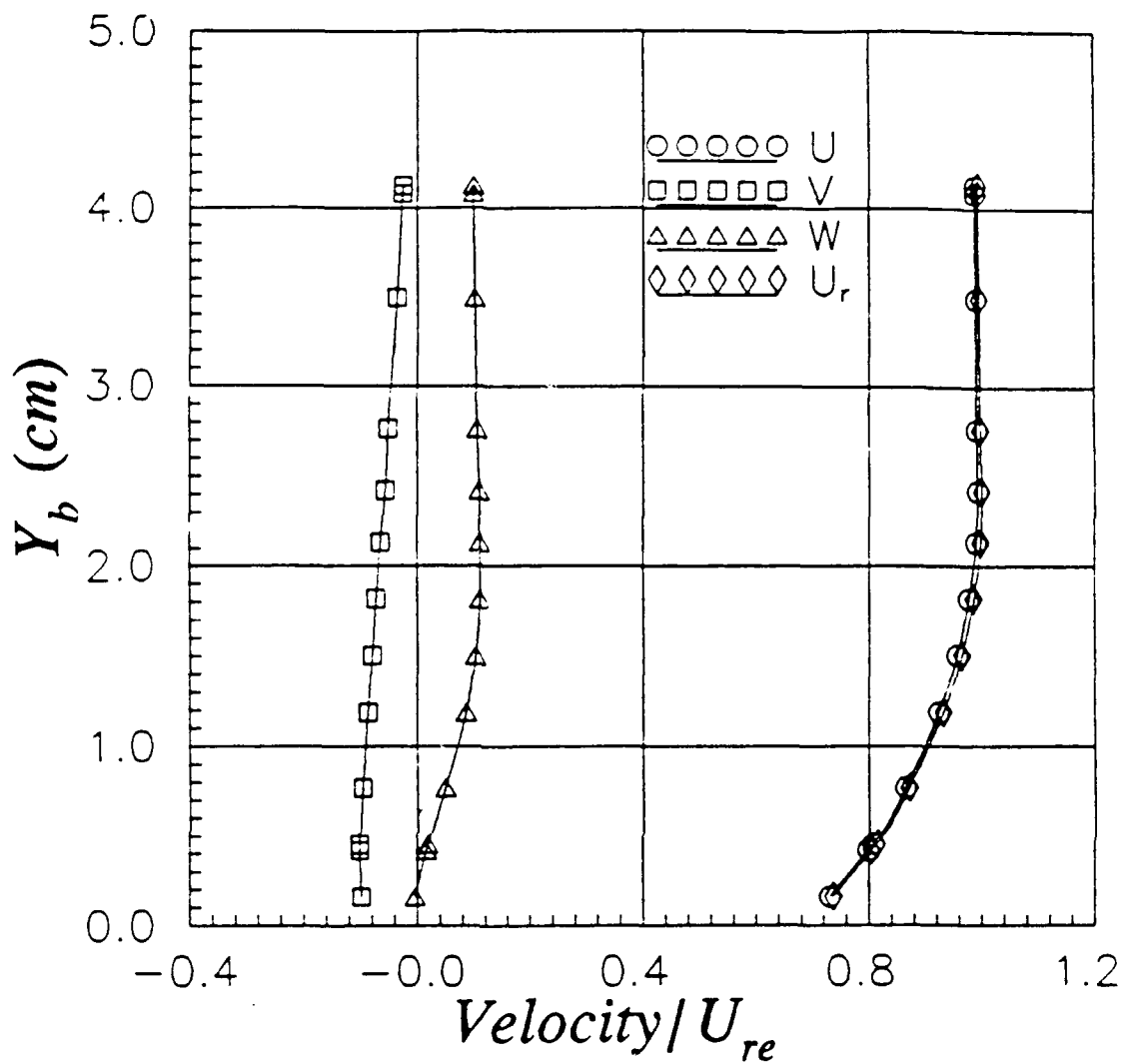
Figure 64. X-Wire Velocity Profiles and U-W Crossflow Vectors, $\varphi = 70°$, X/L=0.7, Re=$4.0 \times 10^6$, $\alpha = 10°$, Local Body Coordinates, Direction of Arrow on Hodograph Plot Indicates Variation from Wall to Free Stream.
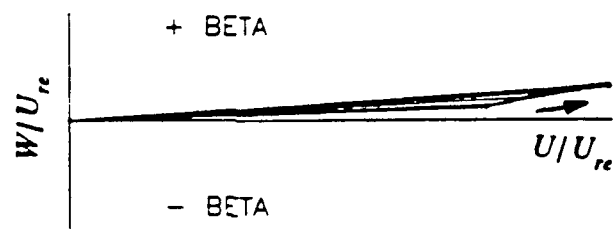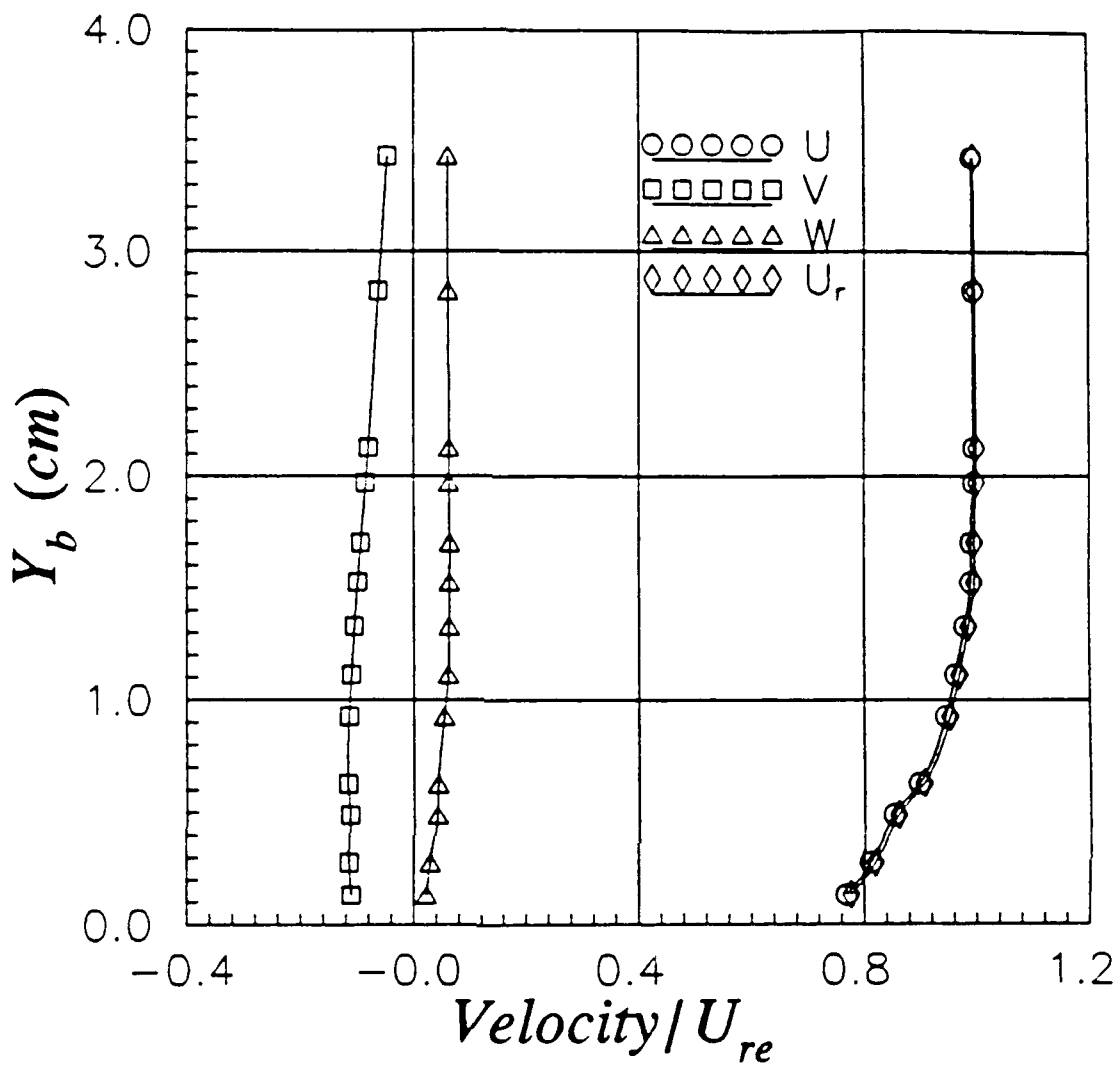
Figure 65.   X-Wire Velocity Profiles and U-W Crossflow Vectors, $\varphi=80°$, X/L=0.7, Re=$4.0\times10^6$, $\alpha=10°$, Local Body Coordinates, Direction of Arrow on Hodograph Plot Indicates Variation from Wall to Free Stream.
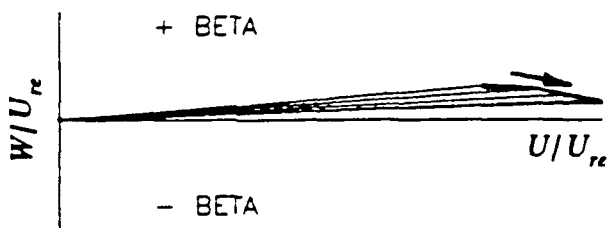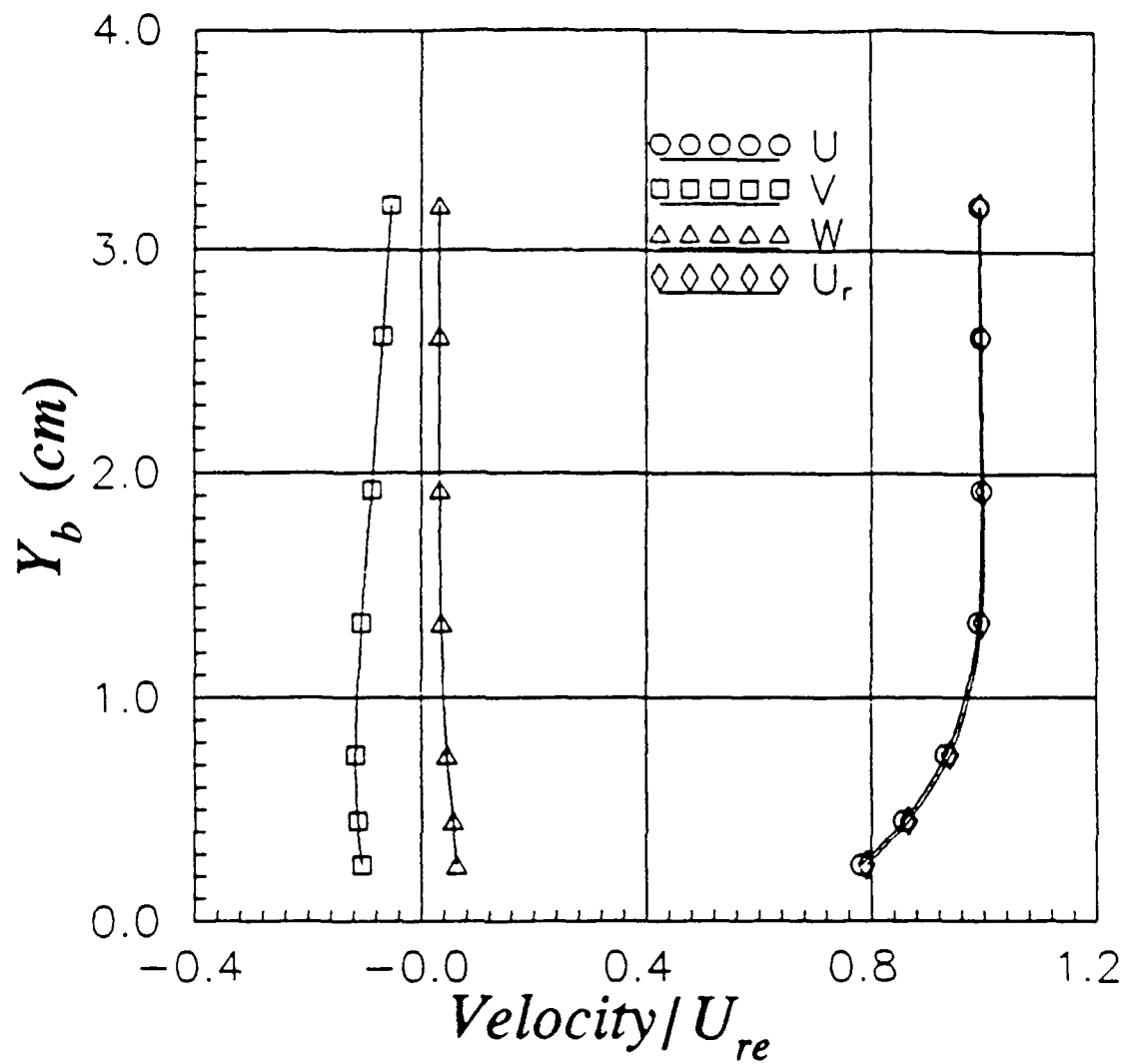
Figure 66. X-Wire Velocity Profiles and U-W Crossflow Vectors, $\varphi = 90°$, X/L = 0.7, Re = $4.0 \times 10^6$, $\alpha = 10°$, Local Body Coordinates, Direction of Arrow on Hodograph Plot Indicates Variation from Wall to Free Stream.
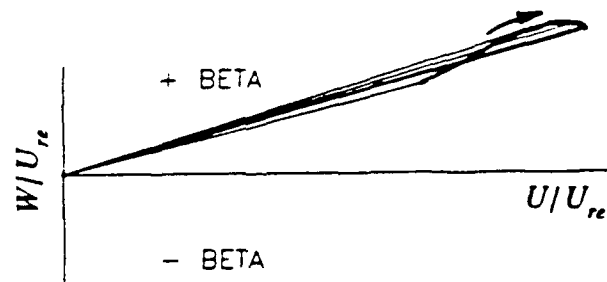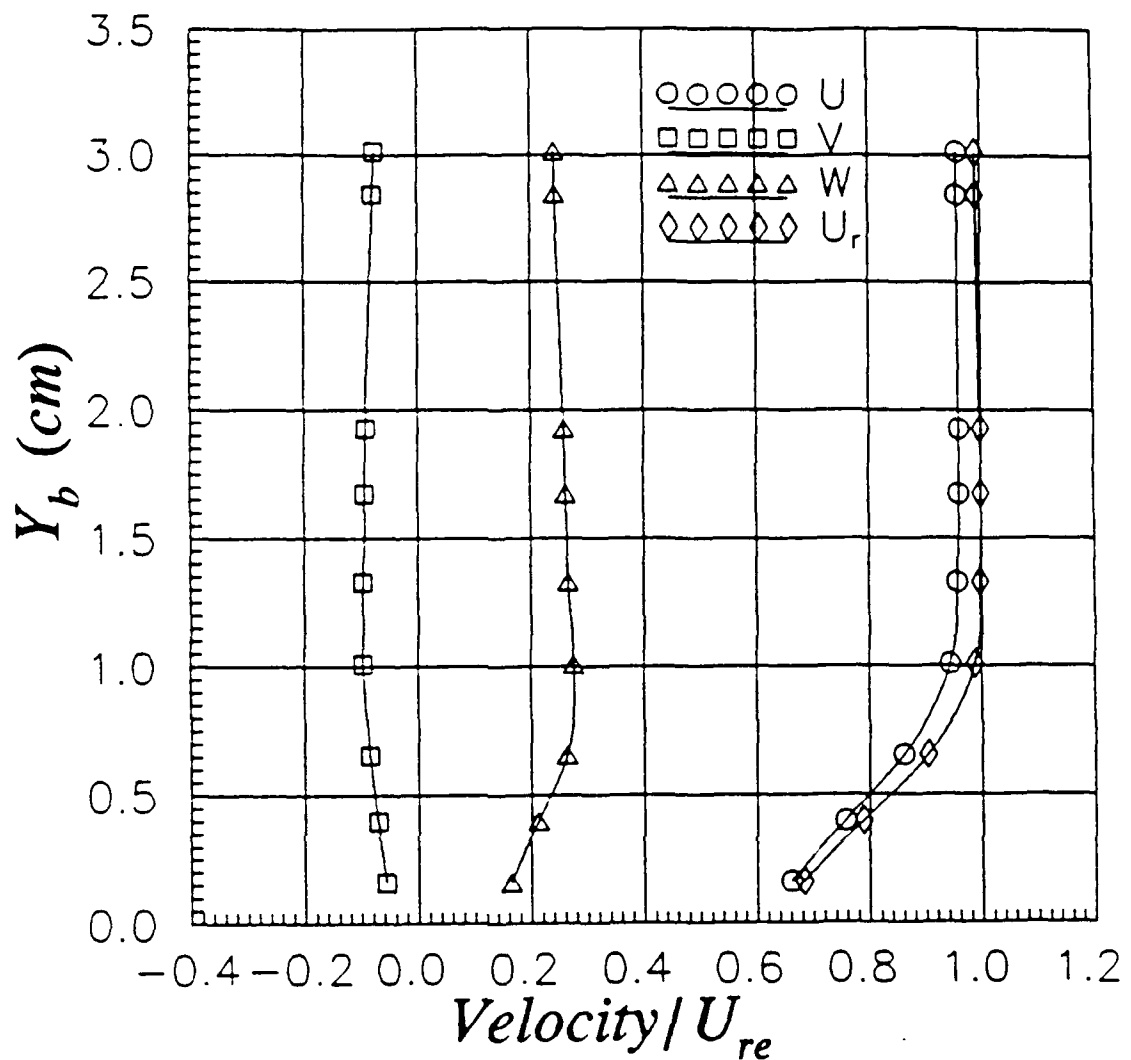
Figure 67.    X-Wire Velocity Profiles and U-W Crossflow Vectors, $\varphi=20°$, X/L=0.8, Re=$4.0\times10^6$, $\alpha=10°$, Local Body Coordinates, Direction of Arrow on Hodograph Plot Indicates Variation from Wall to Free Stream.
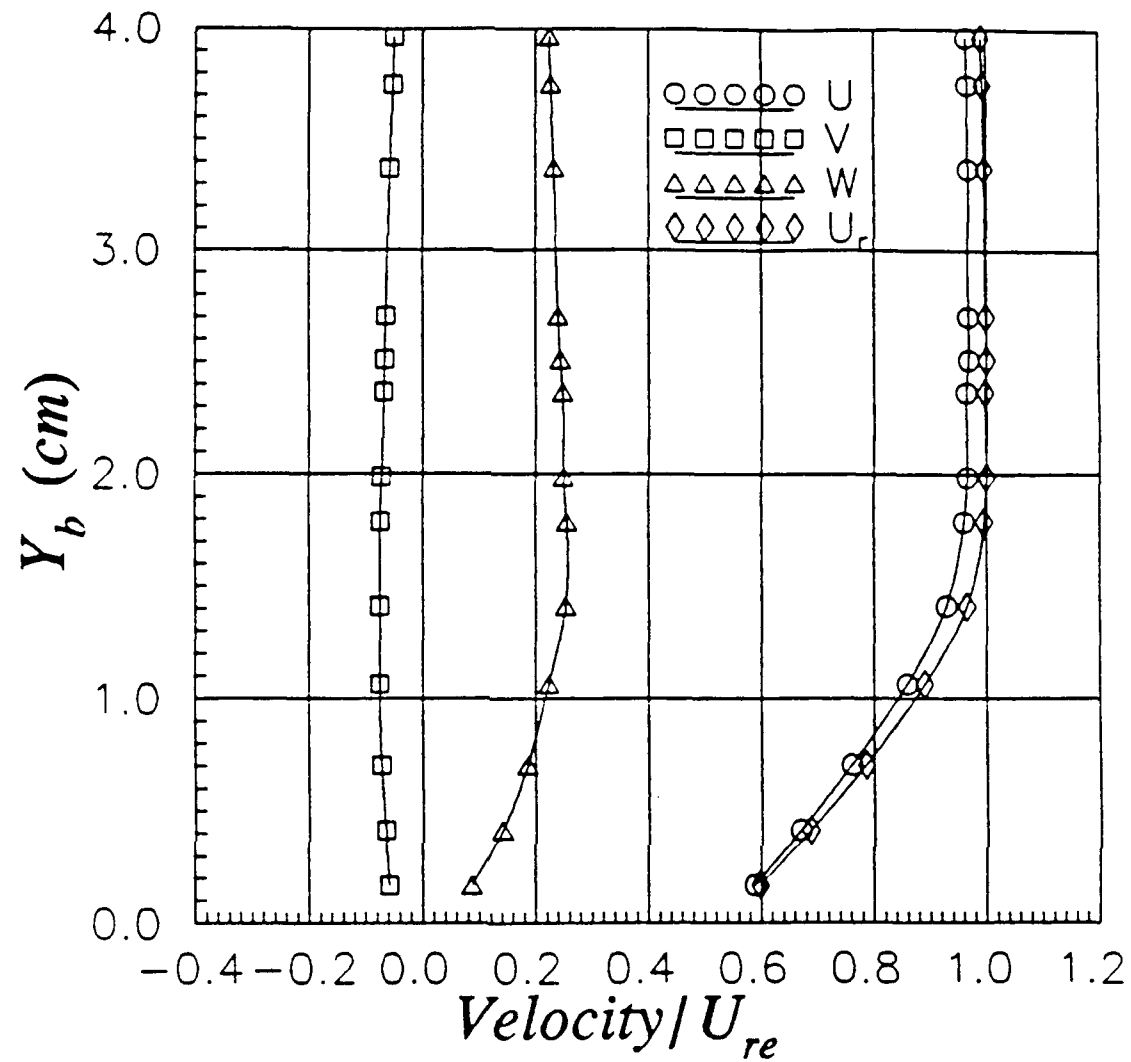
Figure 68.    X-Wire Velocity Profiles and U-W Crossflow Vectors, $\varphi=30°$, X/L=0.8, Re=$4.0\times10^6$, $\alpha=10°$, Local Body Coordinates, Direction of Arrow on Hodograph Plot Indicates Variation from Wall to Free Stream.

**Illustrations**
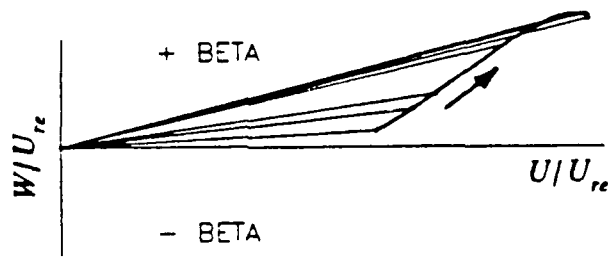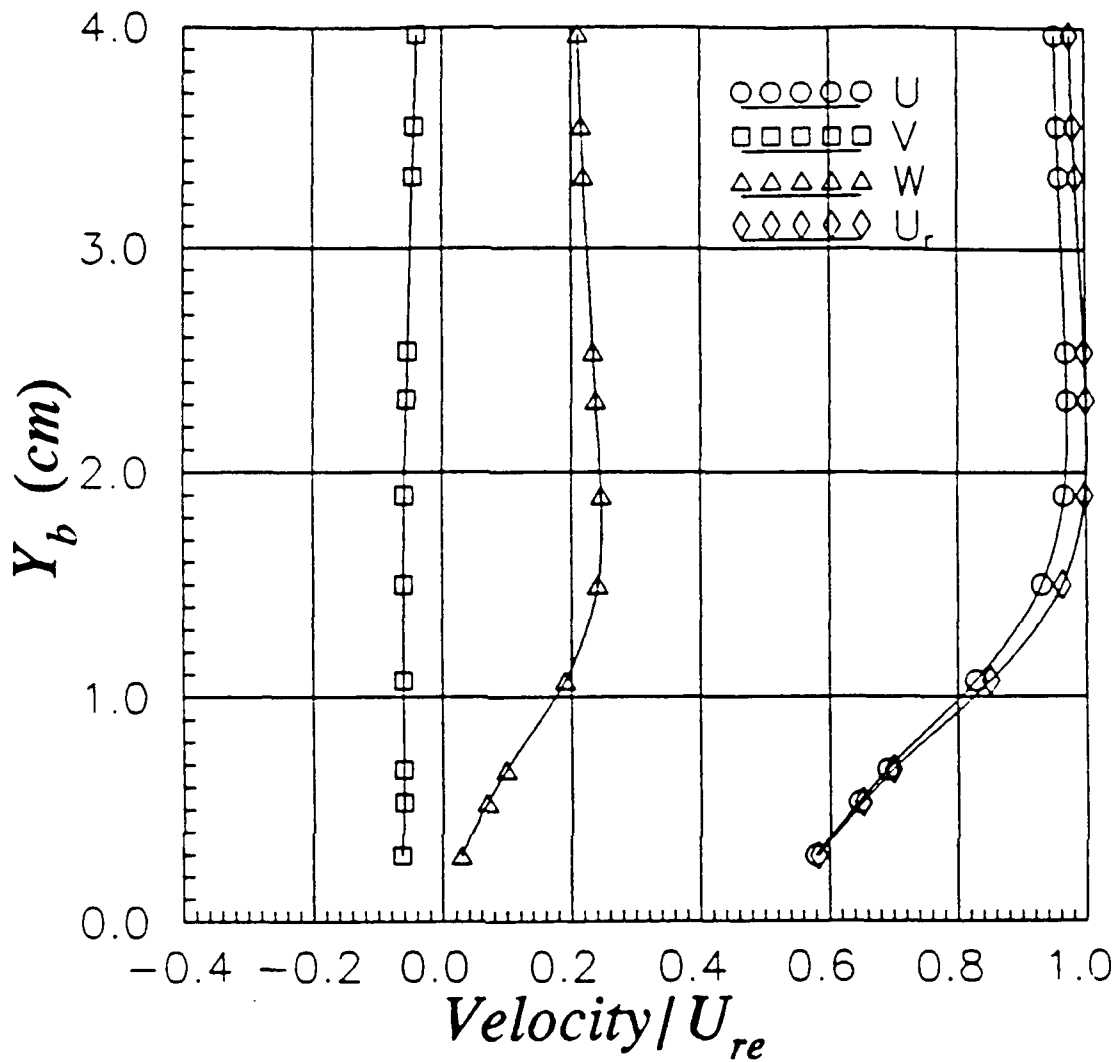
Figure 69. X-Wire Velocity Profiles and U-W Crossflow Vectors, $\varphi=40°$, X/L=0.8, Re=$4.0\times10^6$, $\alpha=10°$, Local Body Coordinates, Direction of Arrow on Hodograph Plot Indicates Variation from Wall to Free Stream.
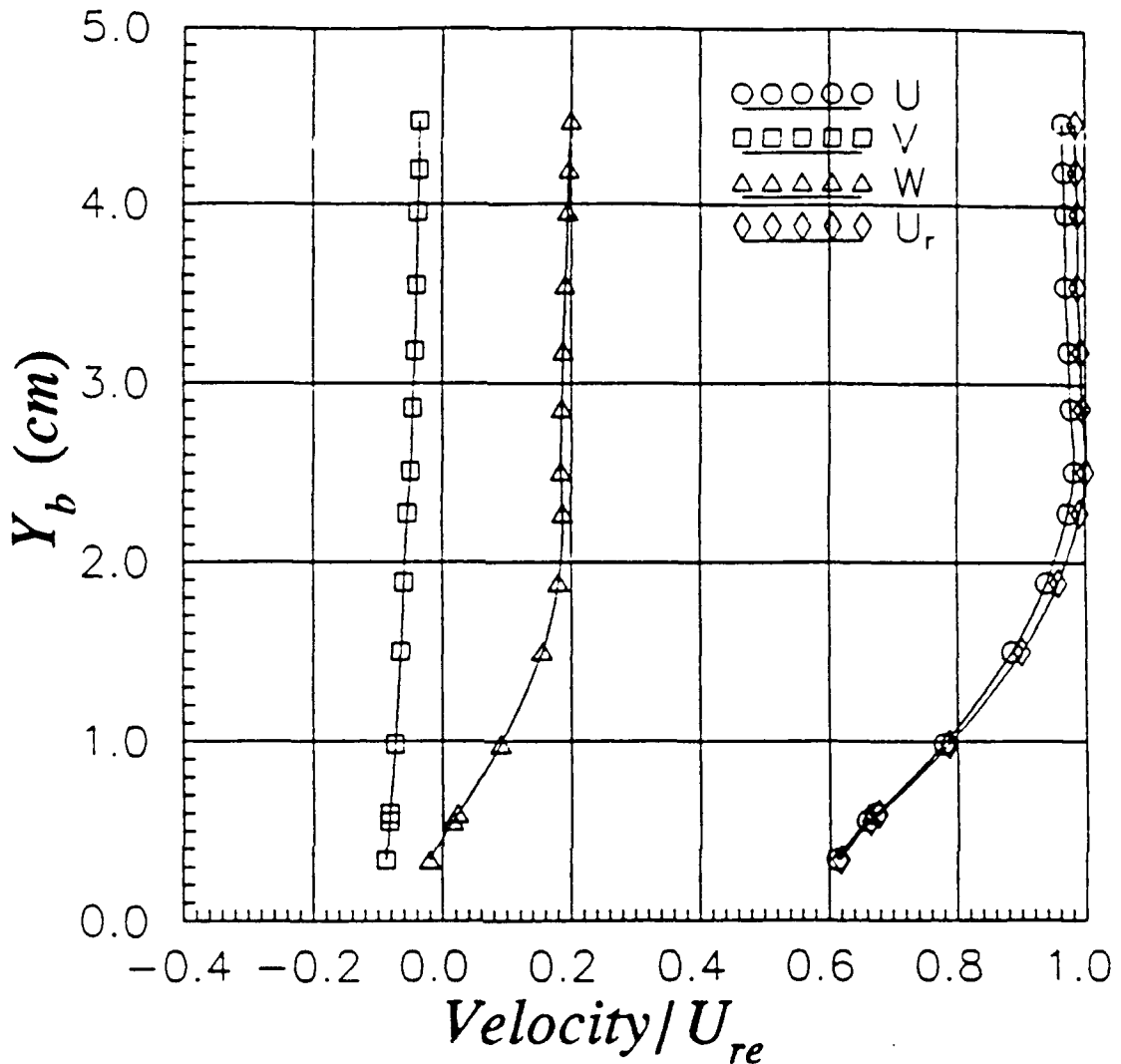
Figure 70.   X-Wire Velocity Profiles and U-W Crossflow Vectors, $\varphi = 50°$, X/L=0.8, Re=$4.0 \times 10^6$, $\alpha = 10°$, Local Body Coordinates, Direction of Arrow on Hodograph Plot Indicates Variation from Wall to Free Stream.
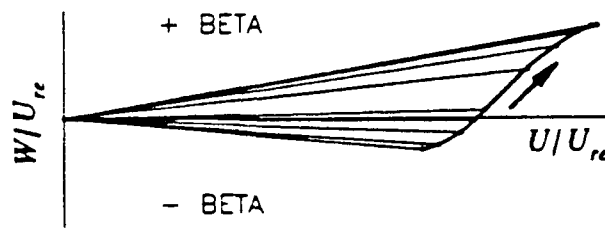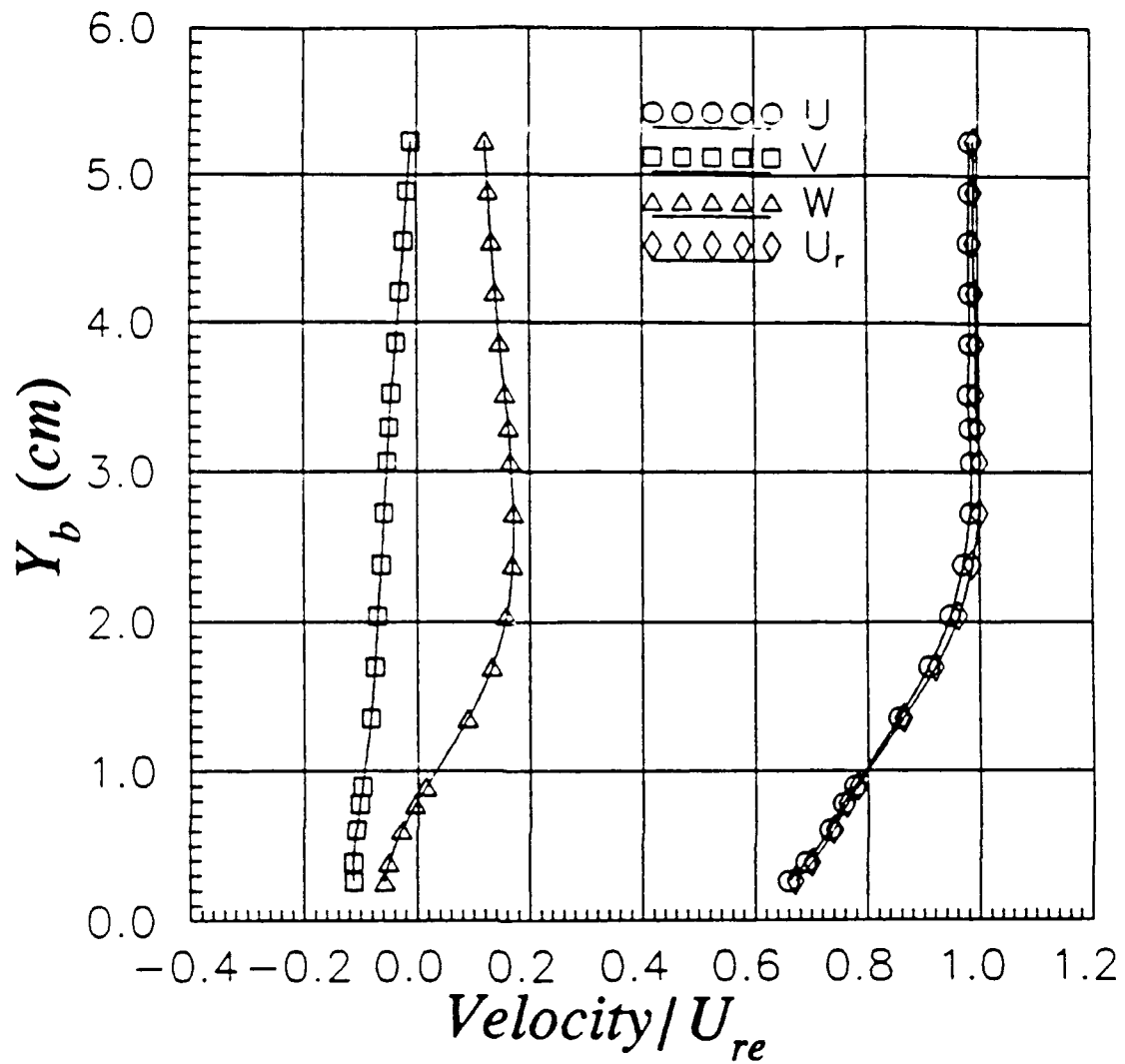
Figure 71.    X-Wire Velocity Profiles and U-W Crossflow Vectors, $\varphi = 60°$, X/L=0.8, Re=4.0×10⁶, $\alpha = 10°$, Local Body Coordinates, Direction of Arrow on Hodograph Plot Indicates Variation from Wall to Free Stream.
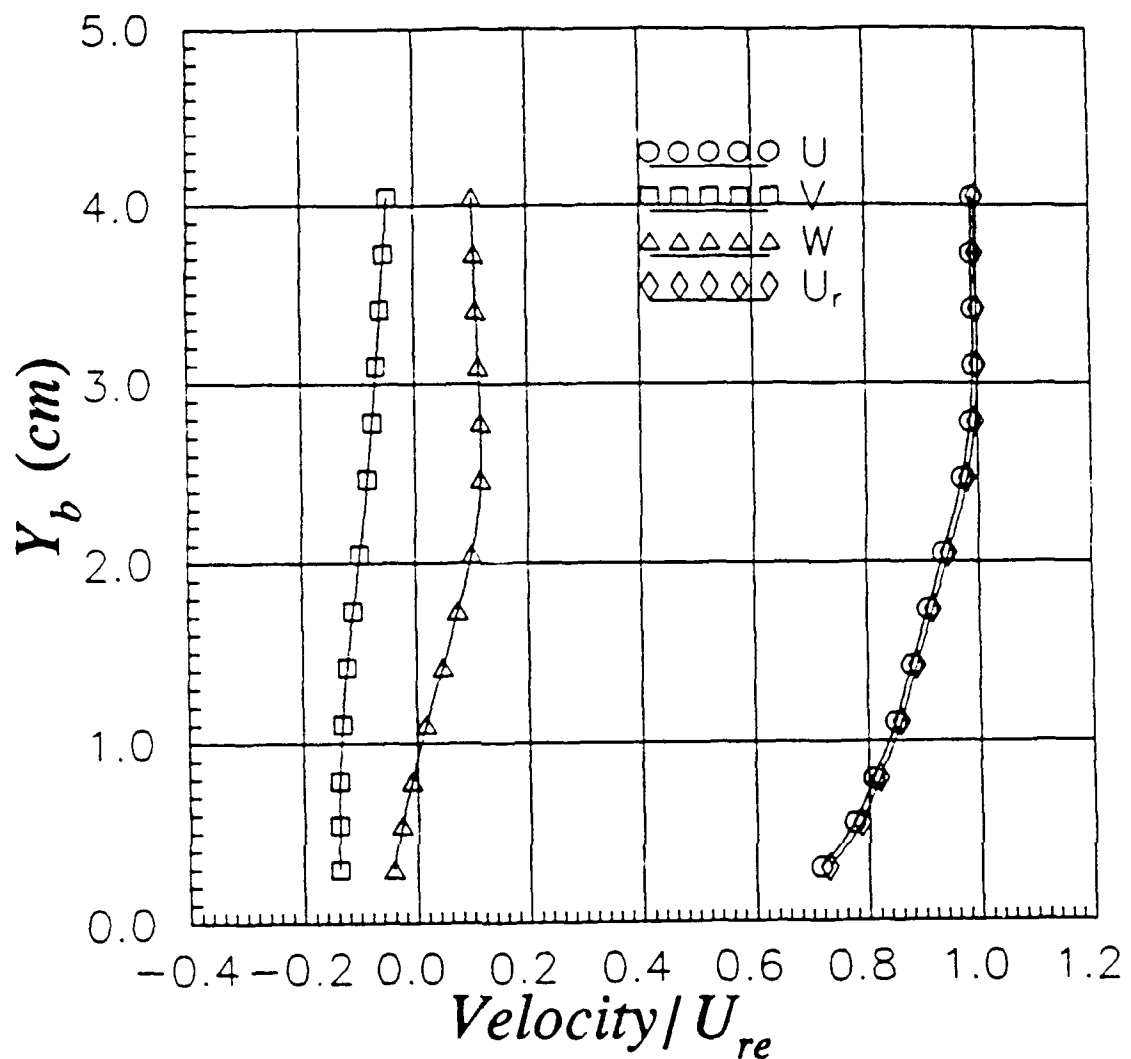
Figure 72.    X-Wire Velocity Profiles and U-W Crossflow Vectors, $\varphi=70°$, X/L=0.8, Re=$4.0\times10^6$, $\alpha=10°$, Local Body Coordinates, Direction of Arrow on Hodograph Plot Indicates Variation from Wall to Free Stream.
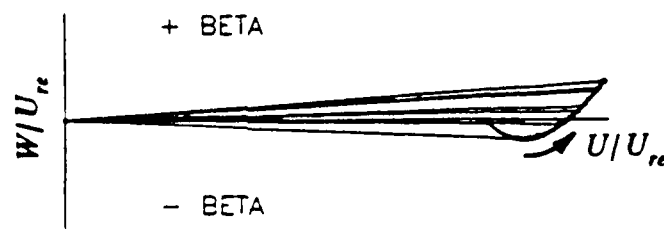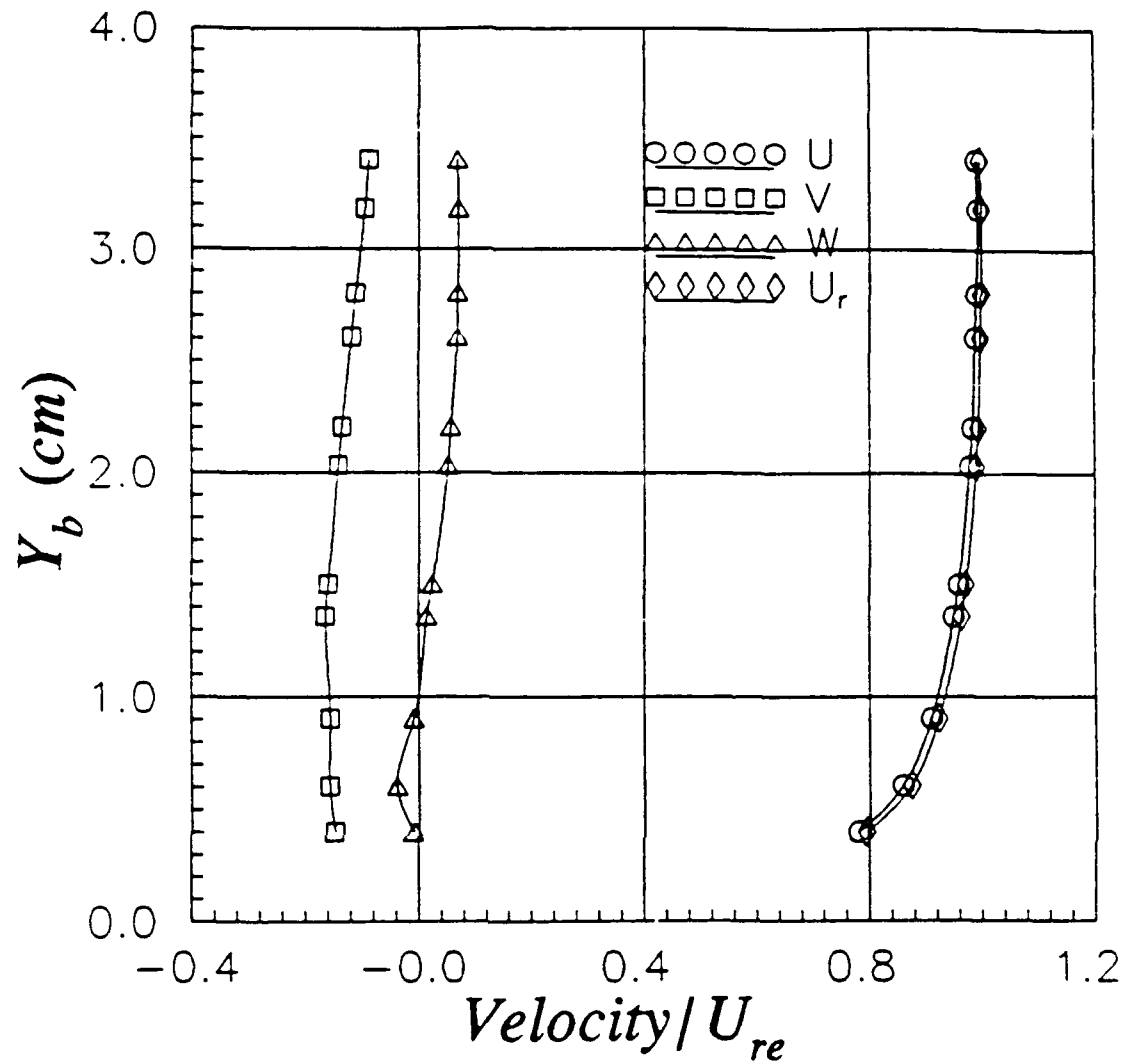
Figure 73. X-Wire Velocity Profiles and U-W Crossflow Vectors, $\varphi=80°$, X/L=0.8, $R_f=4.0\times10^6$, $\alpha=10°$, Local Body Coordinates, Direction of Arrow on Hodograph Plot Indicates Variation from Wall to Free Stream.
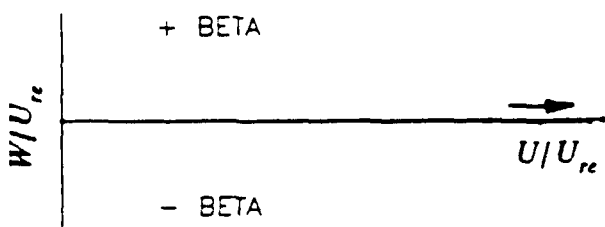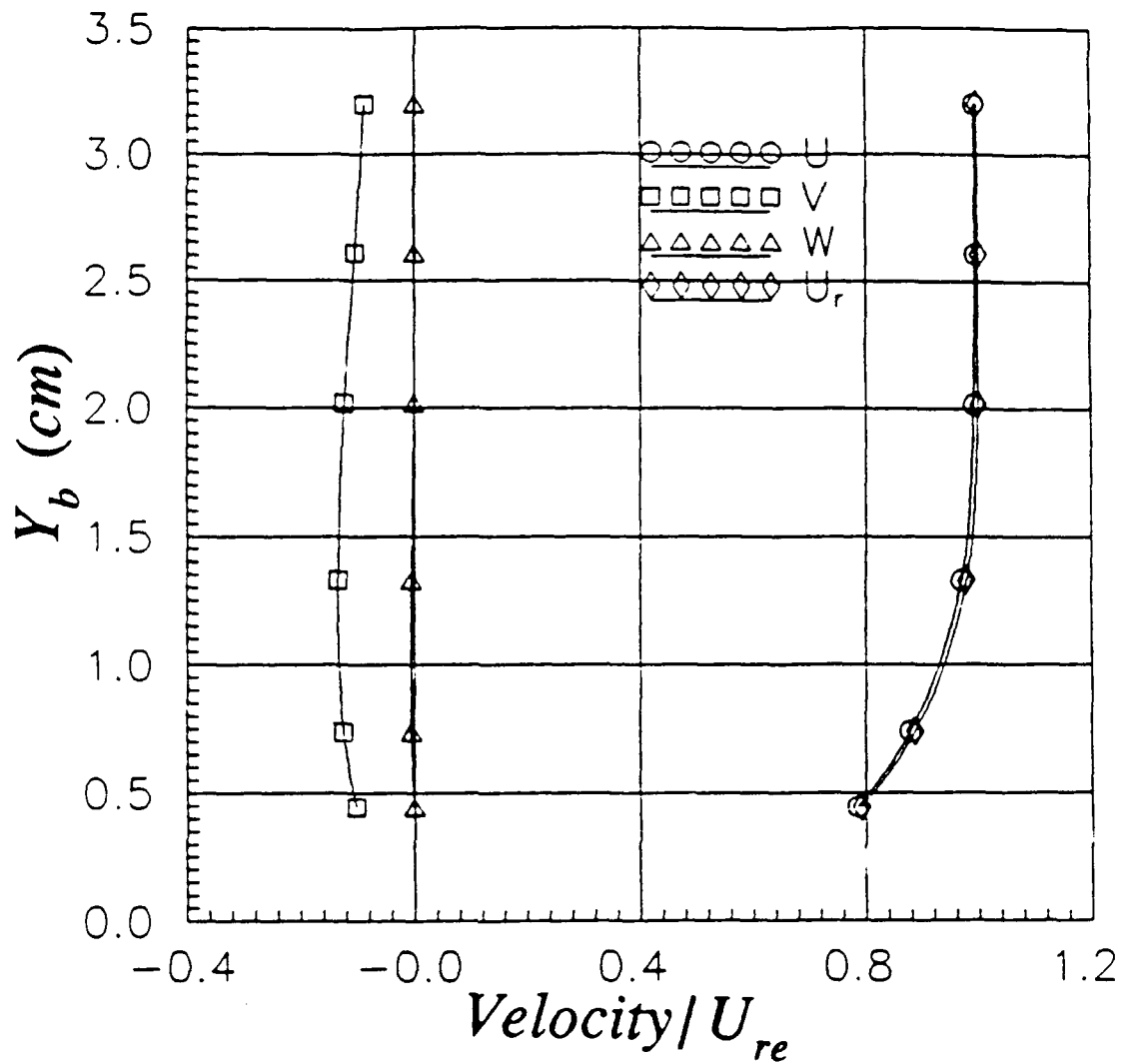
Figure 74.    X-Wire Velocity Profiles and U-W Crossflow Vectors, $\varphi=90°$, X/L=0.8, Re=$4.0\times10^6$, $\alpha=10°$, Local Body Coordinates, Direction of Arrow on Hodograph Plot Indicates Variation from Wall to Free Stream.
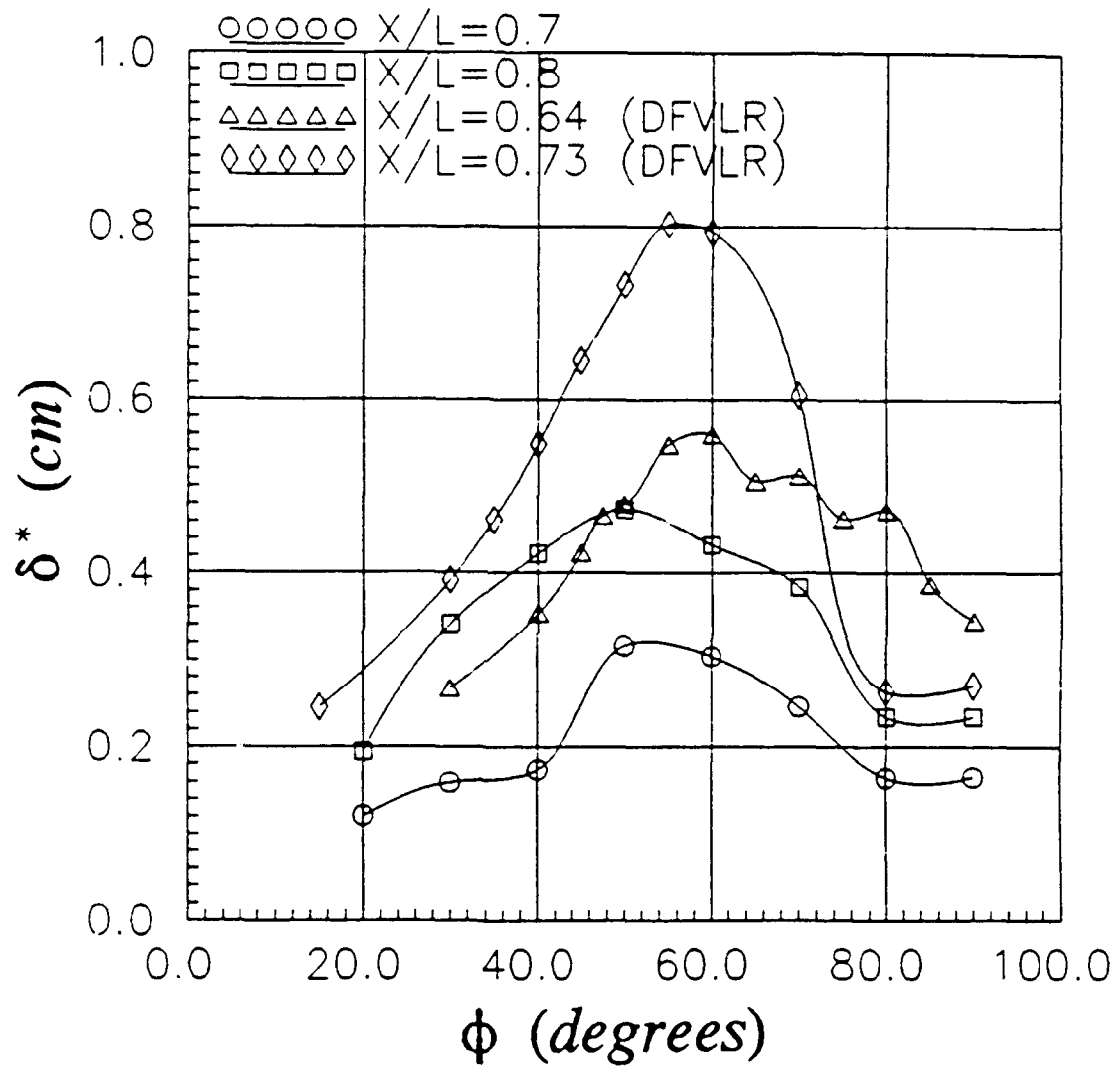
Figure 75.    Displacement Thickness $\delta^*$ with respect to Circumferential Angle $\varphi$, $Re=4.0\times10^6$, $\alpha=10°$, Compared to DFVLR Data at $Re=7.2\times10^6$ (Meier, *et al.*,1984a).
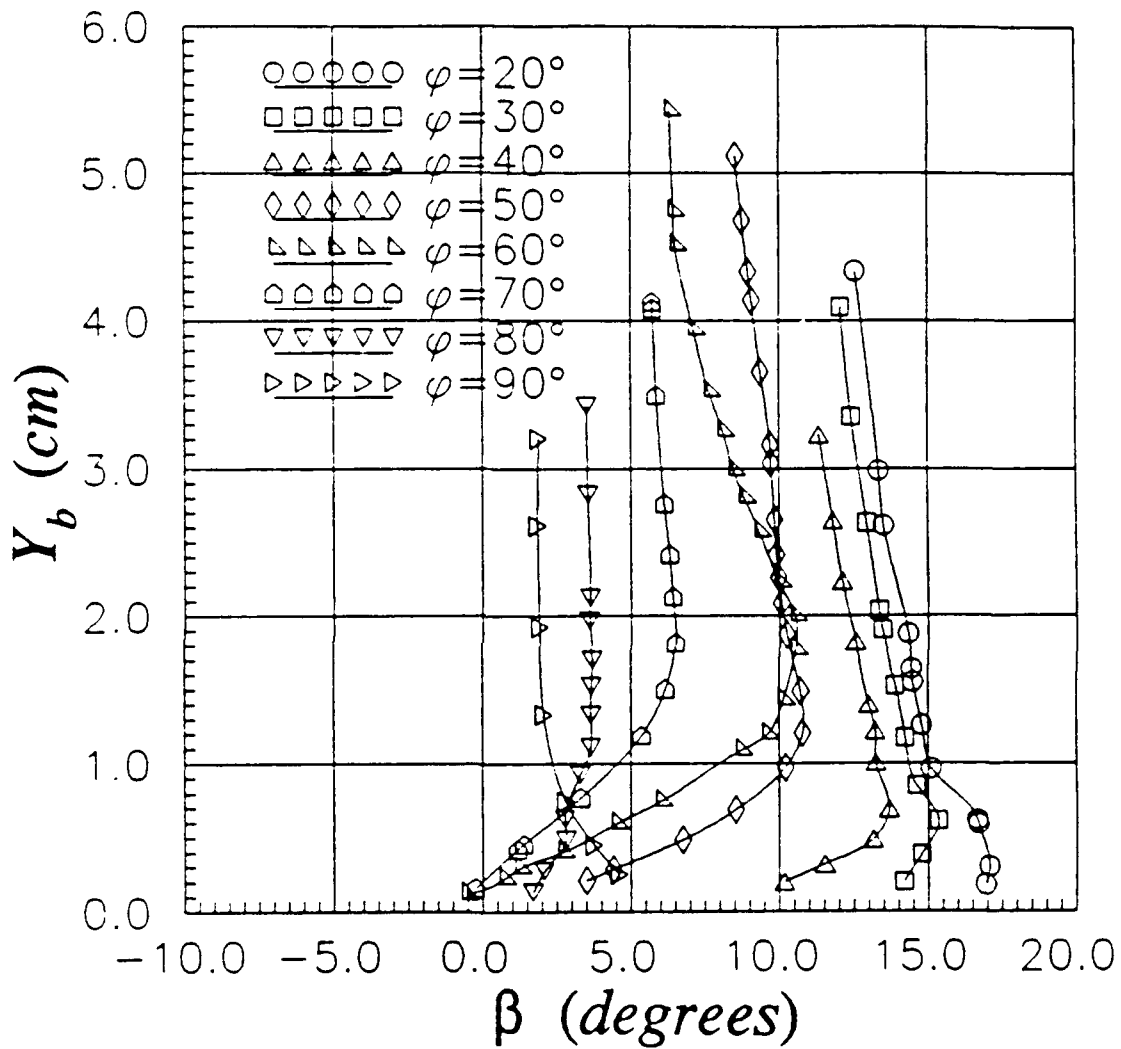
Figure 76.   Profiles of Flow Angle ß = arctan(W/U), X/L = 0.7, Re = 4.0 × 10⁶, α = 10°,
Local Body Coordinates.
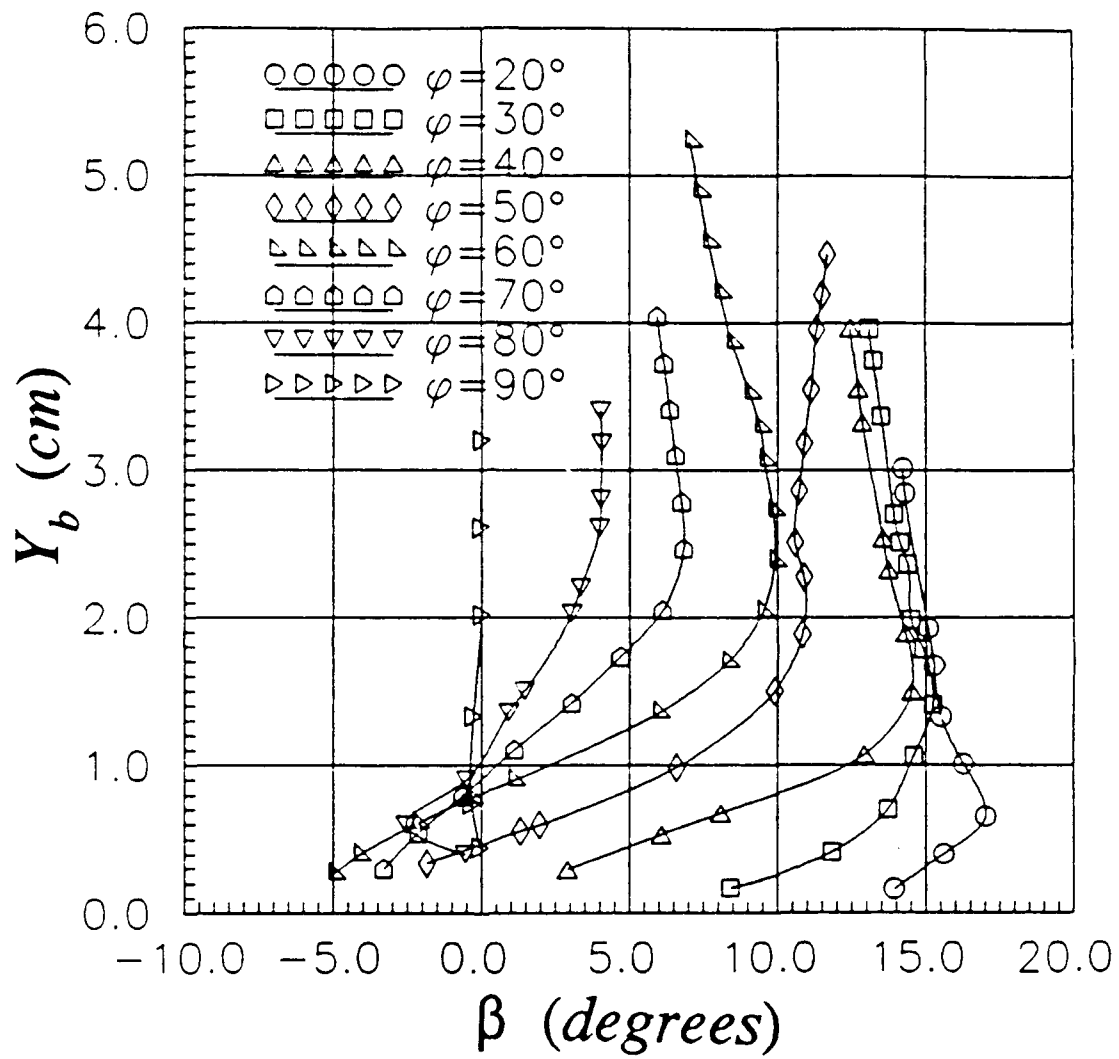
Figure 77.    Profiles of Flow Angle ß =arctan(W/U), X/L=0.8, Re =4.0×10⁶, α = 10°, Local   Body Coordinates.
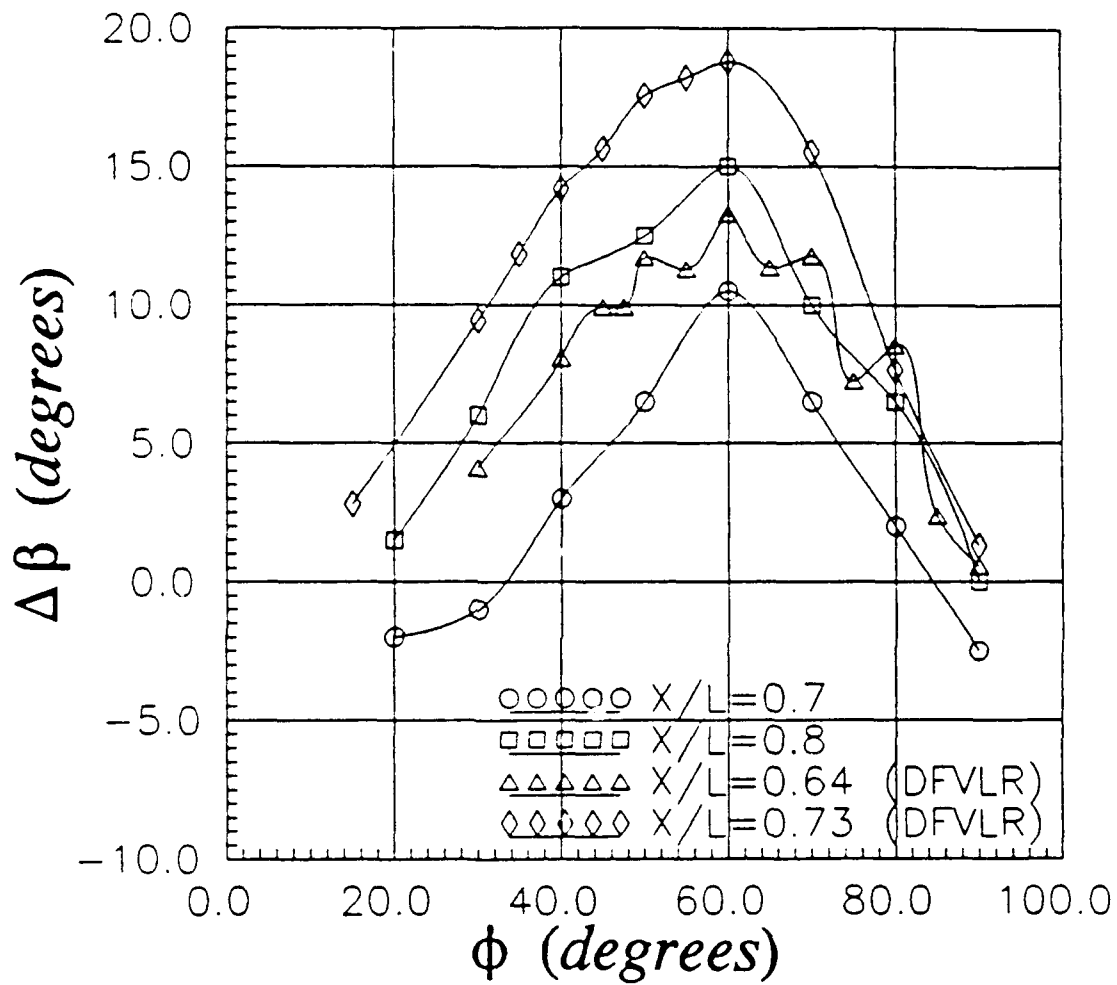
Figure 78.    Difference Between Flow Angle of Local Free-Stream Velocity and Flow Angle of Velocity at the Surface with respect to Circumferential Angle φ, Re=4.0×10⁶, α=10°, Compared to DFVLR Data at Re=7.2×10⁶ (Meier, *et al.*, 1984a).
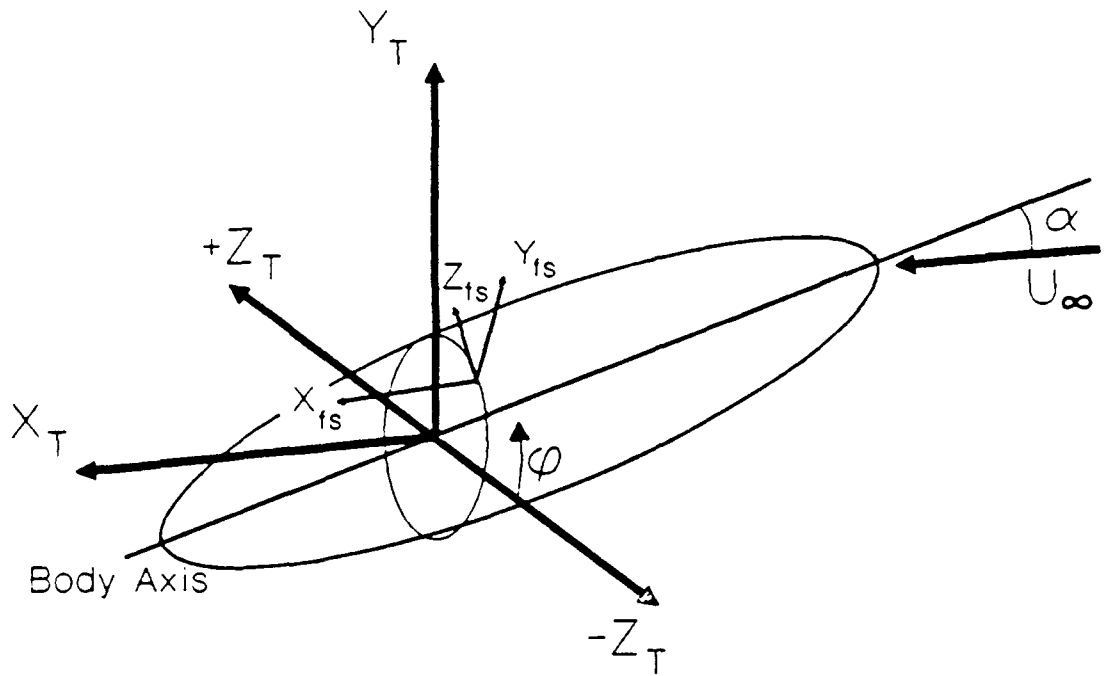
Figure 79. Local Free-Stream ($X_{fs}$-$Y_{fs}$-$Z_{fs}$) Coordinate System, with $X_{fs}$ Aligned with the Local Free-Stream Velocity and $Y_{fs}$ out from Surface of Model.
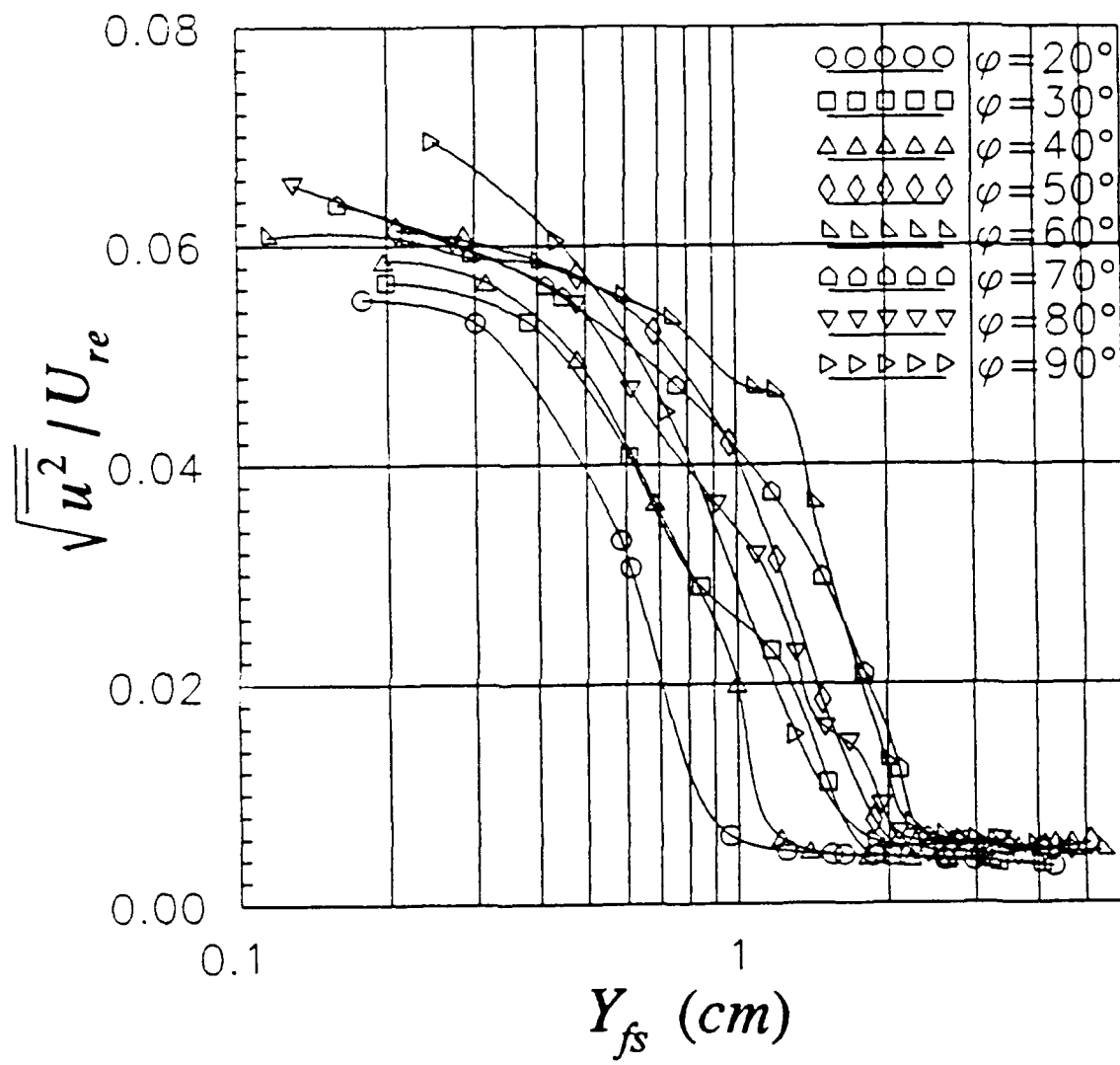
Figure 80. Profiles of $\overline{u^2}$ Reynolds Stress, X/L=0.7, Re=4.0×10⁶, $\alpha$=10°, Local Free-Stream Coordinates.
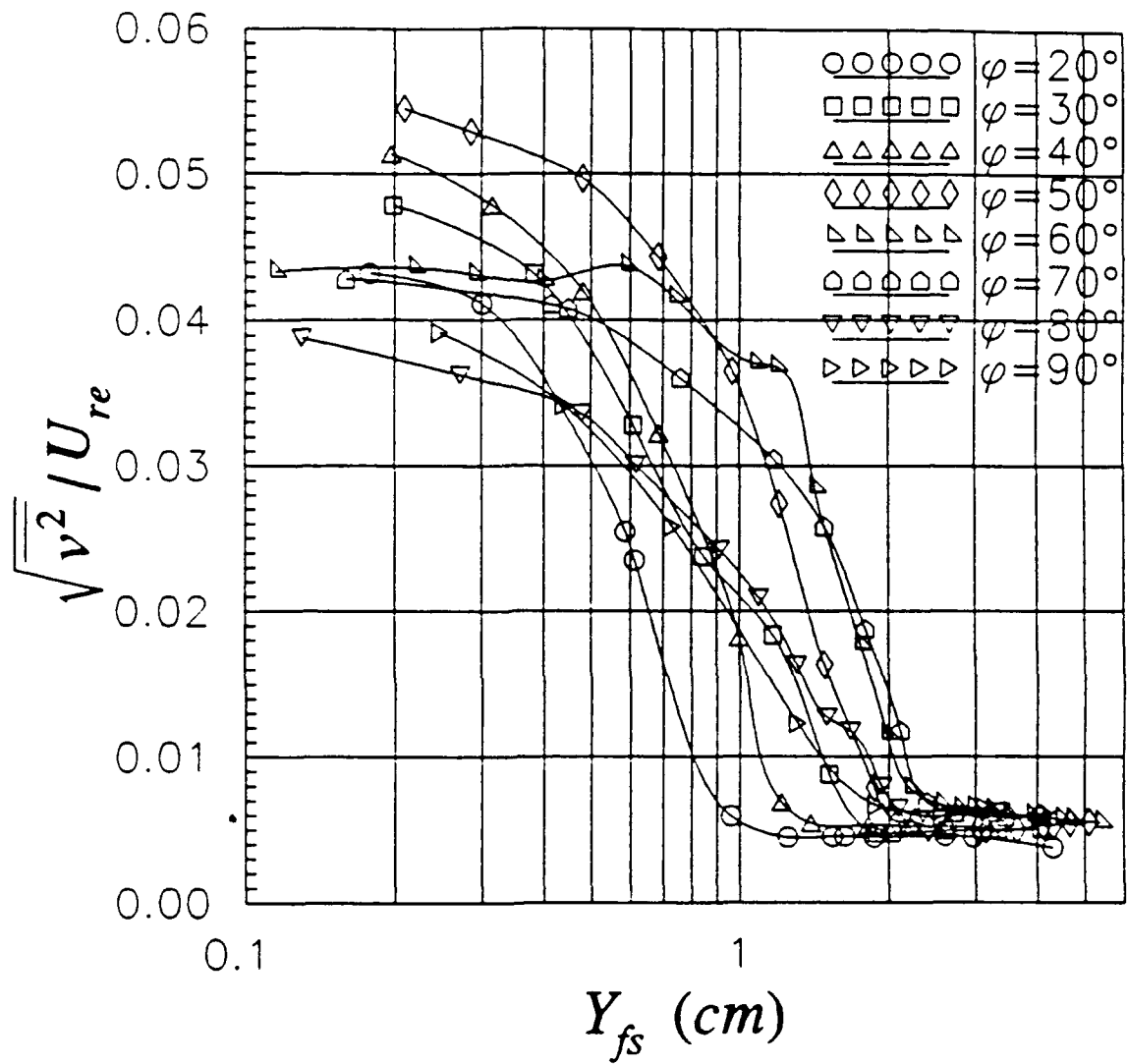
Figure 81.    Profiles of $\overline{v^2}$ Reynolds Stress, X/L=0.7, Re=4.0×10⁶, $\alpha$=10°, Local
Free-Stream Coordinates.
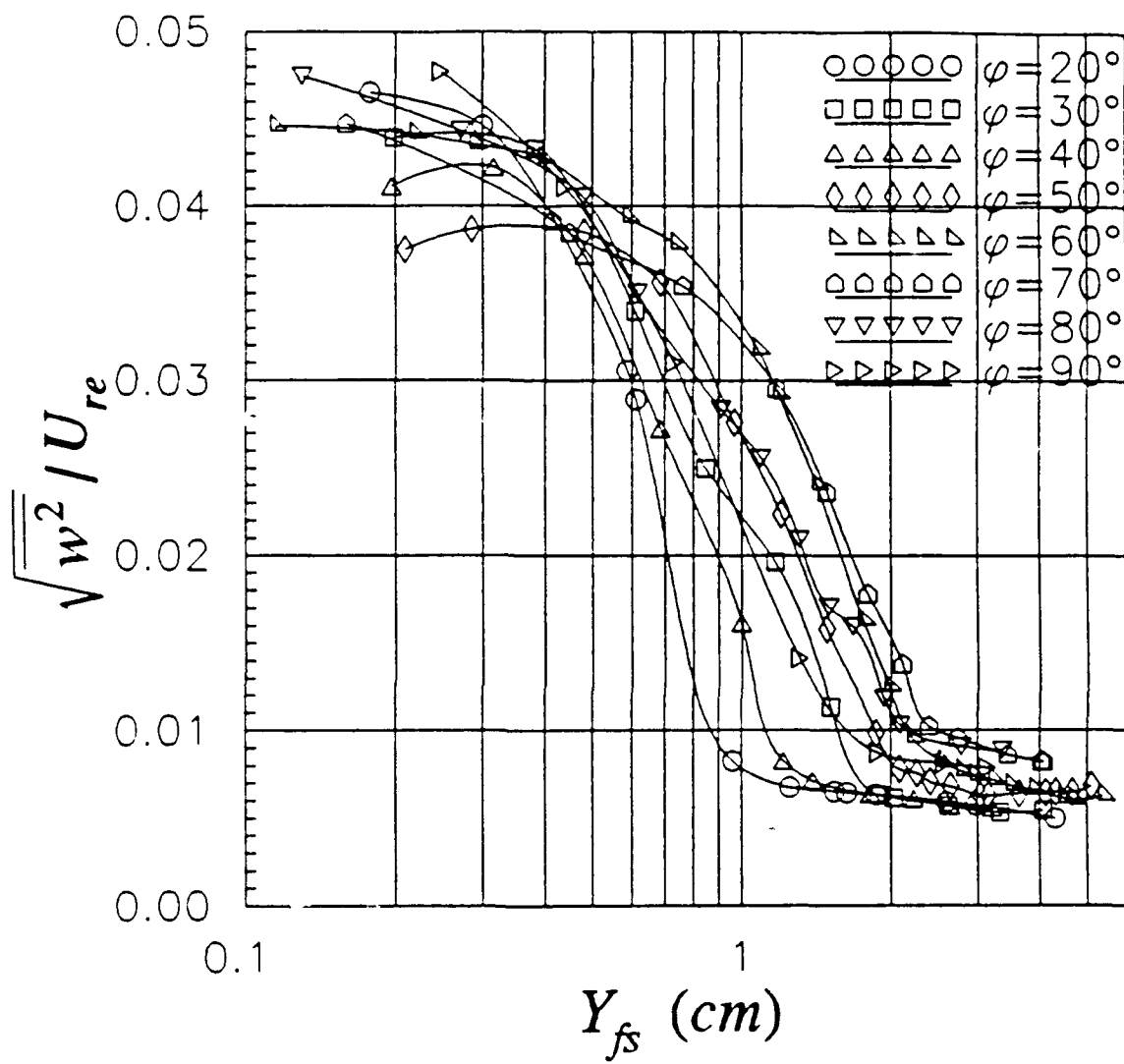
Figure 82.    Profiles of  $\overline{w^2}$   Reynolds Stress, X/L=0.7, Re=4.0×10$^6$, $\alpha$=10°, Local
Free-Stream Coordinates.
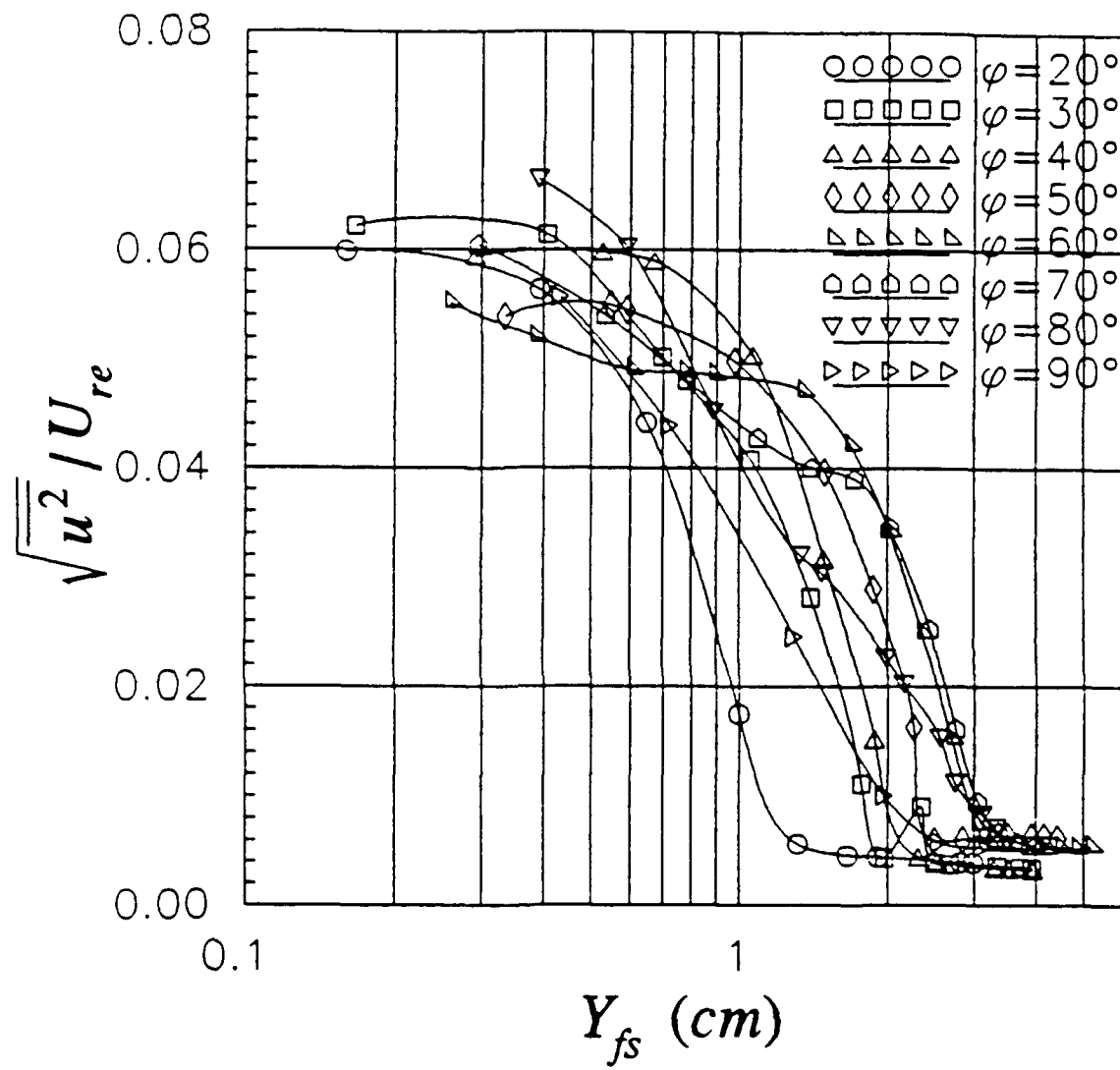
Figure 83.    Profiles of $\overline{u^2}$ Reynolds Stress, X/L=0.8, Re=4.0×10⁶, $\alpha$=10°, Local
Free-Stream Coordinates.
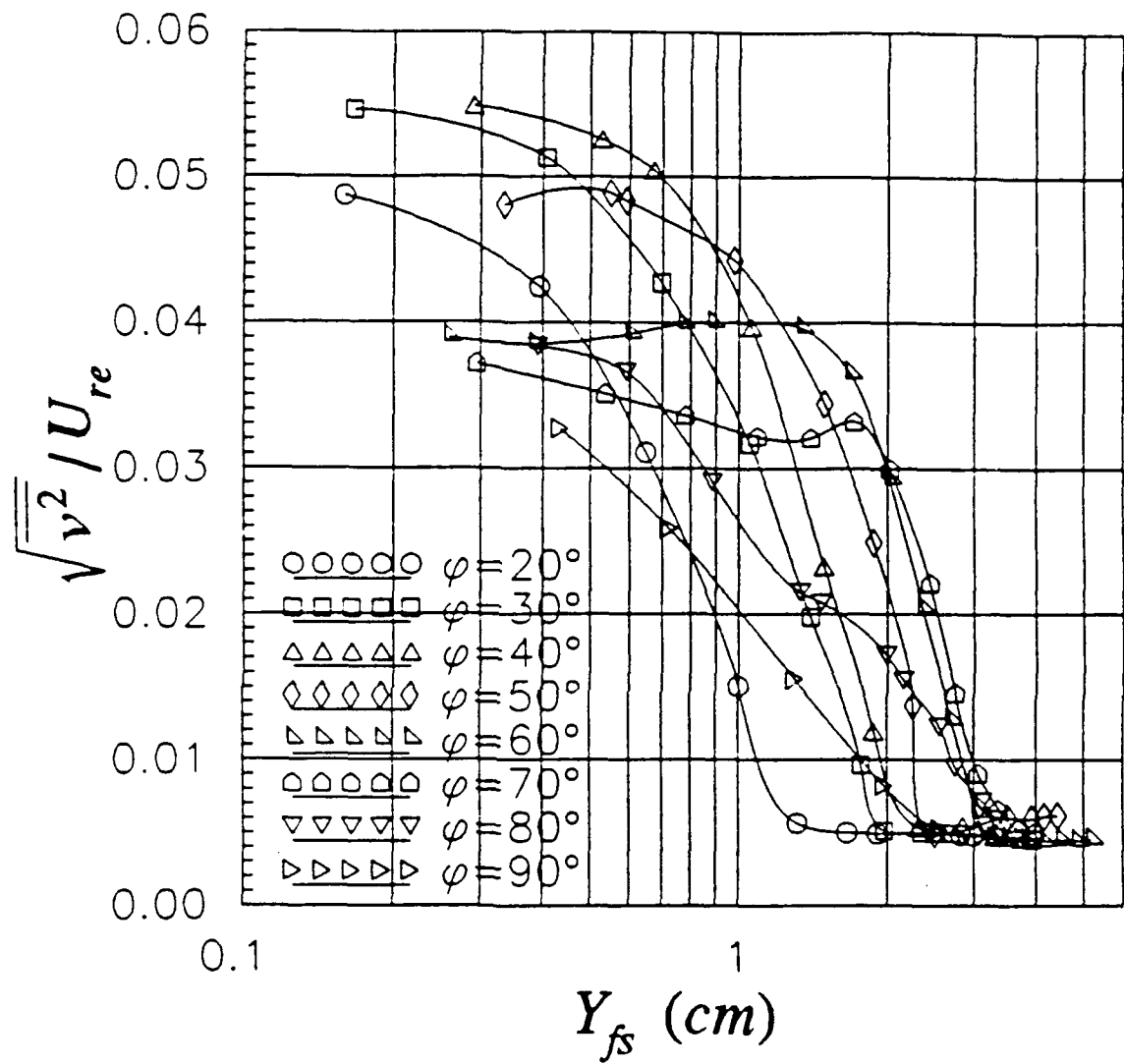
Figure 84. Profiles of $\overline{v^2}$ Reynolds Stress, X/L=0.8, Re=$4.0 \times 10^6$, $\alpha = 10°$, Local Free-Stream Coordinates.
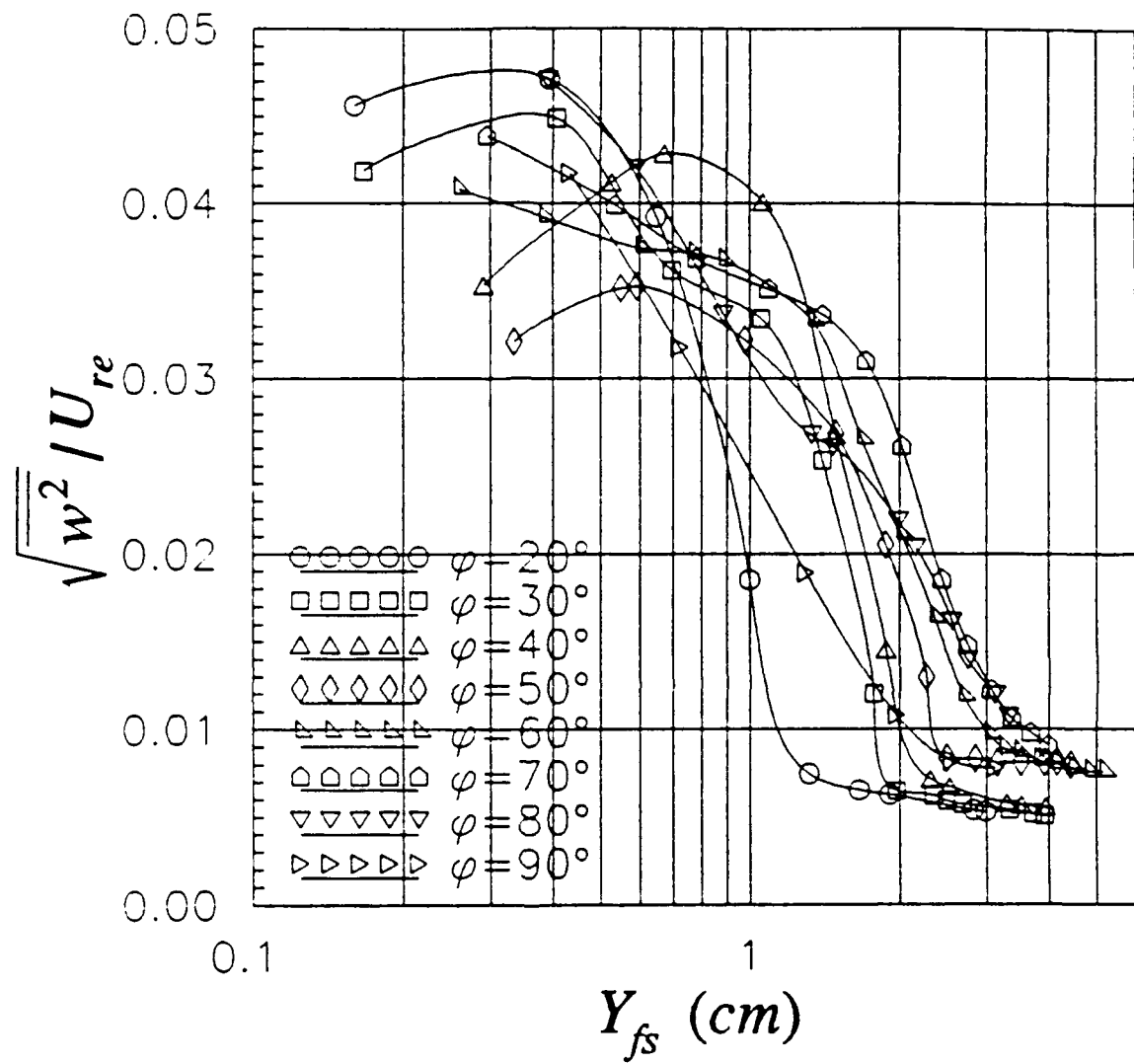
Figure 85.    Profiles of $\overline{w^2}$ Reynolds Stress, X/L=0.8, Re=4.0×10⁶, $\alpha$=10°, Local Free-Stream Coordinates.
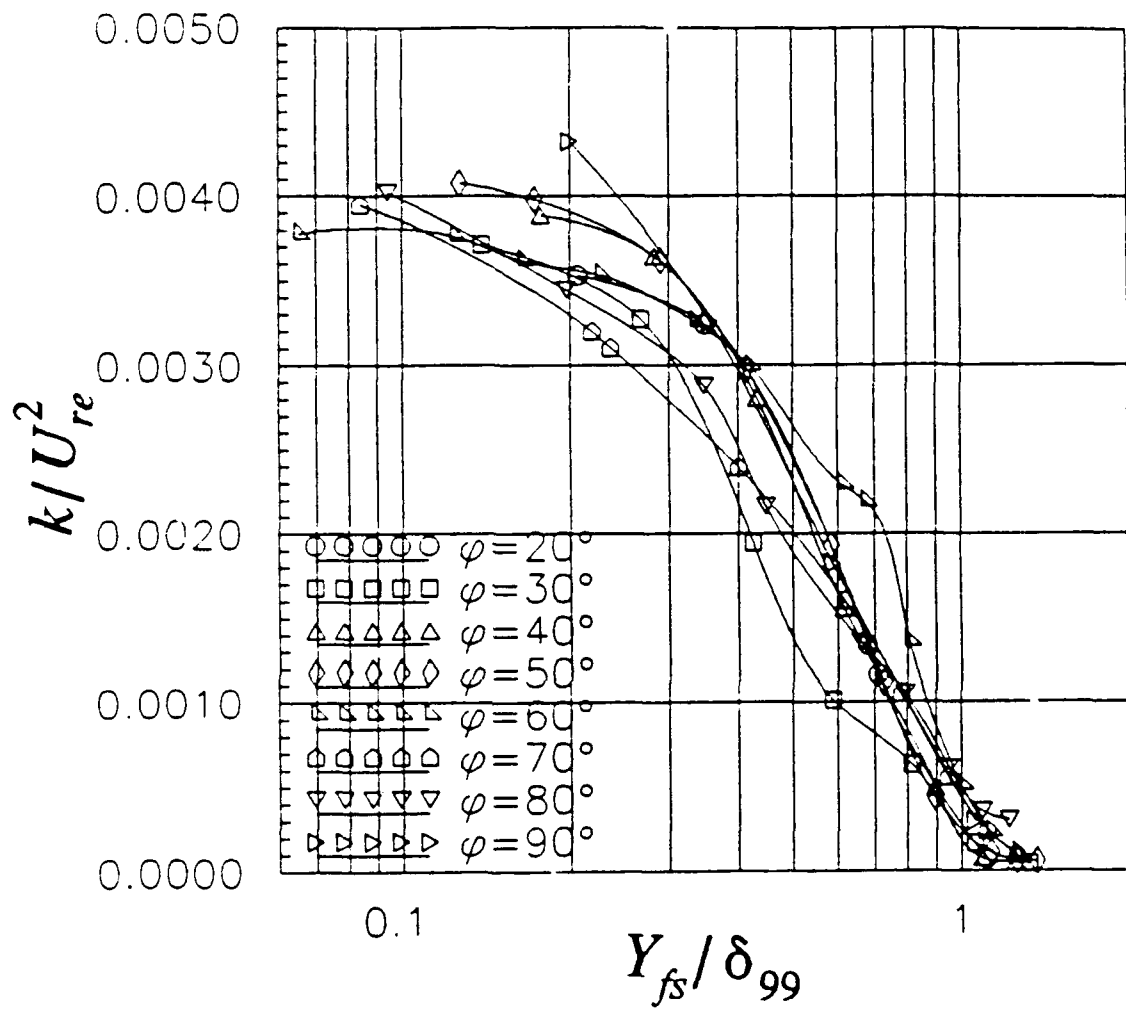
Figure 86.    Profiles of Turbulent Kinetic Energy k with respect to $Y_{fs}/\delta_{99}$, X/L=0.7, Re=4.0×10$^5$, α=10°, Local Free-Stream Coordinates.
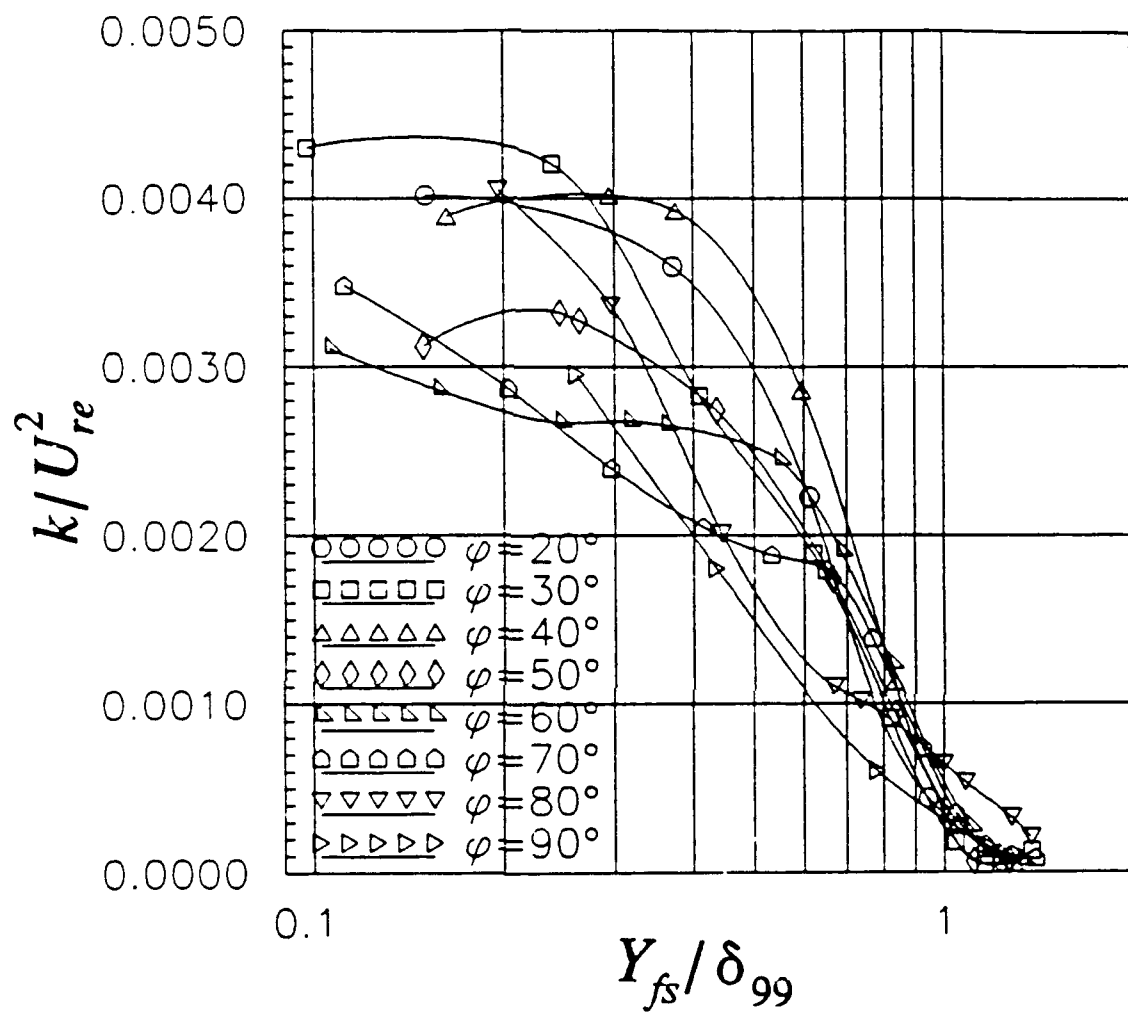
Figure 87. Profiles of Turbulent Kinetic Energy k with respect to $Y_{fs}/\delta_{99}$, X/L=0.8, Re=4.0×10$^6$, $\alpha$=10°, Local Free-Stream Coordinates.
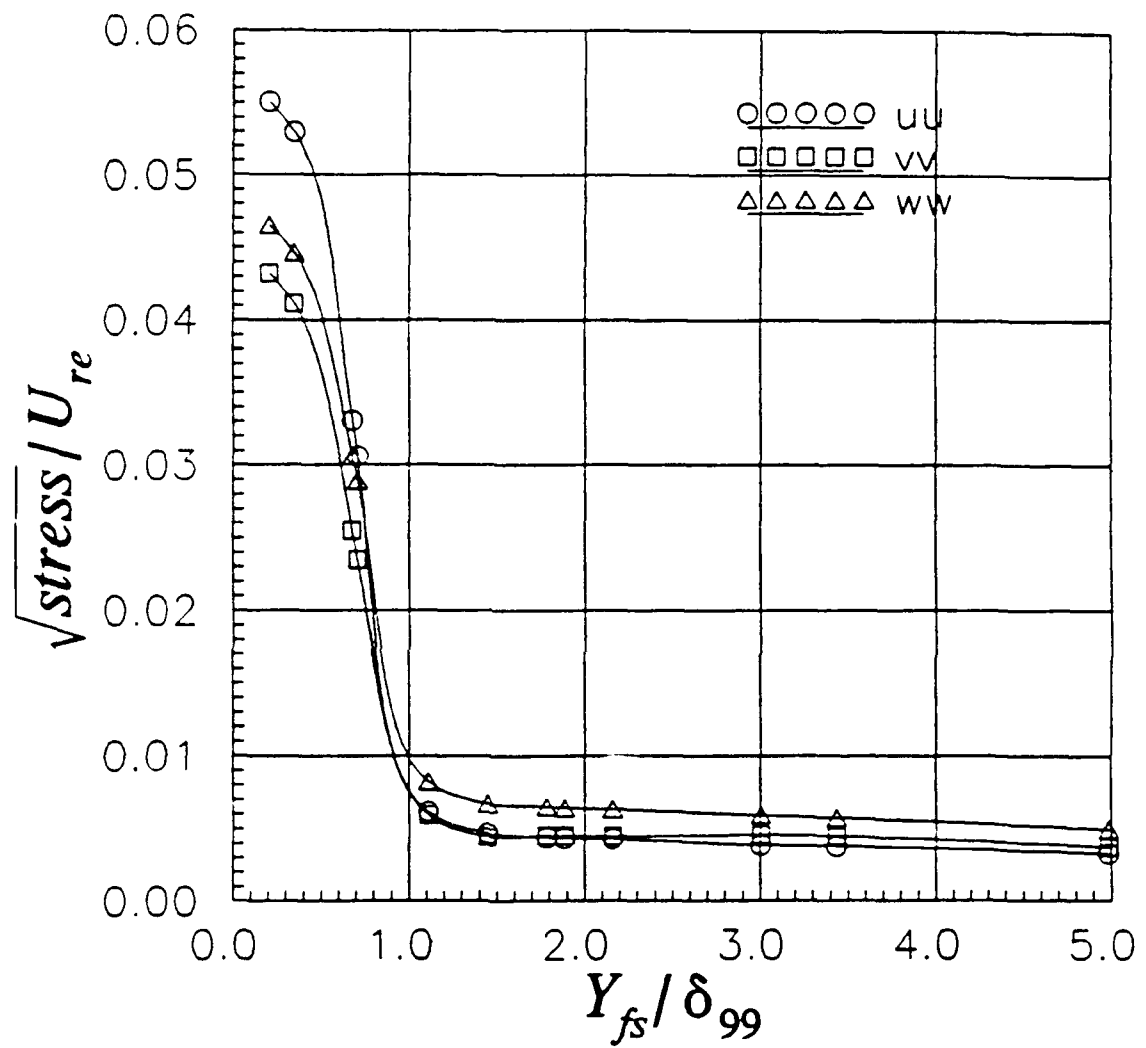
Figure 88. Profiles of Reynolds Normal Stresses with respect to $Y_{fs}/\delta_{99}$, $\varphi=20°$, $X/L=0.7$, $Re=4.0\times10^6$, $\alpha=10°$, Local Free-Stream Coordinates.
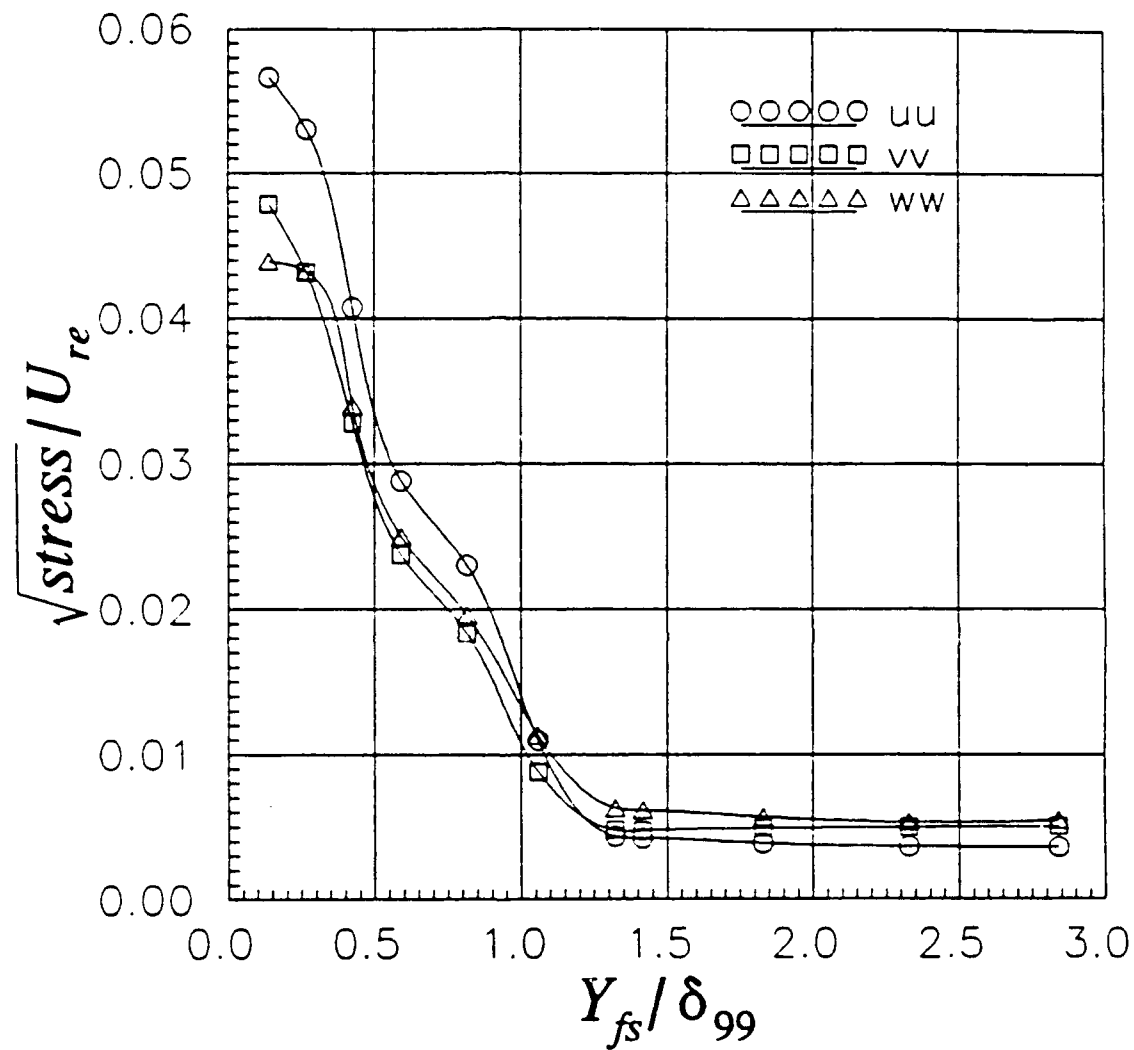
Figure 89.     Profiles of Reynolds Normal Stresses with respect to $Y_{fs}/\delta_{99}$, $\varphi=30°$, $X/L=0.7$, $Re=4.0\times10^6$, $\alpha=10°$, Local Free-Stream Coordinates.
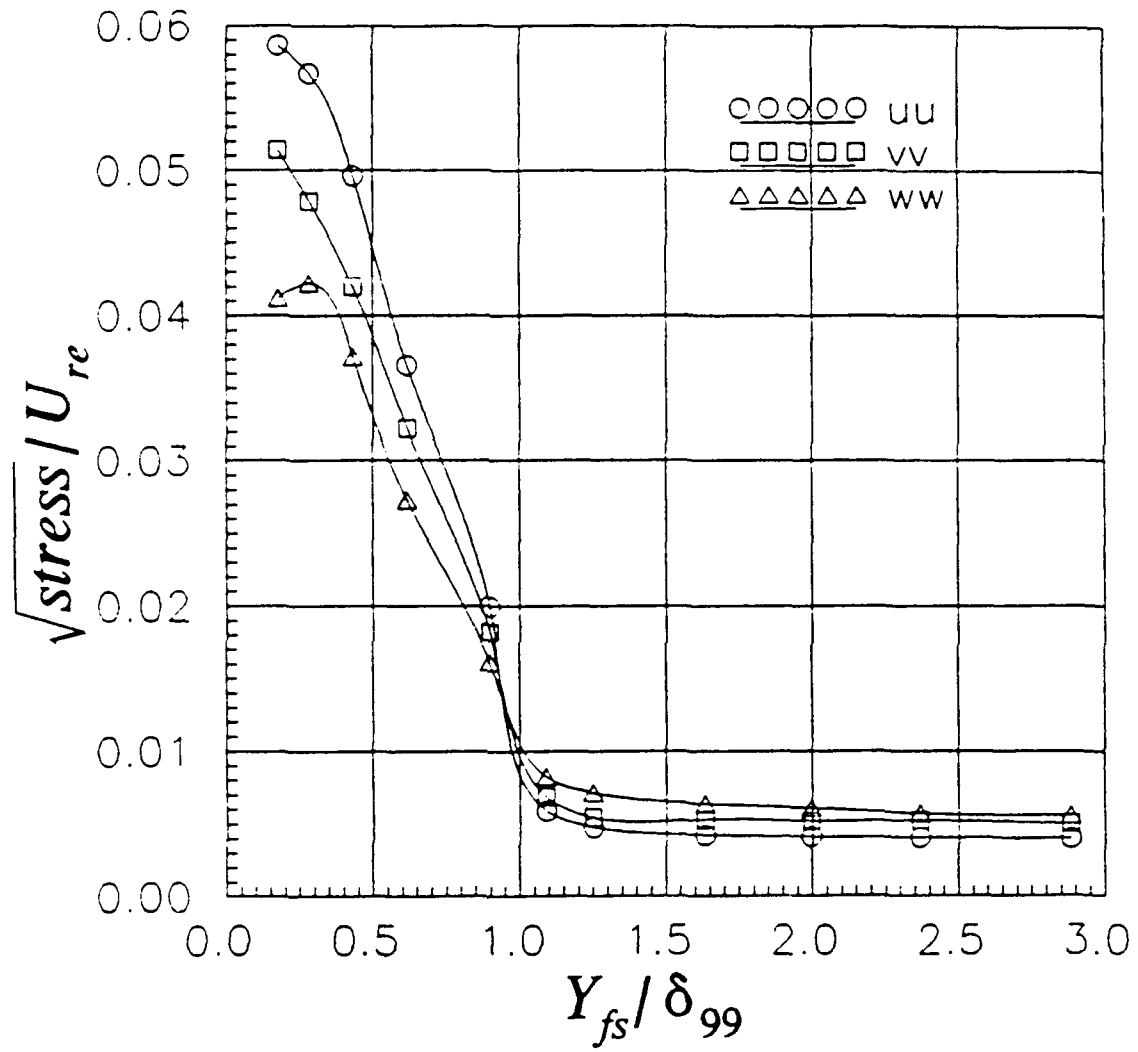
Figure 90.    Profiles of Reynolds Normal Stresses with respect to $Y_{fs}/\delta_{99}$, $\varphi=40°$, $X/L=0.7$, $Re=4.0\times10^6$, $\alpha=10°$, Local Free-Stream Coordinates.
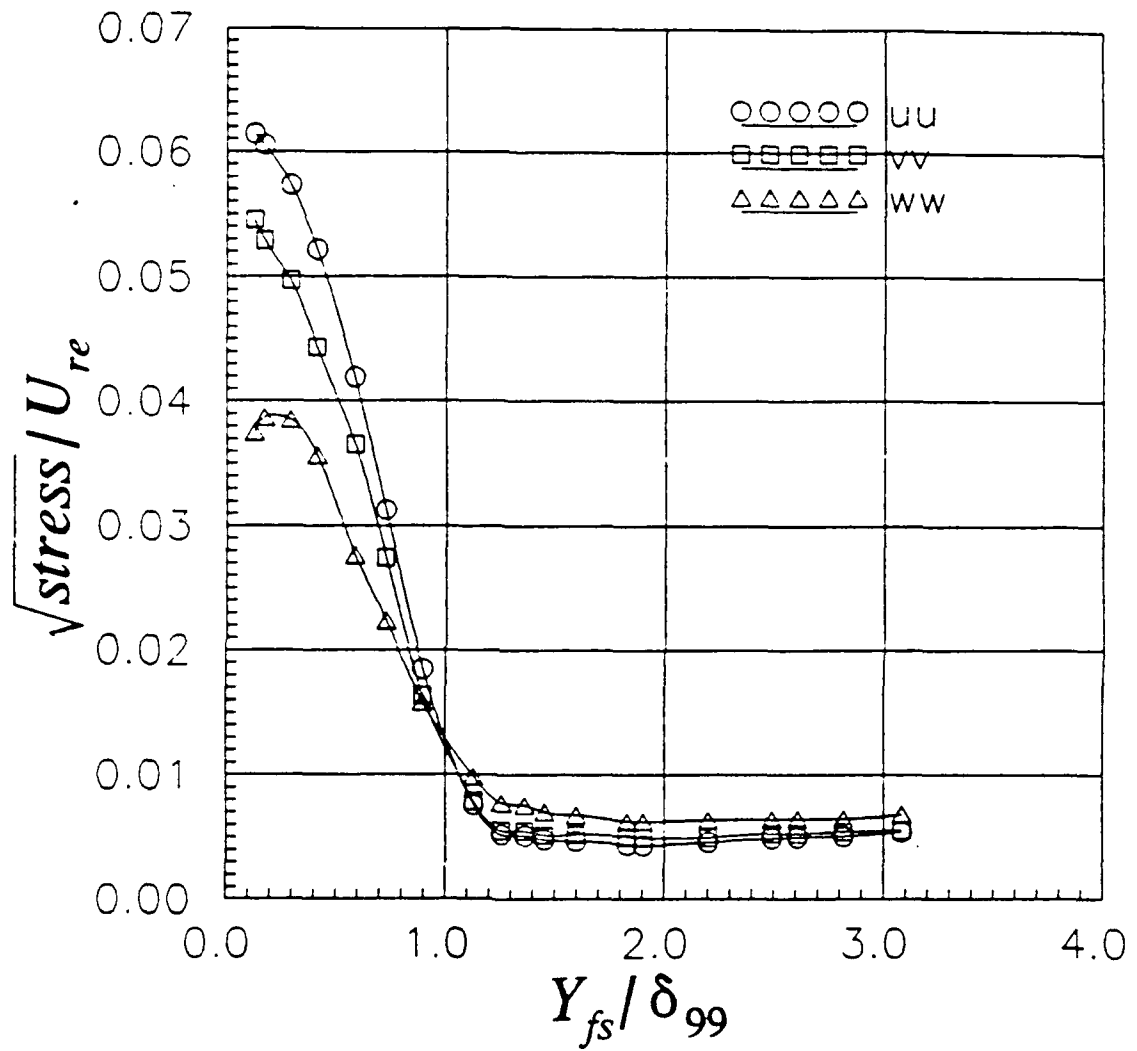
Figure 91.   Profiles of Reynolds Normal Stresses with respect to $Y_{fs}/\delta_{99}$, $\varphi = 50°$, $X/L = 0.7$, $Re = 4.0 \times 10^6$, $\alpha = 10°$, Local Free-Stream Coordinates.
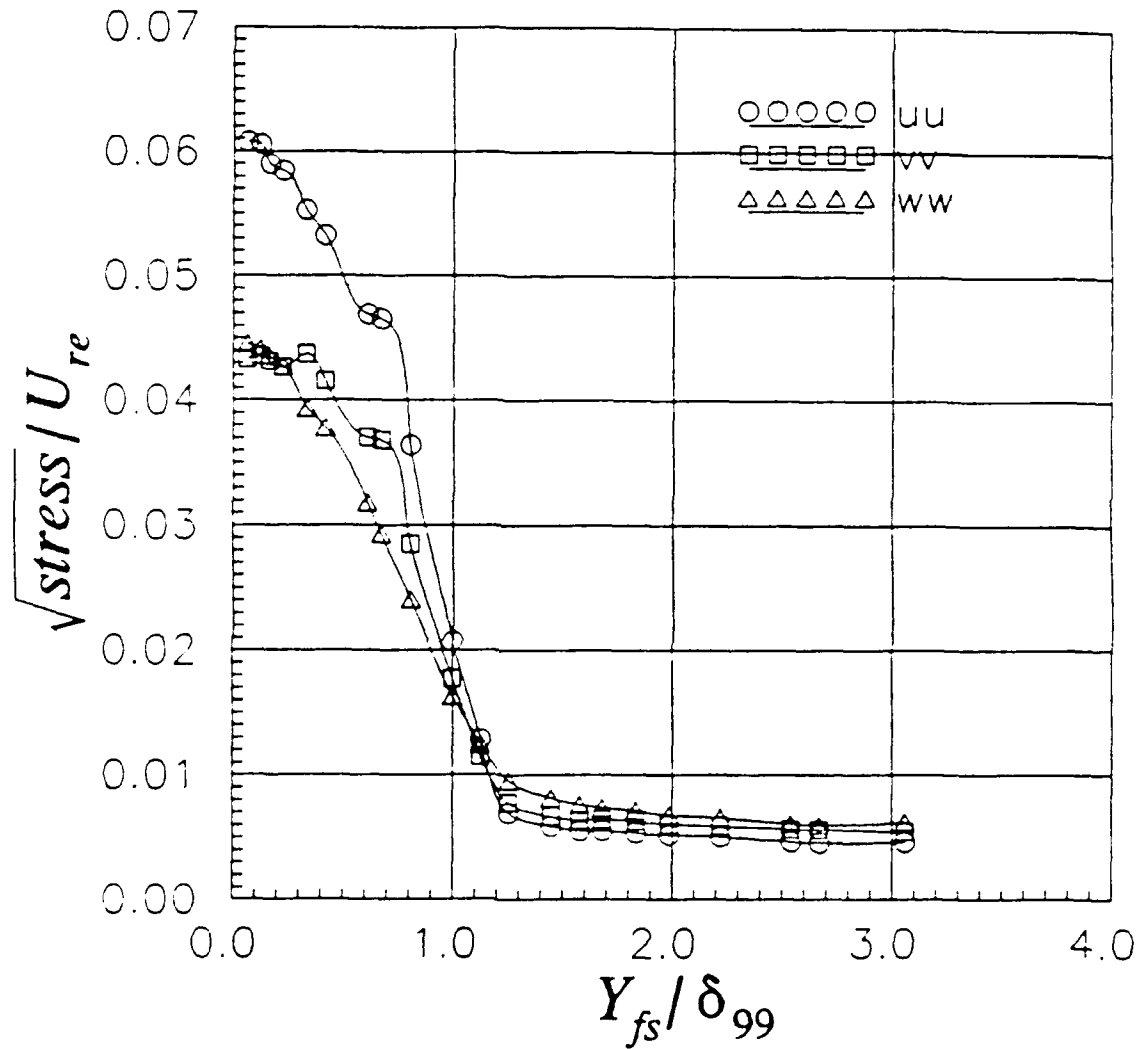
Figure 92. Profiles of Reynolds Normal Stresses with respect to $Y_{fs}/\delta_{99}$. $\varphi = 60°$, $X/L = 0.7$, $Re = 4.0 \times 10^6$, $\alpha = 10°$, Local Free-Stream Coordinates.
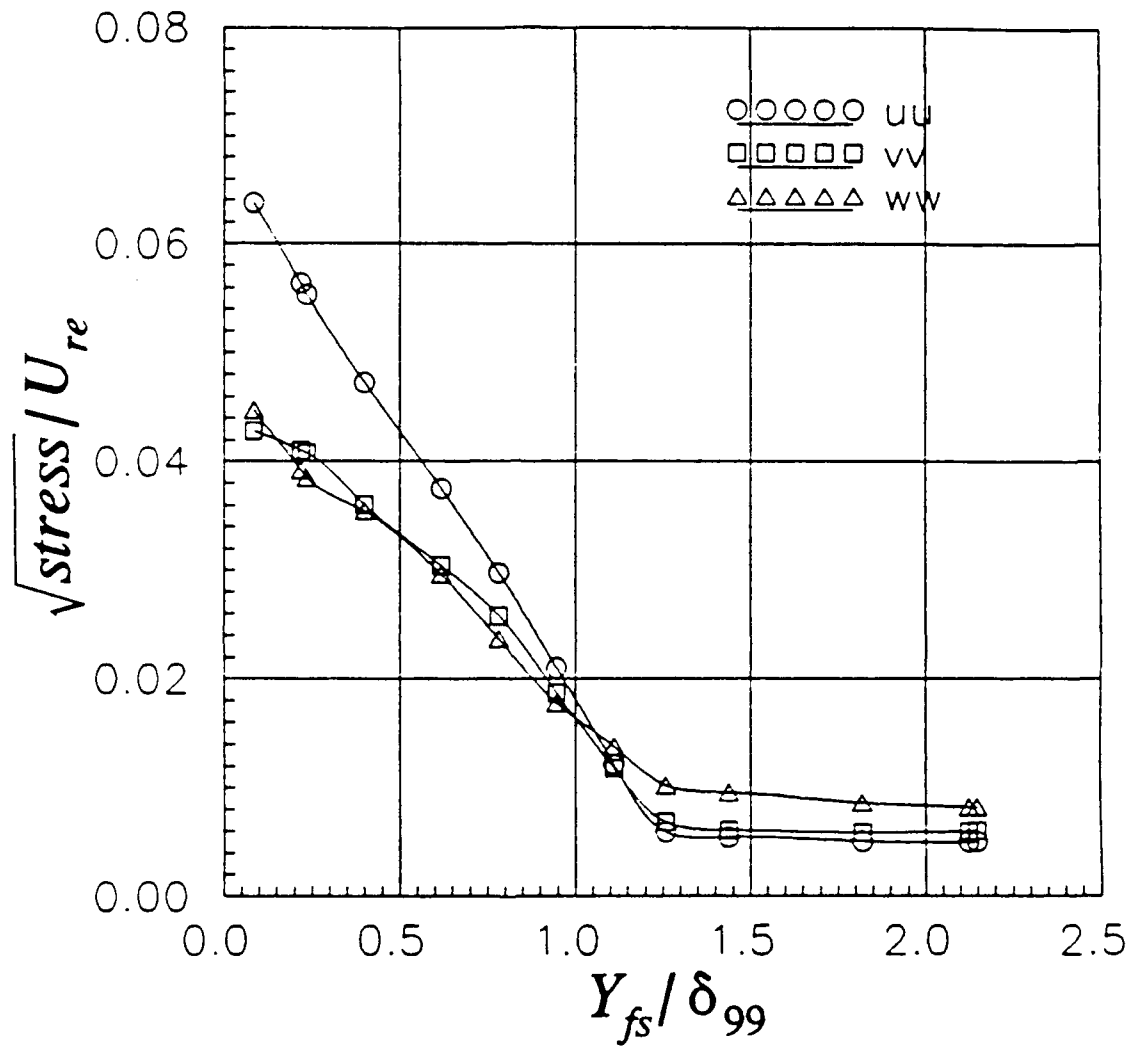
Figure 93. Profiles of Reynolds Normal Stresses with respect to $Y_{fs}/\delta_{99}$, $\varphi=70°$, $X/L=0.7$, $Re=4.0\times10^6$, $\alpha=10°$, Local Free-Stream Coordinates.
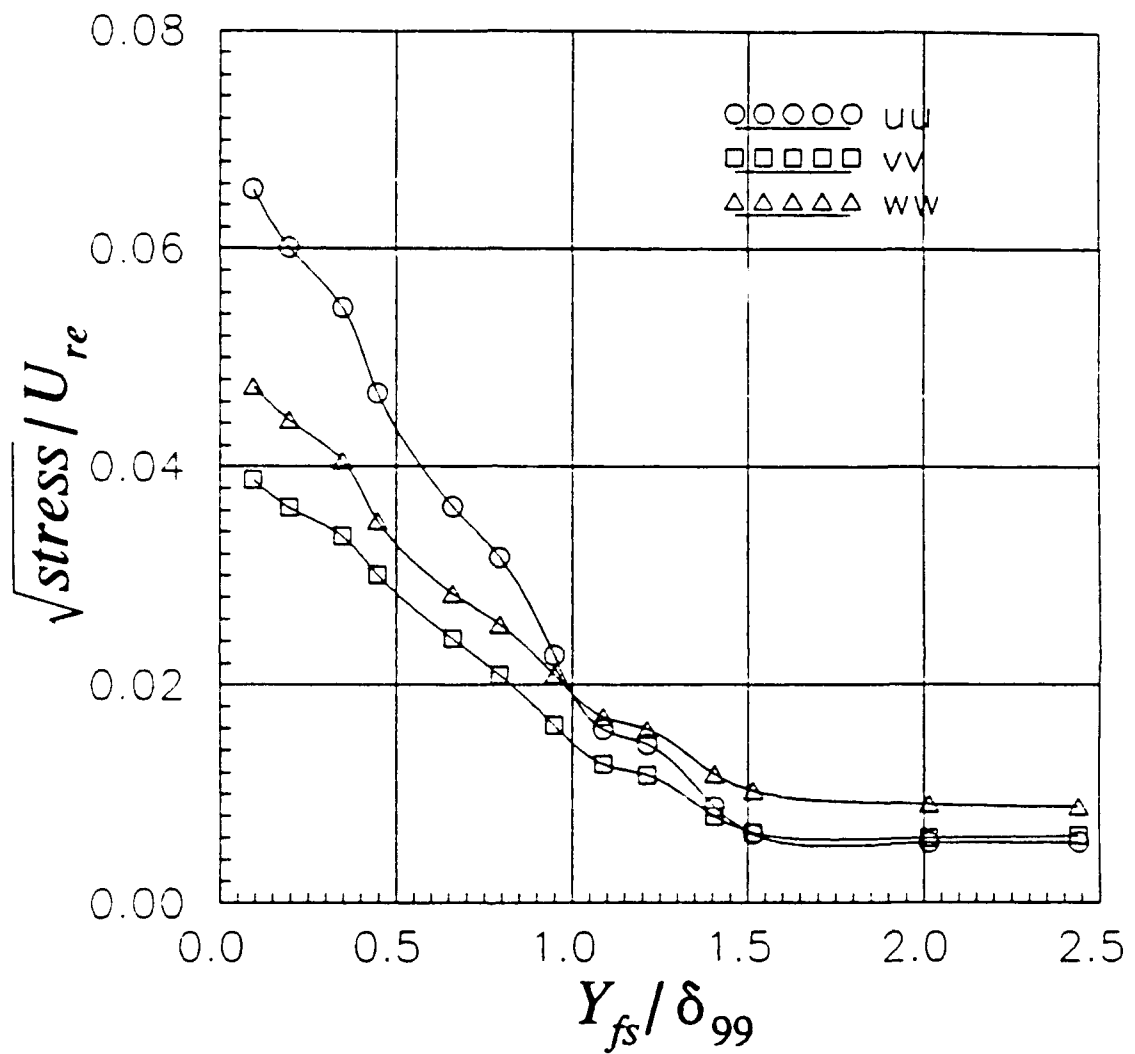
Figure 94.    Profiles of Reynolds Normal Stresses with respect to $Y_{fs}/\delta_{99}$, $\varphi = 80°$, $X/L = 0.7$, $Re = 4.0 \times 10^6$, $\alpha = 10°$, Local Free-Stream Coordinates.
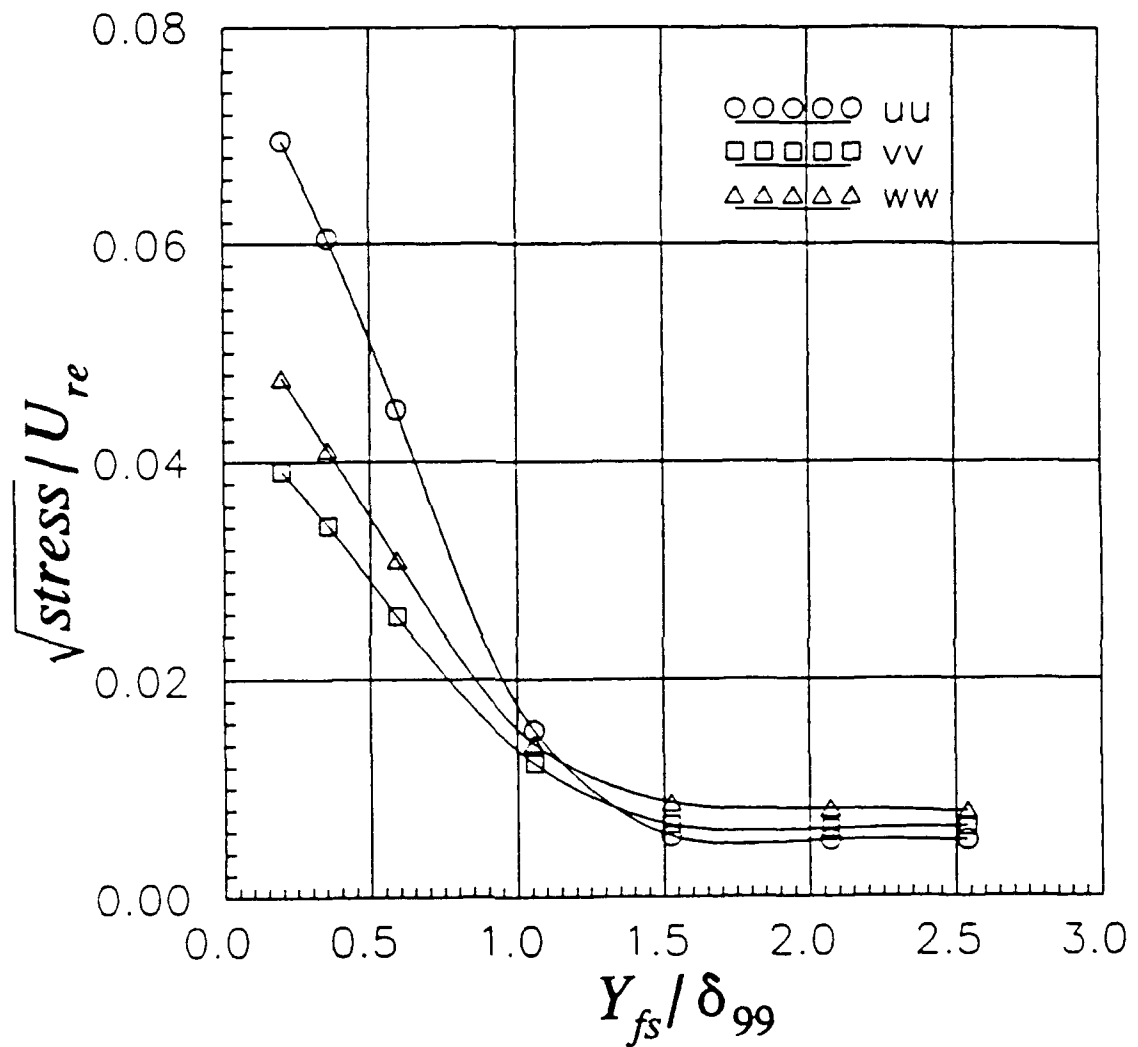
Figure 95.    Profiles of Reynolds Normal Stresses with respect to $Y_{fs}/\delta_{99}$, $\varphi=90°$, $X/L=0.7$, $Re=4.0\times10^6$, $\alpha=10°$, Local Free-Stream Coordinates.
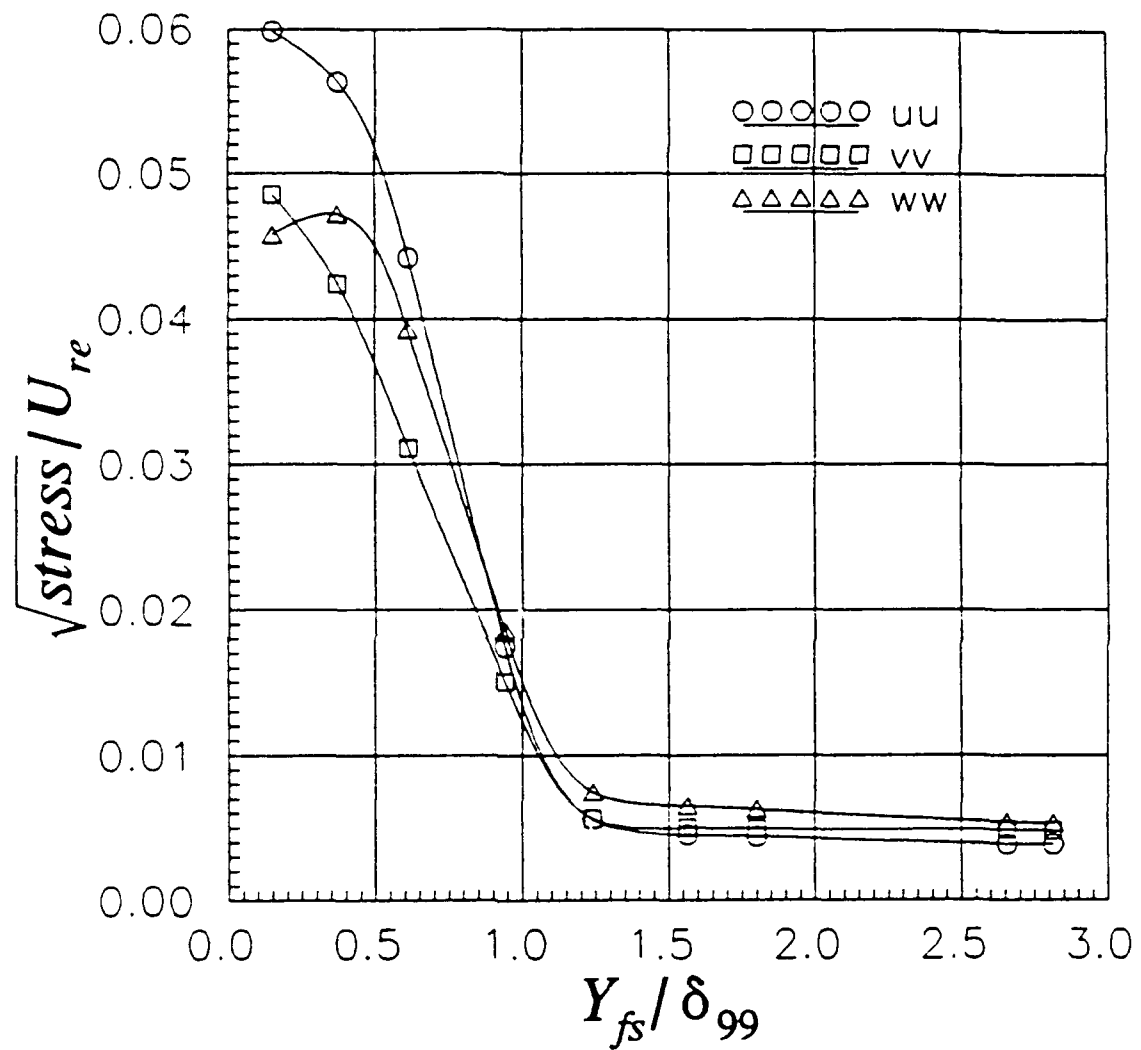
Figure 96.    Profiles of Reynolds Normal Stresses with respect to $Y_{fs}/\delta_{99}$, $\varphi=20°$, X/L=0.8, Re=4.0×10$^6$, $\alpha=10°$, Local Free-Stream Coordinates.
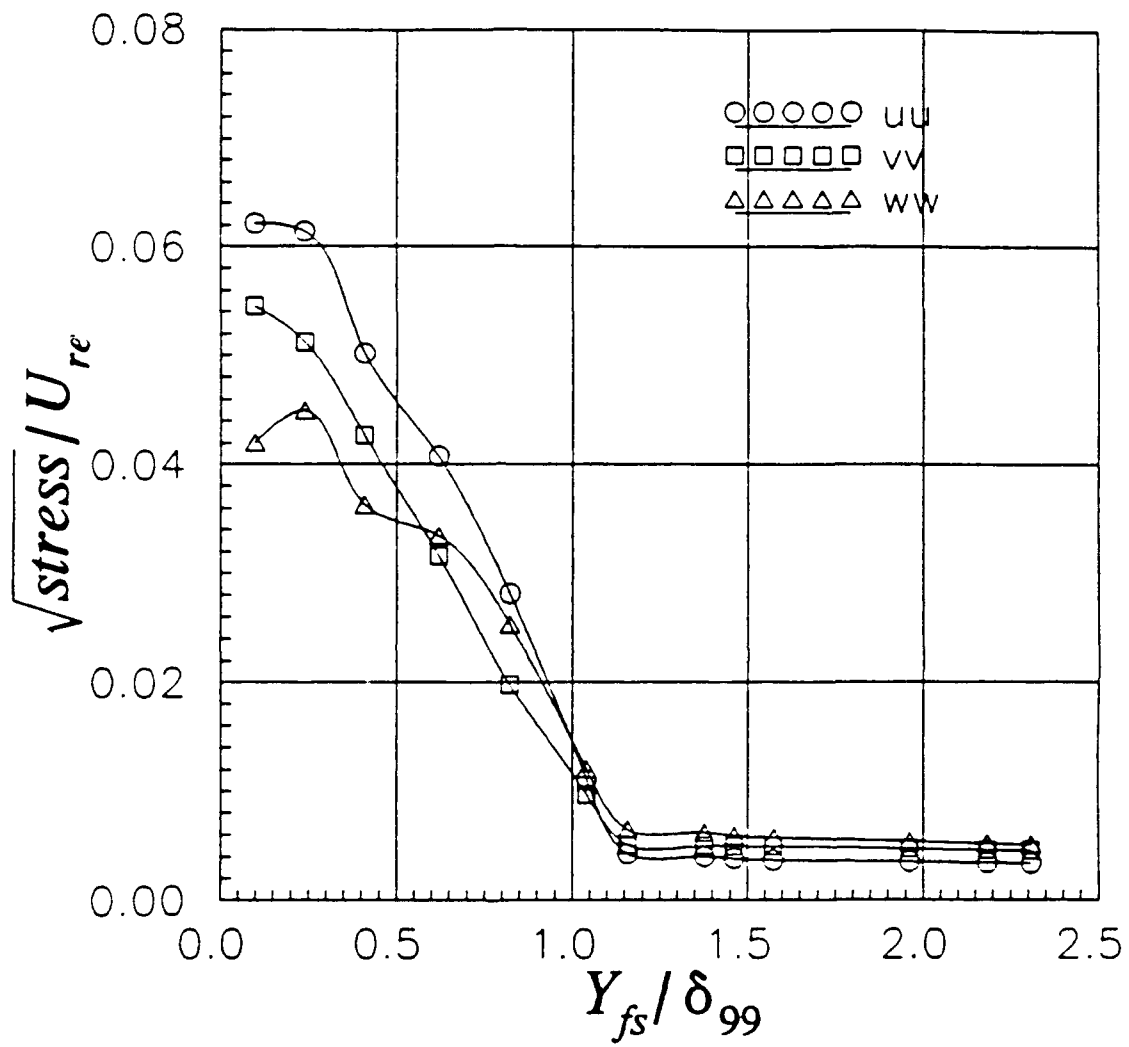
Figure 97.     Profiles of Reynolds Normal Stresses with respect to $Y_{fs}/\delta_{99}$, $\varphi=30°$, $X/L=0.8$, $Re=4.0\times10^6$, $\alpha=10°$, Local Free-Stream Coordinates.
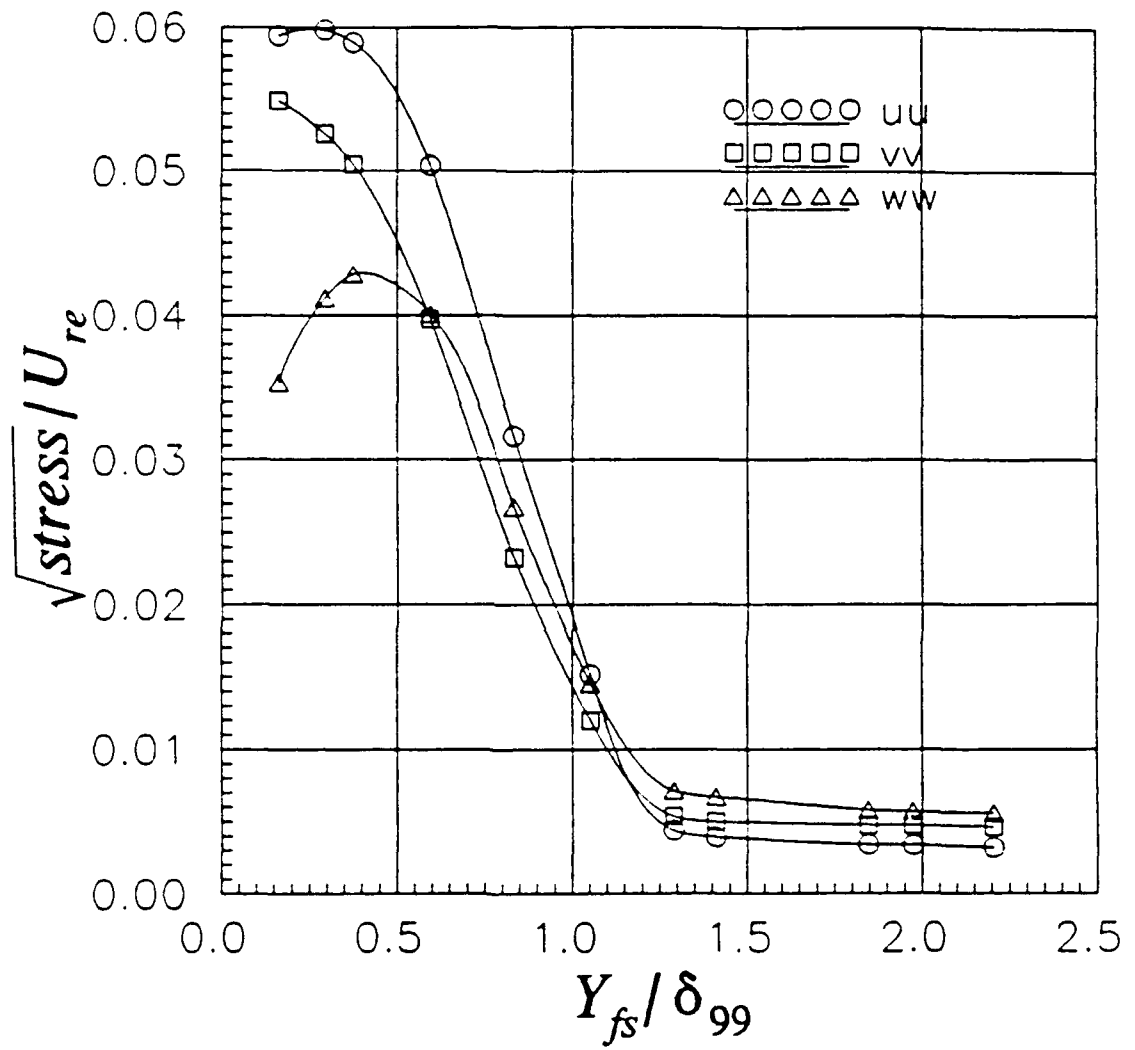
Figure 98. Profiles of Reynolds Normal Stresses with respect to $Y_{fs}/\delta_{99}$, $\varphi=40°$, $X/L=0.8$, $Re=4.0\times10^6$, $\alpha=10°$, Local Free-Stream Coordinates.
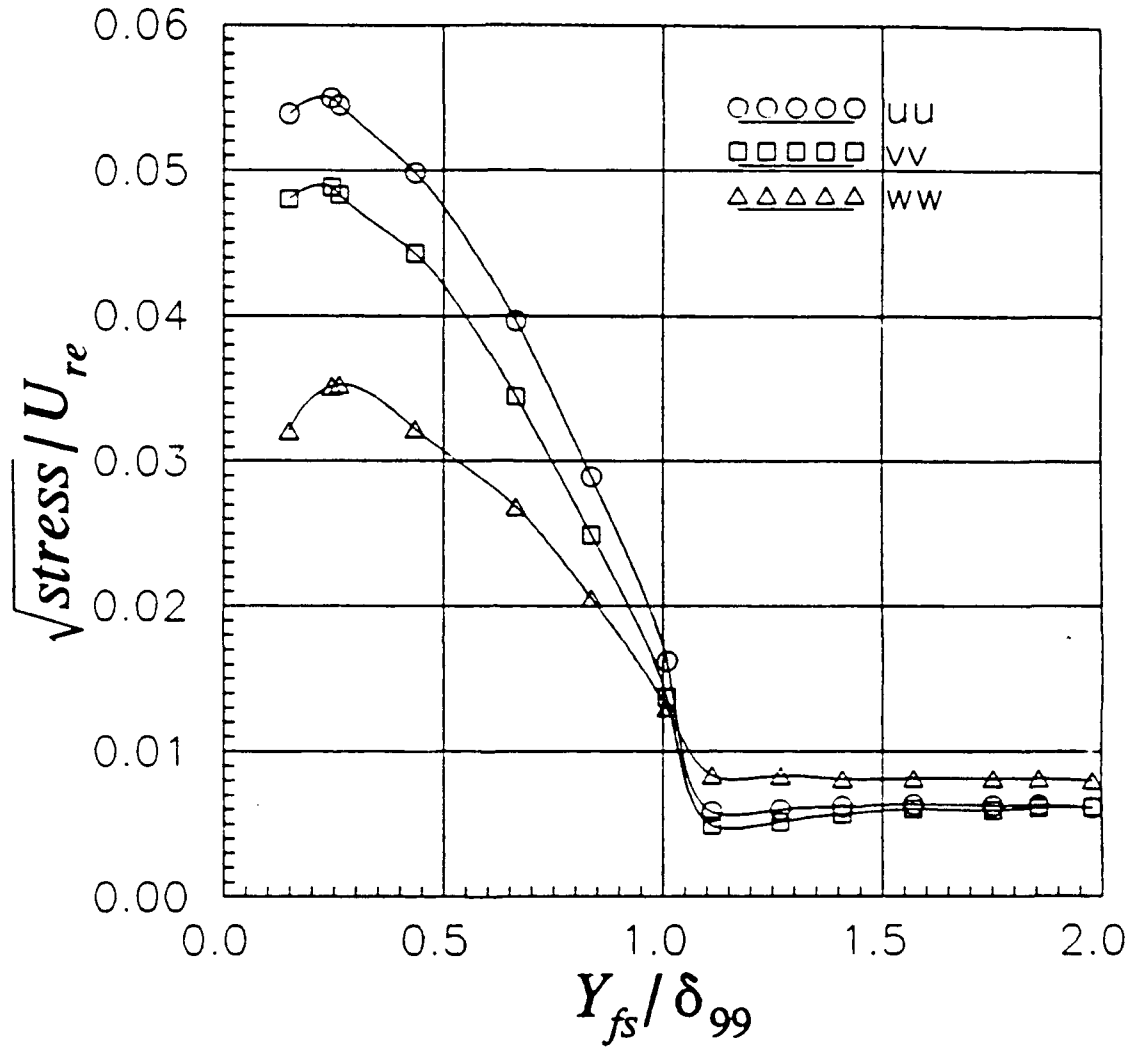
Figure 99. Profiles of Reynolds Normal Stresses with respect to $Y_{fs}/\delta_{99}$, $\varphi=50°$, X/L=0.8, Re=$4.0\times10^6$, $\alpha=10°$, Local Free-Stream Coordinates.
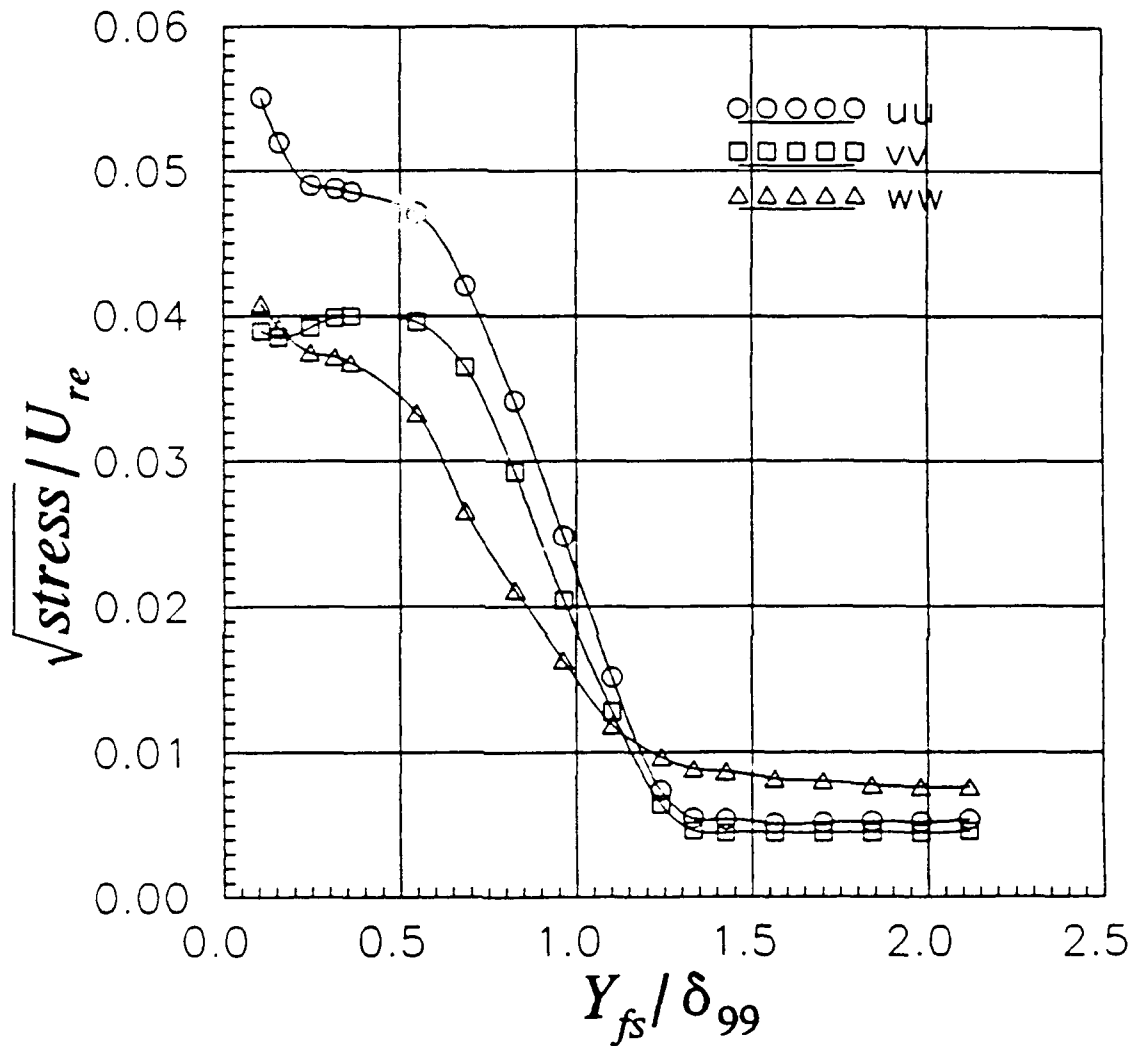
Figure 100. Profiles of Reynolds Normal Stresses with respect to $Y_{fs}/\delta_{99}$, $\varphi = 60°$, $X/L = 0.8$, $Re = 4.0 \times 10^6$, $\alpha = 10°$, Local Free-Stream Coordinates.
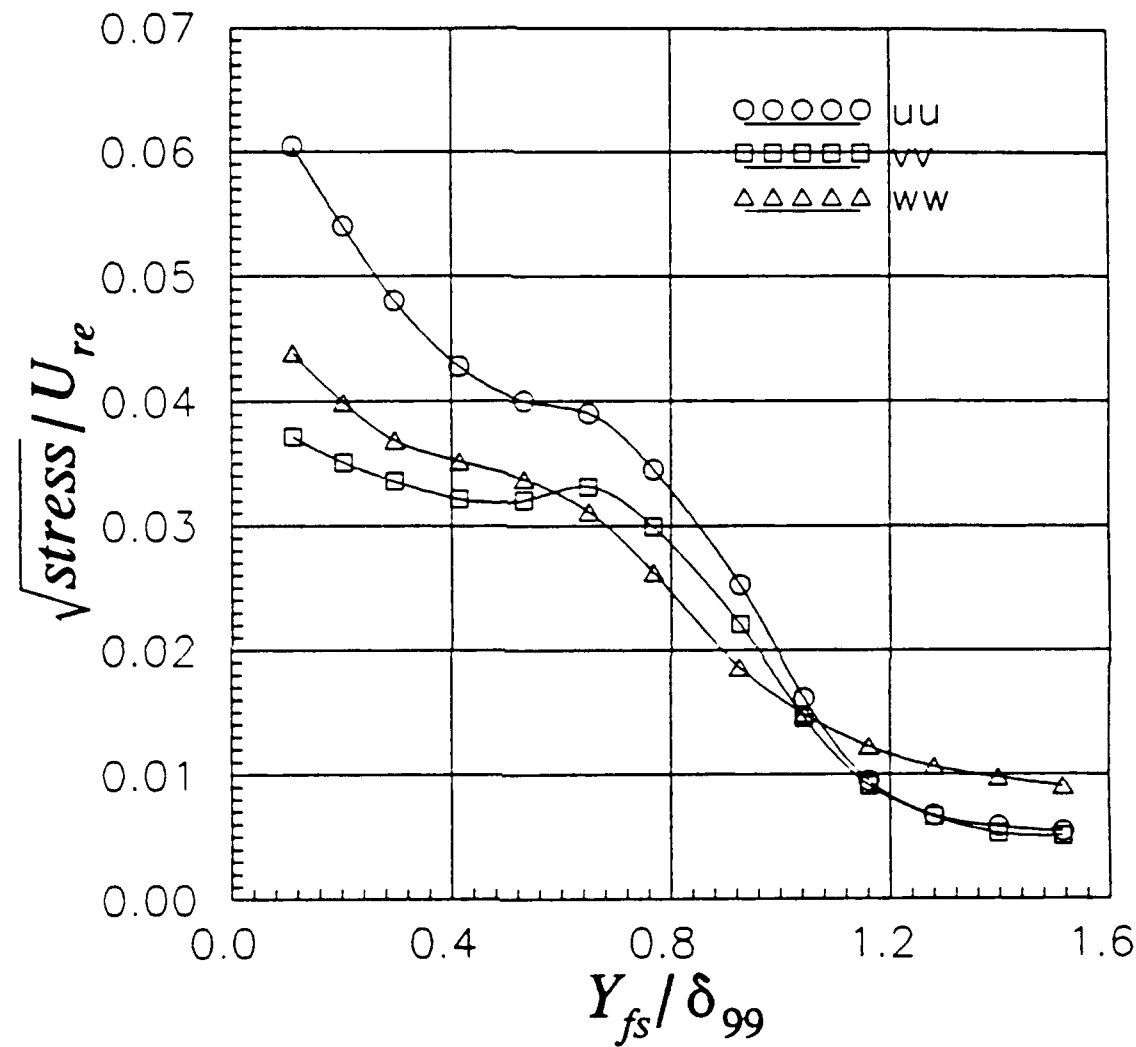
Figure 101. Profiles of Reynolds Normal Stresses with respect to $Y_{fs}/\delta_{99}$, $\varphi = 70°$, $X/L = 0.8$, $Re = 4.0 \times 10^6$, $\alpha = 10°$, Local Free-Stream Coordinates.
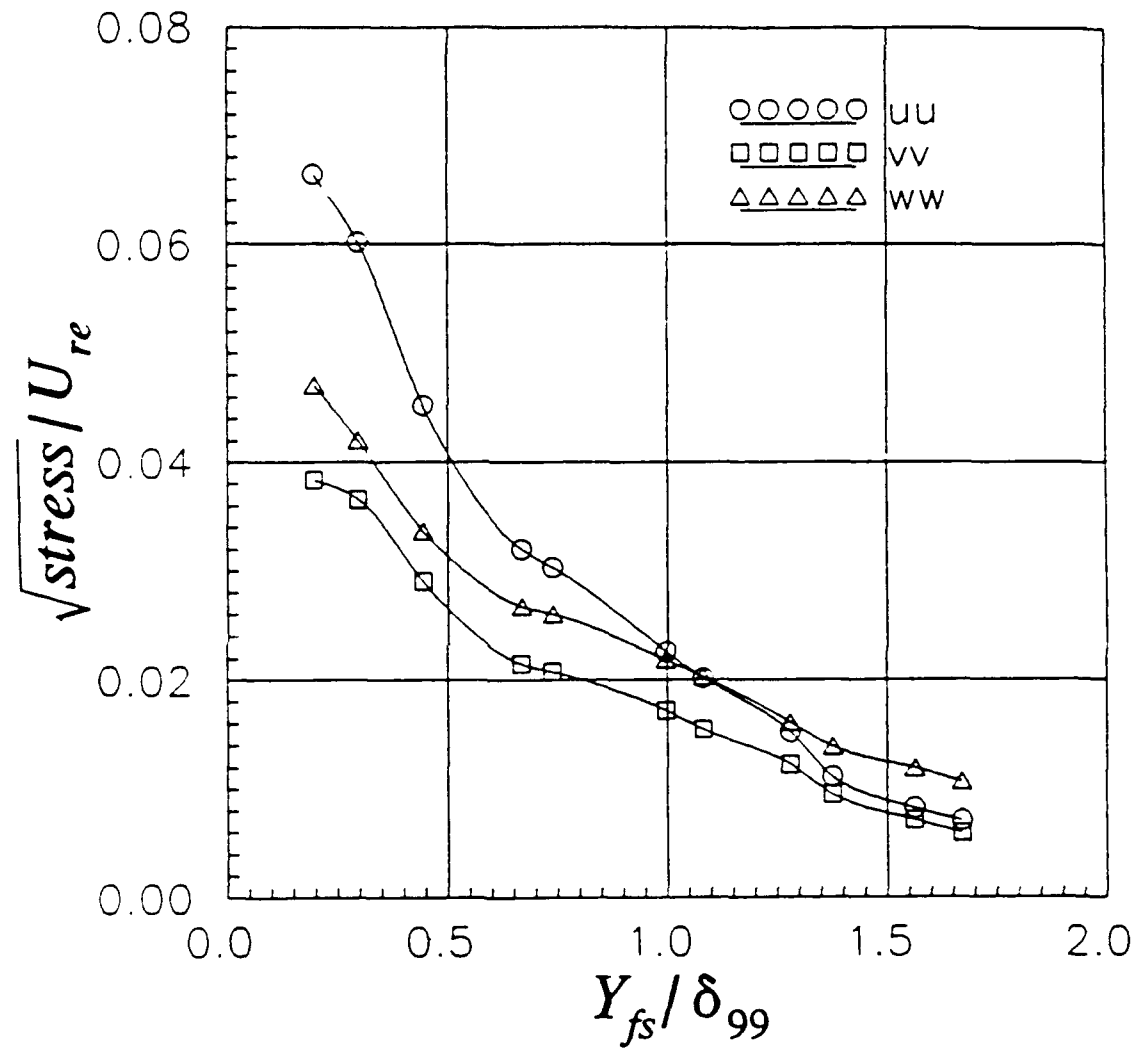
Figure 102.    Profiles of Reynolds Normal Stresses with respect to $Y_{fs}/\delta_{99}$, $\varphi = 80°$, $X/L = 0.8$, $Re = 4.0 \times 10^6$, $\alpha = 10°$, Local Free-Stream Coordinates.
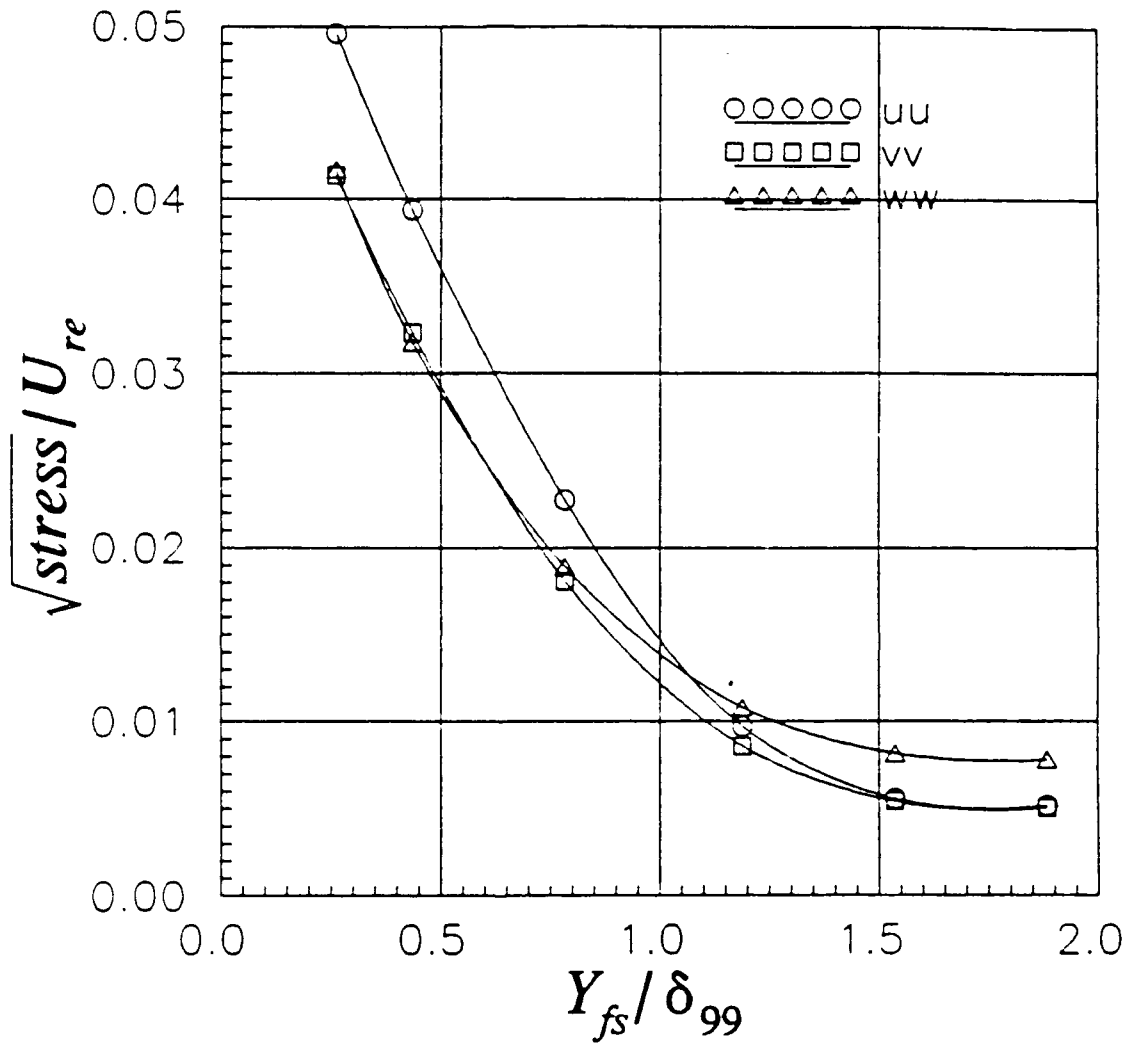
Figure 103. Profiles of Reynolds Normal Stresses with respect to $Y_{fs}/\delta_{99}$, $\varphi=90°$, X/L=0.8, Re=4.0×10^6, $\alpha=10°$, Local Free-Stream Coordinates.
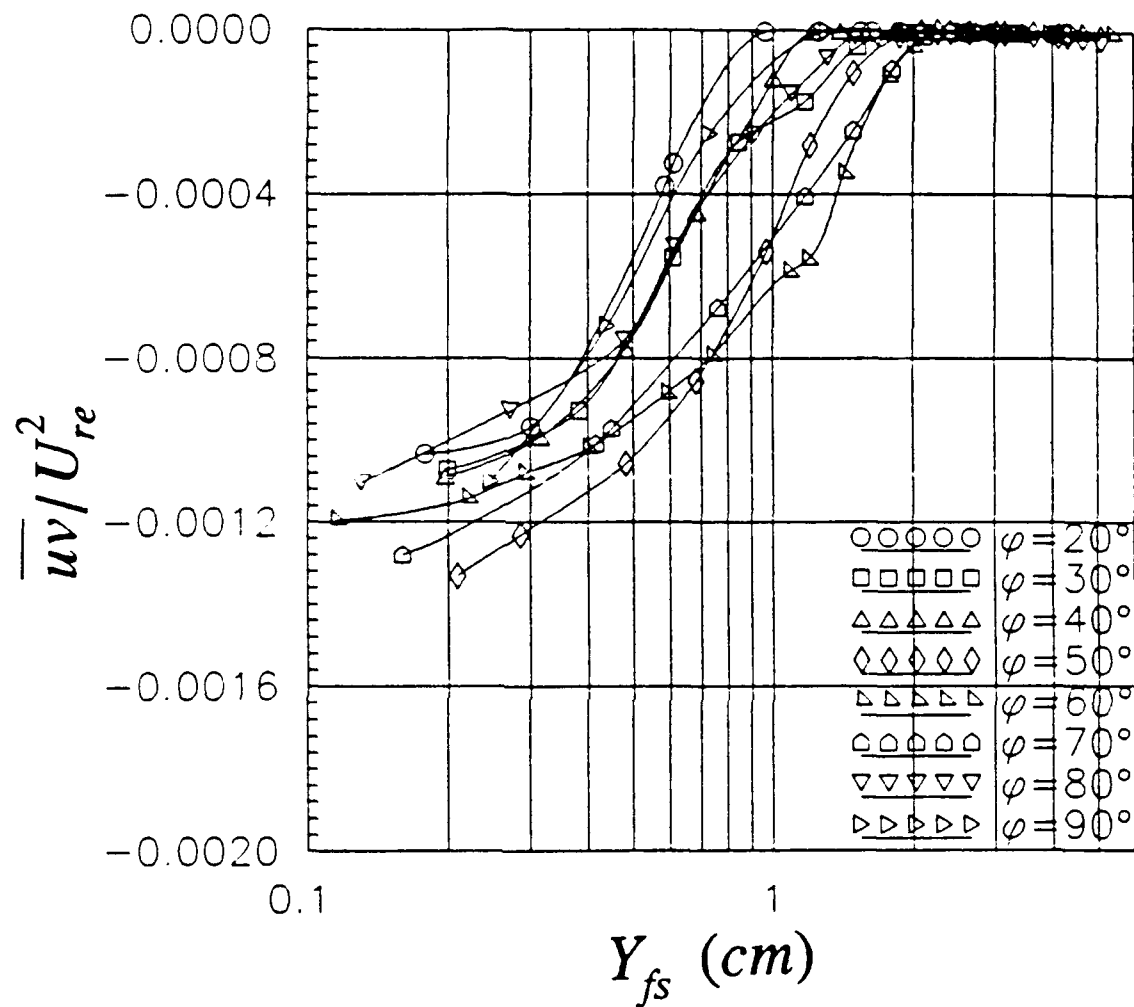
Figure 104. Profiles of $\overline{uv}$ Reynolds Stresses, X/L=0.7, Re=4.0×10⁶, α=10°, Local Free-Stream Coordinates.
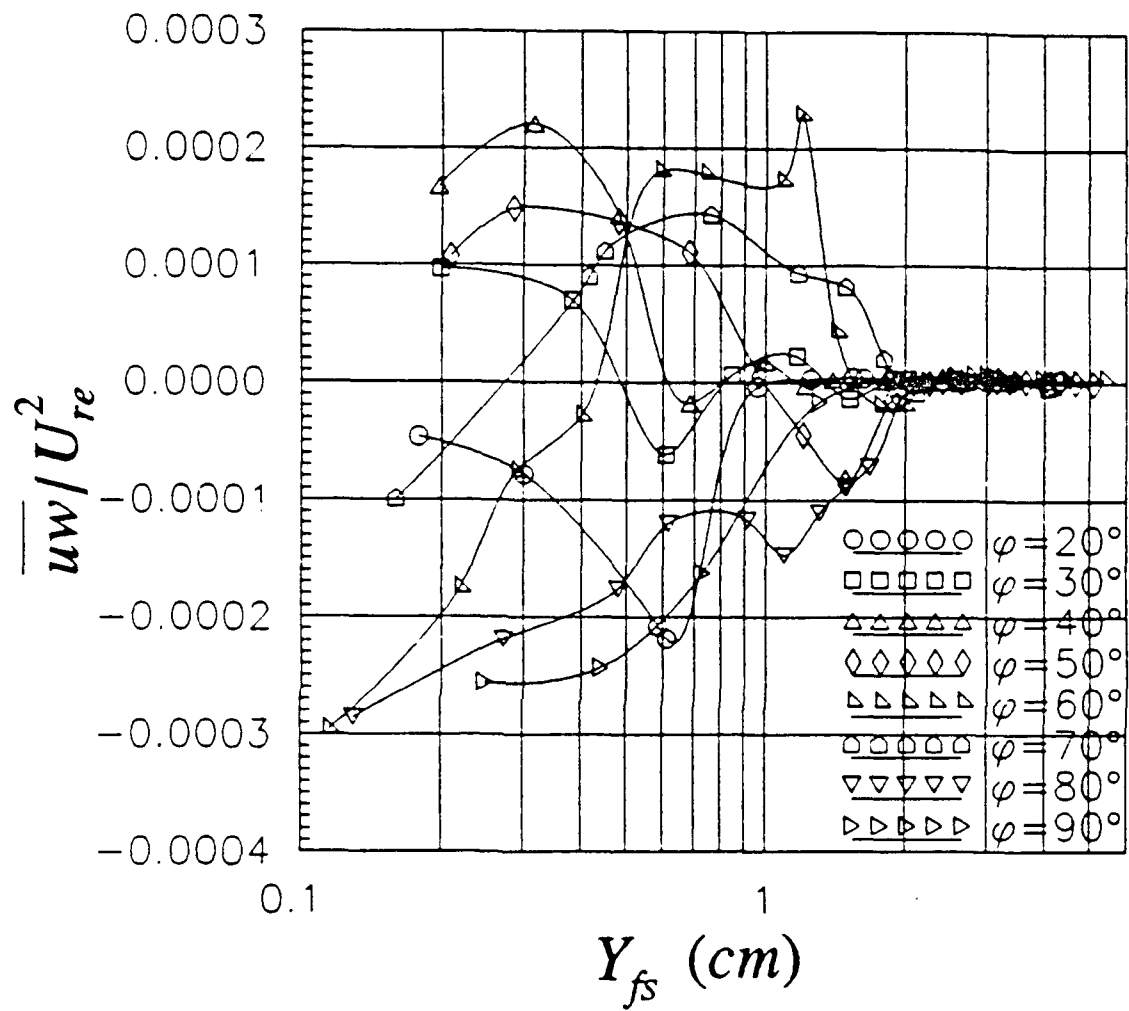
Figure 105.   Profiles of  $\overline{uw}$   Reynolds Stresses,  X/L=0.7,  Re=4.0×10⁶,  α=10°,
Local Free-Stream Coordinates.
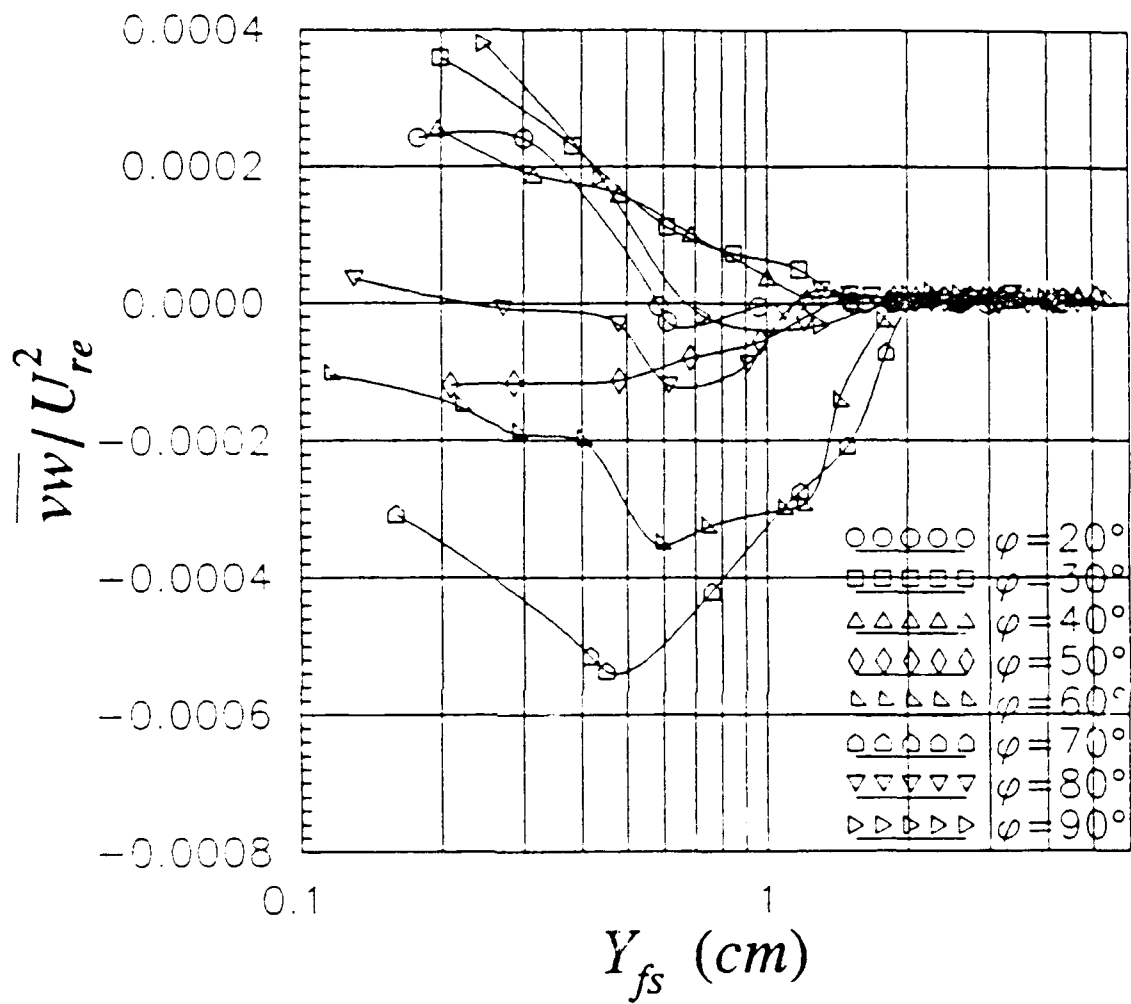
Figure 106. Profiles of $\overline{vw}$ Reynolds Stresses, X/L=0.7, Re=4.0×10⁶, α=10°, Local Free-Stream Coordinates.
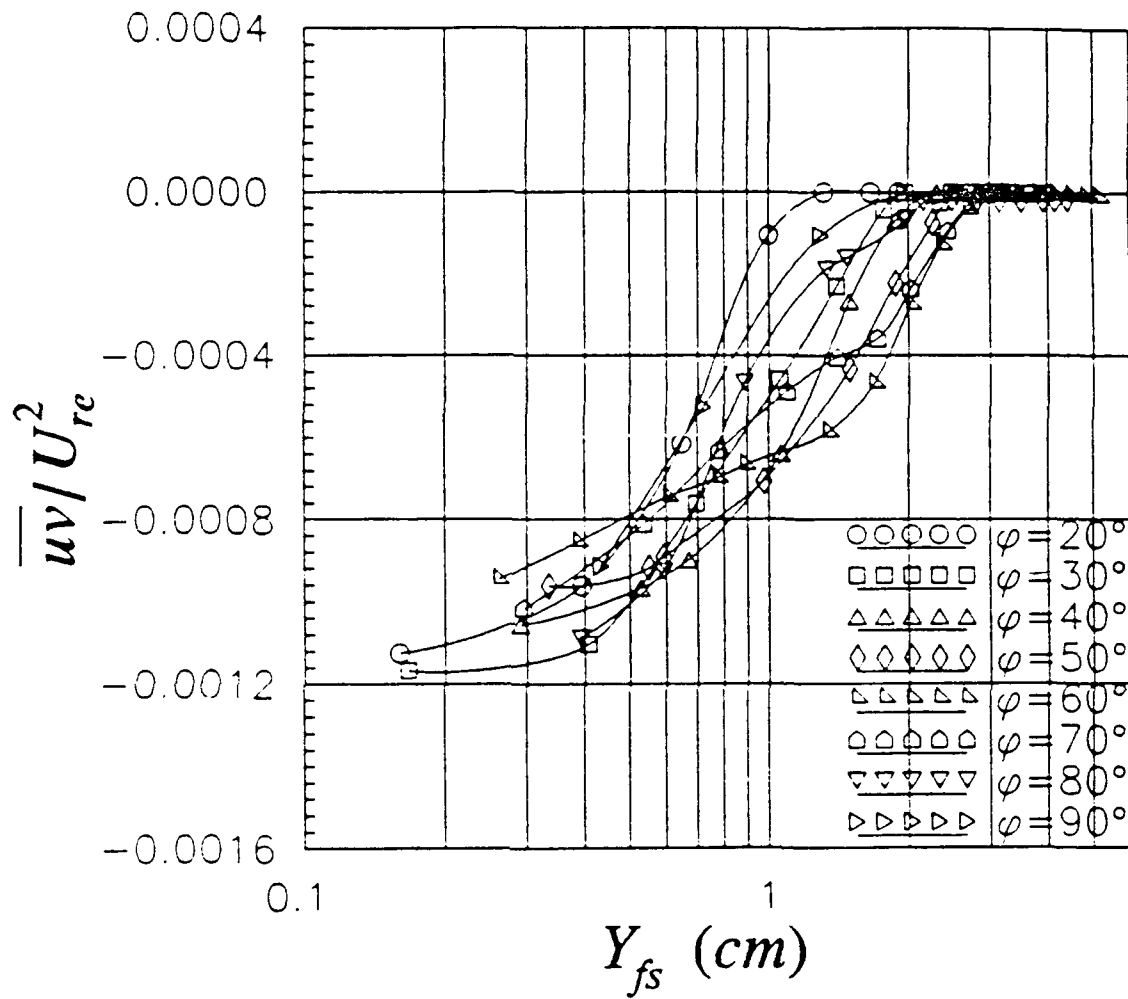
Figure 107. Profiles of $\overline{uv}$ Reynolds Stresses, X/L=0.8, Re=4.0×10⁶, α=10°, Local Free-Stream Coordinates.
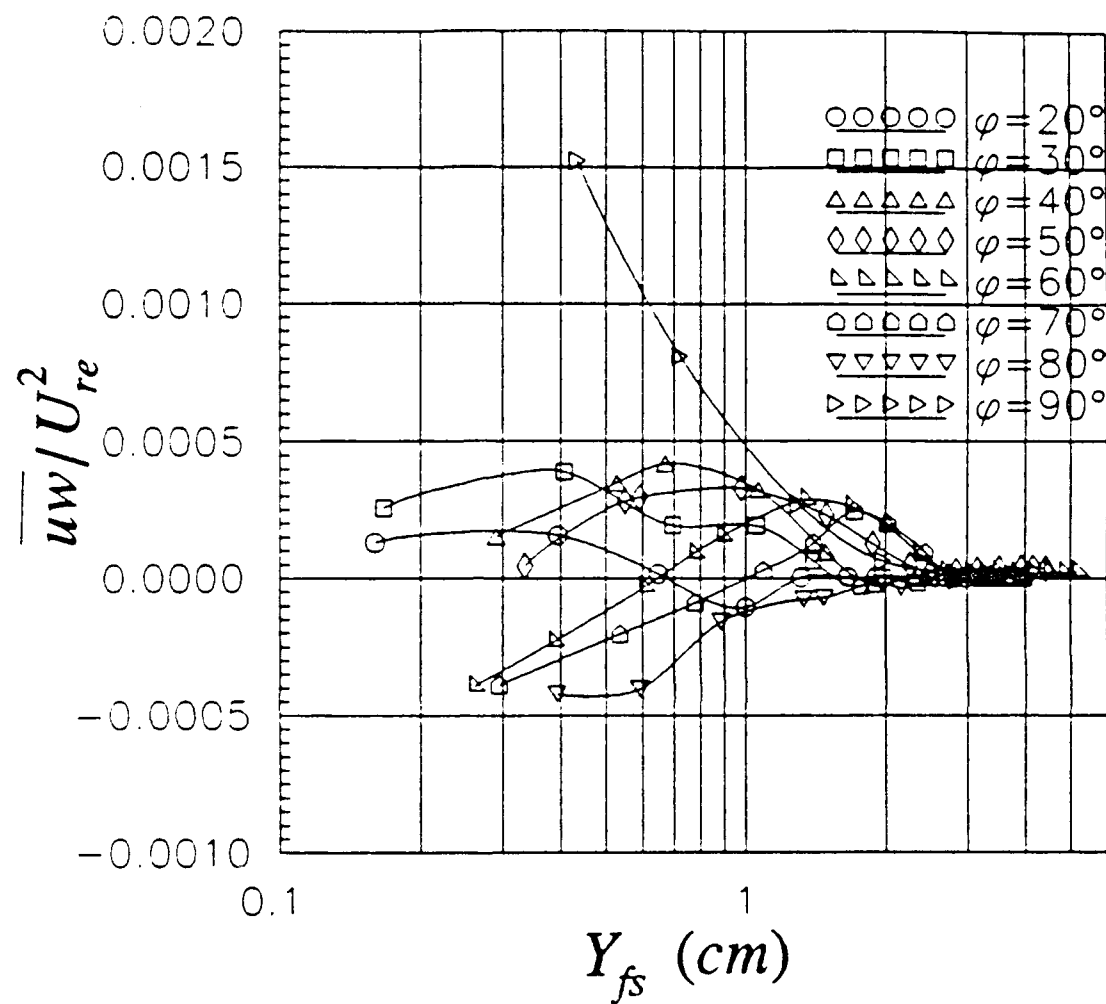
Figure 108. Profiles of $\overline{uw}$ Reynolds Stresses, X/L=0.8, Re=4.0×10⁶, α=10°, Local Free-Stream Coordinates.
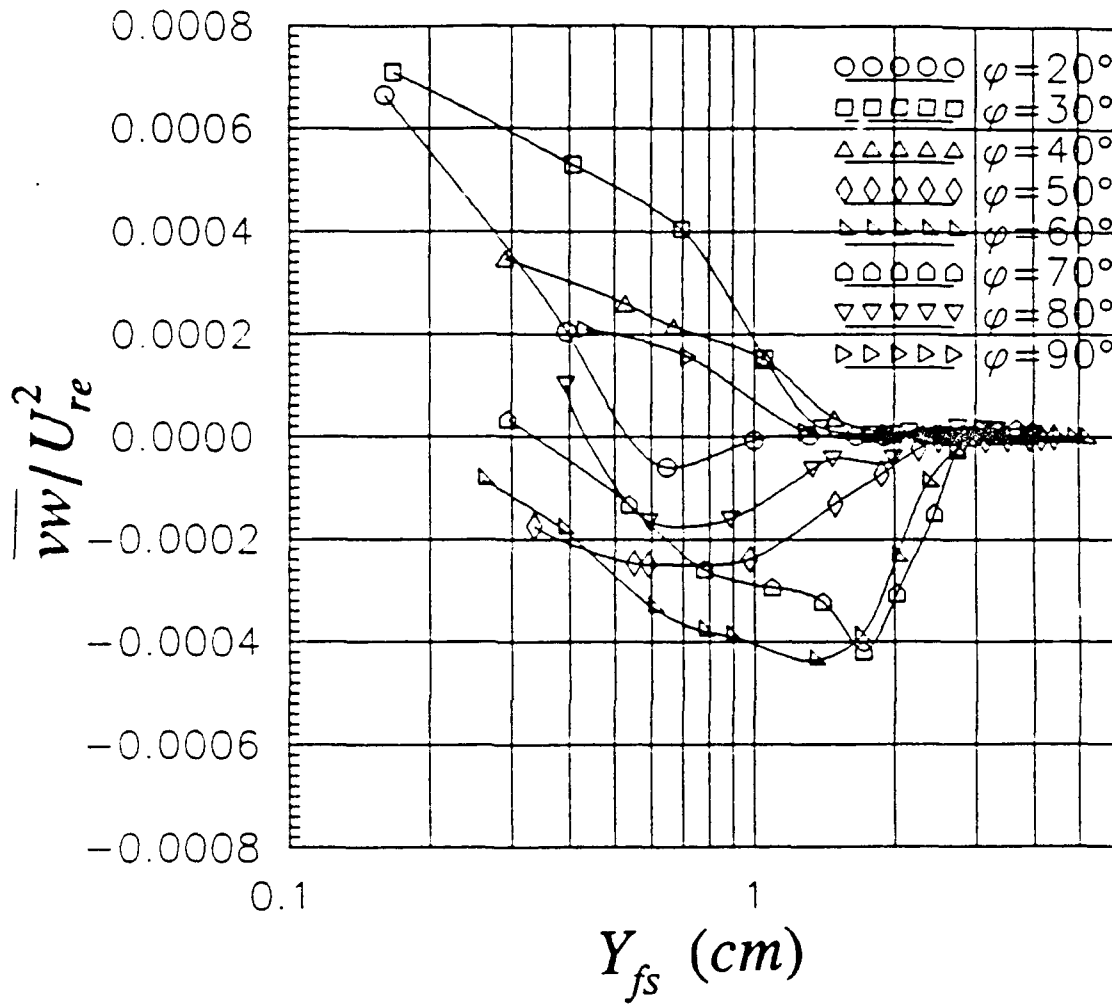
Figure 109.   Profiles of $\overline{vw}$   Reynolds Stresses, X/L=0.8, Re=4.0×10⁶, α=10°, Local Free-Stream Coordinates.
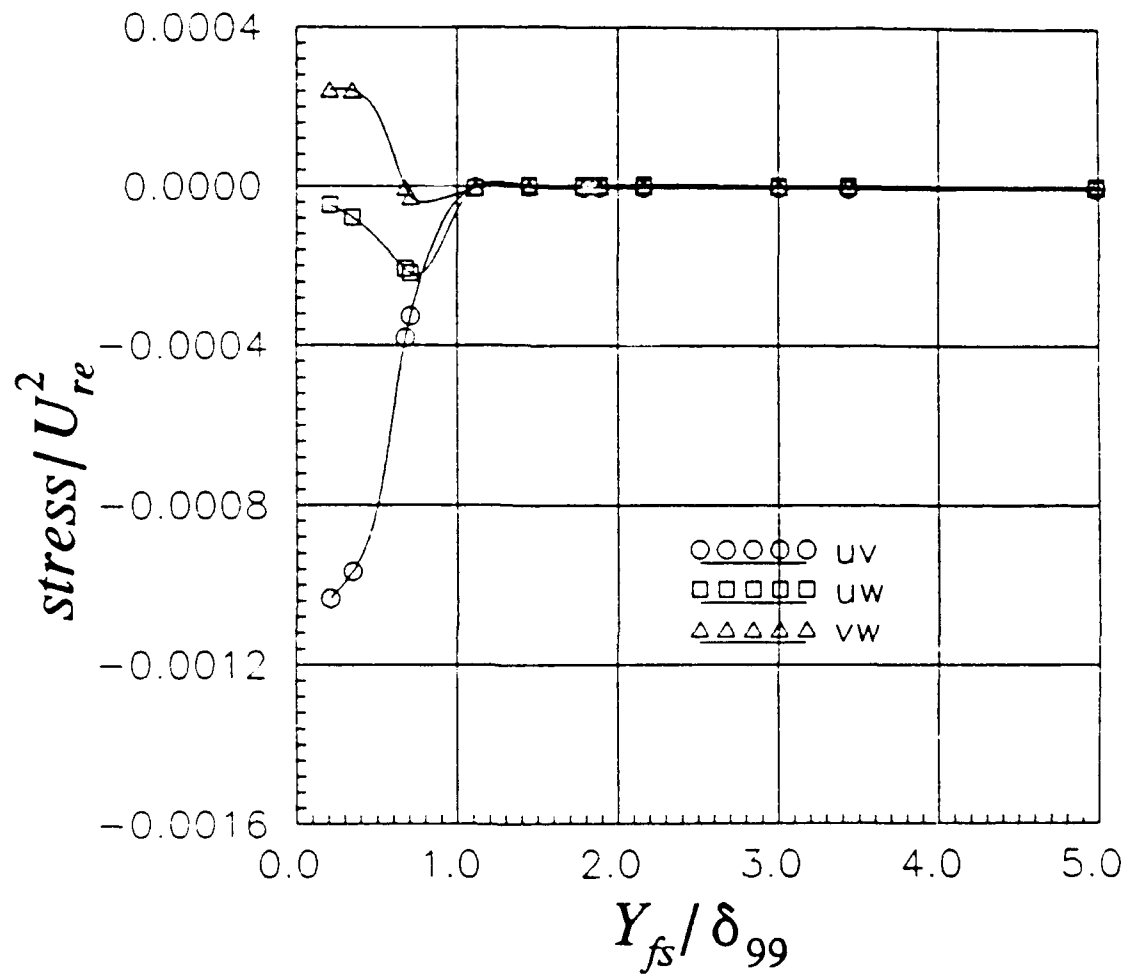
Figure 110. Profiles of Reynolds Shear Stresses with respect to $Y_{fs}/\delta_{99}$, $\varphi=20°$, $X/L=0.7$, $Re=4.0\times10^6$, $\alpha=10°$, Local Free-Stream Coordinates.
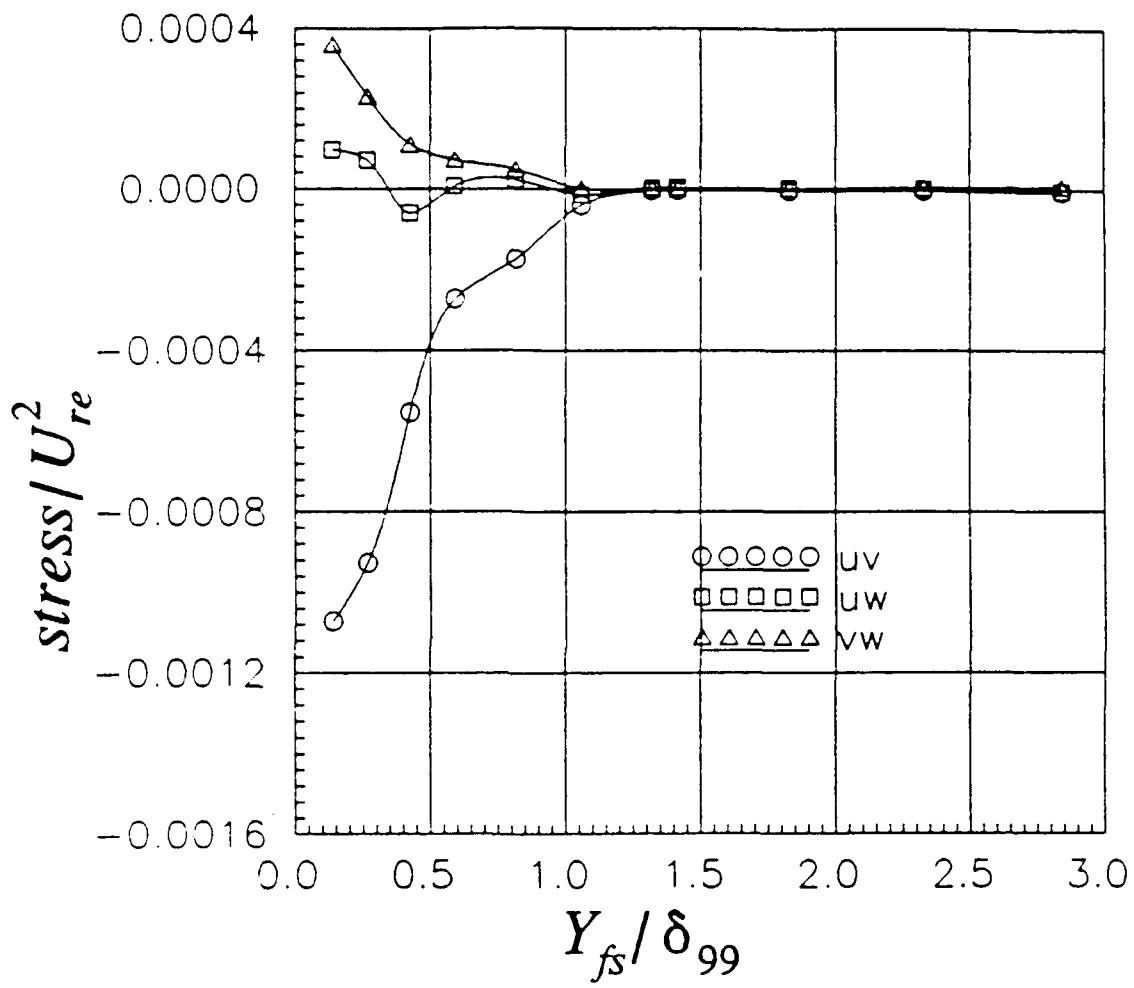
Figure 111. Profiles of Reynolds Shear Stresses with respect to $Y_{fs}/\delta_{99}$, $\varphi=30°$, X/L=0.7, Re=4.0×10$^6$, $\alpha=10°$, Local Free-Stream Coordinates.
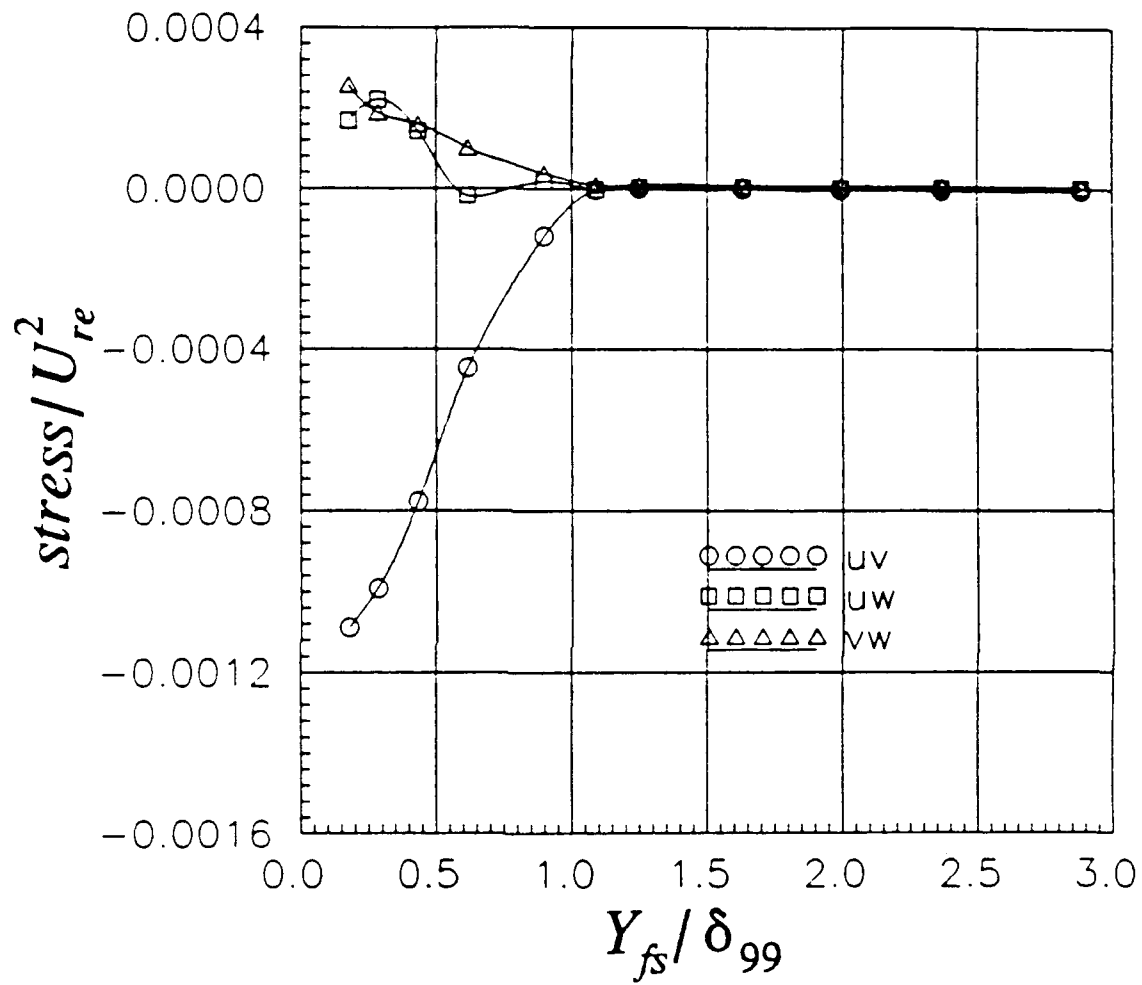
Figure 112.  Profiles of Reynolds Shear Stresses with respect to $Y_{fs}/\delta_{99}$, $\varphi=40°$, $X/L=0.7$, $Re=4.0\times10^6$, $\alpha=10°$, Local Free-Stream Coordinates.
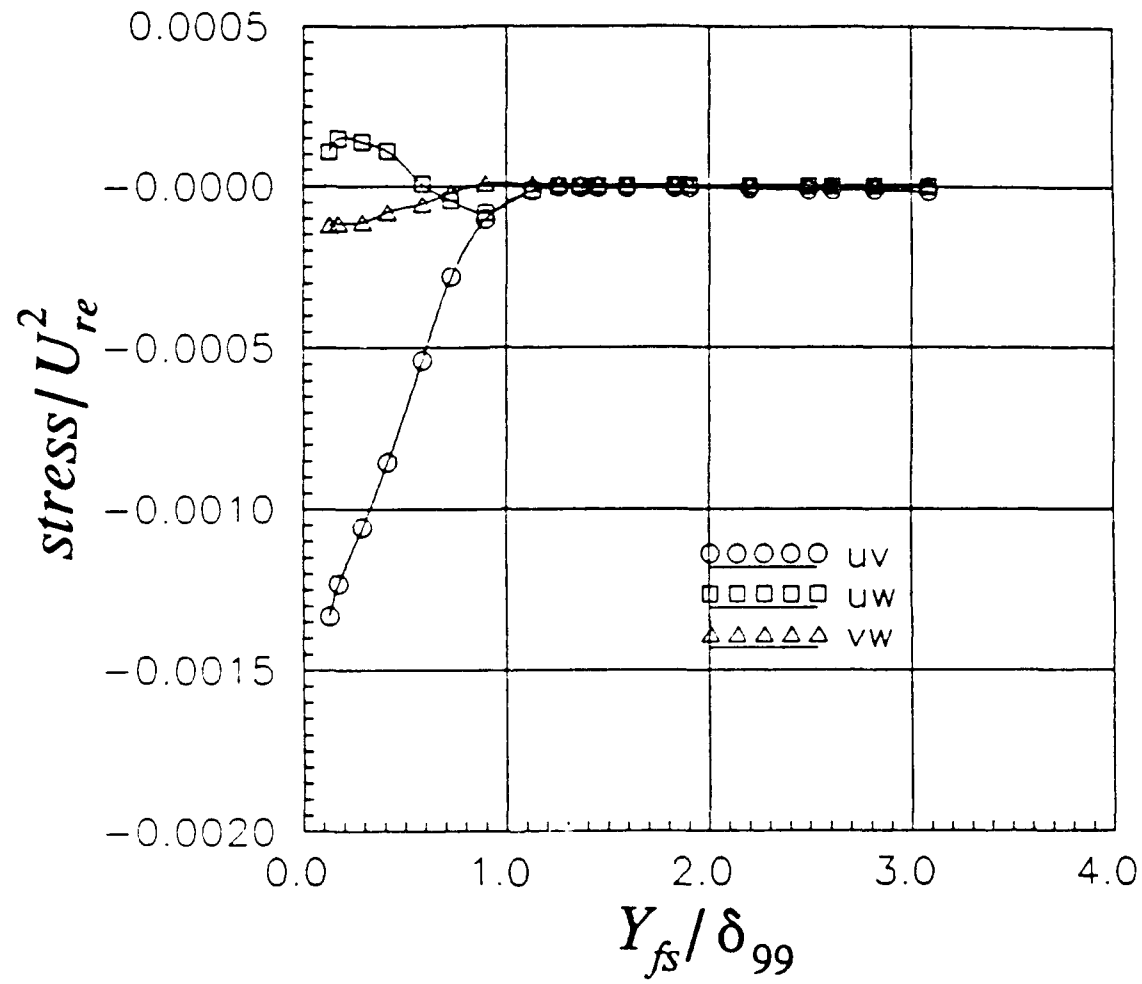
Figure 113. Profiles of Reynolds Shear Stresses with respect to $Y_{fs}/\delta_{99}$, $\varphi=50°$, $X/L=0.7$, $Re=4.0\times10^6$, $\alpha=10°$, Local Free-Stream Coordinates.
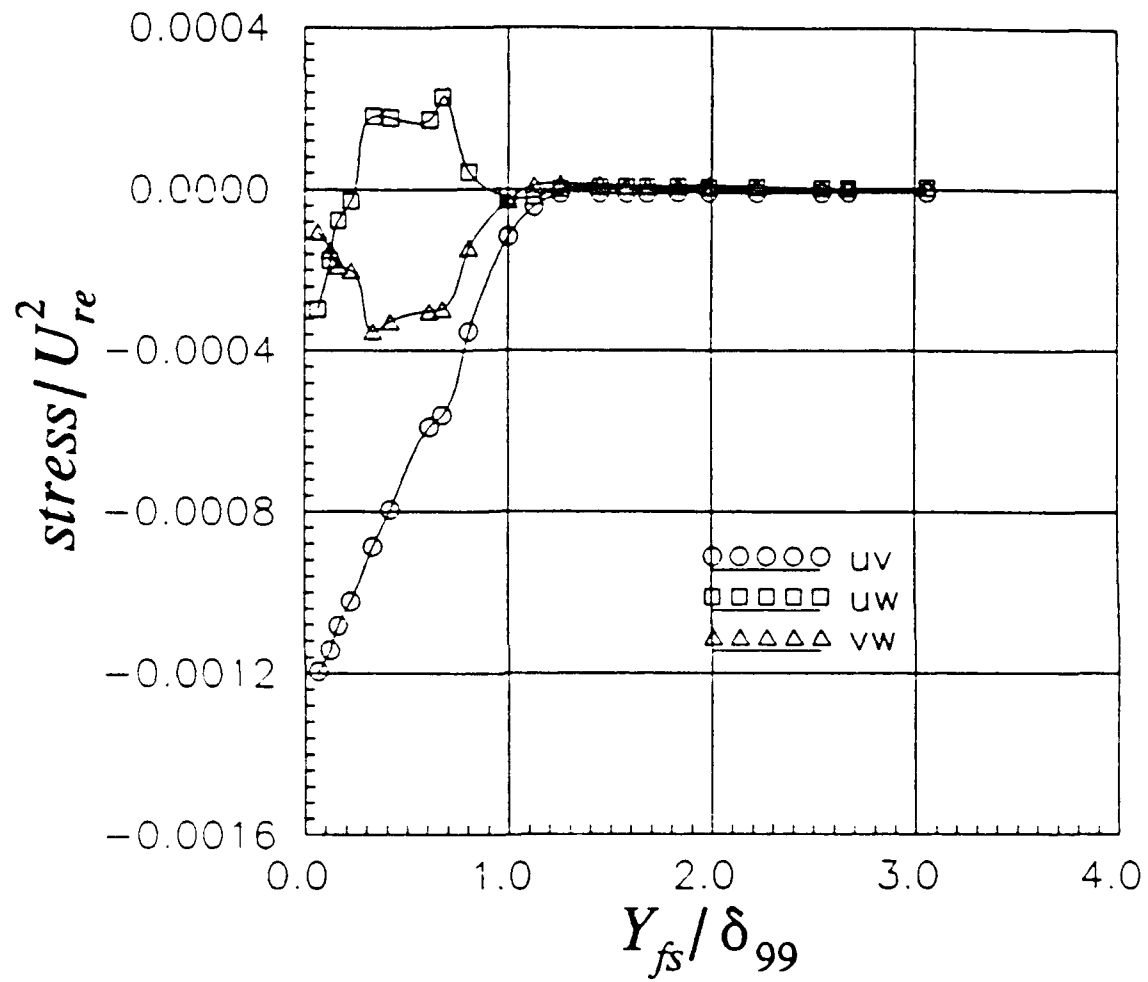
Figure 114.   Profiles of Reynolds Shear Stresses with respect to $Y_{fs}/\delta_{99}$, $\varphi=60°$, $X/L=0.7$, $Re=4.0\times10^6$, $\alpha=10°$, Local Free-Stream Coordinates.
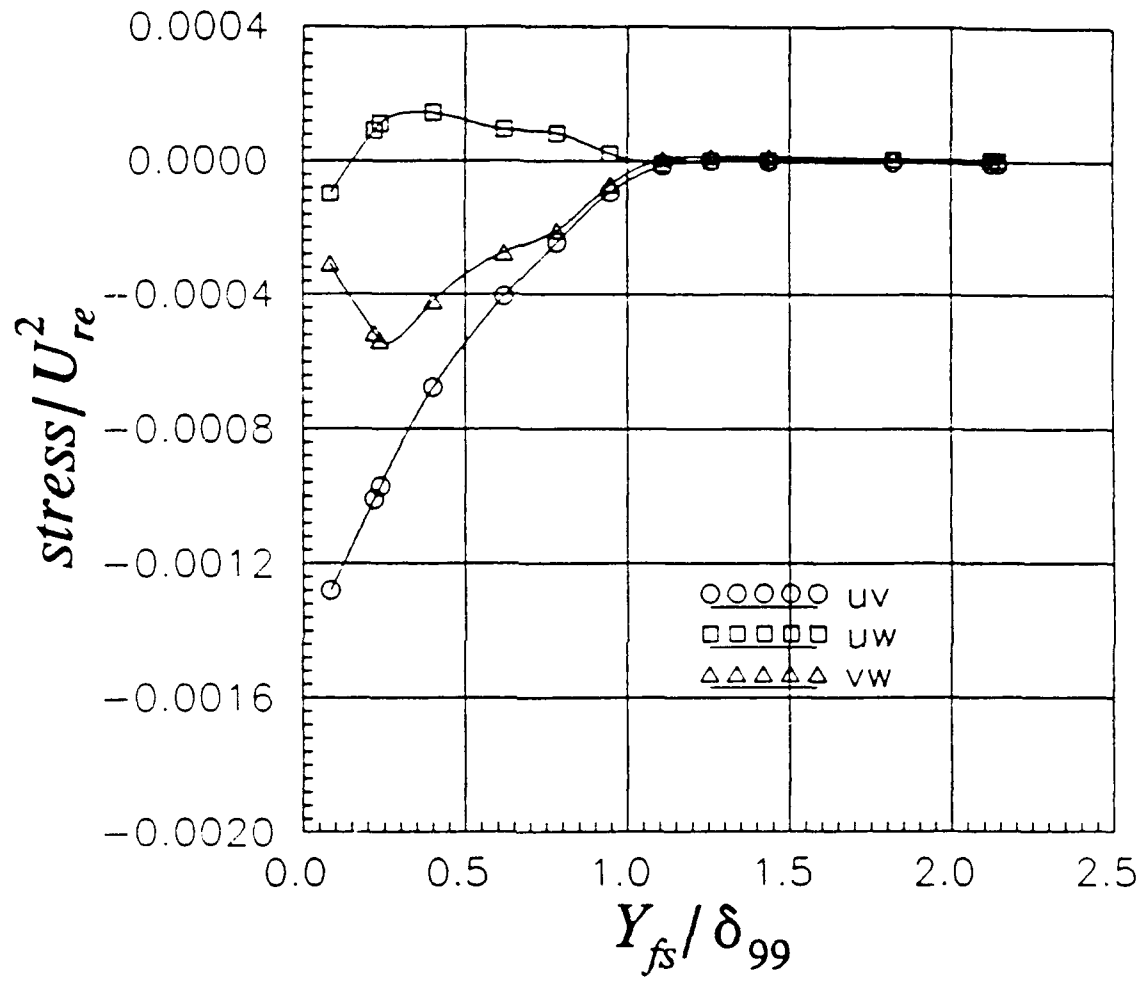
Figure 115. Profiles of Reynolds Shear Stresses with respect to $Y_{fs}/\delta_{99}$, $\varphi = 70°$, $X/L = 0.7$, $Re = 4.0 \times 10^6$, $\alpha = 10°$, Local Free-Stream Coordinates.
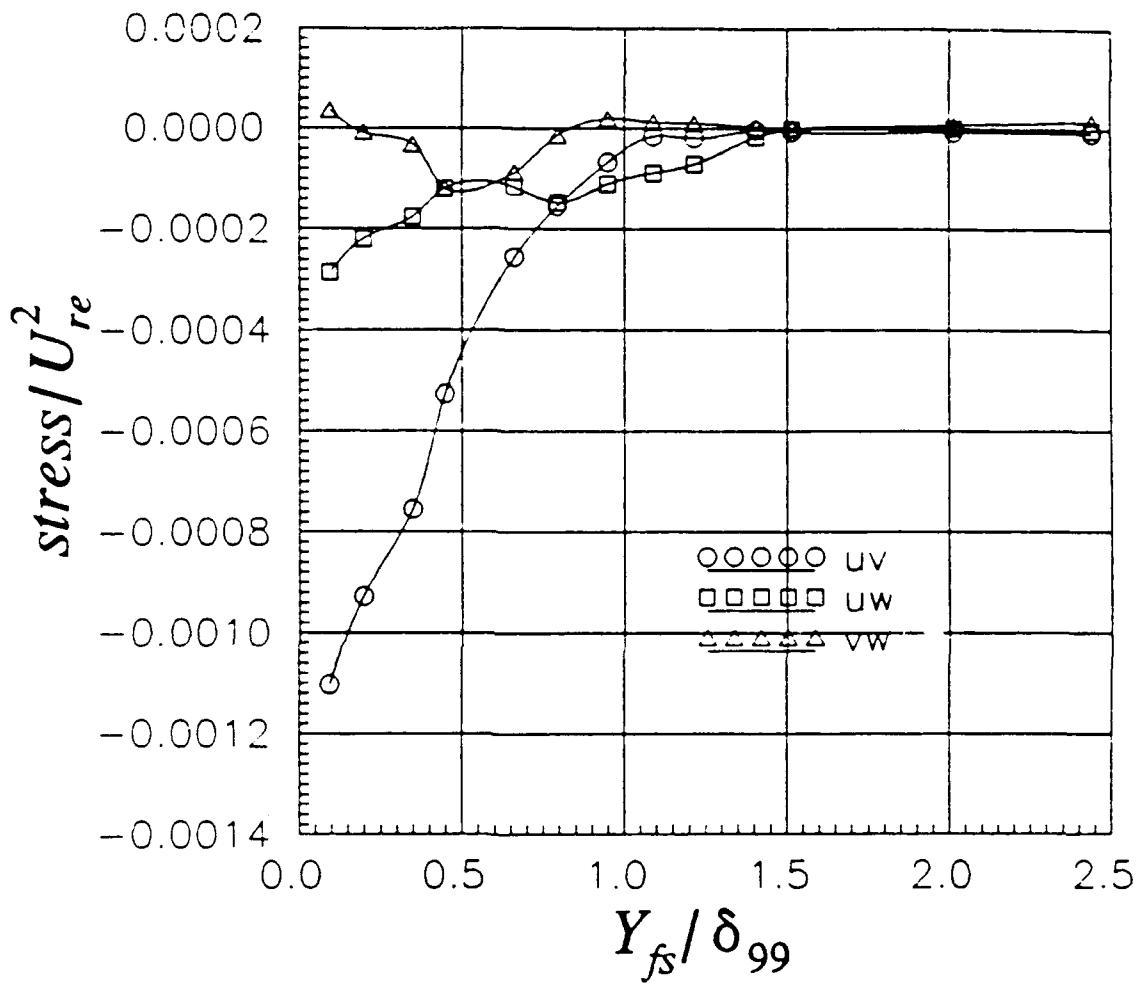
Figure 116.   Profiles of Reynolds Shear Stresses with respect to $Y_{fs}/\delta_{99}$, $\varphi = 80°$, $X/L = 0.7$, $Re = 4.0 \times 10^6$, $\alpha = 10°$, Local Free-Stream Coordinates.
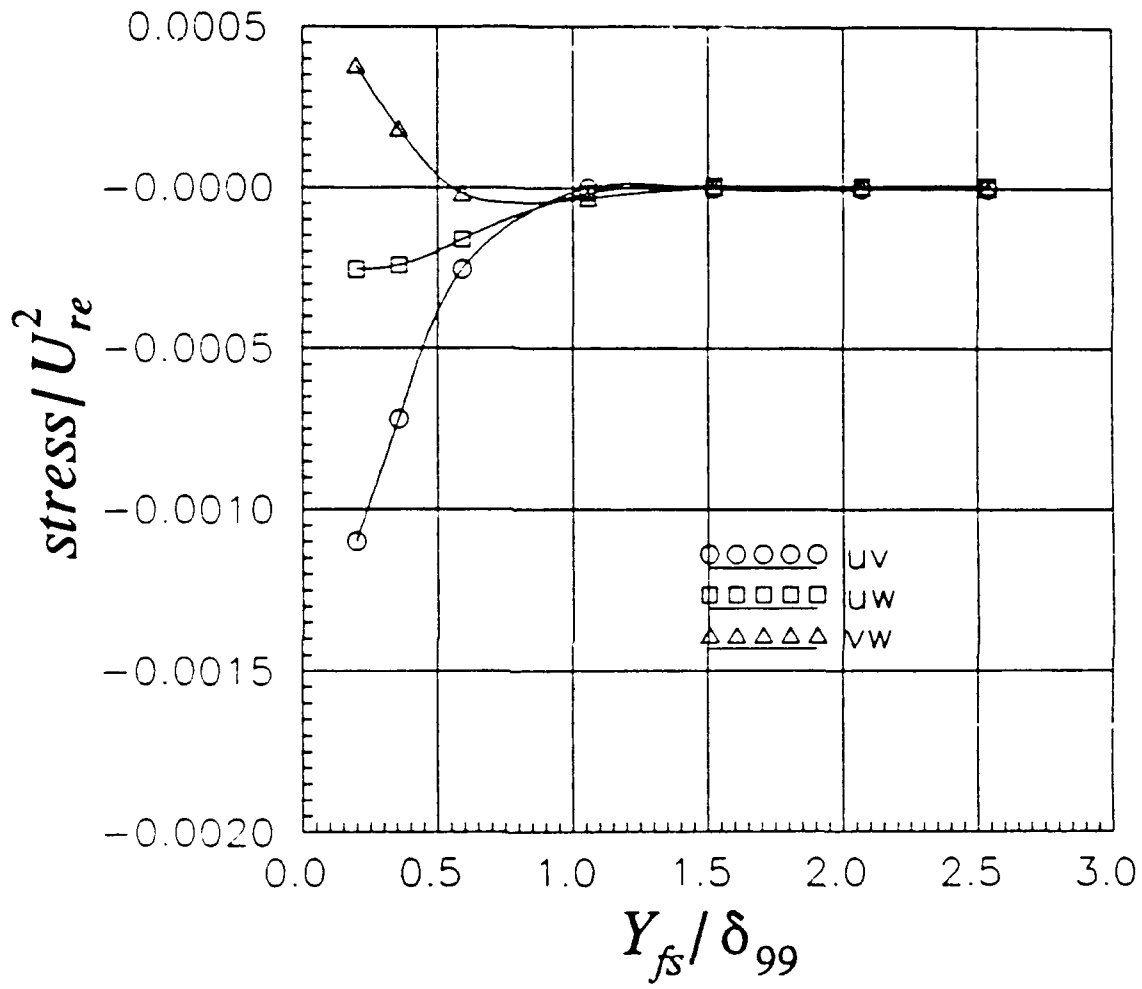
Figure 117. Profiles of Reynolds Shear Stresses with respect to $Y_{fs}/\delta_{99}$, $\varphi=90°$, $X/L=0.7$, $Re=4.0\times10^6$, $\alpha=10°$, Local Free-Stream Coordinates.
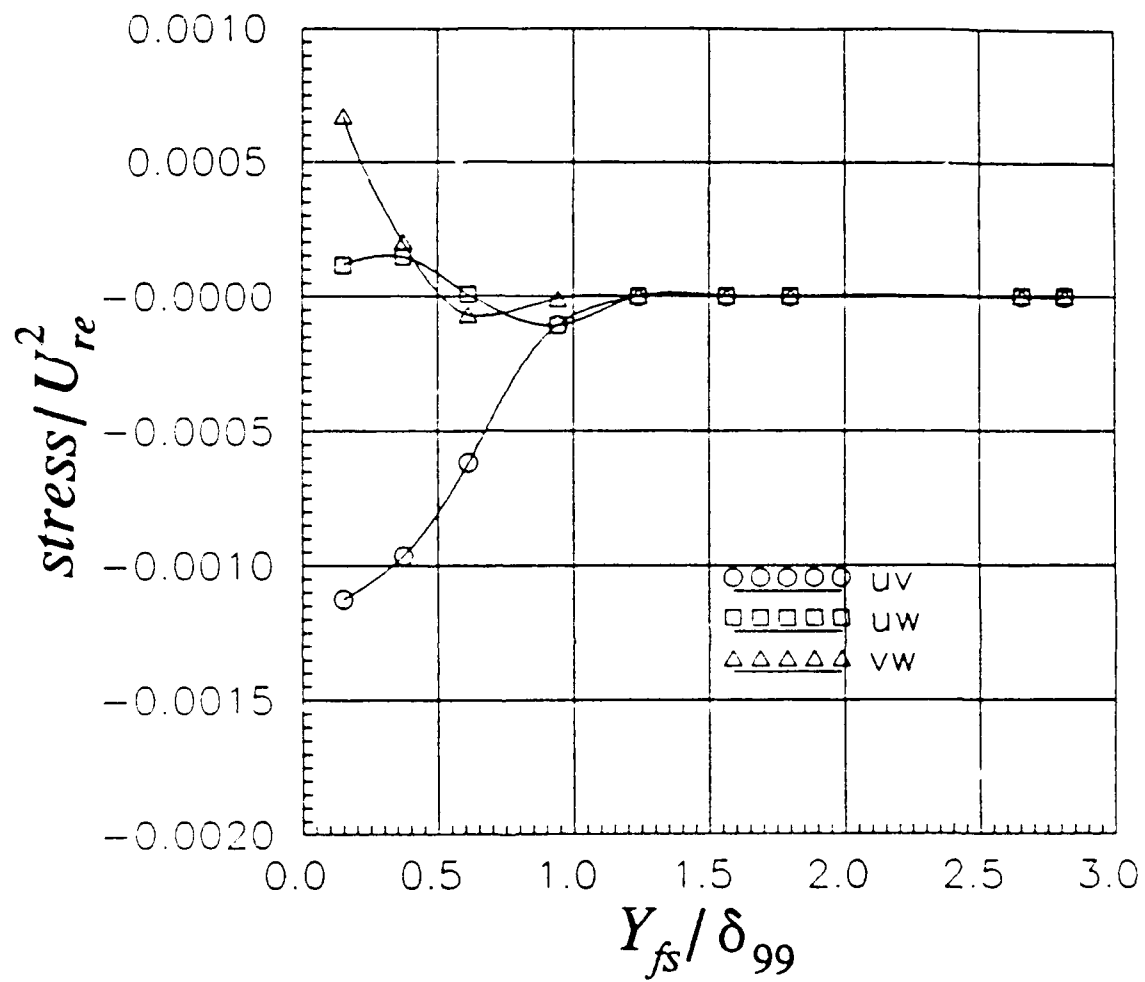
Figure 118. Profiles of Reynolds Shear Stresses with respect to $\overline{Y}_{fs}/\delta_{99}$, $\varphi = 20°$, $X/L = 0.8$, $Re = 4.0 \times 10^6$, $\alpha = 10°$, Local Free-Stream Coordinates.
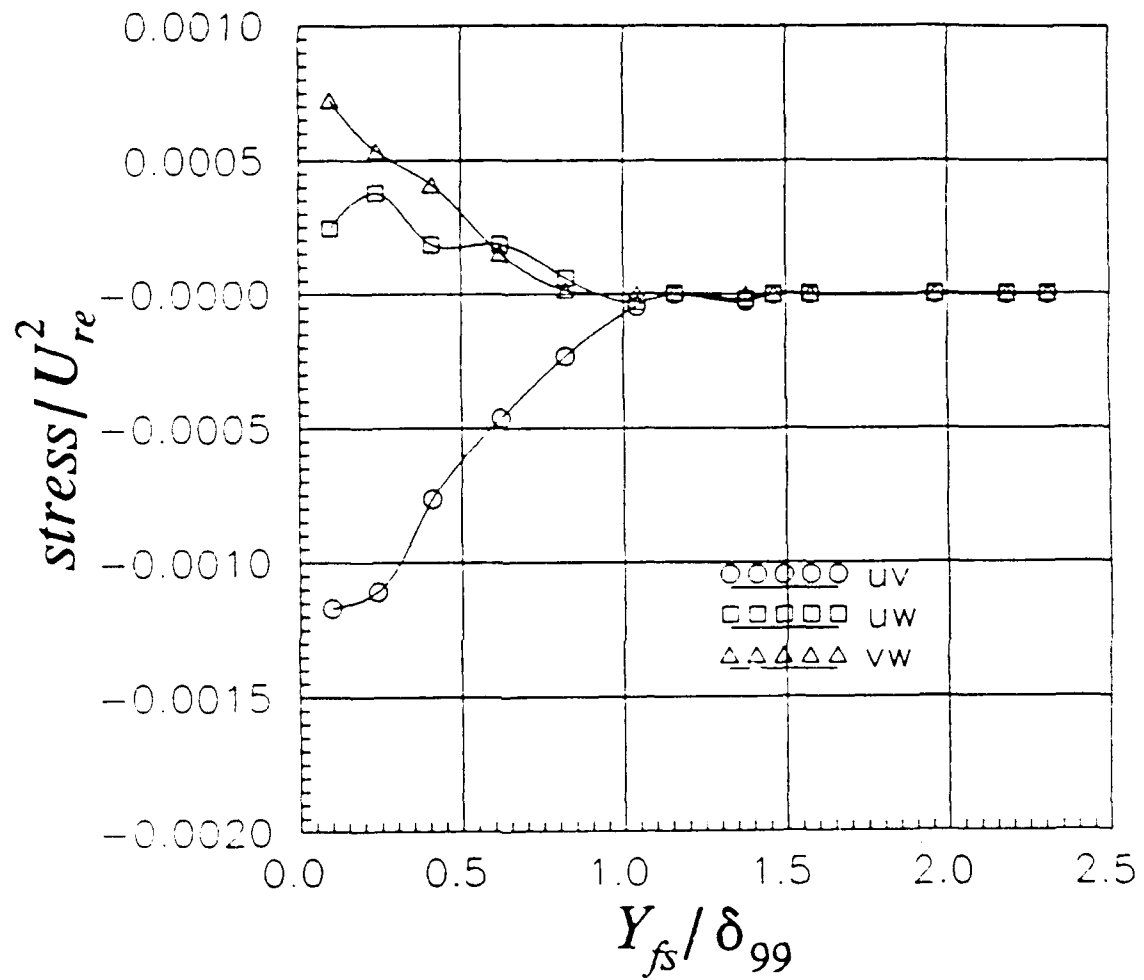
Figure 119. Profiles of Reynolds Shear Stresses with respect to $Y_{fs}/\delta_{99}$, $\varphi = 30°$, $X/L = 0.8$, $Re = 4.0 \times 10^6$, $\alpha = 10°$, Local Free-Stream Coordinates.
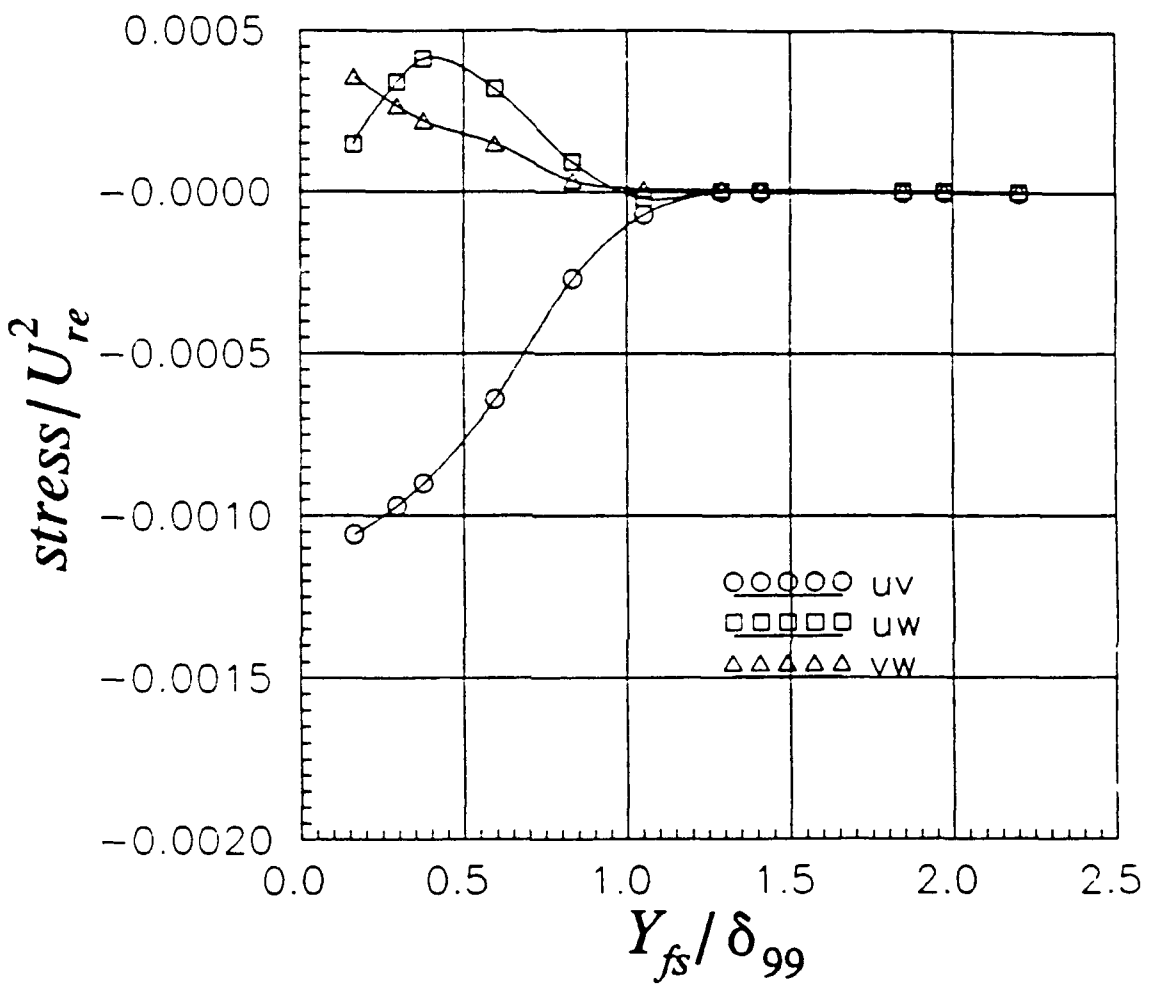
Figure 120. Profiles of Reynolds Shear Stresses with respect to $Y_{fs}/\delta_{99}$, $\varphi=40°$, $X/L=0.8$, $Re=4.0\times10^6$, $\alpha=10°$, Local Free-Stream Coordinates.
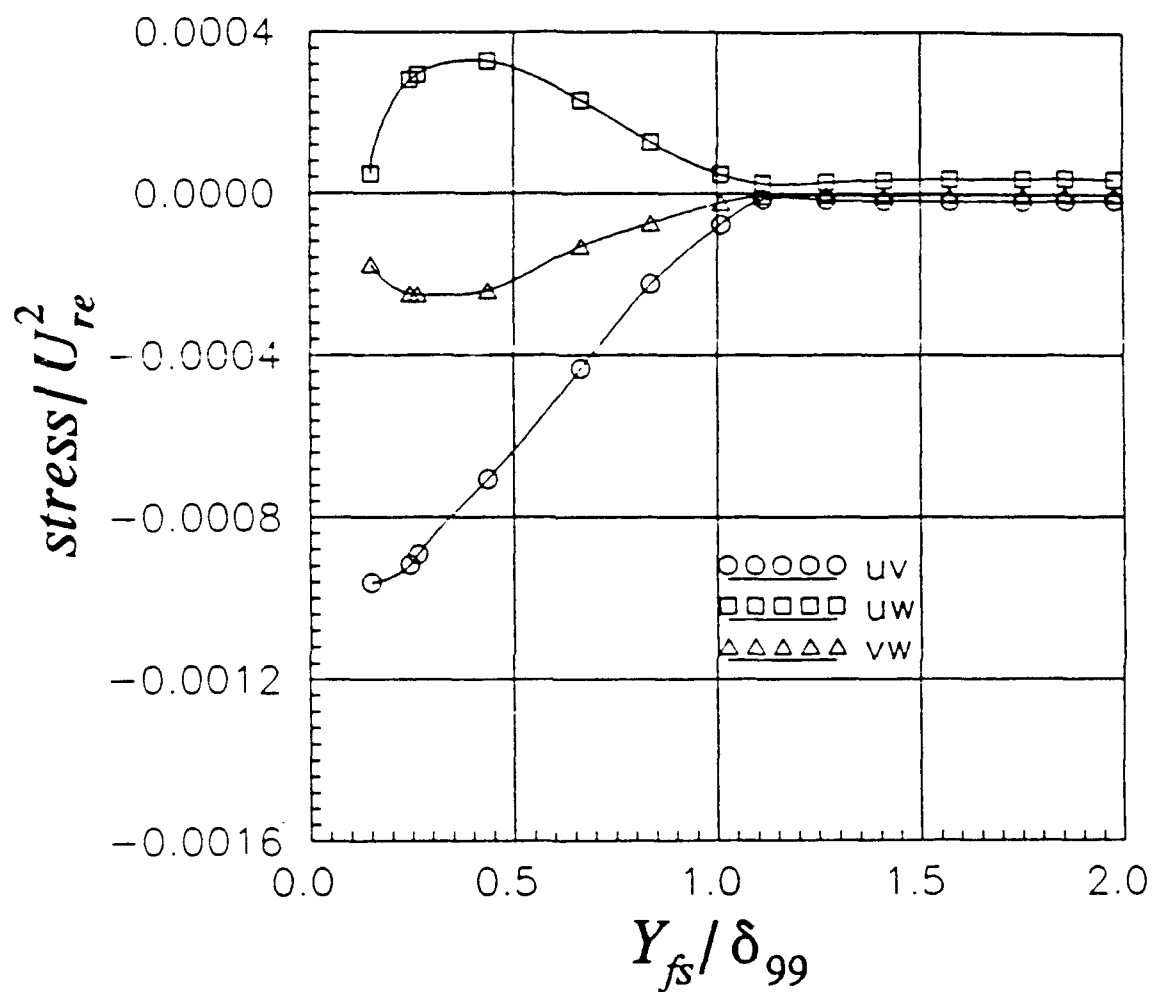
Figure 121. Profiles of Reynolds Shear Stresses with respect to $Y_{fs}/\delta_{99}$, $\varphi = 50°$, $X/L = 0.8$, $Re = 4.0 \times 10^6$, $\alpha = 10°$, Local Free-Stream Coordinates.
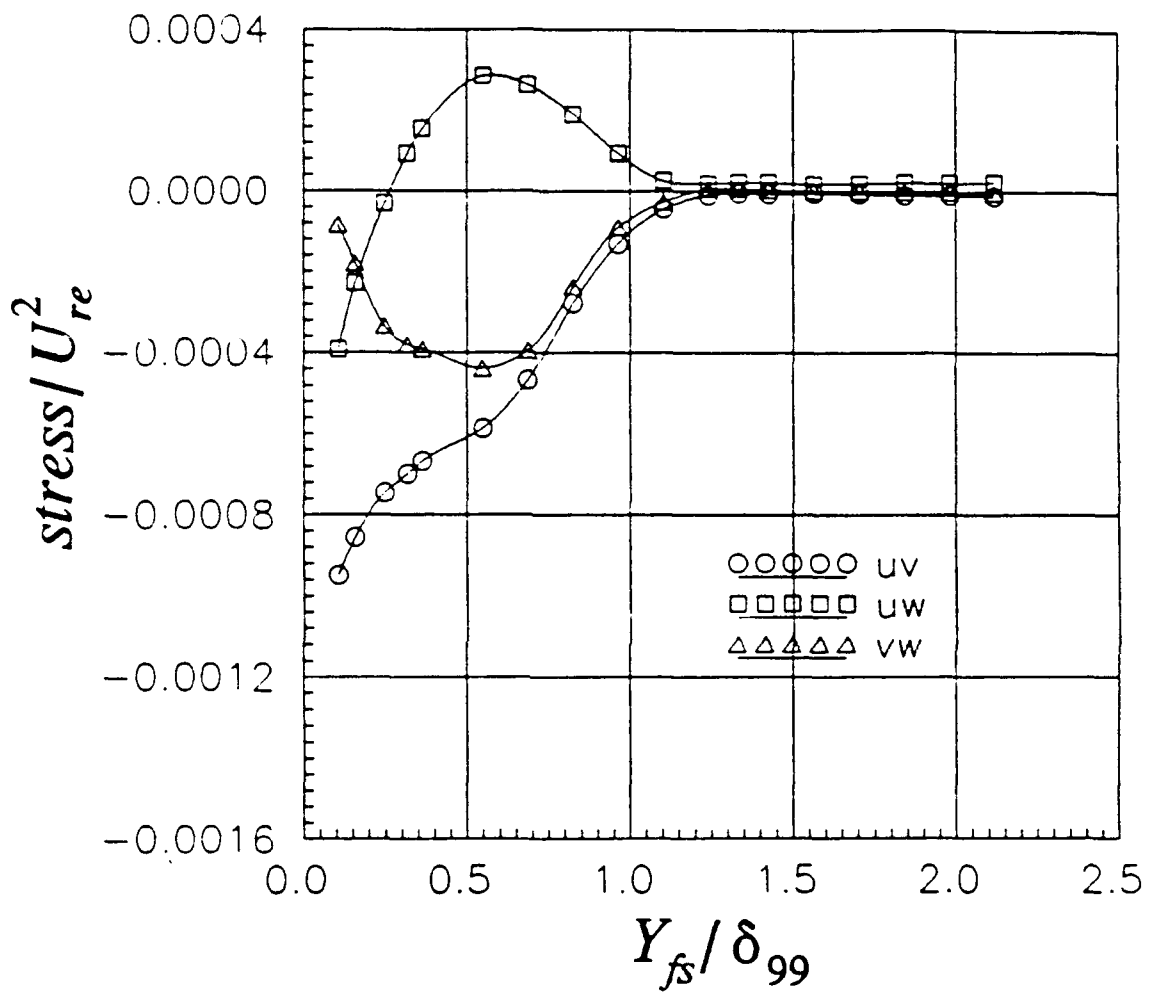
Figure 122.   Profiles of Reynolds Shear Stresses with respect to $Y_{fs}/\delta_{99}$, $\varphi = 60°$, $X/L = 0.8$, $Re = 4.0 \times 10^6$, $\alpha = 10°$, Local Free-Stream Coordinates.
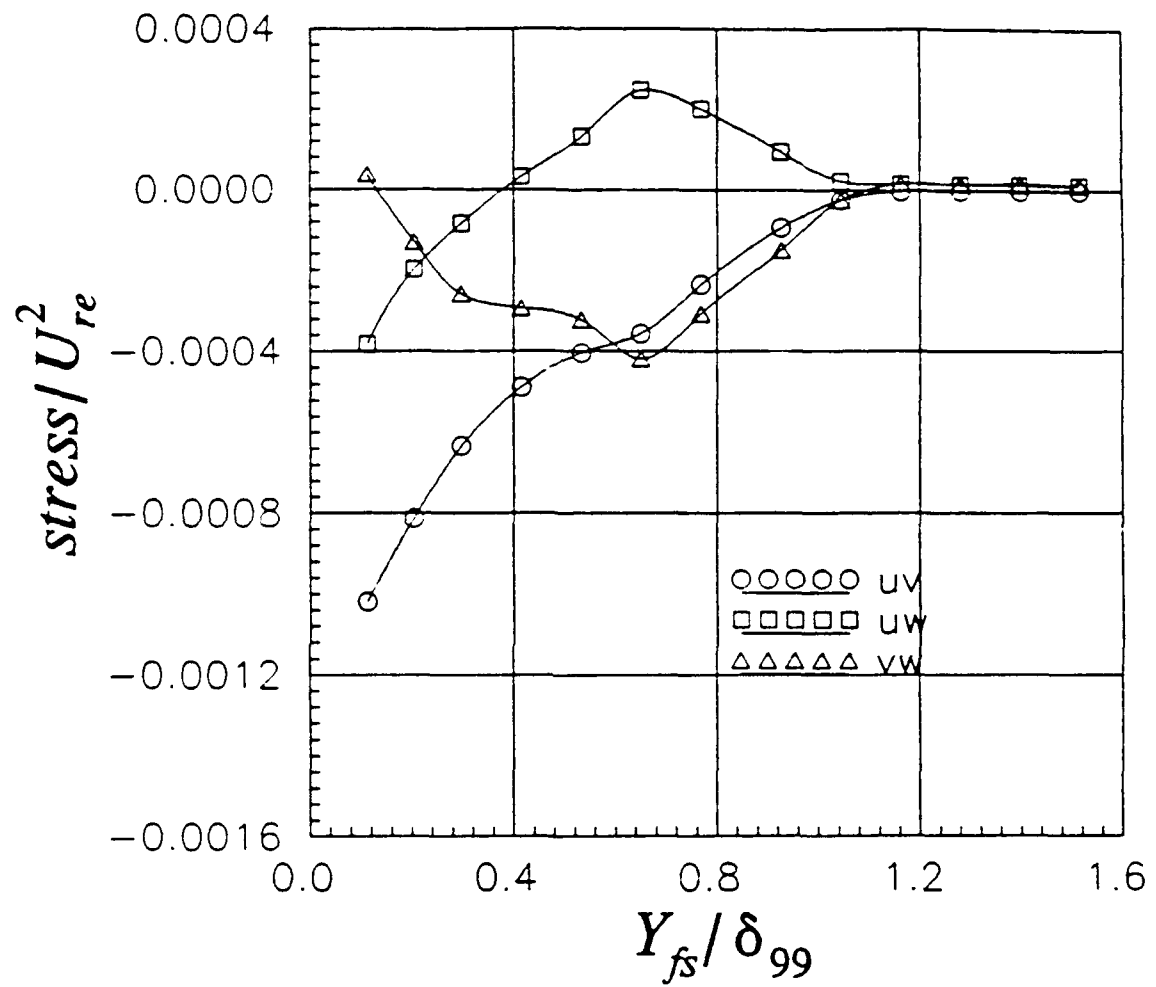
Figure 123. Profiles of Reynolds Shear Stresses with respect to $Y_{fs}/\delta_{99}$, $\varphi=70°$, X/L=0.8, Re=4.0×10$^6$, $\alpha=10°$, Local Free-Stream Coordinates.
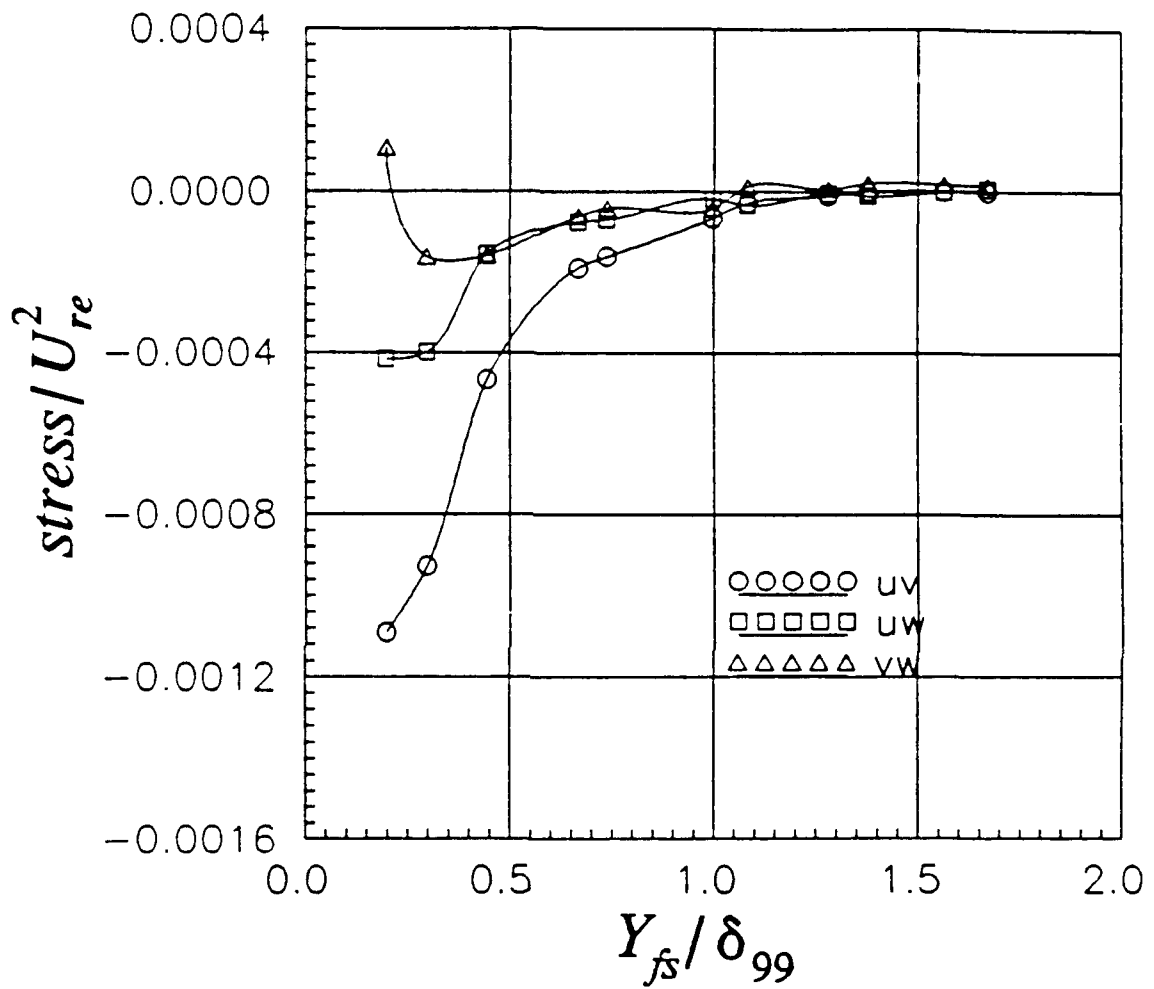
Figure 124. Profiles of Reynolds Shear Stresses with respect to $Y_{fs}/\delta_{99}$, $\varphi=80°$, X/L=0.8, Re=$4.0 \times 10^6$, $\alpha=10°$, Local Free Stream Coordinates.
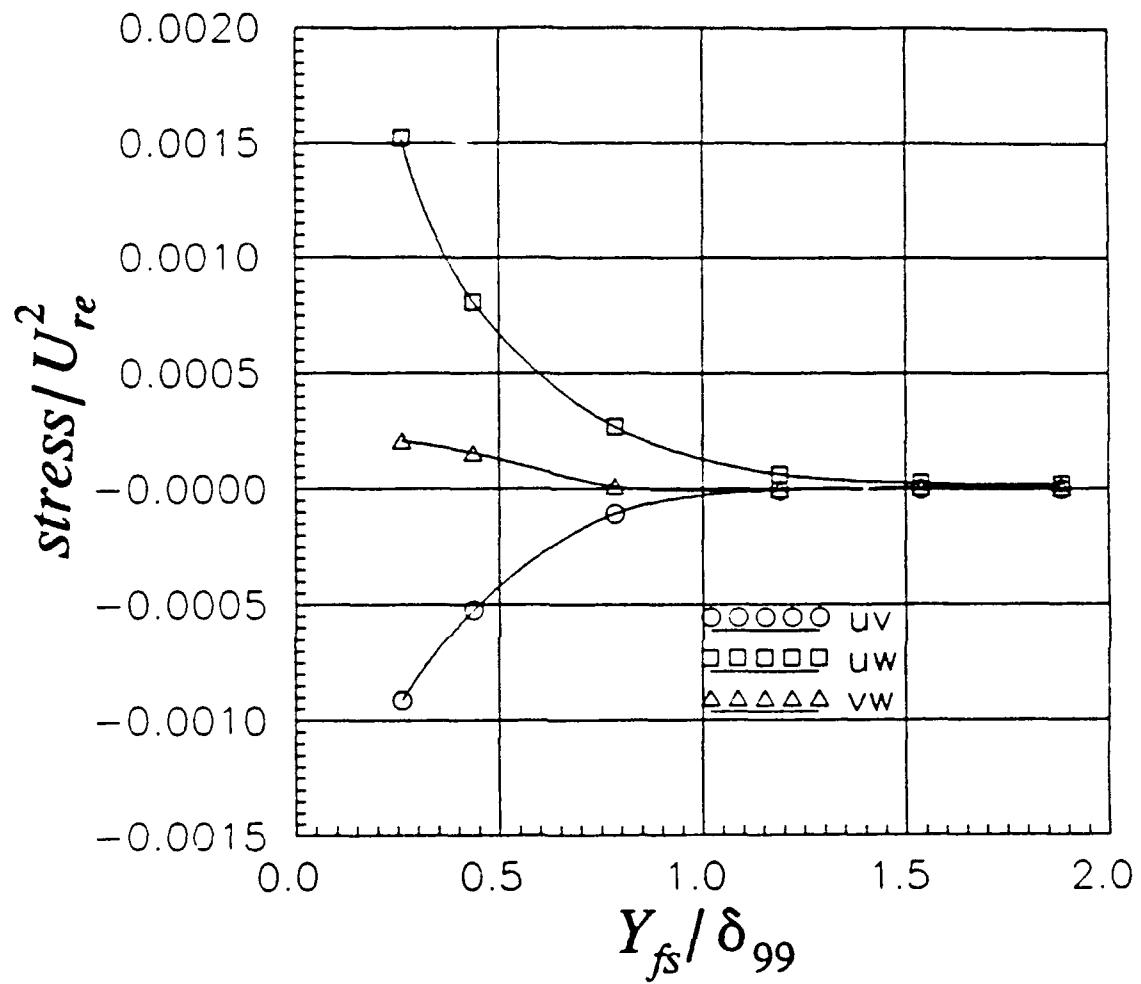
Figure 125. Profiles of Reynolds Shear Stresses with respect to $Y_{fs}/\delta_{99}$, $\varphi = 90°$, X/L=0.8, Re=4.0×10⁶, $\alpha = 10°$, Local Free-Stream Coordinates.
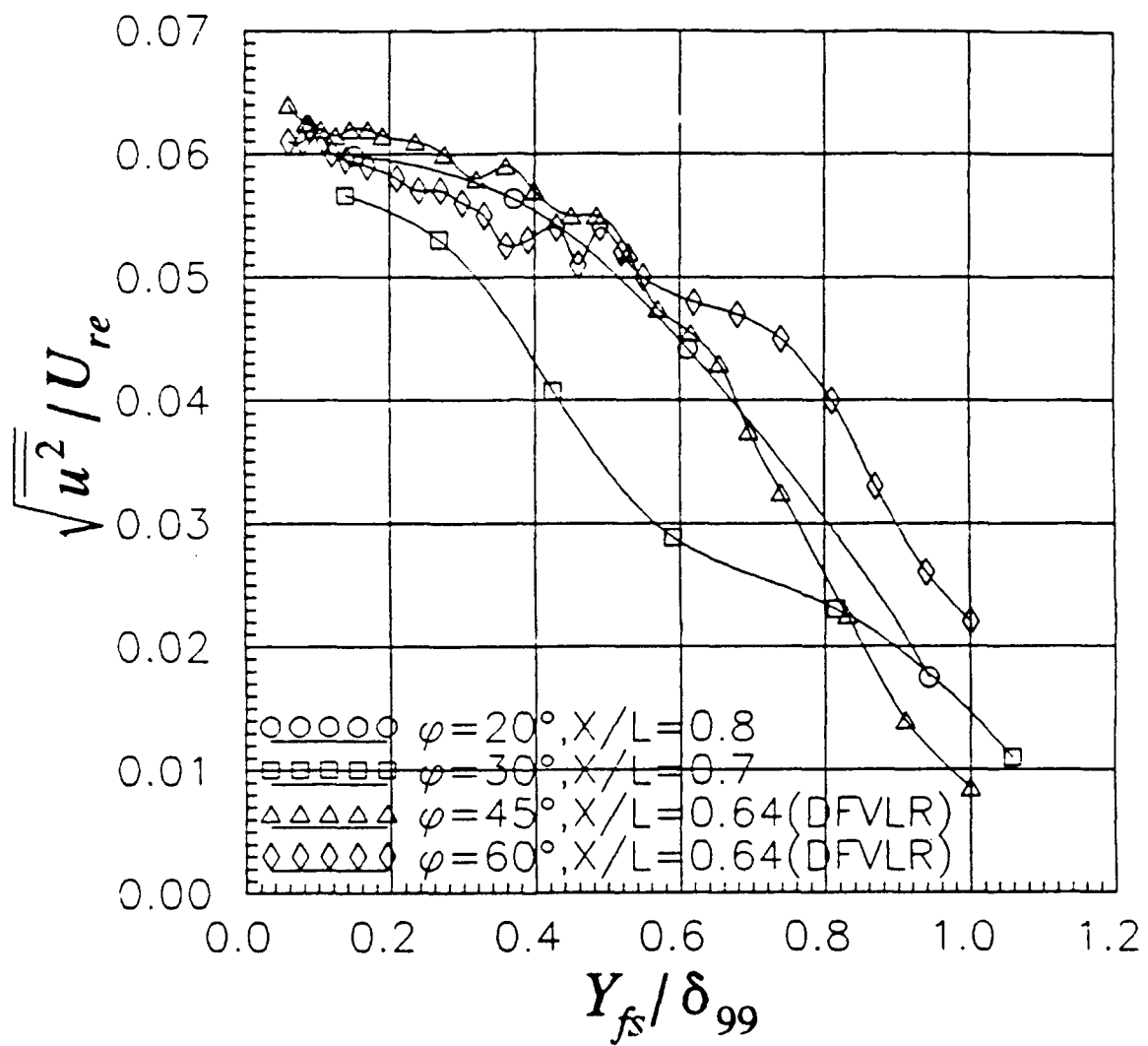
Figure 126. Comparison of $\overline{u^2}$ Reynolds Stress in Regions of Converging Streamlines, Re=$4.0 \times 10^6$, $\alpha = 10°$, DFVLR Data at Re=$7.2 \times 10^6$ (Kreplin and Vollmers, 1981).
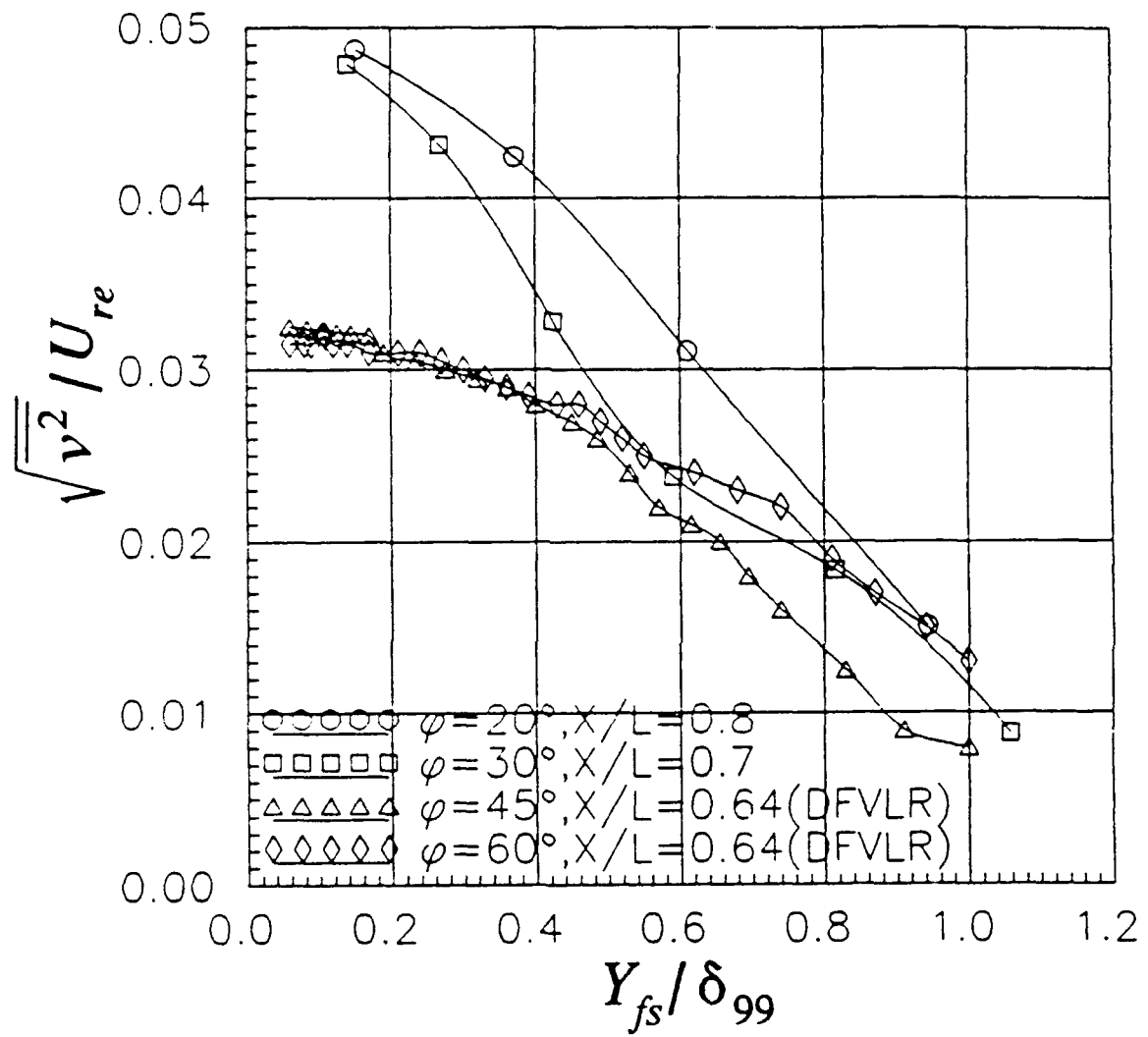
Figure 127. Comparison of $\overline{v^2}$ Reynolds Stress in Regions of Converging Streamlines, Re=4.0×10⁶, DFVLR Data at Re=7.2×10⁶ (Kreplin and Vollmers, 1981).
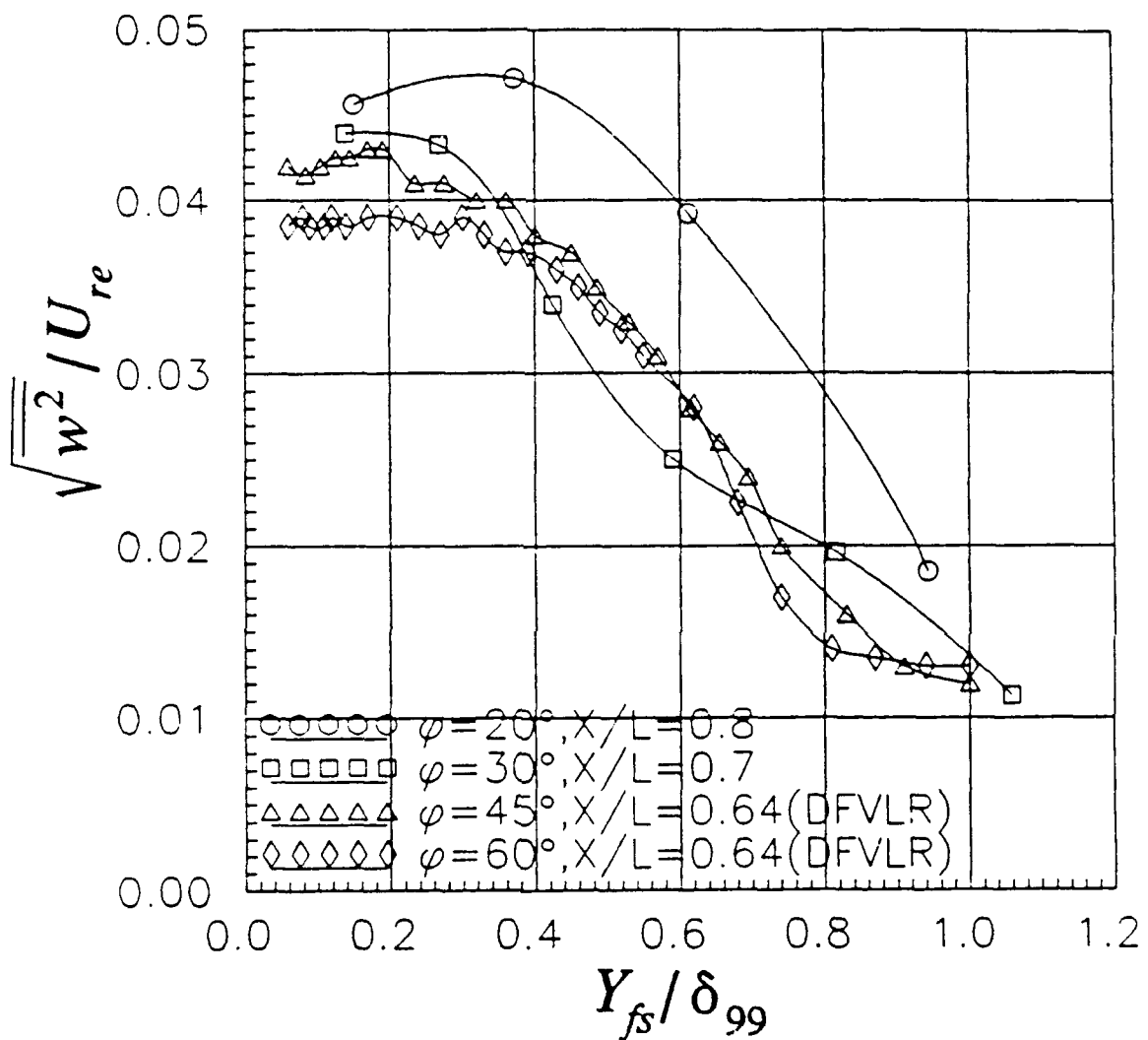
Figure 128. Comparison of $\overline{w^2}$ Reynolds Stress in Regions of Converging Streamlines, $Re=4.0\times10^6$, $\alpha=10°$, DFVLR Data at $Re=7.2\times10^6$ (Kreplin and Vollmers, 1981).
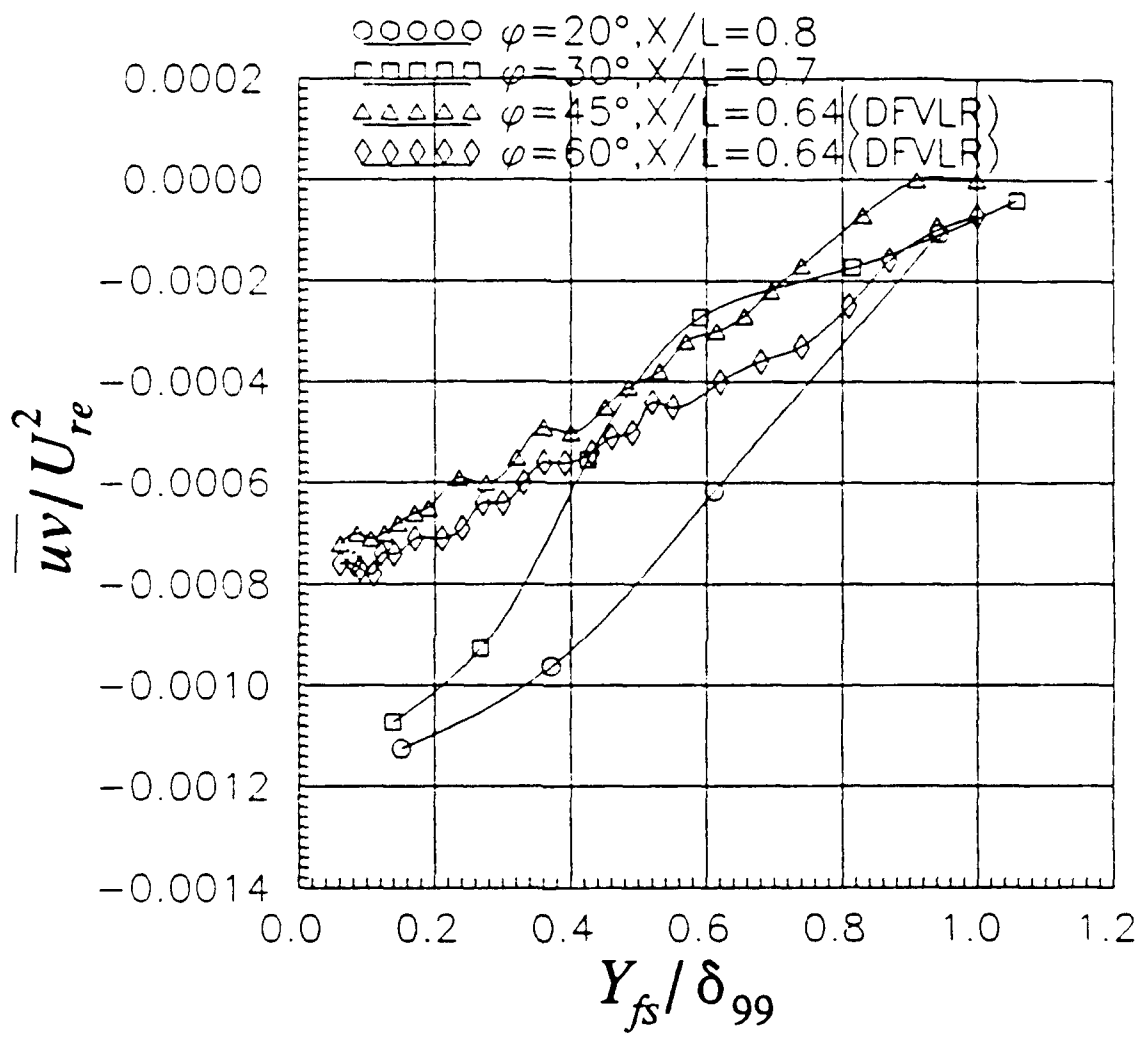
Figure 129.   Comparison of $\overline{uv}$   Reynolds Stress in Regions of Converging Streamlines,   Re$=4.0\times10^6$,   $\alpha=10°$,   DFVLR   Data   at   Re$=7.2\times10^6$ (Kreplin and Vollmers, 1981).
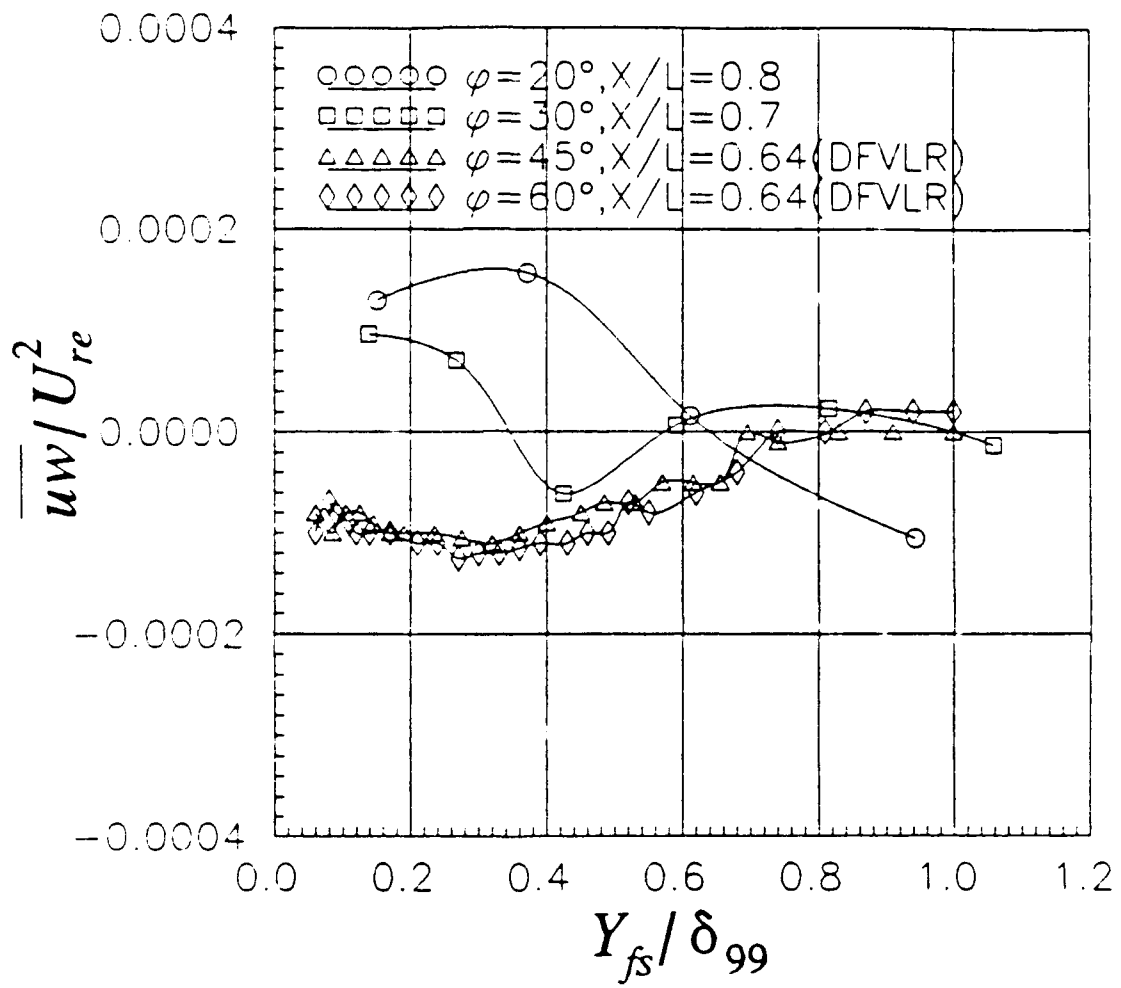
Figure 130. Comparison of $\overline{uw}$ Reynolds Stress in Regions of Converging Streamlines, $Re=4.0\times10^6$, $\alpha=10°$, DFVLR Data at $Re=7.2\times10^6$ (Kreplin and Vollmers, 1981).
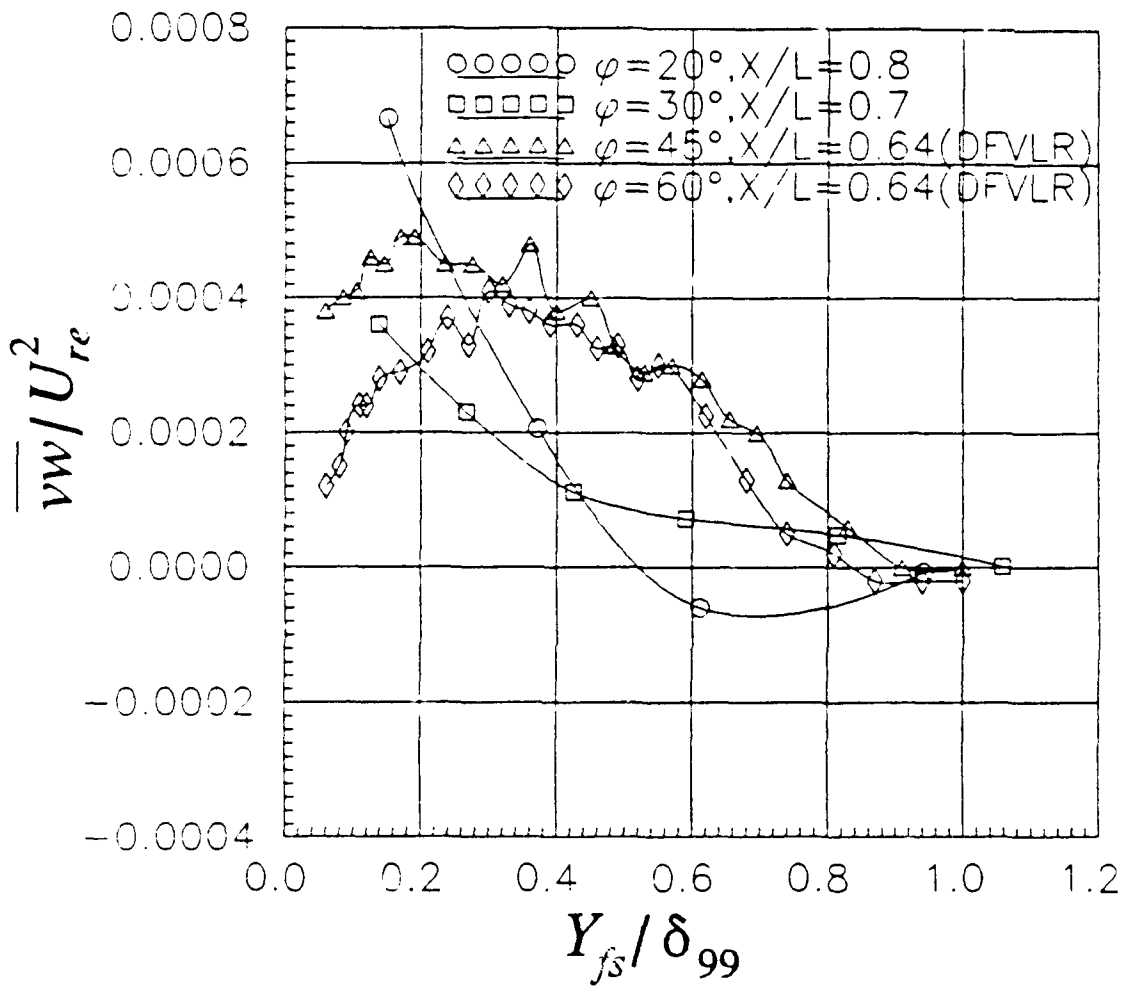
Figure 131. Comparison of $\overline{vw}$ Reynolds Stress in Regions of Converging Streamlines, $Re=4.0\times10^{6}$, $\alpha=10°$, DFVLR Data at $Re=7.2\times10^{6}$ (Kreplin and Vollmers, 1981).
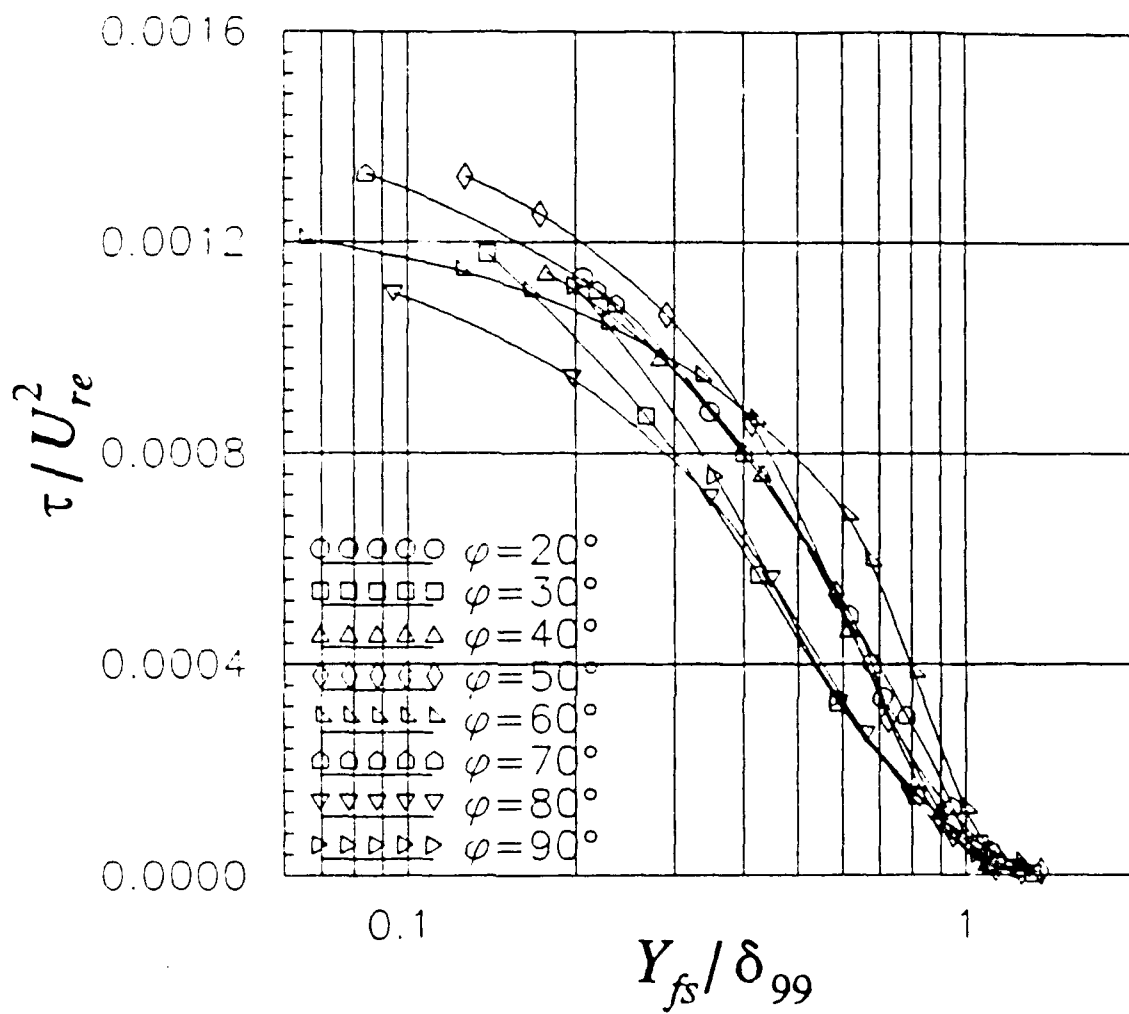
Figure 132.  Profiles of Total Turbulent Shear Stress $\tau$, X/L=0.7, Re=4.0×10⁶, $\alpha = 10°$, Local Free-Stream Coordinates.
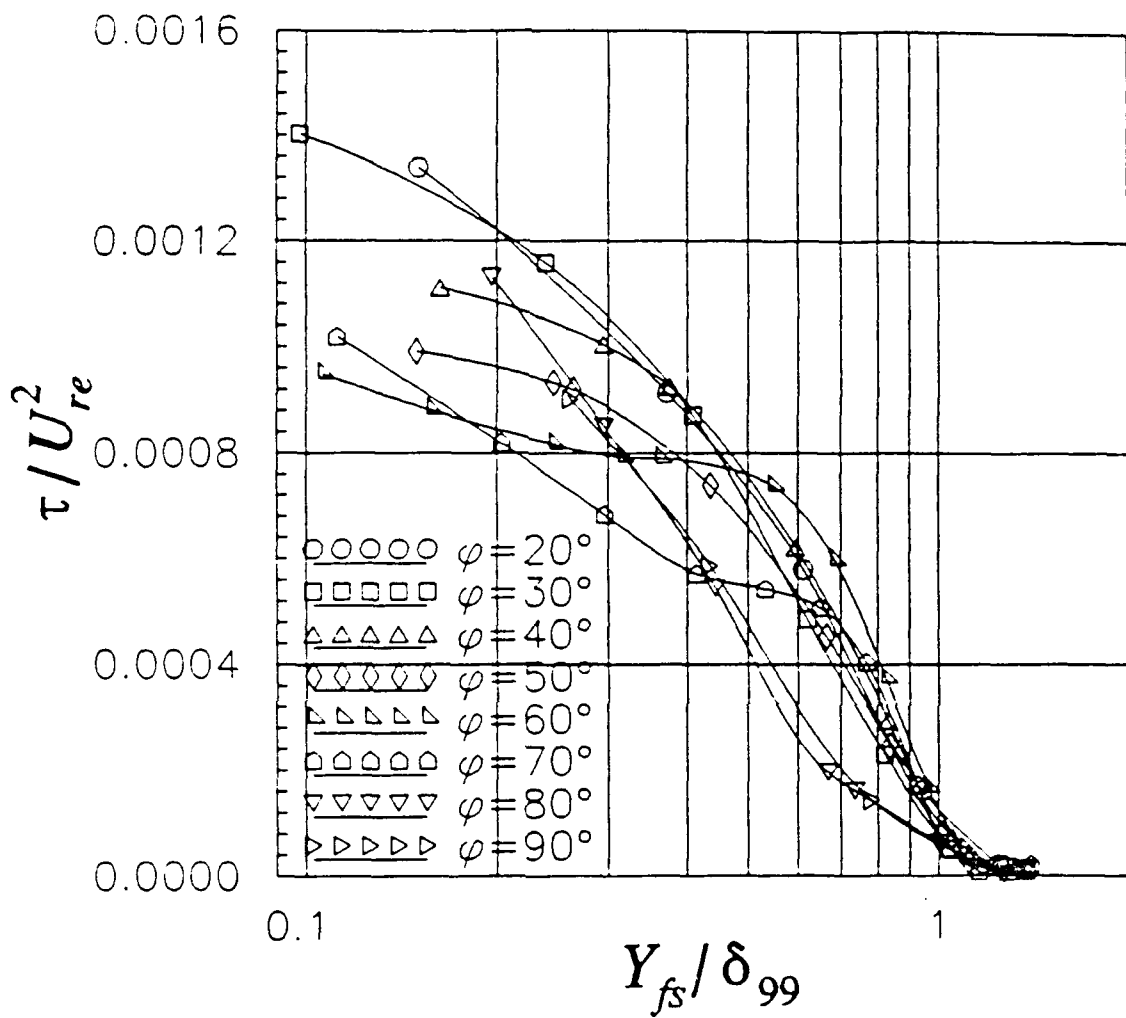
Figure 133. Profiles of Total Turbulent Shear Stress $\tau$, X/L=0.8, Re=$4.0 \times 10^6$, $\alpha = 10°$, Local Free-Stream Coordinates.
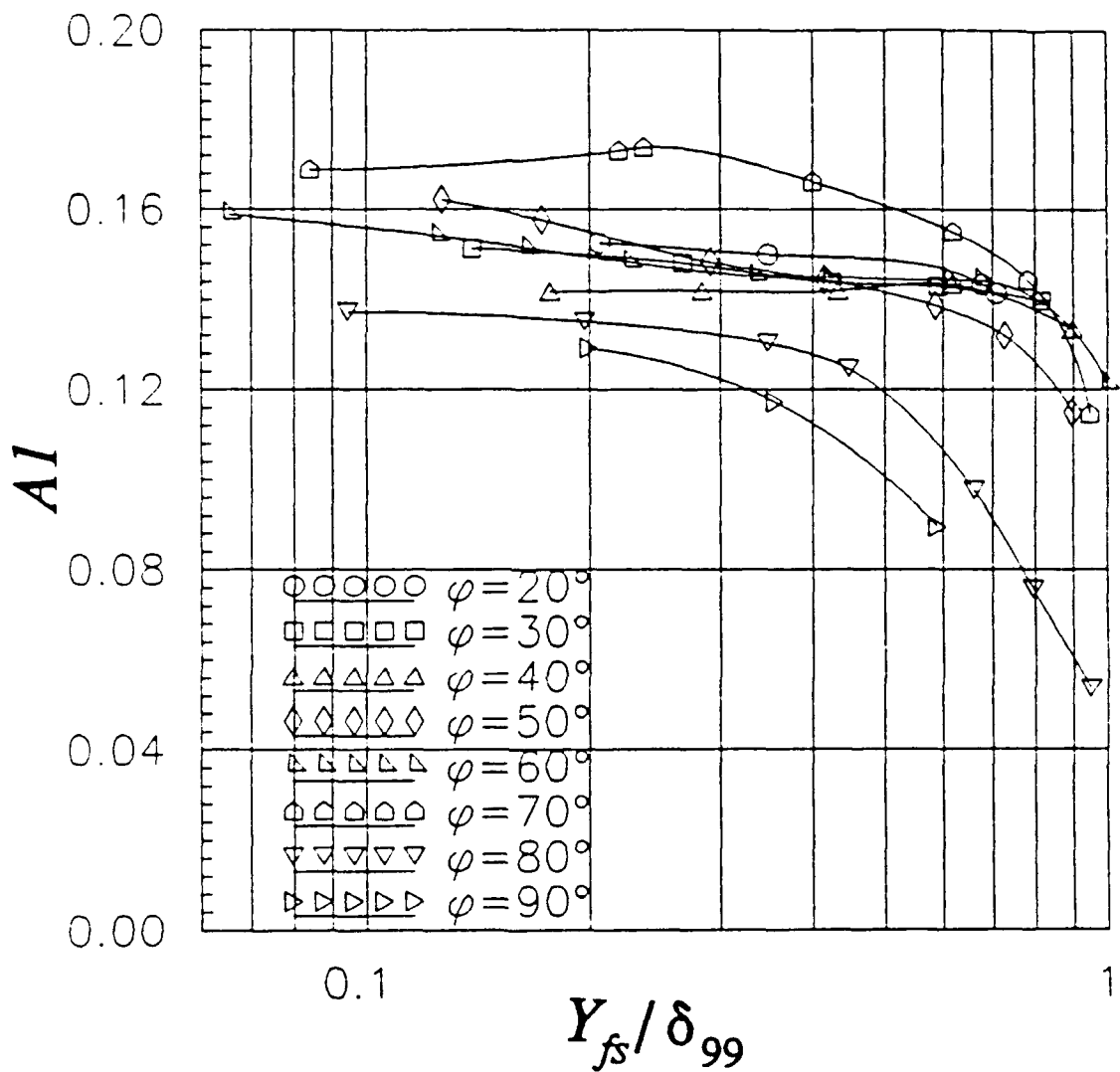
Figure 134.    Profiles of Townsend's Structural Parameter A1, X/L=0.7, Re=4.0×10$^6$, $\alpha$= 10°, Local Free-Stream Coordinates.
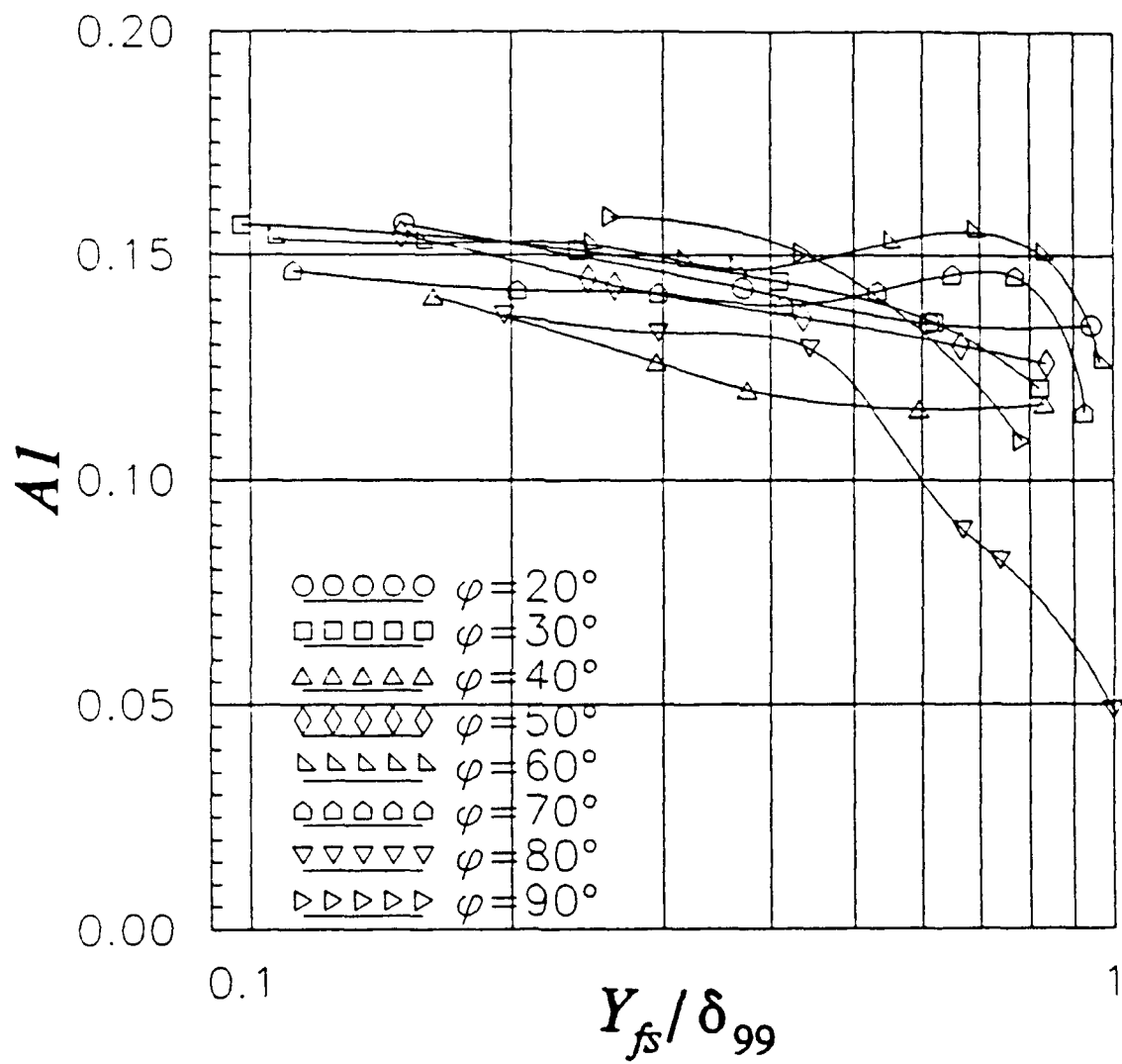
Figure 135.   Profiles of Townsend's Structural Parameter A1, X/L=0.8, Re=4.0×10$^6$, $\alpha$=10°, Local Free-Stream Coordinates.
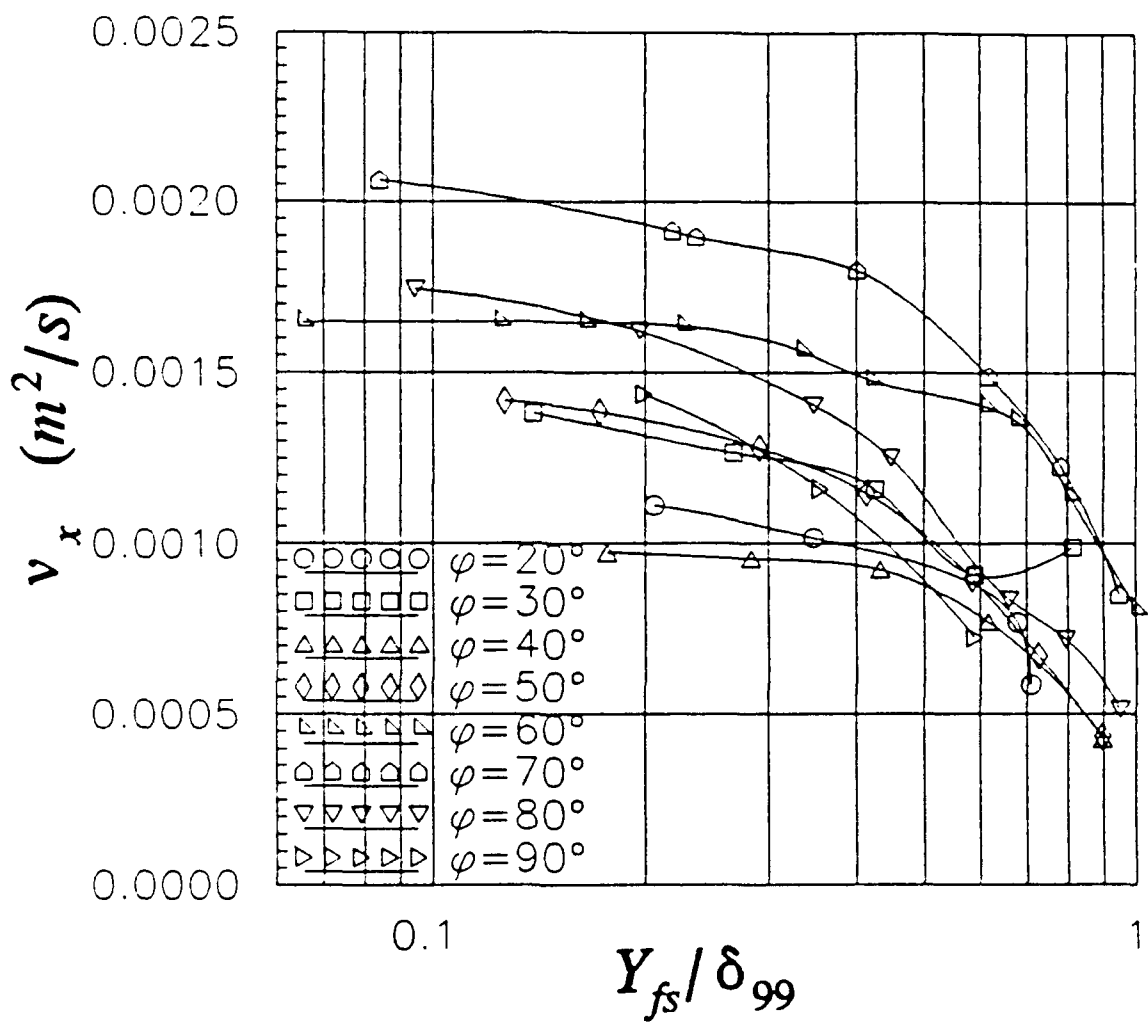
Figure 136. Profiles of X Eddy Viscosity $\nu_x$, X/L=0.7, Re=$4.0\times10^6$, $\alpha=10°$, Local Free-Stream Coordinates.
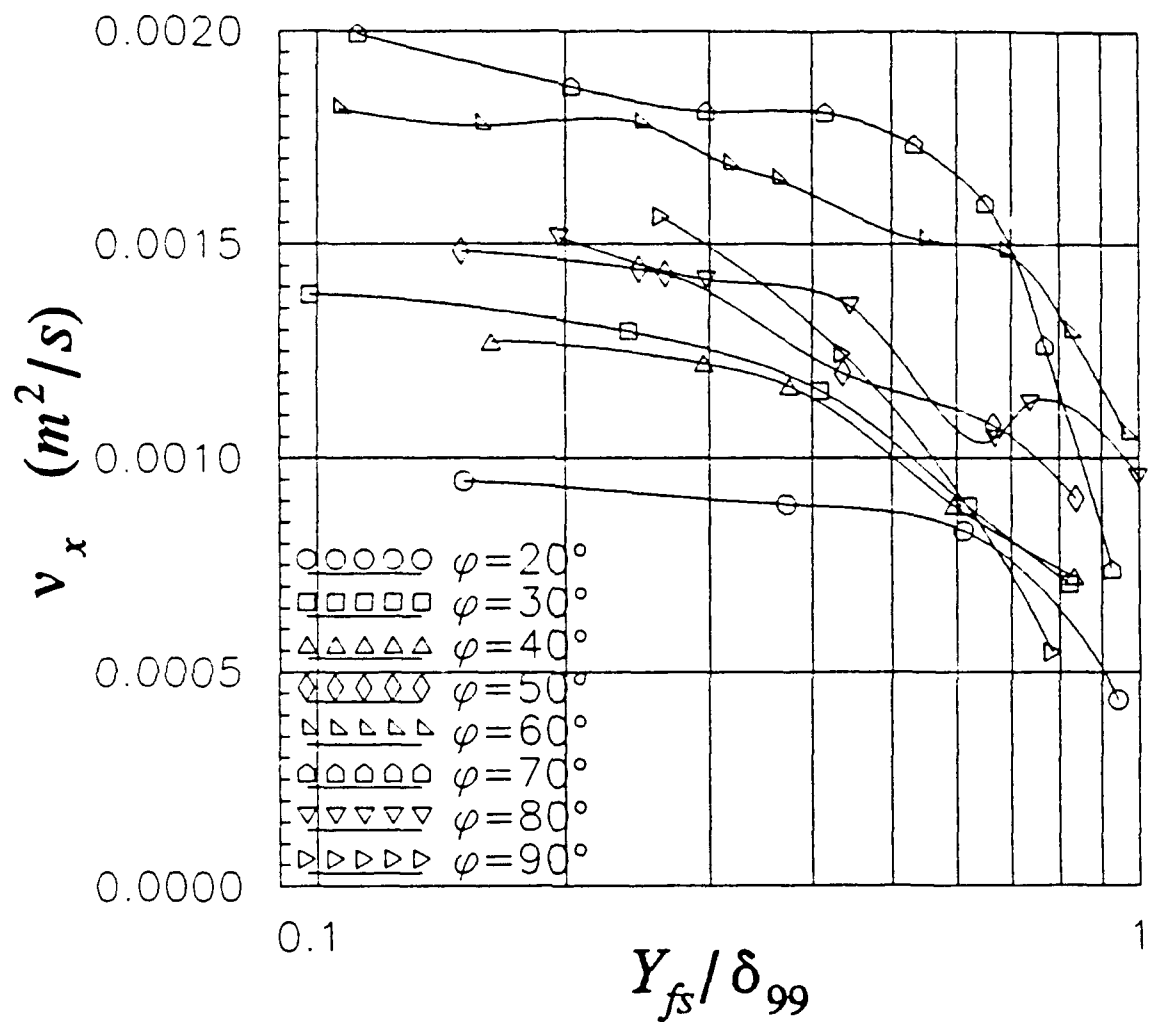
Figure 137. Profiles of X Eddy Viscosity $v_x$, X/L=0.8, Re=4.0×10⁶, $\alpha$=10°, Local Free-Stream Coordinates.
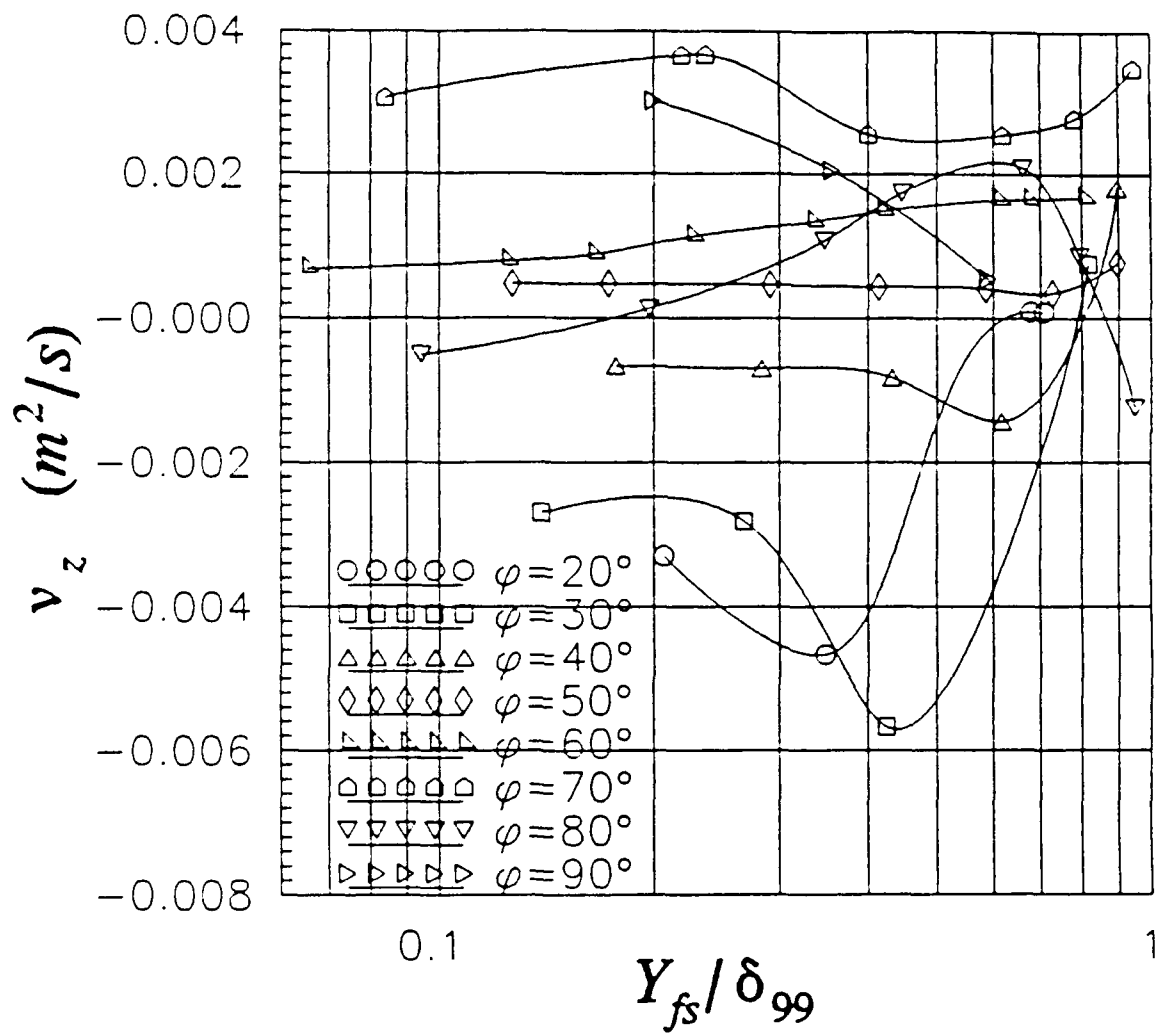
Figure 138.  Profiles of Z Eddy Viscosity $\nu_z$, X/L=0.7, Re=4.0×10⁶, $\alpha$=10°, Local Free-Stream Coordinates.
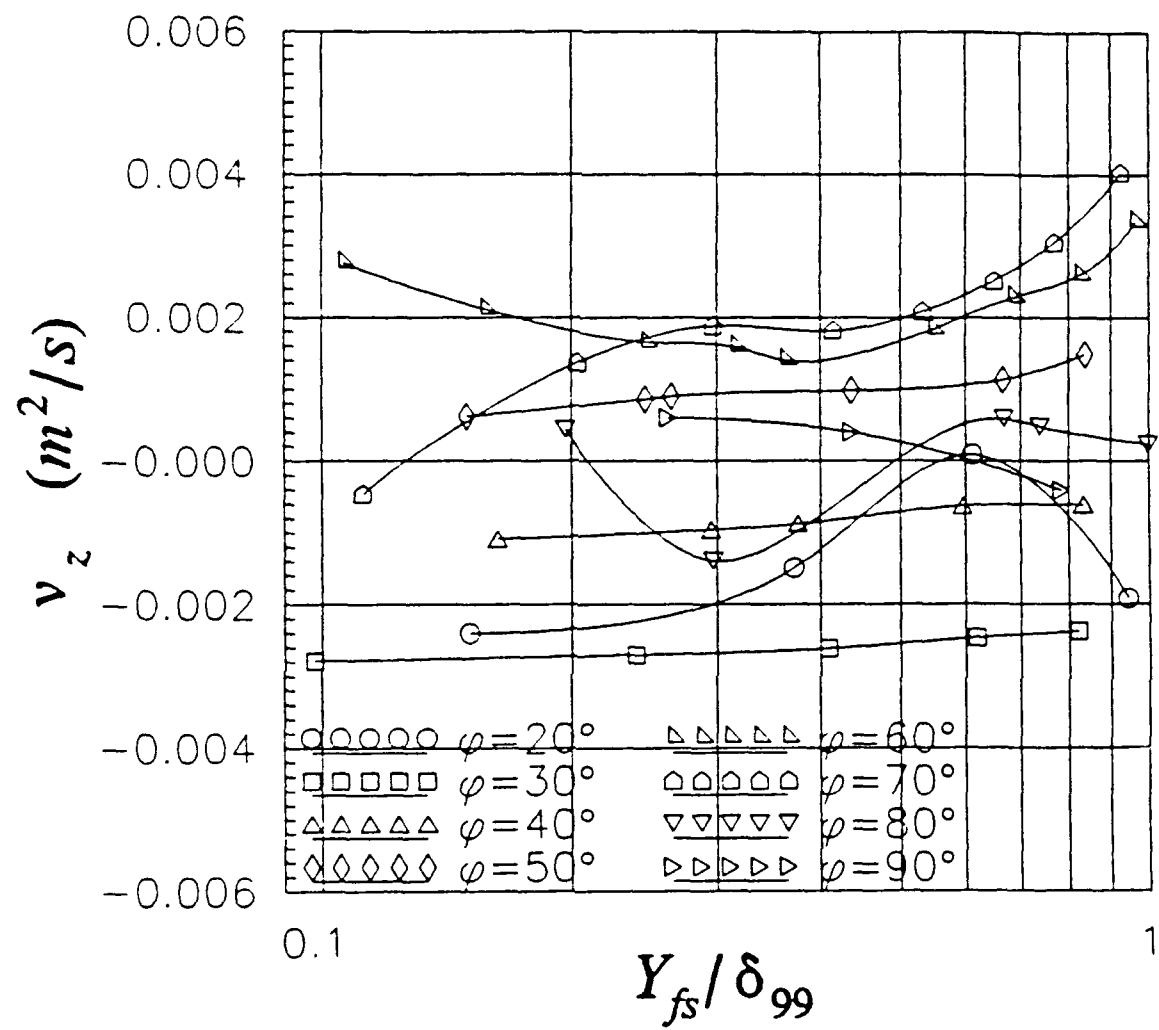
Figure 139. Profiles of Z Eddy Viscosity $\nu_z$, X/L=0.8, Re=4.0×10$^6$, $\alpha$=10°, Local Free-Stream Coordinates.
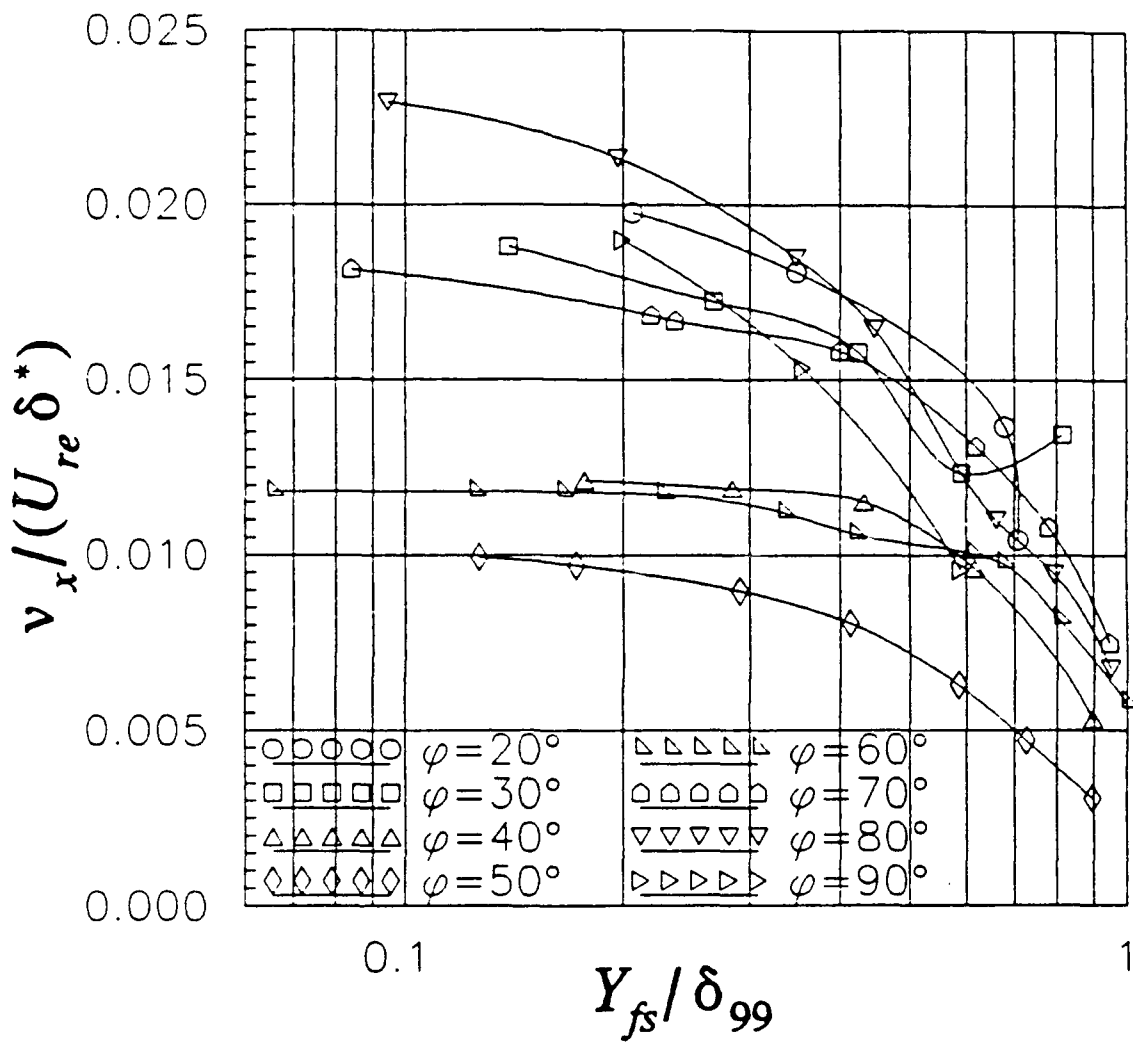
Figure 140. Profiles of $v_X/(U_{re}\delta^*)$, X/L=0.7, Re=4.0×10⁶, α=10°, Local Free-Stream Coordinates.
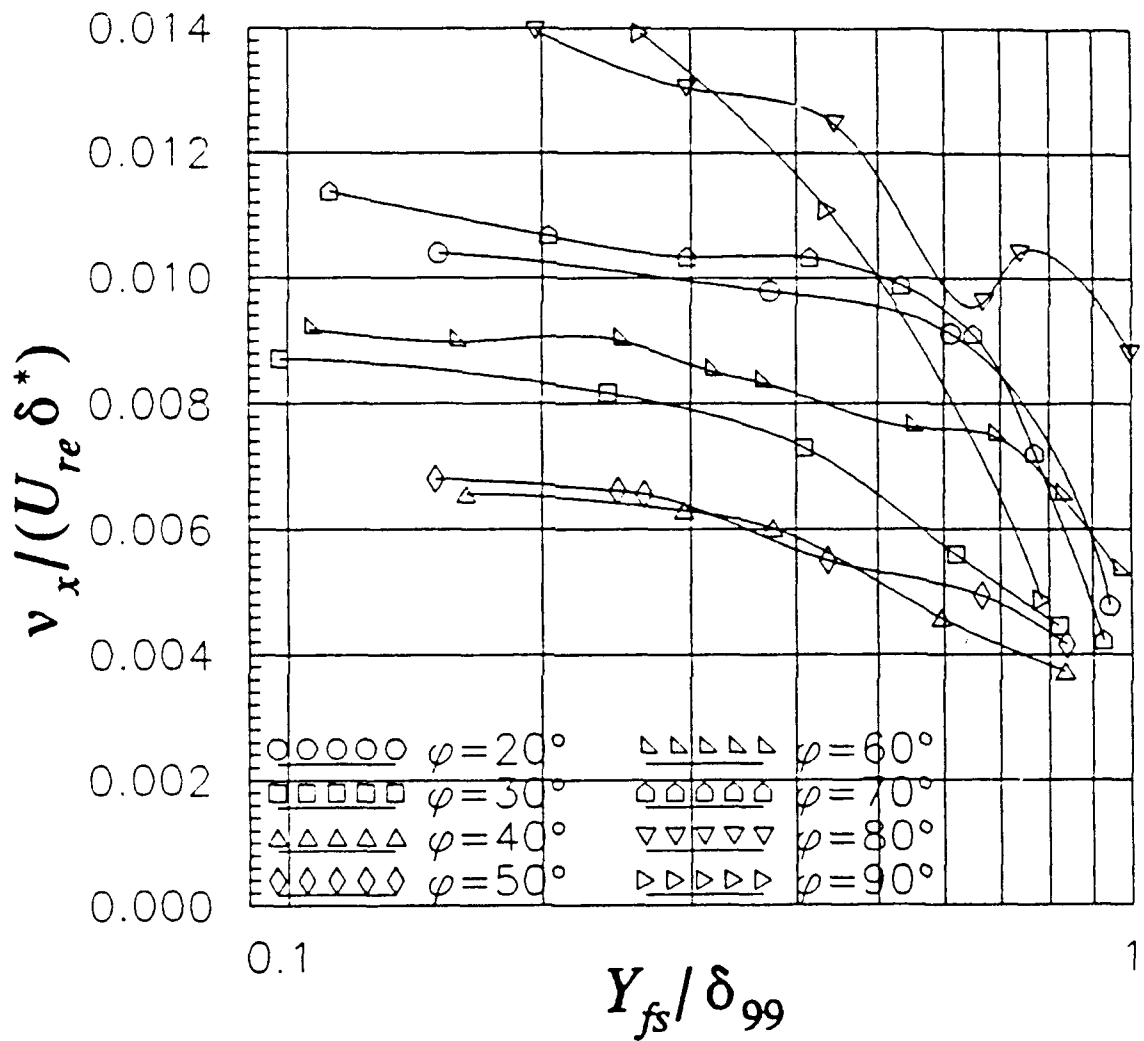
Figure 141.    Profiles of $v_x/(U_{re}\delta^*)$,  X/L=0.8,  Re=4.0×10⁶,  α=10°,  Local Free-Stream Coordinates.
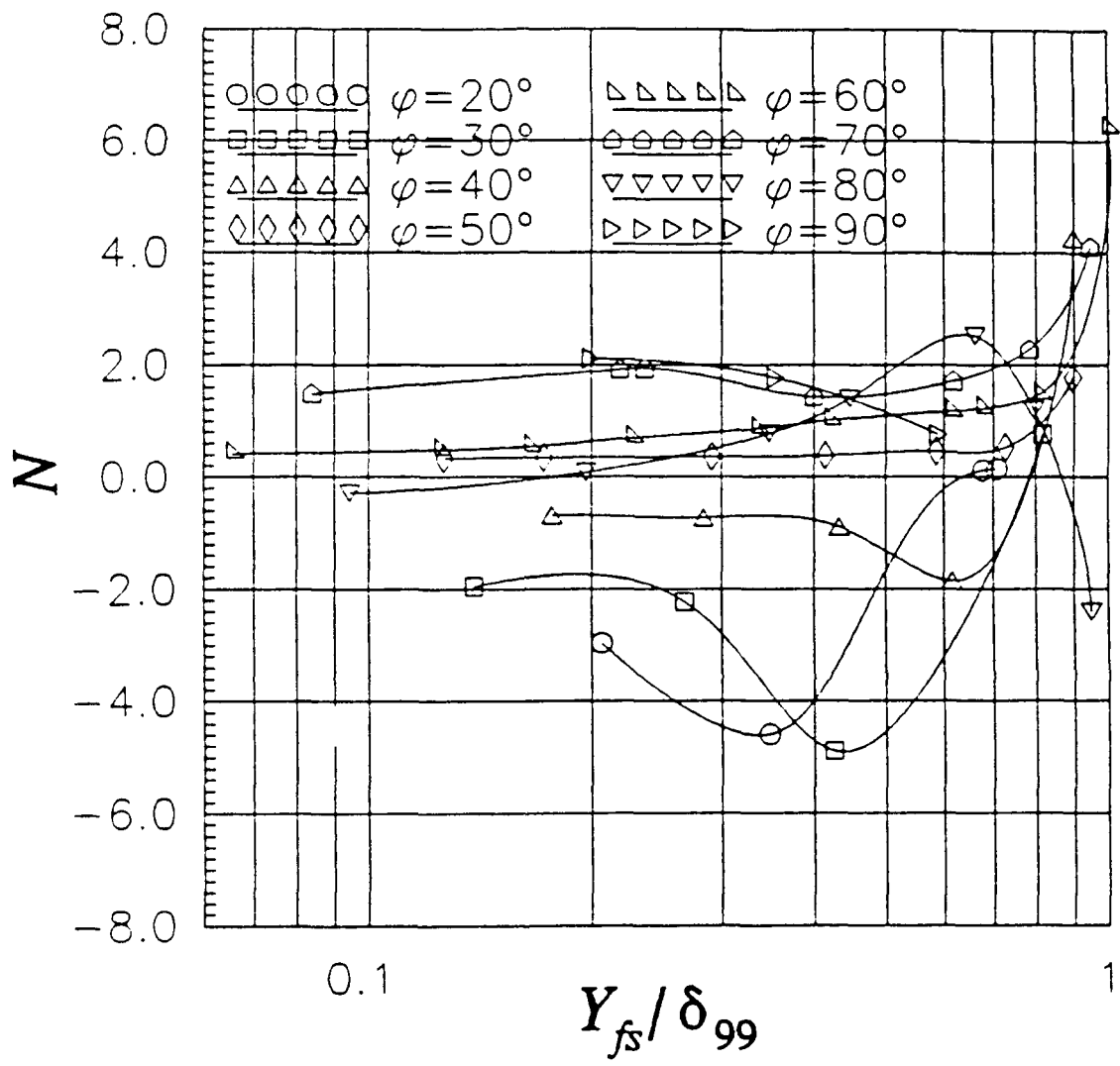
Figure 142.   Profiles of Anisotropy Constant N, X/L=0.7, Re=4.0×10⁶, α=10°, Local Free-Stream Coordinates.
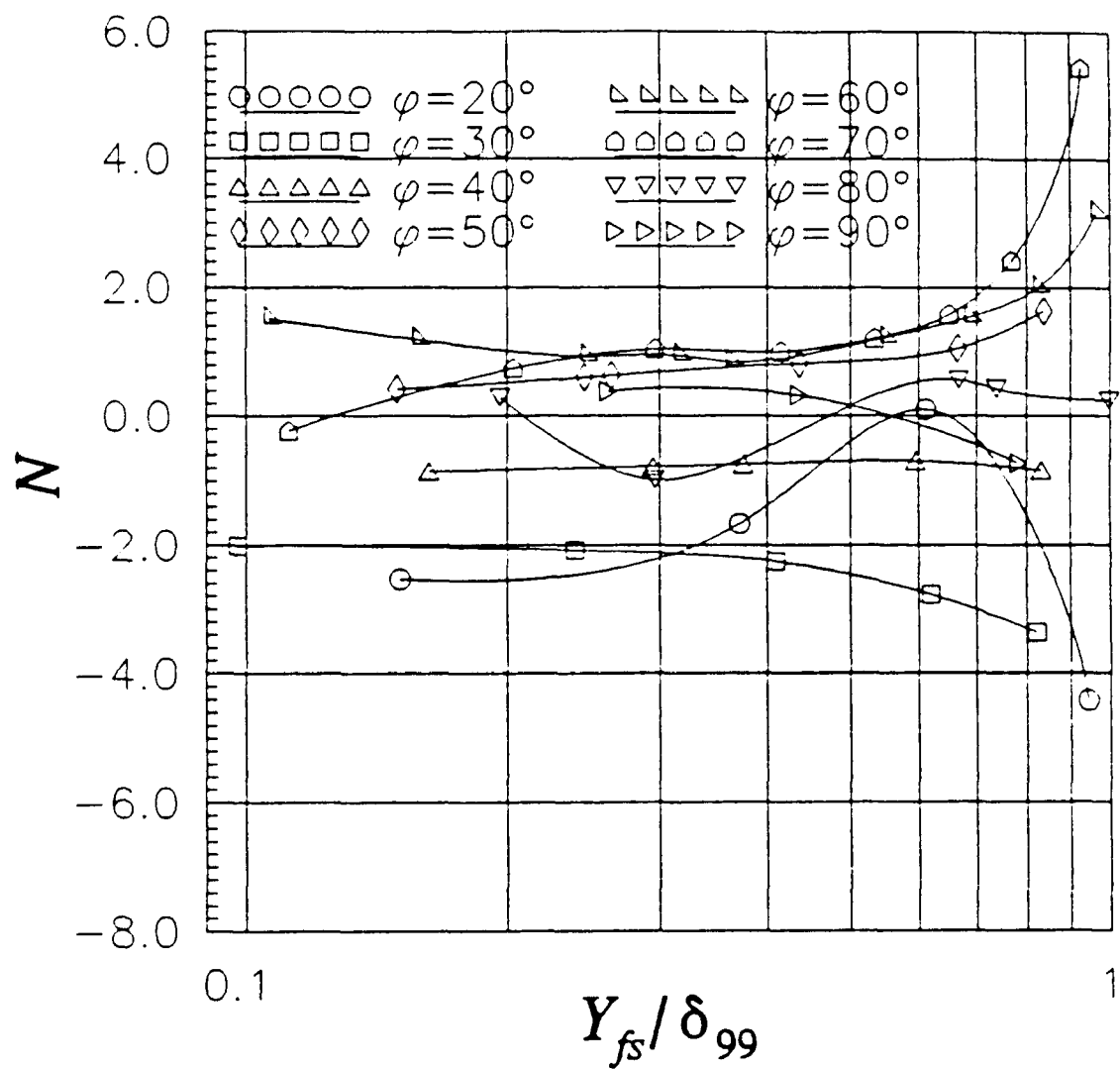
Figure 143.    Profiles of Anisotropy Constant N, X/L=0.8, Re=4.0×10⁶, α=10°, Local Free-Stream Coordinates.
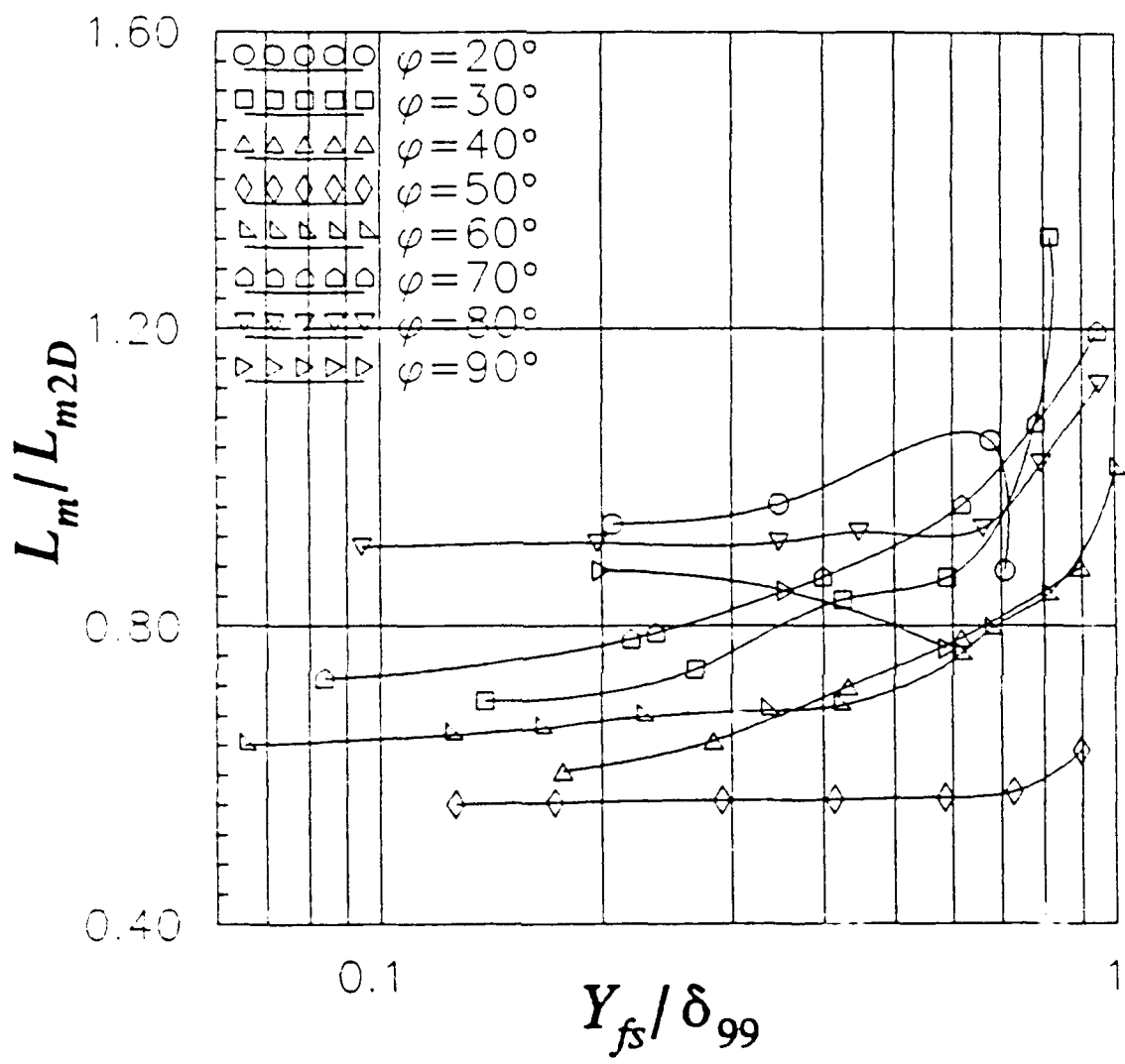
Figure 144.    Profiles of Mixing Length $L_m/L_{m2D}$, $X/L=0.7$, $Re=4.0\times10^6$, $\alpha=10°$, Local Free-Stream Coordinates.
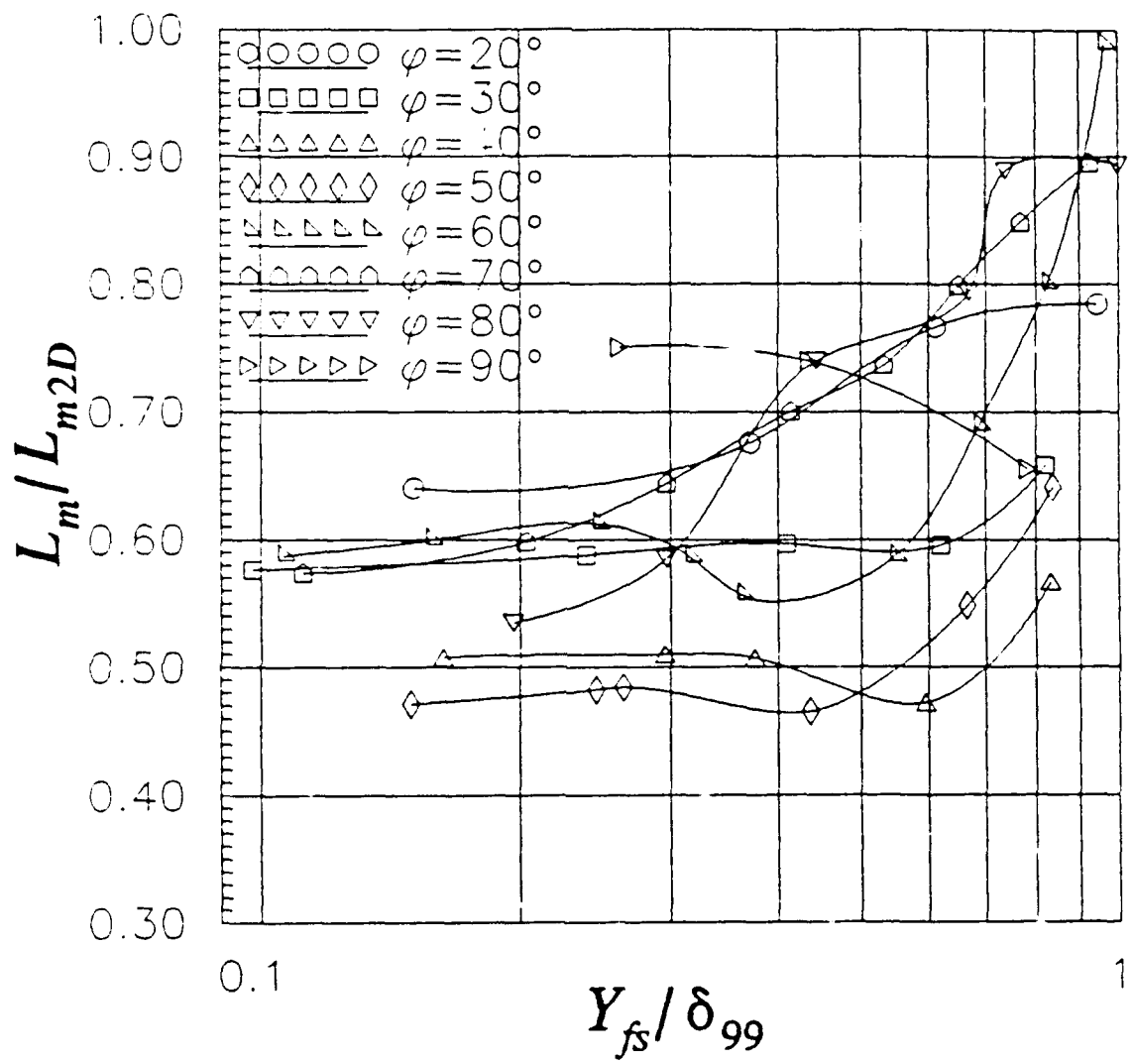
Figure 145.  Profiles of Mixing Length $L_m/L_{m2D}$, $X/L=0.8$, $Re=4.0\times10^6$, $\alpha=10°$, Local Free-Stream Coordinates.
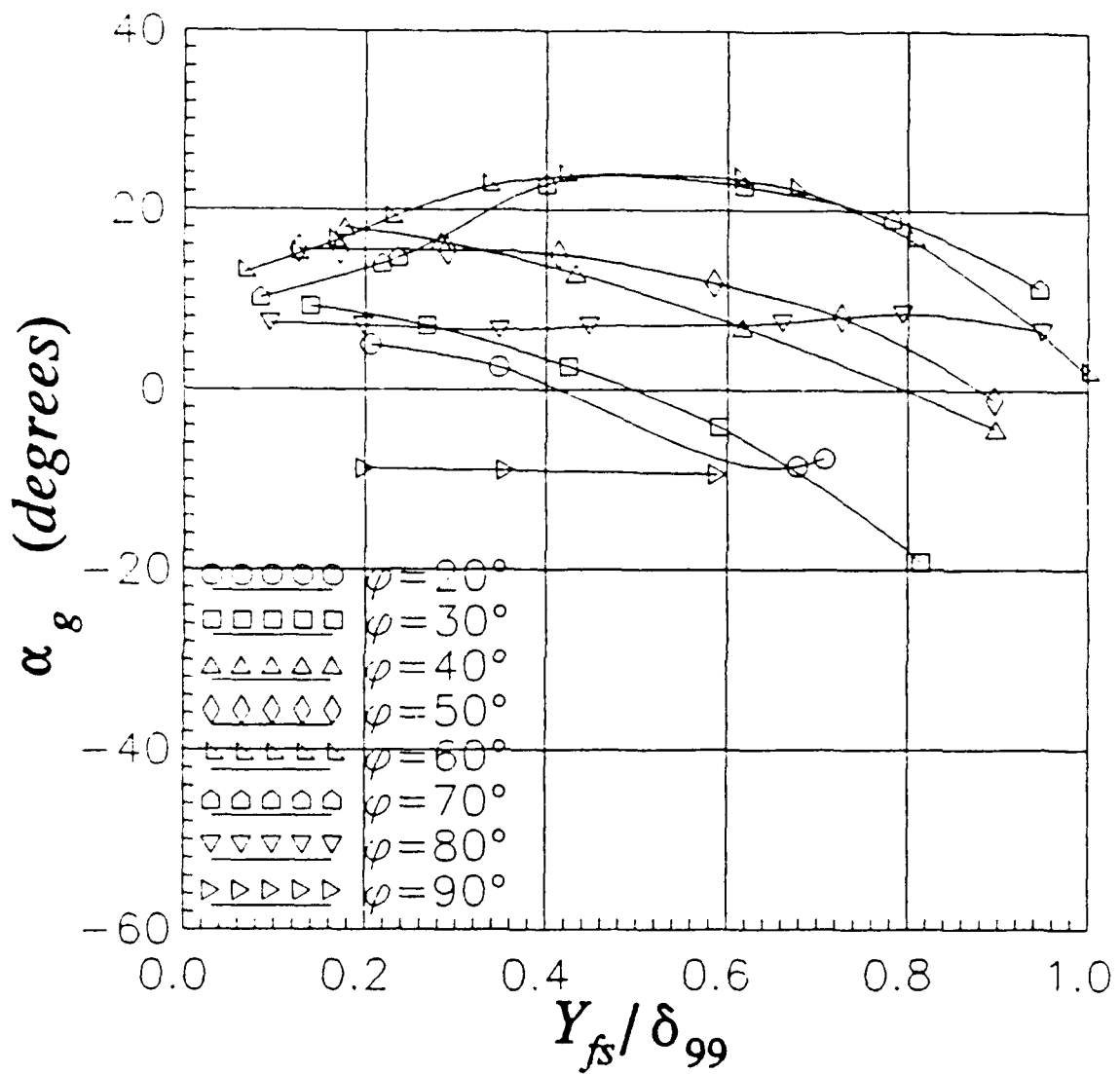
Figure 146.    Profiles of Flow Gradient Angle $\alpha_g$, X/L=0.7, Re=$4.0\times10^6$, $\alpha=10°$, Local Free-Stream Coordinates.
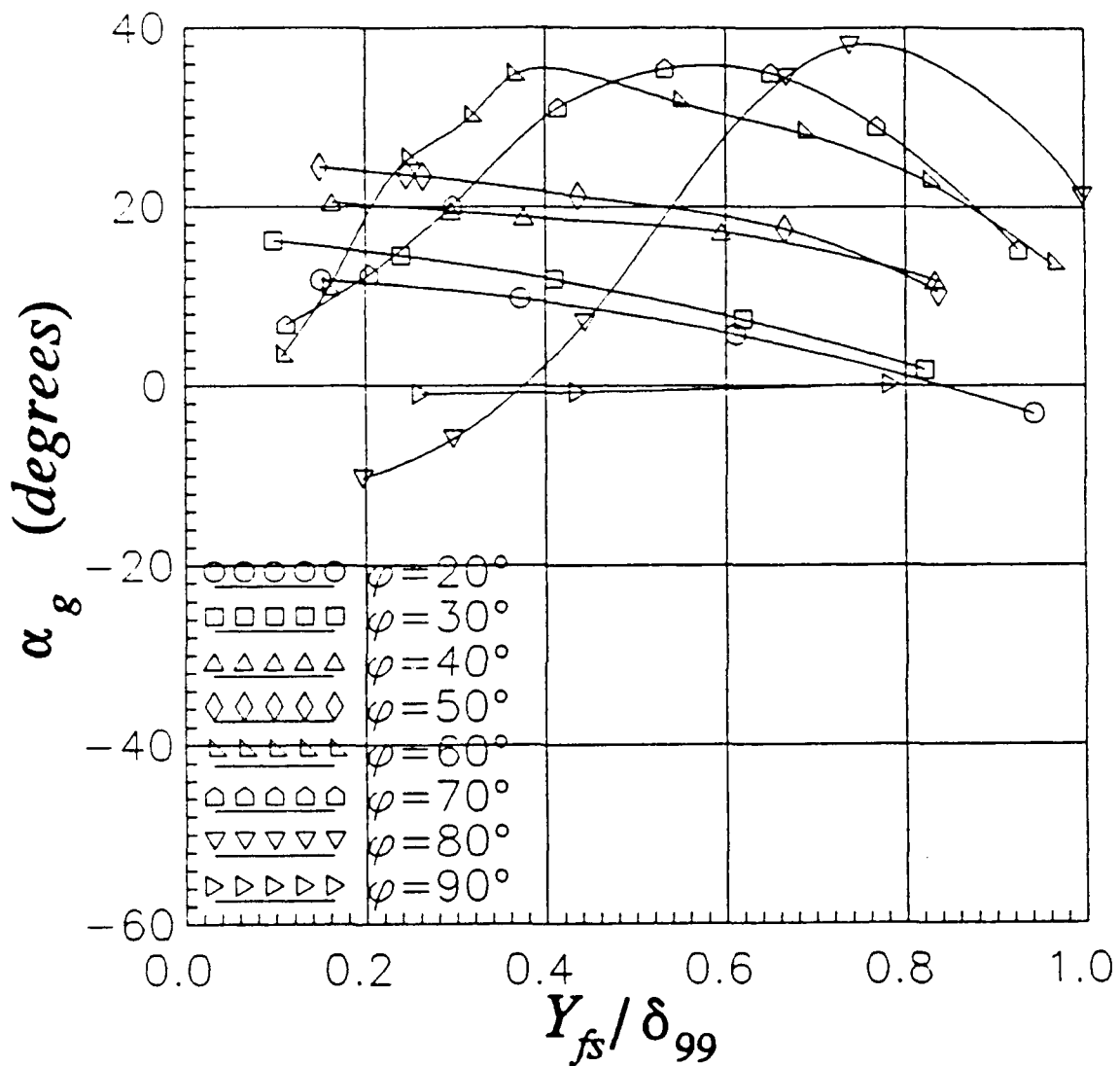
Figure 147.    Profiles of Flow Gradient Angle $\alpha_g$, X/L=0.8, Re=4.0×10$^6$, $\alpha$=10°, Local Free-Stream Coordinates.
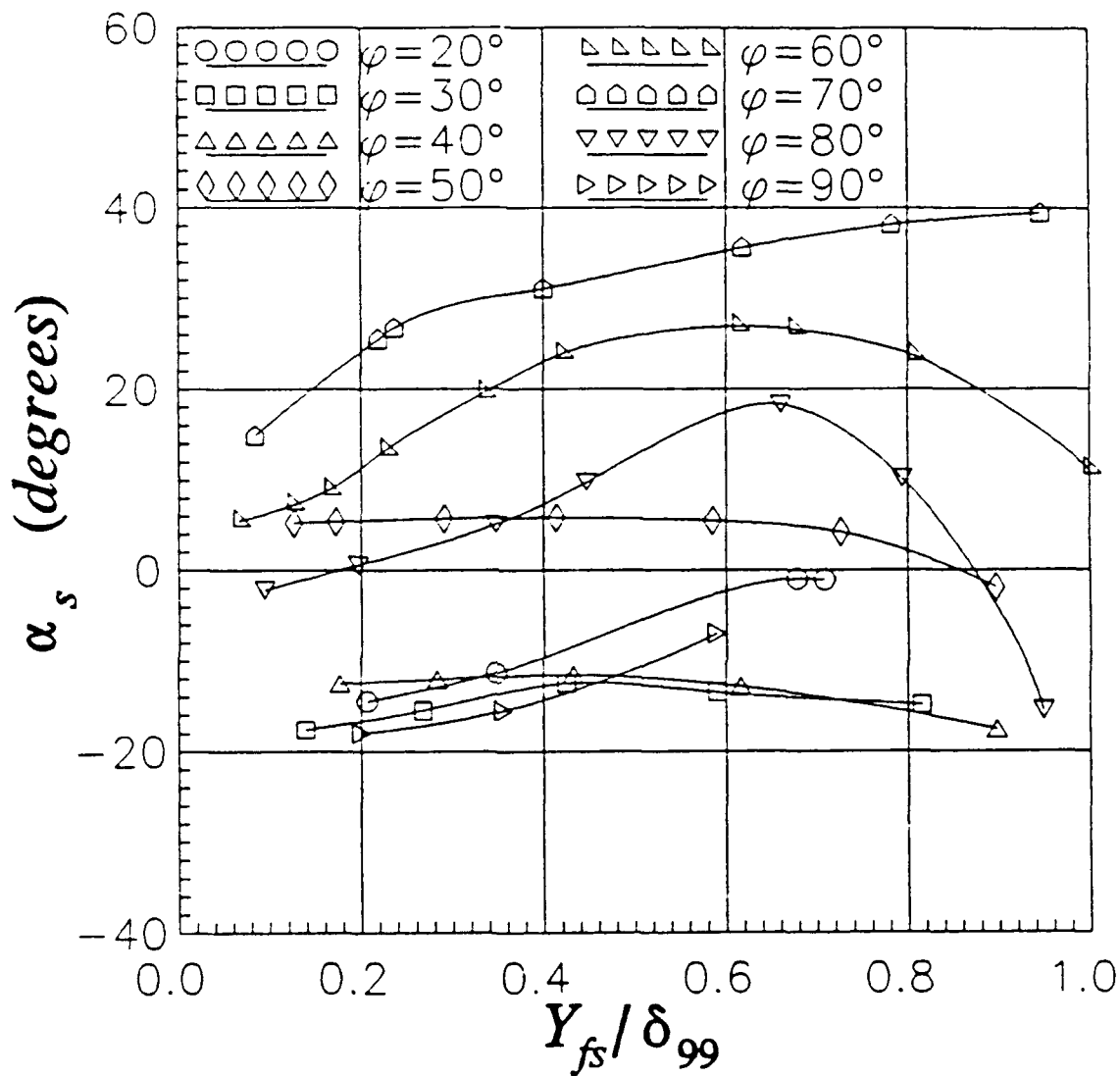
Figure 148.    Profiles of Shear Stress Angle $\alpha_s$, X/L=0.7, Re=4.0×10⁶, $\alpha$=10°, Local Free-Stream Coordinates.
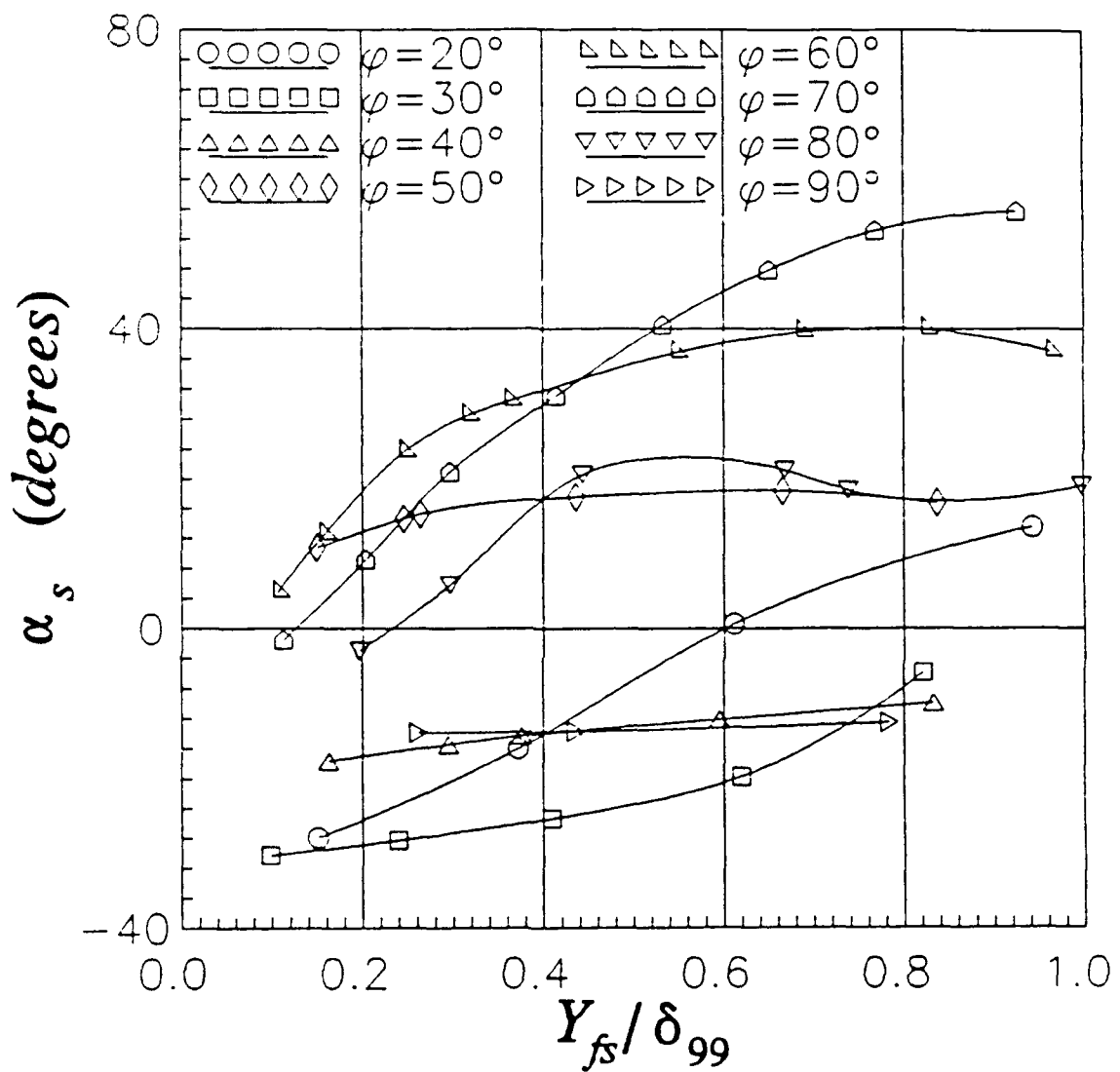
Figure 149. Profiles of Shear Stress Angle $\alpha_s$, X/L=0.8, Re=$4.0 \times 10^6$, $\alpha = 10°$, Local Free-Stream Coordinates.
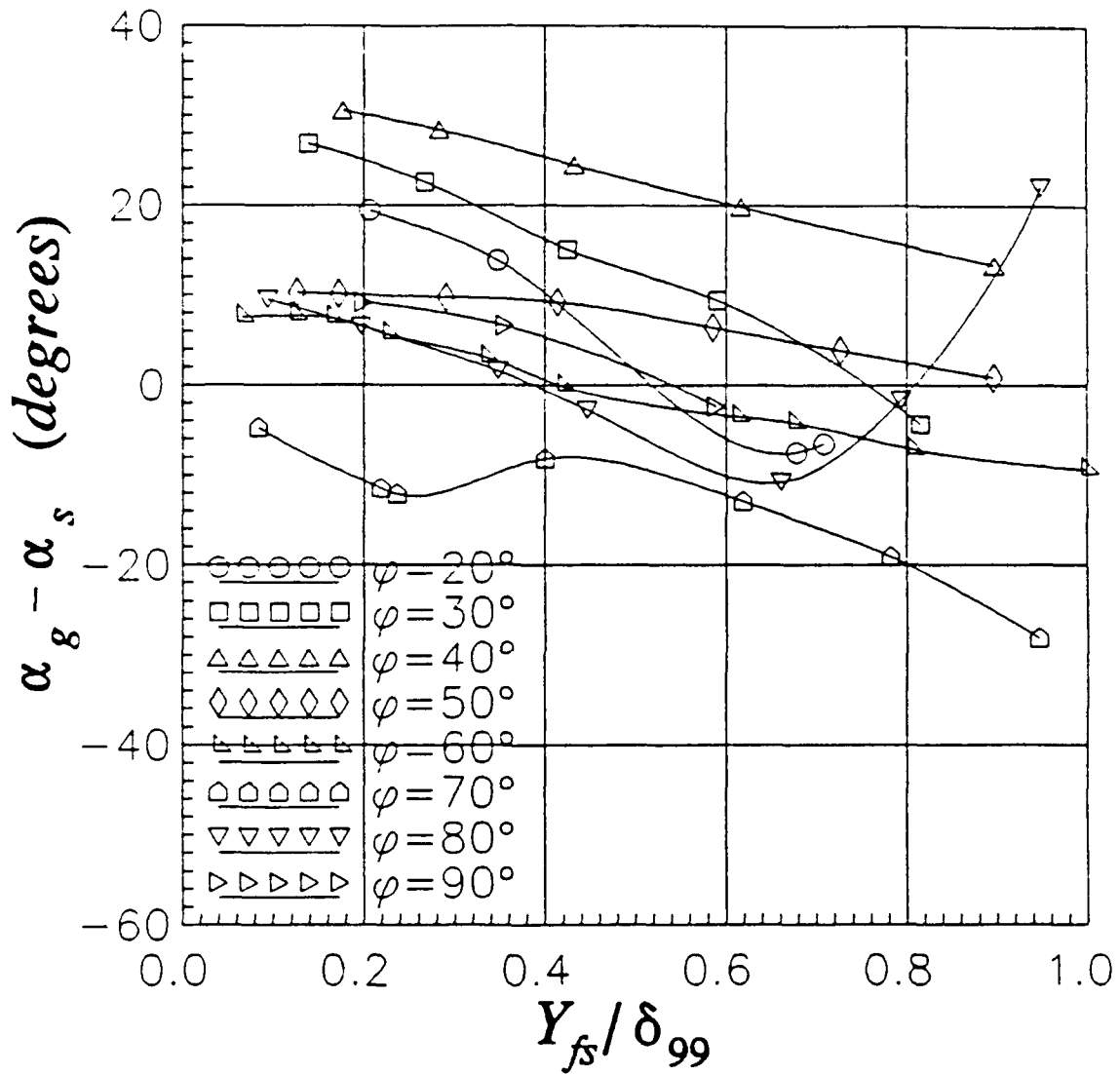
Figure 150. Profiles of Difference Between Flow Gradient Angle and Shear Stress Angle $\alpha_g\text{-}\alpha_s$, X/L=0.7, Re=4.0×10$^6$, $\alpha$=10°, Local Free-Stream Coordinates.
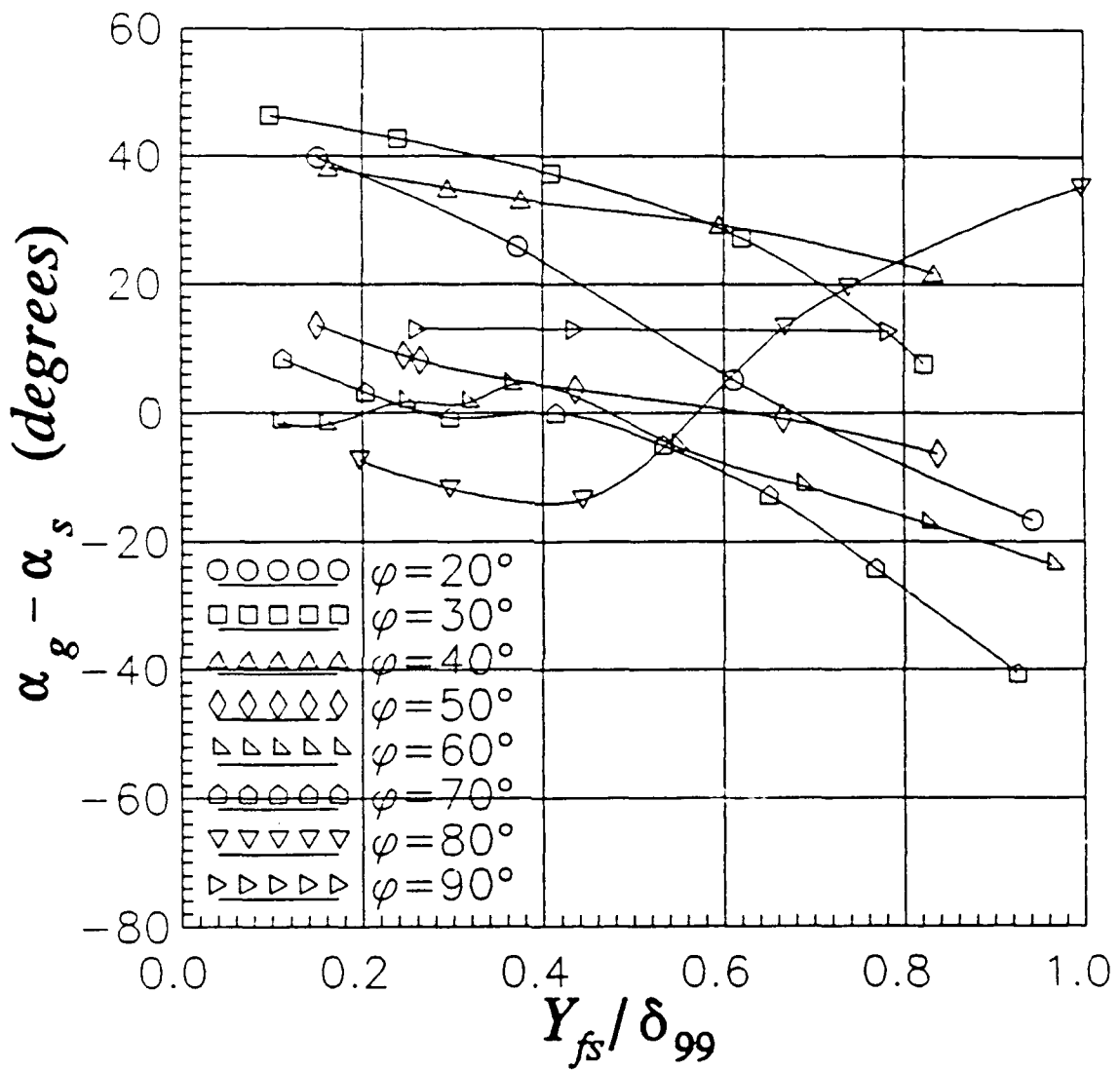
Figure 151.   Profiles of Difference Between Flow Gradient Angle and Shear Stress
Angle $\alpha_g$-$\alpha_s$,  X/L=0.8,  Re=4.0×10$^6$,  $\alpha$=10°,  Local  Free-Stream
Coordinates.

# Tables

Table 1.    DFVLR, West Germany, Measurements and Flow Conditions
            6:1 Prolate Spheroid

| Measurements | Reynolds Number | Angle of Attack (deg) |
|---|---|---|
| Skin friction | $1.6 \times 10^6$ <br> $7.2 \times 10^6$ | 0, 2.5, 5, 10, 30 |
| Surface oil-flow visualizations | $1.6 \times 10^6$ <br> $7.2 \times 10^6$ | 0, 2.5, 5, 10, 30 |
| Surface pressures | $1.6 \times 10^6$ <br> $7.2 \times 10^6$ | 0, 2.5, 5, 10, 30 |
| Boundary layer profiles | $1.6 \times 10^6$ <br> $7.2 \times 10^6$ | 10, 30 |
| Mean velocity field | $1.6 \times 10^6$ <br> $7.2 \times 10^6$ | 10, 30 |
| Reynolds stresses in boundary layer | $7.2 \times 10^6$ | 10 |

Table 2. Boundary Layer Parameters, X/L=0.7

| $\varphi$ | $\delta_{99}$ (cm) | $\delta^*$ (cm) | $\theta$ (cm) | H |
|-----------|--------------------|-----------------|---------------|-------|
| 20° | 0.870 | 0.121 | 0.085 | 1.424 |
| 30° | 1.041 | 0.159 | 0.119 | 1.336 |
| 40° | 1.121 | 0.174 | 0.122 | 1.426 |
| 50° | 1.677 | 0.315 | 0.212 | 1.486 |
| 60° | 1.773 | 0.304 | 0.219 | 1.388 |
| 70° | 1.923 | 0.246 | 0.187 | 1.316 |
| 80° | 1.404 | 0.164 | 0.125 | 1.312 |
| 90° | 1.263 | 0.165 | 0.120 | 1.375 |

Table 3. Boundary Layer Parameters, X/L=0.8

| $\varphi$ | $\delta_{99}$ (cm) | $\delta^*$ (cm) | $\theta$ (cm) | H |
|---|---|---|---|---|
| 20° | 1.072 | 0.194 | 0.132 | 1.470 |
| 30° | 1.718 | 0.341 | 0.228 | 1.496 |
| 40° | 1.802 | 0.422 | 0.266 | 1.586 |
| 50° | 2.258 | 0.474 | 0.315 | 1.505 |
| 60° | 2.470 | 0.433 | 0.311 | 1.392 |
| 70° | 2.669 | 0.384 | 0.292 | 1.315 |
| 80° | 2.038 | 0.235 | 0.175 | 1.343 |
| 90° | 1.699 | 0.234 | 0.169 | 1.385 |

# Appendix A.  Yawhead Probe Data Reduction

The data reduction method and equations for the mean flow measurements performed using the three-dimensional yawhead probe are taken from Sung (1985). At each data point, the pressures at each of the five ports on the probe, shown in Figure 10, were measured and recorded, along with the tunnel free-stream temperature and pressure. Once the data were taken at a measurement point, the following sets of equations were used to obtain the three components of the velocity in probe coordinates.

The dimensionless pressure coefficients are given by:

$$
\begin{aligned}
C_{P_{pitch}} &= \frac{(P_4 - P_5)}{A} = f_1(\alpha,\beta) \\[2mm]
C_{P_{yaw}} &= \frac{(P_2 - P_3)}{A} = f_2(\alpha,\beta) \\[2mm]
C_{P_{total}} &= \frac{(P_1 - P_T)}{A} = f_3(\alpha,\beta) \\[2mm]
C_{P_{static}} &= \frac{(P_{S,avg} - P_S)}{A} = f_4(\alpha,\beta)
\end{aligned}
\tag{A.1}
$$

where $P_1$ through $P_5$ refer to the pressures at the five ports, $P_T$ is the total pressure, $P_S$ is the static pressure, $\alpha$ is the pitch angle, $\beta$ is the yaw angle, and $A$ and $P_{S,avg}$ are given by:

$$A = P_1 - P_{S_{avg}}$$
$$P_{S_{avg}} = \frac{(P_2 + P_3 + P_4 + P_5)}{4} \qquad \text{(A.2)}$$

The functions $f_1$ through $f_4$ are calibration curves determined by Sung (1985).

After the pressures $P_1$ through $P_5$ are measured, the quantities $A$, $P_{S,avg}$, $C_{p,pitch}$, and $C_{p,yaw}$ are determined. The calibration curves $f_1$ and $f_2$ are used to determine $\alpha$ and $\beta$. Then $P_T$ and $P_S$ are found using the calibration curves $f_3$ and $f_4$. The magnitude of the velocity vector $U_{tot}$ is found using the incompressible form of Bernoulli's equation as follows:

$$U_{tot} = \sqrt{\frac{2(P_T - P_S)}{\rho_\infty}} \qquad \text{(A.3)}$$

The components of the velocity vector in probe coordinates are calculated from:

$$U = |U_{tot}| \cos\alpha \cos\beta$$
$$V = |U_{tot}| \sin\beta \qquad \text{(A.4)}$$
$$W = |U_{tot}| \sin\alpha \cos\beta$$

# Appendix B. X-Wire Data Reduction Methods

## Appendix B.1 X-Wire Response Equations

This appendix describes the techniques used with the x-wire hot-wire anemometer

to obtain mean velocity and turbulence quantities. As shown in Figure 6, the DANTEC

55P61 probe has two sensors, denoted by subscripts 1 and 2, arranged nominally at

$\theta = \pm 45°$ with respect to the $X_H$ axis (probe axis). According to Jorgensen (1971), the

relationship between the effective cooling velocity of a sensor and the normal, tangential,

and out-of-plane cooling velocities is given by:

$$U_{eff}^2 = U_N^2 + k_T^2 U_T^2 + k_N^2 U_B^2 \qquad (B.1)$$

The tangential and normal coefficients, $k_T$ and $k_N$, were initially estimated by placing the

probe at different orientations in a TSI Model 1125 calibrator, assuming that $\theta = \pm 45°$.

The resulting values were compared with those obtained by Ha (1989) for an identical

DANTEC 55P61 probe, and found to be within 15% of that data. Therefore, because

the calibrations from Ha were made using a more precise set-up for measuring the pitch

and yaw angles of the probe, the values from Ha (1989) were used in the data reduction. Because the coefficients are dependent upon the orientation of the sensor with respect to the free-stream velocity and the present data acquisition and reduction method utilizes rolling of the probe about its axis to obtain all six Reynolds stress quantities, curve fits of $k_T$ and $k_N$ with respect to yaw and pitch angles were made with the data from Ha and used during the data reduction.

Before and after acquiring data for each run, the probe was calibrated in the Stability Wind Tunnel by placing the probe axis parallel to the tunnel free-stream velocity. The tunnel velocity was run at different settings between 0 fps and 180 fps, and at each velocity the linearized output voltages from the sensors were stored. A linear least squares curve fit was made for each calibration, of the form:

$$E = A + BV \qquad\qquad (B.2)$$

where E is the output voltage, V is the effective cooling velocity, and A and B are constants. In each case, the correlation coefficient was greater than 0.999. The tunnel temperature and static pressure were also stored for each calibration.

For each measurement location, the probe was oriented to five different probe roll angles shown in Figure 6 and mean and rms voltages for each sensor were recorded. After acquiring all the data for a run, the voltages were converted to effective cooling velocities for each sensor using the linearized calibrations, and corrections for temperature changes were made using the method from Larsen and Busch (1974). These involved corrections of the constant B in equation (B.2) for each data point, of the form:

$$B_{corr} = B(1 - \beta_1 \epsilon)^{1/n} \frac{p}{p_0}$$

where p is the tunnel static pressure, $p_0$ is the calibration reference pressure, n is the exponent from King's Law determined during the calibrations, $\beta_1$ is a parameter equal to 1.09 according to Larsen and Busch, and $\epsilon$ is given by:

$$\epsilon = \frac{T_g - T_0}{T_w - T_0}$$

In this expression, $T_g$ is the tunnel free-stream temperature, $T_0$ is the calibration reference temperature, and $T_w$ is the temperature of the hot-wire sensors.

The resulting velocities consisted of the mean effective cooling velocity $\overline{U_{eff}}$ and the fluctuating effective cooling velocity $\overline{u_{eff}^2}$ for each sensor and the correlation velocity $\overline{u_{eff1} u_{eff2}}$, at each probe roll angle $\psi$.

In order to obtain all the mean velocity and turbulence measurements at a point, equations for the effective cooling values must be solved. The following derivation gives the required equations.

According to the geometry of the sensor in Figure 6 (Acrivlellis, 1978):

$$\begin{aligned}
U_N &= (U+u)\cos\theta + [(V+v)\cos\psi + (W+w)\sin\psi]\sin\theta \\
U_T &= -(U+u)\sin\theta + [(V+v)\cos\psi + (W+w)\sin\psi]\cos\theta \\
U_B &= -(V+v)\sin\psi + (W+w)\cos\psi
\end{aligned} \qquad (B.3)$$

Now define:

$$A = \cos^2\theta + k_T^2\sin^2\theta$$

$$B = \sin^2\theta + k_T^2\sin^2\theta$$

$$D = 2\cos\theta\sin\theta - 2k_T^2\cos\theta\sin\theta$$

$$= \left(1 - k_T^2\right)\sin 2\theta \qquad\qquad (B.4)$$

$$F = \sin^2\theta + k_T^2\cos^2\theta - k_N^2$$

$$= B - k_N^2$$

Substitute equations (B.3) and (B.4) into equation (B.1) to obtain:

$$U_{\text{eff}}^2 = (U + u)^2 A$$

$$+ (V + v)^2\left(B\cos^2\psi + k_N^2 \sin^2\psi\right)$$

$$+ (W + w)^2\left(B\sin^2\psi + k_N^2 \sin^2\psi\right) \qquad (B.5)$$

$$+ (U + u)(V + v)D\cos\psi$$

$$+ (U + u)(V + v)D\sin\psi$$

$$+ (V + v)(W + w)F\sin 2\psi$$

Expand the products in equation (B.5), and assume $u^2$, $v^2$, $w^2$, uv, uw, and vw are much smaller than U. Now define the following:

$$A' = A$$

$$B' = B\cos^2\psi + k_N^2\sin^2\psi$$

$$C' = B\sin^2\psi + k_N^2\cos^2\psi \qquad\qquad (B.6)$$

$$D' = D\cos\psi$$

$$E' = D\sin\psi$$

$$F' = F\sin 2\psi$$

and substitute equation (B.6) into equation (B.5) to obtain:

$$U_{eff}^2 = A'U^2 + 2A'Uu + B'V^2 + 2B'Vv$$
$$+ C'W^2 + 2C'Ww + D'UV + D'Uv \qquad \text{(B.7)}$$
$$+ D'uV + E'UW + E'Uw + E'uW$$
$$+ F'VW + F'Vw + F'vW$$

Factor out $A'U^2$ in equation (B.7) and use binomial expansion to find the square root, neglecting higher order terms. The result is:

$$U_{eff} = \sqrt{A'}(U+u) + \frac{D'}{2\sqrt{A'}}(V+v) + \frac{E'}{2\sqrt{A'}}(W+w)$$
$$+ \frac{B'V}{2\sqrt{A'}U}(V+2v) + \frac{C'W}{2\sqrt{A'}U}(W+2w) \qquad \text{(B.8)}$$
$$+ \frac{F'}{2\sqrt{A'}U}(VW+Vw+vW) + \frac{u}{2\sqrt{A'}U}(D'V+E'W)$$

Take the time mean and neglect smaller terms in equation (B.8) to obtain:

$$\overline{U_{eff}} = \sqrt{A'}U + \frac{D'}{2\sqrt{A'}}V + \frac{E'}{2\sqrt{A'}}W \qquad \text{(B.9)}$$

To find the turbulence quantity, use the fact that:

$$u_{eff} = U_{eff} - \overline{U_{eff}} \qquad \text{(B.10)}$$

to obtain:

$$u_{eff} = \left(\sqrt{A'} + \frac{D'V+E'W}{2\sqrt{A'}U}\right)u + \left(\frac{D'}{2\sqrt{A'}} + \frac{B'V}{\sqrt{A'}U} + \frac{F'W}{2\sqrt{A'}U}\right)v$$
$$+ \left(\frac{E'}{2\sqrt{A'}} + \frac{C'W}{\sqrt{A'}U} + \frac{F'V}{2\sqrt{A'}U}\right)w \qquad \text{(B.11)}$$

Define the terms in brackets in equation (B.11) as P, Q, and R to obtain the following for each sensor:

$$u_{eff1} = P_1 u + Q_1 v + R_1 w$$
$$u_{eff2} = P_2 u + Q_2 v + R_2 w$$

(B.12)

Square each of the expressions in equation (B.12) and take the time mean, and also find the product of the two expressions in equation (B.12) and take the time mean to obtain:

$$\overline{u_{eff1}^2} = P_1^2 \overline{u^2} + Q_1^2 \overline{v^2} + R_1^2 \overline{w^2} + 2P_1 Q_1 \overline{uv} + 2P_1 R_1 \overline{uw} + 2Q_1 R_1 \overline{vw}$$

$$\overline{u_{eff2}^2} = P_2^2 \overline{u^2} + Q_2^2 \overline{v^2} + R_2^2 \overline{W^2} + 2P_2 Q_2 \overline{uv} + 2P_2 R_2 \overline{uw} + 2Q_2 R_2 \overline{vw}$$

(B.13)

$$\overline{u_{eff1} u_{eff2}} = P_1 P_2 \overline{u^2} + Q_1 Q_2 \overline{v^2} + R_1 R_2 \overline{w^2} + (P_1 Q_2 + P_2 Q_1)\overline{uv}$$
$$+ (P_1 R_2 + P_2 R_1)\overline{uw} + (Q_1 R_2 + Q_2 R_1)\overline{vw}$$

Equation (B.9) contains the three desired mean velocities U, V, and W. To solve for these quantities, three independent equations are necessary. The three equations (B.13) contain the six desired Reynolds stress quantities. In order to solve for these quantities, six independent equations are necessary. Therefore, the x-wire probe was rolled to the five different angles shown in Figure 6. At each roll angle, as previously described, $\overline{U_{eff}}$ and $\overline{u_{eff}^2}$ for each sensor and the correlation $\overline{u_{eff1} u_{eff2}}$ were obtained.

To obtain estimates of the three components of the mean velocities, the expressions for $\overline{U_{eff}}$ (equation B.9) for each sensor at the various roll angles were grouped as follows:

Group 1: $\overline{U_{eff1}}(\psi = 0°)$, $\overline{U_{eff1}}(\psi = 90°)$, $\overline{U_{eff1}}(\psi = 180°)$

Group 2: $\overline{U_{eff2}}(\psi = 0°)$, $\overline{U_{eff2}}(\psi = 90°)$, $\overline{U_{eff2}}(\psi = 180°)$

Group 3: $\overline{U_{\mathit{eff1}}}(\psi=45°)$, $\overline{U_{\mathit{eff1}}}(\psi=90°)$, $\overline{U_{\mathit{eff1}}}(\psi=135°)$

Group 4: $\overline{U_{\mathit{eff2}}}(\psi=45°)$, $\overline{U_{\mathit{eff2}}}(\psi=90°)$, $\overline{U_{\mathit{eff2}}}(\psi=135°)$

The three equations in each of the four groups were solved simultaneously to find estimates of U, V, and W, and these estimates were averaged to obtain the final values. The estimates for each mean velocity agreed to within approximately 3% of the averages.

To find the turbulence quantities, the expressions in equation (B.13) for each sensor at the various roll angles were grouped as follows:

Group 1: $\overline{u_{\mathit{eff1}}^{2}}(\psi=0°)$, $\overline{u_{\mathit{eff1}}^{2}}(\psi=45°)$, $\overline{u_{\mathit{eff1}}^{2}}(\psi=90°)$,

$\overline{u_{\mathit{eff1}}^{2}}(\psi=135°)$, $\overline{u_{\mathit{eff1}}^{2}}(\psi=180°)$, $\overline{u_{\mathit{eff1}}u_{\mathit{eff2}}}(\psi=0°)$

Group 2: $\overline{u_{\mathit{eff2}}^{2}}(\psi=0°)$, $\overline{u_{\mathit{eff2}}^{2}}(\psi=45°)$, $\overline{u_{\mathit{eff2}}^{2}}(\psi=90°)$,

$\overline{u_{\mathit{eff2}}^{2}}(\psi=135°)$, $\overline{u_{\mathit{eff2}}^{2}}(\psi=180°)$, $\overline{u_{\mathit{eff1}}u_{\mathit{eff2}}}(\psi=0°)$

Group 3: $\overline{u_{\mathit{eff1}}^{2}}(\psi=0°)$, $\overline{u_{\mathit{eff1}}^{2}}(\psi=45°)$, $\overline{u_{\mathit{eff1}}^{2}}(\psi=90°)$,

$\overline{u_{\mathit{eff1}}^{2}}(\psi=135°)$, $\overline{u_{\mathit{eff1}}^{2}}(\psi=180°)$, $\overline{u_{\mathit{eff1}}u_{\mathit{eff2}}}(\psi=45°)$

Group 4: $\overline{u_{\mathit{eff2}}^{2}}(\psi=0°)$, $\overline{u_{\mathit{eff2}}^{2}}(\psi=45°)$, $\overline{u_{\mathit{eff2}}^{2}}(\psi=90°)$,

$\overline{u_{\mathit{eff2}}^{2}}(\psi=135°)$, $\overline{u_{\mathit{eff2}}^{2}}(\psi=180°)$, $\overline{u_{\mathit{eff1}}u_{\mathit{eff2}}}(\psi=45°)$

Group 5: $\overline{u_{\mathit{eff1}}^{2}}(\psi=0°)$, $\overline{u_{\mathit{eff1}}^{2}}(\psi=45°)$, $\overline{u_{\mathit{eff1}}^{2}}(\psi=90°)$,

$\overline{u_{\mathit{eff1}}^{2}}(\psi=135°)$, $\overline{u_{\mathit{eff1}}^{2}}(\psi=180°)$, $\overline{u_{\mathit{eff1}}u_{\mathit{eff2}}}(\psi=90°)$

Group 6: $\overline{u_{\mathit{eff2}}^{2}}(\psi=0°)$, $\overline{u_{\mathit{eff2}}^{2}}(\psi=45°)$, $\overline{u_{\mathit{eff2}}^{2}}(\psi=90°)$,

$\overline{u_{\mathit{eff2}}^{2}}(\psi=135°)$, $\overline{u_{\mathit{eff2}}^{2}}(\psi=180°)$, $\overline{u_{\mathit{eff1}}u_{\mathit{eff2}}}(\psi=90°)$

Group 7: $\overline{u_{\mathit{eff1}}^{2}}(\psi=0°)$, $\overline{u_{\mathit{eff1}}^{2}}(\psi=45°)$, $\overline{u_{\mathit{eff1}}^{2}}(\psi=90°)$,

$\overline{u_{\mathit{eff1}}^{2}}(\psi=135°)$, $\overline{u_{\mathit{eff1}}^{2}}(\psi=180°)$, $\overline{u_{\mathit{eff1}}u_{\mathit{eff2}}}(\psi=135°)$

Group 8: $\overline{u_{\mathit{eff2}}^{2}}(\psi=0°)$, $\overline{u_{\mathit{eff2}}^{2}}(\psi=45°)$, $\overline{u_{\mathit{eff2}}^{2}}(\psi=90°)$,

$\overline{u_{\mathit{eff2}}^{2}}(\psi=135°)$, $\overline{u_{\mathit{eff2}}^{2}}(\psi=180°)$, $\overline{u_{\mathit{eff1}}u_{\mathit{eff2}}}(\psi=135°)$

Group 9: $\overline{u_{\mathit{eff1}}^{2}}(\psi=0°)$, $\overline{u_{\mathit{eff1}}^{2}}(\psi=45°)$, $\overline{u_{\mathit{eff1}}^{2}}(\psi=90°)$,

$$\overline{u^2_{\mathit{eff1}}}(\psi = 135°), \ \overline{u^2_{\mathit{eff1}}}(\psi = 180°), \ \overline{u_{\mathit{eff1}}u_{\mathit{eff2}}}(\psi = 180°)$$

Group 10: $\quad \overline{u^2_{\mathit{eff2}}}(\psi = 0°), \ \overline{u^2_{\mathit{eff2}}}(\psi = 45°), \ \overline{u^2_{\mathit{eff2}}}(\psi = 90°),$

$$\overline{u^2_{\mathit{eff2}}}(\psi = 135°), \ \overline{u^2_{\mathit{eff2}}}(\psi = 180°), \ \overline{u_{\mathit{eff1}}u_{\mathit{eff2}}}(\psi = 180°)$$

The six equations in each group were solved simultaneously to obtain a total of ten estimates for each of the desired turbulence values, and these estimates were averaged to obtain the final values. The estimates for $\overline{u^2}$, $\overline{v^2}$, and $\overline{w^2}$ agreed to within 6% of the averages. The estimates for $\overline{uv}$ and $\overline{uw}$ agreed to within 12% of the averages, and the estimates for $\overline{vw}$ agreed to within 20% of the averages.

After the desired values were obtained in probe coordinates, they were transformed to tunnel coordinates using a tensor transformation, taking into account the pitch angle $\alpha_H$ of the probe with respect to the $X_T$ axis, as shown in Figure 6. The equations for this transformation are given below, in which the subscript H refers to the hot-wire probe coordinates and the subscript T refers to tunnel coordinates:

$$U_T = U_H\cos\alpha_H + V_H\sin\alpha_H$$
$$V_T = -U_H\sin\alpha_H + V_H\cos\alpha_H$$
$$W_T = W_H$$
$$\overline{u^2}_T = \overline{u^2}_H\cos^2\alpha_H + 2\overline{uv}_H\cos\alpha_H\sin\alpha_H + \overline{v^2}_H\sin^2\alpha_H$$
$$\overline{v^2}_T = \overline{u^{2\prime}}_H\sin^2\alpha_H - 2\overline{uv}_H\cos\alpha_H\sin\alpha_H + \overline{v^2}_H\cos^2\alpha_H$$
$$\overline{w^2}_T = \overline{w^2}_H$$
$$\overline{uv}_T = \left(\overline{v^2}_H - \overline{u^2}_H\right)\cos\alpha_H\sin\alpha_H + \overline{uv}_H\left(\cos^2\alpha_H - \sin^2\alpha_H\right)$$
$$\overline{uw}_T = \overline{uw}_H\cos\alpha_H + \overline{vw}_H\sin\alpha_H$$
$$\overline{vw}_T = -\overline{uw}_H\sin\alpha_H + \overline{vw}_H\cos\alpha_H$$

# Appendix B.2  Data Reduction FORTRAN Program

```
C    XWIRE.FOR                    JANUARY 16, 1990.
C
C   THIS PROGRAM SOLVES FOR THE SIX REYNOLDS STRESSES AND THE THREE
C   MEAN VELOCITY COMPONENTS AT A POINT, WITH MEAN AND RMS VOLTAGES
C   AS INPUTS.  IT SOLVES THE EQUATIONS SIMULTANEOUSLY USING
C   SUBROUTINE
C   THE INPUT VOLTAGES ARE CORRECTED FOR TEMPERATURE DIFFERENCES,
C   USING THE METHOD FROM LARSEN AND BUSCH (1974).  THE QUANTITIES
C   ARE WRITTEN TO A DATA FILE IN PROBE COORDINATES.
C
      REAL UEFF1(10),UEFF2(10),UBAR(10),VBAR(10),WBAR(10)
      REAL UPEFF1(10),UPEFF2(10),U12PEFF(10),UP2(10),VP2(10),WP2(10)
      REAL UVP(10),UWP(10),VWP(10),PHI(5)
      REAL A(2,2),B(2),X(2),AA(6,6),BB(6),XX(6)
      REAL AP1(5),BP1(5),CP1(5),DP1(5),EP1(5),FP1(5)
      REAL AP2(5),BP2(5),CP2(5),DP2(5),EP2(5),FP2(5)
      REAL P1(5),Q1(5),R1(5),P2(5),Q2(5),R2(5)
      REAL KN1(5),KN2(5),KT1(5),KT2(5),NCAL1,NCAL2
      REAL A1(5),A2(5),B1(5),B2(5),D1(5),D2(5),F1(5),F2(5)
      INTEGER ORDER(2),ORDER1(6)
C
C   BETA1 IS GIVEN IN LARSEN AND BUSCH (1974)
C   TWIRE IS HOT-WIRE TEMPERATURE
C   PROMPTS FOR CONDITIONS AT CALIBRATION
C
      BETA1=1.09
      TWIRE=200.0
      WRITE(*,*) 'ENTER CALIBRATION TEMP(F), PRESSURE(PSI), N1 AND N2'
      READ(*,*) TCAL,PCAL,NCAL1,NCAL2
      TCAL=(TCAL-32.0)*5.0/9.0
C
C   READS CALIBRATION CONSTANTS AND LOCATIONS OF MEASUREMENT.
C
      READ(7,*,END=999) AW1,BW1,AW2,BW2
      WRITE(*,*) 'ENTER Y-LOCATION OF LOWEST PT., IN CM'
      READ(*,*) YFINAL
      WRITE(*,*) 'ENTER DISTANCE FROM LOWEST PT. TO SURFACE, IN CM'
      READ(*,*) DIST
      DIST=YFINAL-DIST
      WRITE(*,*) 'ENTER Z-LOCATION IN INCHES'
      READ(*,*) ZLOC
      PI=3.141592654
```

```
C
C  INITIALIZE TANGENTIAL AND NORMAL COOLING COEFFICIENTS.
C
      DO 2 I=1,5
        KT1(I)=0.3
        KT2(I)=0.3
        KN1(I)=1.14
        KN2(I)=1.14
    2 CONTINUE
C
C  READ WIRE ANGLES
C
      WRITE(*,*) 'INPUT THETA1 AND THETA2 IN DEGREES'
      READ(*,*) THETA1,THETA2
      THETA1=THETA1*PI/180.0
      THETA2=THETA2*PI/180.0
      CT1=COS(THETA1)
      ST1=SIN(THETA1)
      CT2=COS(THETA2)
      ST2=SIN(THETA2)
C
C  CALCULATE COEFFICIENTS FOR DATA REDUCTION EQUATIONS
C
      DO 3 I=1,5
        A1(I)=CT1*CT1+KT1(I)*KT1(I)*ST1*ST1
        B1(I)=ST1*ST1+KT1(I)*KT1(I)*CT1*CT1
        D1(I)=2.0*(1.0-KT1(I)*KT1(I))*CT1*ST1
        F1(I)=B1(I)-KN1(I)*KN1(I)
        A2(I)=CT2*CT2+KT2(I)*KT2(I)*ST2*ST2
        B2(I)=ST2*ST2+KT2(I)*KT2(I)*CT2*CT2
        D2(I)=2.0*(1.0-KT2(I)*KT2(I))*CT2*ST2
        F2(I)=B2(I)-KN2(I)*KN2(I)
    3 CONTINUE
C
C  READ IN VOLTAGES AND CONVERT TO EFFECTIVE VELOCITIES
C
    5 DO 10 I=1,5
        READ(7,*,END=999) YLOC,PHI(I)
        READ(7,*,END=999) E1,E2,E1P,E2P
        READ(7,*,END=999) E1E2P,E1SQ,E2SQ,E1E2
        UEFF1(I)=(E1-AW1)/BW1
        UEFF2(I)=(E2-AW2)/BW2
        UPEFF1(I)=E1P/BW1/BW1
        UPEFF2(I)=E2P/BW2/BW2
        U12PEFF(I)=E1E2P/BW1/BW2
        PHI(I)=PHI(I)*PI/180.0
   10 CONTINUE
      READ(7,*,END=999) YLOC,UINF,TINF,PINF
C
C  CORRECTION FOR TEMPERATURE USING LARSEN AND BUSCH EQUATION
C  INCLUDES CORRECTION FACTORS FOR B1 AND B2
C
```

```
C
      TINF = (TINF-32.0)*5.0/9.0
      EPSILON = (TINF-TCAL)/(TWIRE-TCAL)
      BCORR1 = (1.0-BETA1*EPSILON)**NCAL1*PINF/PCAL
      BCORR2 = (1.0-BETA1*EPSILON)**NCAL2*PINF/PCAL
      DO 15 I = 1,5
        UEFF1(I) = UEFF1(I)/BCORR1
        UEFF2(I) = UEFF2(I)/BCORR2
        UPEFF1(I) = UPEFF1(I)/BCORR1/BCORR1
        UPEFF2(I) = UPEFF2(I)/BCORR1/BCORR2
        U12PEFF(I) = U12PEFF(I)/BCORR1/BCORR2
   15 CONTINUE
C
C     CALCULATE MORE COEFFICIENTS FOR DATA REDUCTION EQUATIONS
C
      DO 20 I = 1,5
        CP = COS(PHI(I))
        SP = SIN(PHI(I))
        AP1(I) = A1(I)
        BP1(I) = B1(I)*CP*CP + KN1(I)*KN1(I)*SP*SP
        CP1(I) = B1(I)*SP*SP + KN1(I)*KN1(I)*CP*CP
        DP1(I) = D1(I)*CP
        EP1(I) = D1(I)*SP
        FP1(I) = F1(I)*SIN(2.0*PHI(I))
        AP2(I) = A2(I)
        BP2(I) = B2(I)*CP*CP + KN1(I)*KN1(I)*SP*SP
        CP2(I) = B2(I)*SP*SP + KN1(I)*KN1(I)*CP*CP
        DP2(I) = D2(I)*CP
        EP2(I) = D2(I)*SP
        FP2(I) = F2(I)*SIN(2.0*PHI(I))
   20 CONTINUE
C
C   LOOP TO CALCULATE THE MEAN VELOCITIES USING LUDCMP AND SOLVLU TO
C   SOLVE SIMULTANEOUS EQUATIONS.
C
      DO 58 LOOP = 1,4
      N = 2
      NDIM = 2
      A(1,1) = SQRT(AP1(1))
      A(1,2) = DP1(1)/2.0/SQRT(AP1(1))
      A(2,1) = SQRT(AP2(1))
      A(2,2) = DP2(1)/2.0/SQRT(AP2(1))
      B(1) = UEFF1(1)
      B(2) = UEFF2(1)
      CALL LUDCMP(A,N,NDIM,ORDER)
      CALL SOLVLU(A,B,X,N,NDIM,ORDER)
      UBAR(1) = X(1)
      VBAR(1) = X(2)
      A(1,1) = SQRT(AP1(3))
      A(1,2) = EP1(3)/2.0/SQRT(AP1(3))
      A(2,1) = SQRT(AP2(3))
      A(2,2) = EP2(3)/2.0/SQRT(AP2(3))
```

```fortran
      B(1)=UEFF1(3)
      B(2)=UEFF2(3)
      CALL LUDCMP(A,N,NDIM,ORDER)
      CALL SOLVLU(A,B,X,N,NDIM,ORDER)
      UBAR(2)=X(1)
      WBAR(1)=X(2)
      A(1,1)=SQRT(AP1(5))
      A(1,2)=DP1(5)/2.0/SQRT(AP1(5))
      A(2,1)=SQRT(AP2(5))
      A(2,2)=DP2(5)/2.0/SQRT(AP2(5))
      B(1)=UEFF1(5)
      B(2)=UEFF2(5)
      CALL LUDCMP(A,N,NDIM,ORDER)
      CALL SOLVLU(A,B,X,N,NDIM,ORDER)
      UBAR(3)=X(1)
      VBAR(2)=X(2)
      A(1,1)=SQRT(AP1(2))
      A(1,2)=DP1(2)/2.0/SQRT(AP1(2))
      A(2,1)=SQRT(AP2(2))
      A(2,2)=DP2(2)/2.0/SQRT(AP2(2))
      B(1)=UEFF1(2)
      B(2)=UEFF2(2)
      CALL LUDCMP(A,N,NDIM,ORDER)
      CALL SOLVLU(A,B,X,N,NDIM,ORDER)
      UBAR(4)=X(1)
      VPW=X(2)
      A(1,1)=SQRT(AP1(4))
      A(1,2)=DP1(4)/2.0/SQRT(AP1(4))
      A(2,1)=SQRT(AP2(4))
      A(2,2)=DP2(4)/2.0/SQRT(AP2(4))
      B(1)=UEFF1(4)
      B(2)=UEFF2(4)
      CALL LUDCMP(A,N,NDIM,ORDER)
      CALL SOLVLU(A,B,X,N,NDIM,ORDER)
      UBAR(5)=X(1)
      VMW=X(2)
      VBAR(3)=(VPW+VMW)/2.0
      WBAR(2)=(VPW-VMW)/2.0
      USUM=0.0
      VSUM=0.0
      WSUM=0.0
      DO 30 I=1,5
        WRITE(*,*) 'Uest = ',UBAR(I)
        USUM=USUM+UBAR(I)
   30 CONTINUE
      UAVG=USUM/5.0
      WRITE(*,*) 'Uavg = ',UAVG
      DO 40 I=1,3
        WRITE(*,*) 'Vest = ',VBAR(I)
        VSUM=VSUM+VBAR(I)
   40 CONTINUE
      VAVG=VSUM/3.0
```

```
       WRITE(*,*) 'Vavg = ',VAVG
       DO 50 I=1,2
         WRITE(*,*) 'West = ',WBAR(I)
         WSUM = WSUM + WBAR(I)
   50 CONTINUE
       WAVG = WSUM/2.0
       WRITE(*,*) 'Wavg = ',WAVG
C
C  FIND NEW COOLING COEFFICIENTS BASED ON MEAN VELOCITIES, USING CURVE
C  FITS TO DATA FROM HA (1989).
C
       DO 55 I=1,5
         CP = COS(PHI(I))
         SP = SIN(PHI(I))
         UN = CT1*UAVG + ST1*CP*VAVG + ST1*SP*WAVG
         UT = -ST1*UAVG + CT1*CP*VAVG + CT1*SP*WAVG
         UB = -SP*VAVG + CP*WAVG
         YAW = ABS(ATAN(UT/UN))
         PITCH = ABS(ATAN(UB/UN))
         KT1(I) = -0.25721*YAW**3 + 1.109*YAW*YAW-1.69116*YAW + 1.15076
         KN1(I) = -0.925408*PITCH**5 + 4.97674*PITCH**4-10.2698*PITCH**3 + 10.2
   12954*PITCH*PITCH-5.13504*PITCH + 2.19519
         UN = CT2*UAVG + ST2*CP*VAVG + ST2*SP*WAVG
         UT = -ST2*UAVG + CT2*CP*VAVG + CT2*SP*WAVG
         UB = -SP*VAVG + CP*WAVG
         YAW = ABS(ATAN(UT/UN))
         PITCH = ABS(ATAN(UB/UN))
         KT2(I) = -0.25721*YAW**3 + 1.109*YAW*YAW-1.69116*YAW + 1.15076
         KN2(I) = -0.925408*PITCH**5 + 4.97674*PITCH**4-10.2698*PITCH**3 + 10.2
   12954*PITCH*PITCH-5.13504*PITCH + 2.19519
C
C  RECALCULATE DATA REDUCTION COEFFICIENTS
C
         A1(I) = CT1*CT1 + KT1(I)*KT1(I)*ST1*ST1
         B1(I) = ST1*ST1 + KT1(I)*KT1(I)*CT1*CT1
         D1(I) = 2.0*(1.0-KT1(I)*KT1(I))*CT1*ST1
         F1(I) = B1(I)-KN1(I)*KN1(I)
         A2(I) = CT2*CT2 + KT2(I)*KT2(I)*ST2*ST2
         B2(I) = ST2*ST2 + KT2(I)*KT2(I)*CT2*CT2
         D2(I) = 2.0*(1.0-KT2(I)*KT2(I))*CT2*ST2
         F2(I) = B2(I)-KN2(I)*KN2(I)
         AP1(I) = A1(I)
         BP1(I) = B1(I)*CP*CP + KN1(I)*KN1(I)*SP*SP
         CP1(I) = B1(I)*SP*SP + KN1(I)*KN1(I)*CP*CP
         DP1(I) = D1(I)*CP
         EP1(I) = D1(I)*SP
         FP1(I) = F1(I)*SIN(2.0*PHI(I))
         AP2(I) = A2(I)
         BP2(I) = B2(I)*CP*CP + KN1(I)*KN1(I)*SP*SP
         CP2(I) = B2(I)*SP*SP + KN1(I)*KN1(I)*CP*CP
         DP2(I) = D2(I)*CP
         EP2(I) = D2(I)*SP
```

```
      FP2(I) = F2(I)*SIN(2.0*PHI(I))
  55 CONTINUE
      WRITE(*,*) 'END OF LOOP',LOOP
  58 CONTINUE
C
C   CALCULATE P,Q,R (COEFFICIENTS FOR TURBULENCE EQUATIONS)
C
      DO 60 I=1,5
      SQRAP1 = SQRT(AP1(I))
      P1(I) = SQRAP1 + (DP1(I)*VAVG + EP1(I)*WAVG)/2.0/SQRAP1/UAVG
      Q1(I) = DP1(I)/2.0/SQRAP1 + BP1(I)*VAVG/SQRAP1/UAVG + FP1(I)*WAVG/2.0/SQ
     1RAP1/UAVG
      R1(I) = EP1(I)/2.0/SQRAP1 + CP1(I)*WAVG/SQRAP1/UAVG + FP1(I)*VAVG/2.0/SQ
     1RAP1/UAVG
      SQRAP2 = SQRT(AP2(I))
      P2(I) = SQRAP2 + (DP2(I)*VAVG + EP2(I)*WAVG)/2.0/SQRAP2/UAVG
      Q2(I) = DP2(I)/2.0/SQRAP2 + BP2(I)*VAVG/SQRAP2/UAVG + FP2(I)*WAVG/2.0/SQ
     1RAP2/UAVG
      R2(I) = EP2(I)/2.0/SQRAP2 + CP2(I)*WAVG/SQRAP2/UAVG + FP2(I)*VAVG/2.0/SQ
     1RAP2/UAVG
  60 CONTINUE
      ICOUNT = 5
C
C   THIS LOOP FINDS THE TURBULENCE VALUES FROM VALUES FOR WIRE SENSOR 2.
C   A SIMILAR LOOP CAN BE ADDED FOR SENSOR 1.
C
      DO 65 I=1,5
      AA(1,1) = P2(1)*P2(1)
      AA(1,2) = Q2(1)*Q2(1)
      AA(1,3) = R2(1)*R2(1)
      AA(1,4) = 2.0*P2(1)*Q2(1)
      AA(1,5) = 2.0*P2(1)*R2(1)
      AA(1,6) = 2.0*Q2(1)*R2(1)
      AA(2,1) = P2(2)*P2(2)
      AA(2,2) = Q2(2)*Q2(2)
      AA(2,3) = R2(2)*R2(2)
      AA(2,4) = 2.0*P2(2)*Q2(2)
      AA(2,5) = 2.0*P2(2)*R2(2)
      AA(2,6) = 2.0*Q2(2)*R2(2)
      AA(3,1) = P2(3)*P2(3)
      AA(3,2) = Q2(3)*Q2(3)
      AA(3,3) = R2(3)*R2(3)
      AA(3,4) = 2.0*P2(3)*Q2(3)
      AA(3,5) = 2.0*P2(3)*R2(3)
      AA(3,6) = 2.0*Q2(3)*R2(3)
      AA(4,1) = P2(4)*P2(4)
      AA(4,2) = Q2(4)*Q2(4)
      AA(4,3) = R2(4)*R2(4)
      AA(4,4) = 2.0*P2(4)*Q2(4)
      AA(4,5) = 2.0*P2(4)*R2(4)
      AA(4,6) = 2.0*Q2(4)*R2(4)
      AA(5,1) = P2(5)*P2(5)
```

```fortran
      AA(5,2)=Q2(5)*Q2(5)
      AA(5,3)=R2(5)*R2(5)
      AA(5,4)=2.0*P2(5)*Q2(5)
      AA(5,5)=2.0*P2(5)*R2(5)
      AA(5,6)=2.0*Q2(5)*R2(5)
      AA(6,1)=P1(I)*P2(I)
      AA(6,2)=Q1(I)*Q2(I)
      AA(6,3)=R1(I)*R2(I)
      AA(6,4)=P1(I)*Q2(I)+P2(I)*Q1(I)
      AA(6,5)=P1(I)*R2(I)+P2(I)*R1(I)
      AA(6,6)=Q1(I)*R2(I)+Q2(I)*R1(I)
      BB(1)=UPEFF2(1)
      BB(2)=UPEFF2(2)
      BB(3)=UPEFF2(3)
      BB(4)=UPEFF2(4)
      BB(5)=UPEFF2(5)
      BB(6)=U12PEFF(I)
      N=6
      NDIM=6
      CALL LUDCMP(AA,N,NDIM,ORDER1)
      CALL SOLVLU(AA,BB,XX,N,NDIM,ORDER1)
      IF(XX(1).LE.0.0.OR.XX(2).LE.0.0.OR.XX(3).LE.0.0)THEN
        ICOUNT=ICOUNT-1
        XX(1)=0.0
        XX(2)=0.0
        XX(3)=0.0
        XX(4)=0.0
        XX(5)=0.0
        XX(6)=0.0
        WRITE(*,*) ' NEGATIVE TURBULENCE * * * TOSSED OUT!!!!'
      ENDIF
      UP2(I)=XX(1)
      VP2(I)=XX(2)
      WP2(I)=XX(3)
      UVP(I)=XX(4)
      UWP(I)=XX(5)
      VWP(I)=XX(6)
      WRITE(*,*) 'up^2 = ',UP2(I)
      WRITE(*,*) 'vp^2 = ',VP2(I)
      WRITE(*,*) 'wp^2 = ',WP2(I)
      WRITE(*,*) 'upvp^2 = ',UVP(I)
      WRITE(*,*) 'upwp^2 = ',UWP(I)
      WRITE(*,*) 'vpwp^2 = ',VWP(I)
   65 CONTINUE
C
C   THE ESTIMATES ARE AVERAGED AND WRITTEN TO THE OUTPUT DATA FILE
C
      WRITE(*,*)
      WRITE(*,*)
      UP2SUM=0.0
      VP2SUM=0.0
      WP2SUM=0.0
```

```fortran
      UVPSUM = 0.0
      UWPSUM = 0.0
      VWPSUM = 0.0
      DO 70 I = 1,5
        UP2SUM = UP2SUM + UP2(I)
        VP2SUM = VP2SUM + VP2(I)
        WP2SUM = WP2SUM + WP2(I)
        UVPSUM = UVPSUM + UVP(I)
        UWPSUM = UWPSUM + UWP(I)
        VWPSUM = VWPSUM + VWP(I)
   70 CONTINUE
      XCOUNT = FLOAT(ICOUNT)
      UP2AVG = UP2SUM/XCOUNT
      VP2AVG = VP2SUM/XCOUNT
      WP2AVG = WP2SUM/XCOUNT
      UVPAVG = UVPSUM/XCOUNT
      UWPAVG = UWPSUM/XCOUNT
      VWPAVG = VWPSUM/XCOUNT
      WRITE(*,*) 'up^2avg = ',UP2AVG
      WRITE(*,*) 'vp^2avg = ',VP2AVG
      WRITE(*,*) 'wp^2avg = ',WP2AVG
      WRITE(*,*) 'upvpavg = ',UVPAVG
      WRITE(*,*) 'upwpavg = ',UWPAVG
      WRITE(*,*) 'vpwpavg = ',VWPAVG
      YLOC = (YLOC-DIST)/2.54
      ALPHA = ATAN(VAVG/UAVG)
      BETA = ATAN(WAVG/UAVG)
      ALPHAD = ALPHA*180.0/PI
      BETAD = BETA*180.0/PI
      UR = SQRT(UAVG*UAVG+VAVG*VAVG+WAVG*WAVG)
      WRITE(8,*) YLOC,ZLOC,UINF
      WRITE(8,*) UR,ALPHAD,BETAD
      WRITE(8,*) UAVG,VAVG,WAVG
      WRITE(8,*) UP2AVG,VP2AVG,WP2AVG
      WRITE(8,*) UVPAVG,UWPAVG,VWPAVG
      GOTO 5
  999 STOP
      END
C
C   THE FOLLOWING SUBROUTINES SOLVE SIMULTANEOUS EQUATIONS.
C   THEY ARE TAKEN FROM "APPLIED NUMERICAL ANALYSIS" BY CURTIS GERALD
C   AND PATRICK WHEATLEY.
C
      SUBROUTINE LUDCMP(A,N,NDIM,ORDER)
      REAL A(NDIM,N)
      INTEGER N,NDIM,ORDER(N)
    . REAL SUM
      INTEGER I,KCOL,NM1,JM1,JCOL,JP1,IROW
      DO 10 I = 1,N
        ORDER(I) = I
   10 CONTINUE
      CALL APVT(A,N,NDIM,ORDER,1)
```

```fortran
      IF(ABS(A(1,1)).LT.1.0E-5) THEN
        PRINT 100
        RETURN
      ENDIF
      DO 20 KCOL=2,N
         A(1,KCOL)=A(1,KCOL)/A(1,1)
   20 CONTINUE
      NM1=N-1
      DO 80 JCOL=2,NM1
        JM1=JCOL-1
        DO 50 IROW=JCOL,N
          SUM=0.0
          DO 40 KCOL=1,JM1
            SUM=SUM+A(IROW,KCOL)*A(KCOL,JCOL)
   40       CONTINUE
          A(IROW,JCOL)=A(IROW,JCOL)-SUM
   50     CONTINUE
        CALL APVT(A,N,NDIM,ORDER,JCOL)
        IF(ABS(A(JCOL,JCOL)).LT.1.0E-5) THEN
          PRINT 100
          RETURN
        ENDIF
        JP1=JCOL+1
        DO 70 KCOL=JP1,N
          SUM=0.0
          DO 60 IROW=1,JM1
            SUM=SUM+A(JCOL,IROW)*A(IROW,KCOL)
   60       CONTINUE
          A(JCOL,KCOL)=(A(JCOL,KCOL)-SUM)/A(JCOL,JCOL)
   70     CONTINUE
   80 CONTINUE
      SUM=0.0
      DO 90 KCOL=1,NM1
        SUM=SUM+A(N,KCOL)*A(KCOL,N)
   90 CONTINUE
      A(N,N)=A(N,N)-SUM
      RETURN
C
  100 FORMAT(/,' VERY SMALL PIVOT ELEMENT INDICATES A NEARLY ',
     +       ' SINGULAR MATRIX.  ')
      END
C
C
C
      SUBROUTINE APVT(A,N,NDIM,ORDER,JCOL)
      REAL A(NDIM,N)
      INTEGER ORDER(N),N,NDIM,JCOL
      REAL SAVE,ANEXT,BIG
      INTEGER IPVT,JP1,IROW,KCOL,ISAVE
      IPVT=JCOL
      BIG=ABS(A(JCOL,JCOL))
      JP1=JCOL+1
```

```fortran
      DO 10 IROW=JP1,N
        ANEXT=ABS(A(IROW,JCOL))
        IF(ANEXT.GT.BIG) IPVT=IROW
10    CONTINUE
      IF(IPVT.EQ.JCOL) THEN
        RETURN
      ENDIF
      DO 20 KCOL=1,N
        SAVE=A(JCOL,KCOL)
        A(JCOL,KCOL)=A(IPVT,KCOL)
        A(IPVT,KCOL)=SAVE
20    CONTINUE
      ISAVE=ORDER(JCOL)
      ORDER(JCOL)=ORDER(IPVT)
      ORDER(IPVT)=ISAVE
      RETURN
      END
C
C
C
C
C
      SUBROUTINE SOLVLU(LU,B,X,N,NDIM,ORDER)
      REAL LU(NDIM,N),B(N),X(N)
      INTEGER ORDER(N),N,NDIM
      REAL SUM
      INTEGER I,J,JCOL,IROW,NP1,NVBL,IM1
      DO 10 I=1,N
        J=ORDER(I)
        X(I)=B(J)
10    CONTINUE
      X(1)=X(1)/LU(1,1)
      DO 50 IROW=2,N
        IM1=IROW-1
        SUM=0.0
        DO 40 JCOL=1,IM1
          SUM=SUM+LU(IROW,JCOL)*X(JCOL)
40      CONTINUE
        X(IROW)=(X(IROW)-SUM)/LU(IROW,IROW)
50    CONTINUE
      DO 70 IROW=2,N
        NVBL=N-IROW+1
        SUM=0.0
        NP1=NVBL+1
        DO 60 JCOL=NP1,N
          SUM=SUM+LU(NVBL,JCOL)*X(JCOL)
60      CONTINUE
        X(NVBL)=X(NVBL)-SUM
70    CONTINUE
      RETURN
      END
```